Enabling the 3D atomic-scale imaging of hydrogen in zirconium alloy fuel cladding



Megan Elizabeth Jones

University of Oxford

A thesis submitted for the degree of

Doctor of Philosophy

Hilary Term 2023

Abstract

Zirconium alloys are used as the fuel cladding and structural components in nuclear fission reactors. However, while in service, hydrogen is absorbed into these alloys which leads to the embrittlement of the cladding. When the mechanical properties of the cladding deteriorate to the point that they are no longer safe for deployment within the reactor, the entire fuel rod must be removed and disposed of. Hence hydrogen embrittlement of the Zr cladding is a life-limiting factor for nuclear fuel. Thus, an improved understanding of hydrogen pick up and embrittlement is critical in order for the nuclear industry to achieve its aims of increasing fuel burn up and decreasing waste. However, hydrogen is notoriously difficult to characterise using conventional electron and x-ray microscopy techniques. Alternatively, atom probe tomography (APT) has previously been demonstrated to be capable of analysing the 3D distribution of hydrogen (as the isotope deuterium) on the atomic scale. This thesis focuses on developing new approaches, based around the use of deuterium as an isotopic surrogate for hydrogen and APT, to image hydrogen at the atomic scale in zirconium alloys.

This work studies the production of deuterium charged samples for APT analysis, the analysis of the APT data and its application to neutron irradiated zirconium samples. Protocols were developed to deuterium charge Zircaloy-4 APT needles with deuterium using a gas reaction cell. Furthermore, an alternate method of sample preparation was to produce APT needles from a deuterated bulk specimen. The use of cryogenic focused ion beam (FIB) methods for the final sample preparation stages were investigated and the developed process was implemented in order to analyse the distribution of hydrogen within deuterated Zircaloy-4 samples.

Novel data analysis methods were conceptualised and developed to quantify deuterium concentrations in the APT data by addressing cases where peak overlaps or thermal tail effects limited the accuracy of compositional measurements. This was done by opti-

mising the extraction of data from the mass spectrum and how the data is handled. The developed method was used to quantify deuterium concentrations across a Zr/ deuteride boundary.

The characterisation of cold worked Zircaloy-4 microstructures were investigated via APT as a viable surrogate for irradiation induced damage. Finally, neutron irradiated Zircaloy-2 samples were deuterium charged and prepared for APT using cryogenic FIB and complementary secondary ion mass spectrometry to investigate the interaction of deuterium with irradiation induced defects. Samples were successfully analysed demonstrating a valid experimental technique and an avenue for future research.

Preface

The work presented in this doctoral thesis has been carried out at the Department of Materials, University of Oxford from October 2018 to April 2023, under the supervision of Dr. Daniel Haley, Professor Michael Moody, and Dr. Benjamin Jenkins. All of the research carried out for this thesis is original and where the work of others has been included it has been clearly referenced and acknowledged. No part of this thesis has been submitted for a degree at this, or any other university.

Acknowledgements

This thesis may have my name written as the author on the cover but I would not have been able to conduct the experiments or produce the thesis without the unwavering support of my supervisors, colleagues, friends and family.

To my supervisors Prof. Michael Moody, Dr. Daniel Haley and Dr. Benjamin Jenkins, thank you for all of the help and support during my PhD. Michael, thanks for your unwavering support over the past 8 years and for giving me the chance to work on such an interesting project. Dan, thank you for teaching me everything I know about APT and data analysis. Ben, thank you for the help and the vast amounts of thesis proof reading.

I am grateful for the support from Dr. Paul Styman (National Nuclear Laboratory) and Shyam Sikotra (Rolls-Royce) for providing valuable input and the Zircaloy-4 samples used throughout my project. This project was made possible by the funding provided by the National Nuclear Laboratory and Rolls-Royce.

I owe many people my gratitude for their help with various aspects of this work but a few deserve to be mentioned by name. Firstly, Dr. Andy London, thank you for all of your peak overlap solving (and MATLAB) related help. Dr. James Douglas, your FIB wizardry and APT knowledge were much appreciated, the puns, sometimes. To my office-mates, Dr.'s Anne Callow, Hazel Gardener and James Famelton, thank you for the help, entertaining office antics and the forest of plants. To Dr. Zhao Shen, Dr. David Tweddle and Dr. Jack Haley, thank you for their help producing the TEM data of the cold worked samples. I conducted research at or with the help colleagues at other institutions and I would like to thank the following for their help; Dr. Andrew Breen (University of Sydney), Dr. Chris Parmenter (University of Nottingham), Dr. Adam Qaisar, Dr. Ian Vatter and Richard Cooke (National Nuclear Laboratory).

To the past and present members of the APT Group, your friendship and general craziness made my PhD so much fun. I hope future members have such fond memories of

their time in the group.

To my friends, thanks for the support and sticking with me when life was hard and my atom probe samples kept fracturing. Jack and Lisa, thanks for being wonderful housemates during lockdown.

To my family, thank you for your support and the encouragement you have always given me.

My final thanks goes to Joy Humphrey, my form tutor and maths teacher who gave me the confidence to apply to Oxford, helped with my application and started me off on my journey as a Materials Scientist.

Dominus illuminatio mea

Contents

1 Introduction **1**

1.1 Background 1

1.2 Current Work 1

1.3 Thesis Structure 2

1.4 Publications 3

1.5 Conference Presentations and Posters 4

2 Literature Review **5**

2.1 Zirconium in the Nuclear Industry 5

2.2 Zirconium Alloys 9

2.3 Zirconium Alloy Corrosion 11

2.4 Irradiation Damage of Zirconium alloys 13

2.5 Hydrogen Pick Up in Zirconium Alloys 15

2.5.1 Hydrogen in Zirconium 15

2.5.2 Hydrogen Pick Up Mechanisms 17

2.5.3 Factors affecting Hydrogen Pick Up 22

2.5.4 Growth and Nucleation of Hydrides 25

2.5.5 Effects on Mechanical Properties 27

2.6 Imaging and Detection of Hydrogen 30

2.7 Atom Probe Tomography 32

2.7.1 APT of Zirconium Alloys 32

2.7.2 Imaging of Hydrogen using APT 34

2.8 Summary . . . 39

3 Experimental Methods **41**

3.1 Materials . . . 41

3.1.1 Cold Worked Zircaloy-4 . . . 41

3.1.2 Zirconium Wire . . . 42

3.1.3 Deuterated Zircaloy-4 . . . 42

3.1.4 Neutron-Irradiated Zircaloy-2 samples . . . 42

3.2 Atom Probe Tomography . . . 43

3.2.1 Basic Principles . . . 43

3.2.2 Composition Calculations . . . 46

3.2.3 APT Analysis Conditions . . . 53

3.3 Sample Preparation . . . 56

3.3.1 Scanning Electron Microscopy . . . 56

3.3.2 Atom Probe Tomography: Electropolishing . . . 57

3.3.3 Atom Probe Tomography: Focused Ion Beam . . . 59

3.3.4 Sample Preparation Observations . . . 62

3.3.5 Samples for Transmission Kikuchi Diffraction . . . 62

3.4 Deuterium Charging . . . 63

3.4.1 Reaction Cell . . . 64

3.4.2 Hydrogen Charging Protocol . . . 66

3.5 Developing deuterium charging protocols . . . 67

3.6 Cryogenic focused ion beam sample preparation . . . 71

3.7 APT of Cold Worked Zircaloy-4 . . . 71

3.8 APT of Irradiated Zircaloy-2 . . . 71

4 Deuterium Charging Protocol Development **73**

4.1 Introduction . . . 73

4.2 Preventing sample oxidation during D_2 charging . . . 77

4.2.1 Experimental Methods . . . 77
4.2.2 Oxidation sources . . . 79
4.2.3 Gas filtering . . . 84
4.3 Optimising deuterium charging parameters . . . 91
4.3.1 Expected Data . . . 91
4.3.2 Charging Parameter Optimisation . . . 94
4.4 Conclusions . . . 105

5 Cryogenic Focused Ion Beam Sample Preparation 108
5.1 Introduction . . . 108
5.2 Results and Discussion . . . 111
5.2.1 Effect of cryogenic FIB methods on hydrogen pick up in Zircaloy-4 APT samples . . . 111
5.2.2 Use of cryogenic FIB techniques to prepare APT samples from deuterated Zircaloy-4 . . . 113
5.3 Conclusions . . . 118

6 Improving the Data Analysis of Deuterated Zr Alloy APT Data 119
6.1 Introduction . . . 119
6.1.1 Key Terms . . . 120
6.1.2 Motivation . . . 120
6.2 Nb Composition Verification . . . 123
6.2.1 Nb composition verification between software packages . . . 123
6.2.2 Peak Count Quantification . . . 127
6.3 Improving the analysis of deuterated Zircaloy-4 APT data . . . 134
6.3.1 Improving the quantification of deuterium in Zircaloy-4 APT data . . . 134
6.3.2 Spatially localised peak overlap solving . . . 141
6.4 Conclusions . . . 152

7 Atom Probe Tomography of Cold Worked Zircaloy-4 154

7.1 Introduction . . . 154
7.2 Results and Discussion . . . 156
7.3 Conclusions . . . 169

8 Atom Probe Tomography of Irradiated Zircaloy-2 172
8.1 Introduction . . . 172
8.2 Experimental Methods . . . 172
8.3 Results and Discussion . . . 176
8.4 Conclusions . . . 189

9 Conclusions and Future Work 191
9.1 Conclusions . . . 191
9.1.1 Developing Deuterium Charging Protocols . . . 191
9.1.2 Cryogenic Focused Ion Beam Sample Preparation . . . 192
9.1.3 Improving the Data Analysis of Deuterated Zr Alloy APT Data . . . 193
9.1.4 Atom Probe Tomography of Cold Worked Zircaloy-4 . . . 194
9.1.5 Atom Probe Tomography of Irradiated Zircaloy-2 . . . 194
9.2 Future Work . . . 195

A Experimental Data i
A.1 Experimental Methods . . . i
A.2 Deuterium Charging Protocol Development . . . ii
A.3 Cryogenic Focused Ion Beam Sample Preparation . . . ix
A.4 Improving the Data Analysis of Deuterated Zr Alloy APT Data . . . xi
A.5 Atom Probe Tomography of Cold Worked Zircaloy-4 . . . xii
A.6 Atom Probe Tomography of Irradiated Zircaloy-2 . . . xvi

B Details of Figures xix
B.1 Experimental Methods . . . xix
B.2 Deuterium Charging Protocol Development . . . xx

B.3 Cryogenic Focused Ion Beam Sample Preparation xxi
B.4 Improving the Data Analysis of Deuterated Zr Alloy APT Data xxii
B.5 Atom Probe Tomography of Cold Worked Zircaloy-4 xxiv
B.6 Atom Probe Tomography of Irradiated Zircaloy-2 xxiv

Chapter 1

Introduction

1.1 Background

Zirconium alloys are used in nuclear fission reactors as the cladding, where they contain the fuel and prevent contact between the fuel and the coolant, and the release of fission products. The adsorption of hydrogen during reactor operation leads to the hydrogen embrittlement of the cladding. The effects of hydrogen embrittlement are limiting the life-time of nuclear fuel by the formation of brittle hydride phases which degrade the mechanical properties of the cladding and enable crack propagation via delayed hydride cracking. In order to prevent the effects of hydrogen embrittlement and improve the data behind nuclear safety cases so fuel burn up can be safely increased; hydrogen embrittlement must be fully understood.

1.2 Current Work

Hydrogen is the lightest chemical element so does not interact with x-rays or electron beams sufficiently well, thus it is difficult to unambiguously interpret its signal. As a result it is difficult to characterise hydrogen in materials using common characterisation techniques. APT provides 3D nano-scale chemical information and has high chemical sensitivity and spatial resolution. The focus of this thesis was to develop methods to image and detect

hydrogen in zirconium alloy fuel cladding by developing methods of producing deuterated Zr alloy samples by hydrogen charging prepared needles and optimising the production of specimens from a deuterated bulk sample, and analysing the data of the deuterium charged material. The developed methods were applied to analyse the distribution of hydrogen in neutron irradiated Zircaloy-2 samples.

1.3 Thesis Structure

In Chapter 2, an overview of the role of zirconium alloys in the nuclear industry and the effect of this extreme environment on the cladding will be given. Our current understanding of hydrogen pick up in Zr alloys will be presented. Finally, the current methods of imaging hydrogen in materials, with a focus on current APT techniques will be discussed.

Chapter 3 contains an explanation of the main experimental methods used in the work, namely APT and the custom-built gas reaction cell. Then, the methods of APT sample production and other related experimental details are given.

Chapter 4 is the first of five experimental results chapters. This chapter focuses on the lessons learnt during the development of the deuterium gas charging protocol using the reaction cell.

Chapter 5 discusses the use of cryogenic focused ion beam techniques to produce APT needles from a deuterated Zircaloy-4 sample. This method was explored to develop an understanding of hydrogen pick up during sample preparation.

In Chapter 6 the development of novel methods to quantify the deuterium concentration in Zr alloys APT data is presented. The importance of accurately extracting data from the mass spectrum is demonstrated, and a more accurate method of solving peak overlaps in Zr alloy samples is shown. These methods are used to quantify deuterium concentrations in a Zr/ Zr deuteride boundary. A method of solving peak overlaps at a local scale is trialled and the results discussed.

Chapter 7 looks at the use of cold worked Zircaloy-4 samples as a surrogate for

irradiated materials to investigate the interaction of hydrogen with dislocations.

Chapter 8 uses the methods developed in the previous chapters to analyse deuterium charged, neutron irradiated Zircaloy-2 samples to investigate the interaction of deuterium with irradiation induced defects.

The final chapter summarises the main conclusions of this thesis and avenues for future research are discussed.

There are two appendices to this thesis which contain useful information relating to this work but did not need to be included in the main body of the text. Appendix A is a record of all (useful) APT experiments conducted as part of this work and the APT analysis conditions. Appendix B lists the APT experiment ID and other associated data for each figure to preserve this information for future use.

1.4 Publications

Some of the work presented in this thesis was published in peer-reviewed journals and the author contributed to other works. These are listed below:

M. E. Jones, A. J. London, A. J. Breen, P. D. Styman, S. Sikotra, M. P. Moody, D. Haley, *"Improving the Quantification of Deuterium in Zirconium Alloy Atom Probe Tomography Data Using Existing Analysis Methods,"* Microscopy and Microanalysis, 2021

M. S Meier, **M. E. Jones**, P. Felfer, M. P. Moody, D. Haley, *"Extending Estimating Hydrogen Content in Atom Probe Tomography Experiments Where H2 Molecule Formation Occurs,"* Microscopy and Microanalysis, 2021

Y. Shi, **M. E. Jones**, M. S. Meier, M. Wright, J.-I. Polzin, W. Kwapil, C. Fischer, M. Schubert, C. Grovenor, M. Moody, R. S. Bonilla, *"Towards accurate atom scale characterisation of hydrogen passivation of interfaces in TOPCon architectures,"* Solar Energy Materials and Solar Cells, 2022

1.5 Conference Presentations and Posters

Parts of this thesis were also presented at international conferences. The details of such presentations are given below:

"Developing techniques to image hydrogen at the atomic-scale in zirconium alloys," **M. E. Jones**, D. Haley, P. Styman, S. Sikotra, M. P. Moody, European Atom Probe Workshop, Rouen, France, 2019. Poster Presentation

"Improving the quantification of deuterium in zirconium alloy APT data,", **M. E. Jones**, A. J. London, A. J. Breen, P. D. Styman, S. Sikotra, M. P. Moody, D. Haley, North Rhine-Westphalia Atom Probe Tomography User Meeting, Düsseldorf (virtual), Germany, 2020, Invited Talk

"Improving the quantification of deuterium in Zr alloy APT data" **M. E. Jones**, A. J. London, A. J. Breen, P. D. Styman, S. Sikotra, M. P. Moody, D. Haley, Atom Probe Tomography and Microscopy, Oxford (virtual), U.K., 2021, Short Video Presentation

"Improving the Quantification of Deuterium in Zr Alloy Atom Probe Tomography Data," **M. E. Jones**, A. J. London, A. J. Breen, B. M. Jenkins, P. D. Styman, S. Sikotra, M. P. Moody, D. Haley, Microscopy and Microanalysis Conference, Portland, U.S.A, 2022, Poster Presentation

"Trialling cryogenic FIB sample preparation for the analysis of hydrogen in Zr alloy APT experiments", **M. E. Jones**, C. Parmenter, B. M. Jenkins, P. D. Styman, S. Sikotra, M. P. Moody, D. Haley, Microscopy and Microanalysis Conference, Portland, U.S.A, 2022, Oral Presentation

Chapter 2

Literature Review

2.1 Zirconium in the Nuclear Industry

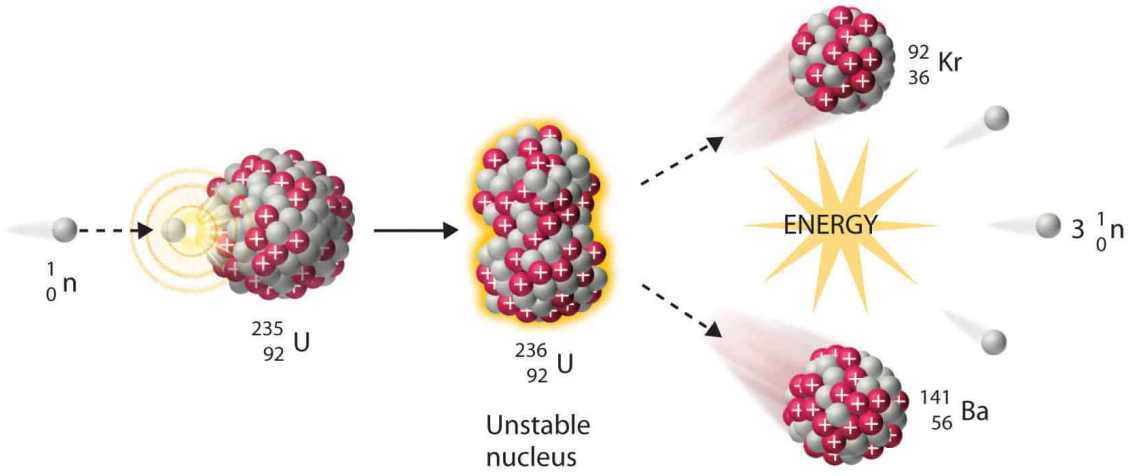


Figure 2.1: Diagram showing example fission reaction of uranium [1].

Nuclear fission reactors produce energy as a result of the uranium fuel undergoing a fission reaction. The uranium nuclei decompose into lighter nuclei, some neutrons and energy is released as part of the fission reaction (Figure 2.1). The energy produced can be harnessed for commercial purposes. Most commercial reactors are light water reactors (LWRs) of which there are two types: pressurized water reactors (PWRs, Figure 2.2) and boiling water reactors (BWRs). In these reactors, the fuel is in the form of fuel rods. These

are tubes of zirconium alloy containing uranium dioxide pellets. The fuel rods are arranged into fuel assemblies that make up the reactor core, as shown in Figure 2.3. These fuel assemblies are submerged in water, which acts as the moderator (and the coolant), slowing down fast neutrons to increase their chances of inducing further fission of the uranium fuel and to conduct heat away from the reactor core. The role of the cladding is to contain the fuel, which prevents its oxidation and the release of fission products into the coolant [2].

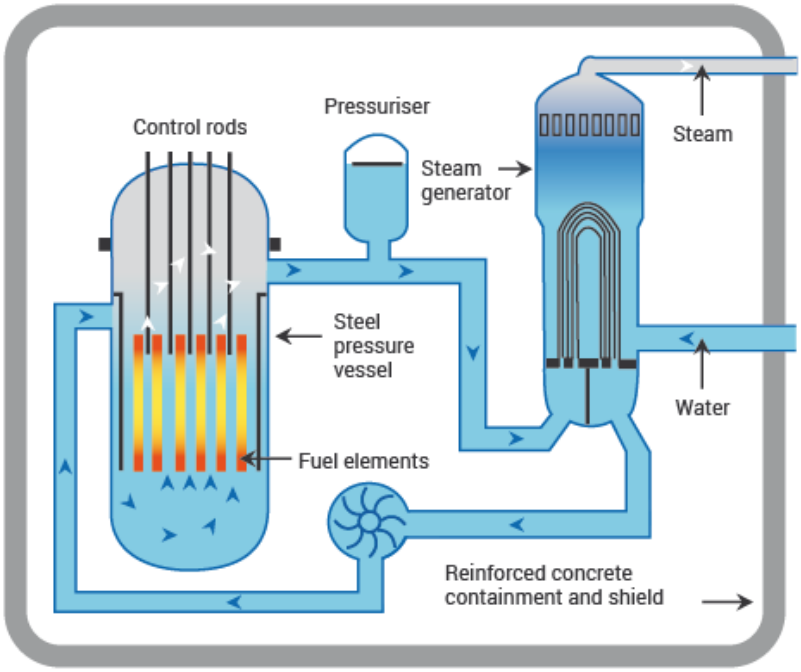


Figure 2.2: Schematic of a pressurised water reactor [3].

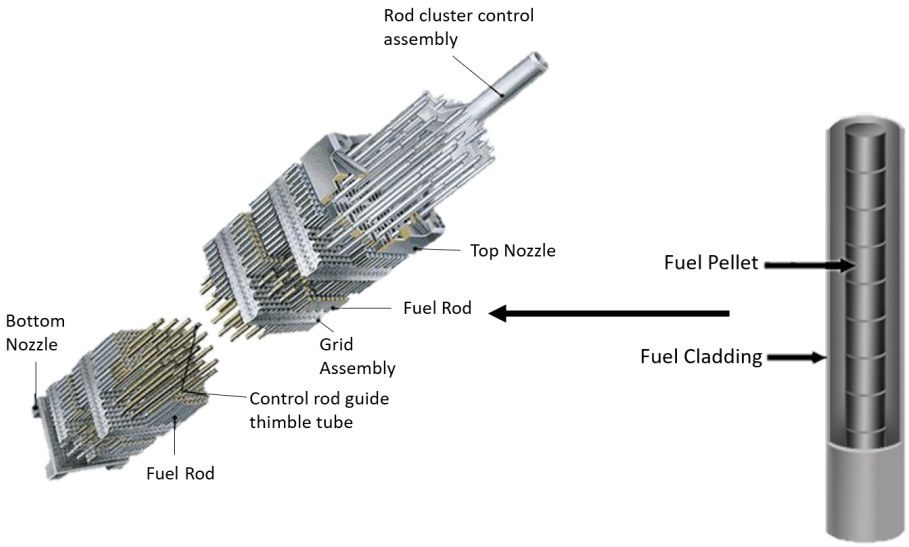


Figure 2.3: Schematic diagram of fuel rod assembly in a PWR (reproduced from [4] and [5]).

Zirconium alloys have been used as the fuel cladding for PWRs and BWRs since the 1960s [6]. Zirconium alloys are used for this application as they have good corrosion resistance, appropriate mechanical properties, including mechanical stability under stresses from high thermal gradients, and a low thermal neutron cross section of 0.185 barns [7].

There is a driving force for the nuclear industry to increase the reactor efficiency, conserving uranium resources and decreasing the quantity of spent fuel. The ability of the nuclear industry to increase burn up (amount of energy produced by the uranium) is currently limited by the integrity of the cladding.

Approximately 4 at.% of the uranium (at 40 GWd/t burn up) present in a fuel rod is ever consumed in a nuclear reactor. Around 1/3 of the spent fuel is removed every 18 months [8] due safety concerns regarding the degradation of the fuel cladding. The fuel cladding cannot be allowed fail as this would lead to the release of highly active fuel and fission products into the reactor. To ensure that the cladding remains intact, fuel elements are removed before they pose a safety issue. Replacing fuel rods is expensive and uranium resources are depleted and should be conserved. Increasing burn-up to 70 GWd/t would allow for longer operation cycles of around 24 months, reducing the number of discharged fuel assemblies by one third and the costs of the fuel cycle by 20% [8]. For this to occur,

improved fuel assemblies and in particular cladding materials are needed.

These materials are also used in other non-civil power applications, including the reactors of nuclear submarines. These reactors have more stringent requirements and re-fuelling is much more difficult. The fuel for these reactors contains a higher enrichment of uranium compared to civil fuel meaning that the fuel cladding is exposed to a higher neutron flux [9].

The reaction of cladding with the water leads to oxidation of the cladding and the production of hydrogen [10]. The absorption of the hydrogen leads to hydride formation, which acts to embrittle the material by decreasing the fracture toughness and the introduction of failure through the hydrides via delayed hydride cracking. This is an issue both in service and also in the storage of the spent fuel. The process of storing spent fuel begins with the fuel rods being placed into cooling ponds known as wet storage. No further degradation of the cladding is expected to occur as a result of corrosion during wet storage [11]. When the waste has been radiation cooled, spent fuel and other high level wastes are sealed in a canister and stored indefinitely in dry storage. The anaerobic corrosion of the canister materials (steel or copper alloys) produces additional hydrogen gas which can result in high hydrogen pressures resulting in further hydrogen absorption by the cladding [12]. The solubility of hydrogen in the Zr alloy matrix is temperature dependent. In service the solubility of hydrogen is in the region of 0.7 at.%, therefore most of the hydrogen is dissolved in the zirconium alloy matrix and is not in the form of hydrides [13]. However, not all of the cladding is at the same temperature due to contact with the coolant water, meaning that hydrides can precipitate at the outer edges forming hydride blisters and rims. In dry storage, the solubility of hydrogen is lower due to decreased temperature so hydride formation and crack growth by delayed hydride cracking are potential issues.

By increasing burn up and the subsequent length of service, enhanced hydrogen pick up is thought to occur and is one of the largest concerns on cladding performance [14]. Enhanced hydrogen pick up could lead to the formation of a hydride rim or other hydride features which may lead to an increase in cladding corrosion at an earlier point in the fuel

cycle. Increased dimensional changes of the fuel assembly components could also occur as a result of hydride formation (hydrides have a higher specific volume that is 10-17% larger than the bulk for γ-, ε- and δ-hydride phases) and the dimensional tolerance for fuel in a nuclear reactor is tight. Increasing hydrogen pick up could also lead to the enhanced embrittlement of Zr alloy components during accident conditions such as loss of coolant (LOCA), reactivity-initiated conditions and casket drop accidents during storage [14].

Hydrogen pick up is a key life-limiting factor for fuel rods, and understanding hydrogen pick up at the nano-scale has been identified as a key route to enhancing fuel life and subsequently reducing waste [15]. Therefore it is essential to understand the mechanisms behind pick up phenomena in order to mitigate their effects. This understanding would enable alloys that are less susceptible to hydrogen embrittlement to be developed. It would allow for guidelines to be modified as an understanding of the mechanisms of embrittlement can improve estimates of fuel degradation and safe operating conditions. Increasing fuel consumption would lead to increased operation time and decreasing waste, both of which will make nuclear power more profitable.

2.2 Zirconium Alloys

Zirconium has an atomic number of 40 and a relative atomic mass of 91.224 amu. Zirconium undergoes an allotropic phase change at 862 °C where the structure changes from hexagonal close packed (HCP) α-Zr to body centred cubic (BCC) β-Zr. The α-Zr phase is stable below 862 °C and has the following lattice constants: an *a* length of 3.24 Å and a *c* length of 5.16 Å [16]. The HCP unit cell is shown in Figure 2.4.

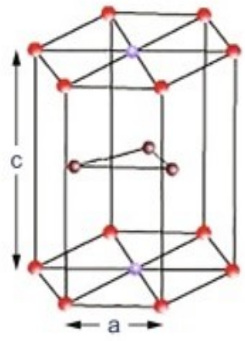


Figure 2.4: Unit cell of α-Zr, adapted from [17].

There are two primary zirconium alloy systems in use in currently operating reactors: the zirconium-tin and zirconium-niobium systems. The Zr-Sn system is used by the USA and in Europe and are known as the Zircaloys. The Zr-Nb system is used in fission reactors by the Canadians and the former USSR. Both of these systems use a minimum of approximately 97 wt.% Zr, with alloying elements including: Sn, Nb, Cr, Fe, Ni, S. Many alloys have been developed, those that are still in service include Zircaloy-2, Zircaloy-4, M4, M5 and ZIRLO. Typical compositions of these alloys are shown in Table 2.1.

Table 2.1: Typical compositions for zirconium alloys used as fuel cladding [7] .

Alloying Element	Zircaloy-2	Zircaloy-4	Zr-2.5Nb
Zr (wt.%)	balance	balance	balance
Sn (wt.%)	1.2-1.7	1.2-1.7	-
Fe (wt.%)	0.07-0.2	0.18-0.24	$<$650 ppm
Cr (wt.%)	0.05-0.15	0.07-0.13	$<$100 ppm
Ni (wt.%)	0.03-0.08	-	$<$35 ppm
Nb (wt.%)	-	-	2.4-2.8
O (ppm)	900-1300	900-1400	900-1300
N (ppm)	$<$80	$<$65	$<$65
H (ppm)	$<$25	$<$25	$<$5
C (ppm)	$<$270	150-400	$<$125

The Zircaloys have good corrosion resistance but are known to oxidise in the coolant, producing hydrogen. Zircaloy-2 and -4 both have corrosion resistance sufficient for BWR use and both of these alloys are still used today. In PWRs, the nickel content in Zircaloy-2 led to high levels of hydrogen being absorbed and the embrittlement of the cladding [18]. Zircaloy-4 was developed for use in PWRs; it has a similar composition to Zircaloy-2, but without any nickel and higher quantities of iron. The Zr-Nb alloys have since been developed to oxidise at a slower rate than Zircaloy-4 [19], [20].

2.3 Zirconium Alloy Corrosion

Zirconium alloys suffer from corrosion in service as a result of the contact with the coolant water. The equation below shows the reaction of water with zirconium to form zirconium oxide and hydrogen.

$$2\,\mathrm{H_2O_{(l)}} + \mathrm{Zr_{(s)}} \longrightarrow \mathrm{ZrO_{2(s)}} + 2\,\mathrm{H_{2(g)}}\ [10] \tag{2.1}$$

The mechanism by which this occurs is shown in Figure 2.5. In Reactions 1 and 2, the water molecule dissociates and is adsorbed onto the surface of the oxide layer. The defect concentration gradient and the electric potential across the oxide causes oxygen anions to diffuse through the bulk or the along grain boundaries in the oxide. At the oxide-metal interface the oxygen anions react with the zirconium cations to form zirconium oxide (Reactions 3 and 4) [21], [22]. The oxide formation releases electrons that move through the oxide using a hopping mechanism to reduce hydrogen ions (Reaction 5). Not all of the hydrogen ions recombine with electrons; these are absorbed by the oxide and diffuse to the metal. This phenomenon is known as hydrogen pick up [23].

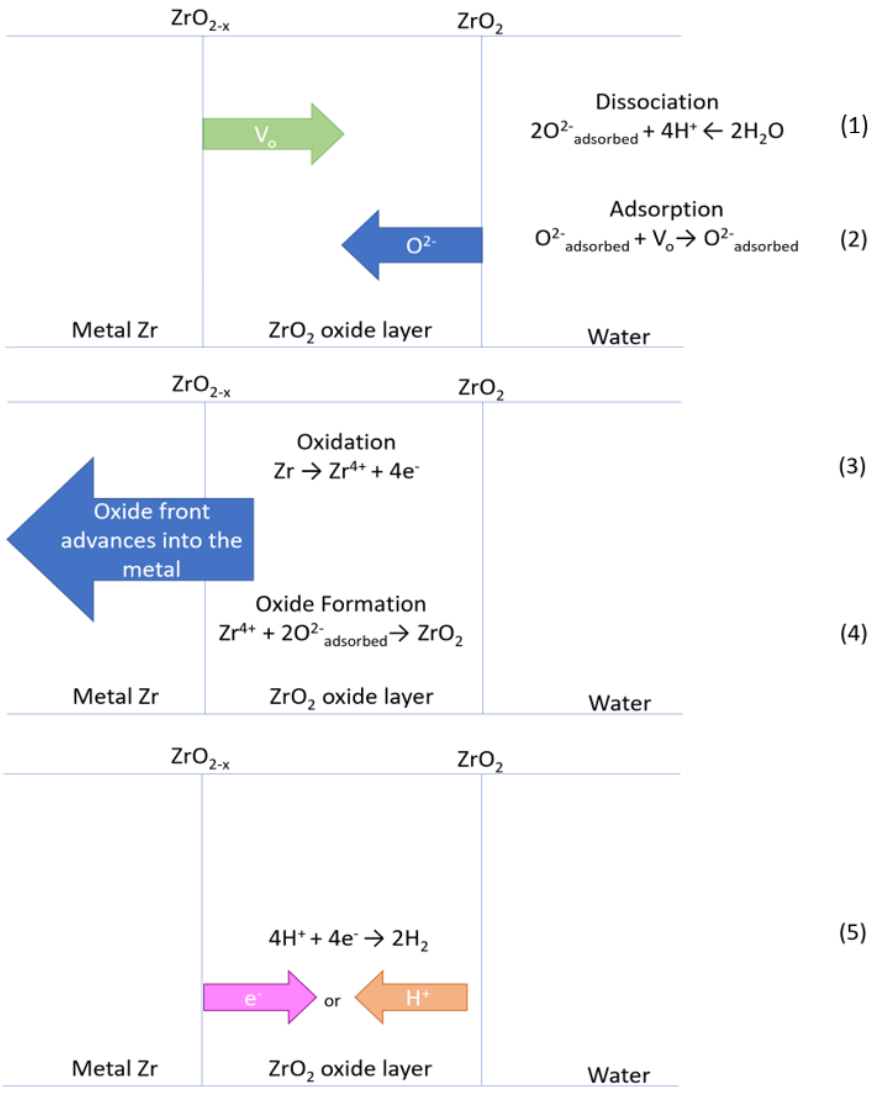


Figure 2.5: Diagram depicting the corrosion mechanism of zirconium leading to the formation of zirconium oxide. Reproduced from [10].

The oxide layer in zirconium alloys is made from different Zr and O containing phases, these include ZrO_2, ZrO and substoichiometric oxide phases. The oxide layer is initially passive, however it undergoes a transition where it loses its protectiveness [24]. As the alloy corrodes, the thickness of the oxide layer increases; at a critical thickness, 1.5-3 μm, the oxide transitions and a new layer of oxide is formed [25]. A feature of the corrosion of some Zr alloys is the repetitive growth of layers of oxide of constant thickness [26].

If the transition is disrupted the oxide grows unstably and the corrosion rate increases rapidly. This is known as breakaway corrosion. After this occurs, the oxide can regain protectiveness but in other instances it does not [10], [26]. Different alloys undergo different transition behaviours as shown in Figure 2.6.

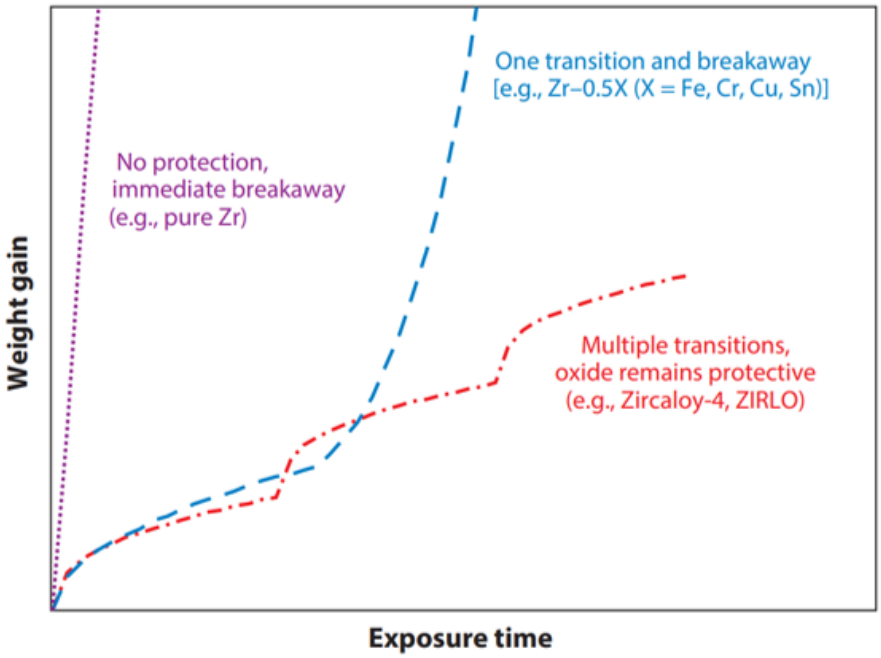


Figure 2.6: Graph showing the different transition behaviours of different zirconium alloys as measured by increase in weight gain due to oxide growth as a function of time [10].

2.4 Irradiation Damage of Zirconium alloys

Neutron bombardment of the cladding occurs during reactor operation as neutrons are produced as a product of the fission of uranium. A neutron of sufficient energy can displace an atom from its lattice site, this atom is called the primary knock on atom (PKA). Depending on its energy, the primary knock on atom can displace further atoms creating a ‘cascade’ of displaced atoms. The displaced atoms form point defects, the displaced atom is no longer on its lattice site and is at an interstitial site in the lattice, and are known as ‘self-interstitial atoms’ if they are of the same species as the lattice. The lattice site where

the self interstitial originated from is empty and called a ‘vacancy’. The self-interstitial and vacancy pair is known as a Frenkel Defect or Pair [27]. Most of these defects recombine and annihilate, however some diffuse until they are absorbed on lattice defects (sinks) such as grain boundaries, second phase particles or dislocations [28].

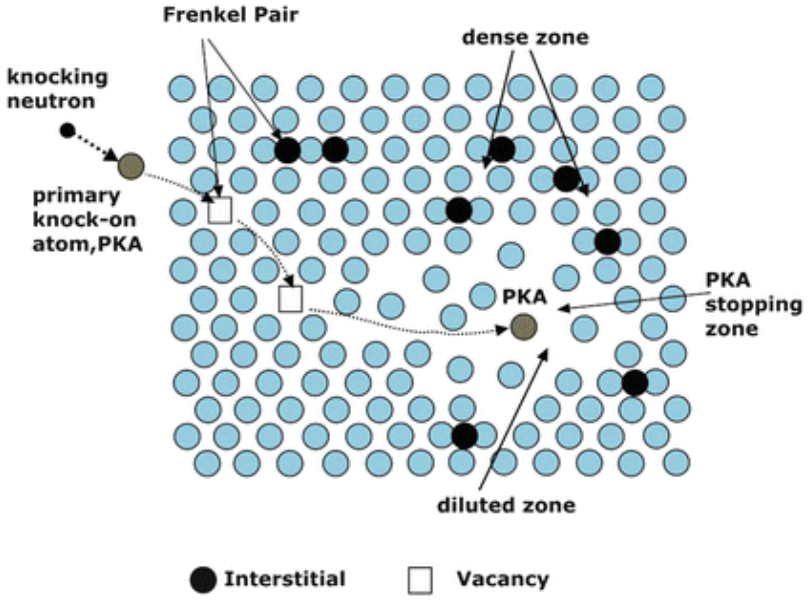


Figure 2.7: Schematic showing how neutrons interact with materials [29].

Dislocations loops can form by the agglomeration of vacancies or interstitials to form disc shaped defects. A vacancy loop forms when vacancies come together on the same lattice plane; whereas an interstitial loop forms when interstitial come together in between the same lattice planes. In Zr alloys, these defects accumulate into <a>- and <c>-loops which form on the prismatic and basal planes of the Zr structure (Figure 2.8)[28]. <a>-loops are both interstitial and vacancy type dislocations where as <c>-loops are only vacancy loops which only form at high irradiation doses [30], [31]. Both of these loop types are obstacles to dislocation motion, strengthening the alloy and the local stacking fault produced during loop formation contributes to irradiation hardening [32].

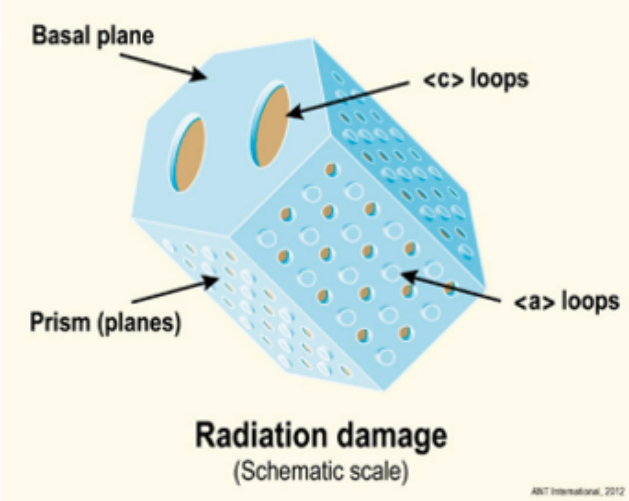


Figure 2.8: Diagram showing where the different types of dislocation loops form [28].

Other microstructural changes include changes in second phase particle (SPP) size, composition and crystallinity due to the irradiation damage changing the solubility of the alloying elements. In the Zircaloys, the Laves phases (Zr-Fe-Cr and Zr-Fe-Ni precipitates) become amorphous and will dissolve in the matrix . The dissolution of the SPPs increases the corrosion rate and hydrogen pick up [33].

The change in microstructure as a result of irradiation changes the properties of the cladding, including the corrosion rate, mechanical properties and the dimensions due to irradiation growth and creep [17].

2.5 Hydrogen Pick Up in Zirconium Alloys

2.5.1 Hydrogen in Zirconium

Hydrogen precipitates as a hydrides when the terminal solid solubility (TSS) is exceeded. The TSS is temperature dependent and decreases rapidly with decreasing temperature. In pure Zr this ranges from 5 at.% at 500°C to 0.7 at.% at 300°C and 10^{-4} at.% at 20°C [34]. There are four different hydride phases (Table 2.2). The hydride phase that forms depends on the hydrogen content and the cooling rate. The δ-hydride and ϵ-hydride are equilibrium phases with the γ and ζ-hydrides being metastable. Adapted from [35],

[36].

Table 2.2: Zirconium hydride phases [35]

Phase	Value of x in ZrH\textsubscript{x}	Structure	Lattice Parameter (nm)	
			a	c
α Zr matrix	0	Hexagonal	0.3232	0.5147
ζ-Hydride	0.5	Trigonal	0.3300	1.0290
γ-Hydride	1.0	Tetragonal	0.4596	0.4969
δ-Hydride	1.66	Cubic	0.4781	-
ϵ-Hydride	2.0	Tetragonal	0.3520	0.4450

Hydrogen is more stable in solid solution in the Zr matrix than as a gas at the operating temperatures and pressures of a nuclear reactor [37]. Under the conditions of a nuclear reactor the stable hydride phases are δ- and γ (temperatures of 275°C to 360°C, range highlighted in Figure 2.9), hence formation of these hydrides are of the most concern.

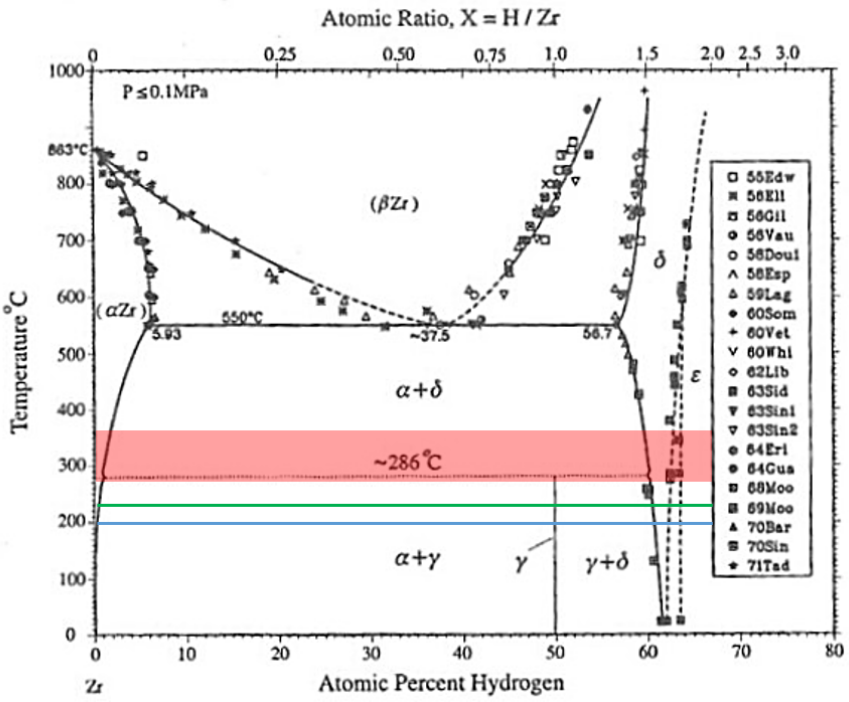


Figure 2.9: Zr-H Phase Diagram (Pressure = 0.1 MPa), the range of working temperatures of nuclear reactors is highlighted. The green line shows the temperature of the fuel rod at discharge and the blue the maximum temperature of the fuel in dry storage [38], [39].

2.5.2 Hydrogen Pick Up Mechanisms

Hydrogen sources in a nuclear reactor include as a product of the corrosion of zirconium alloys, water additives (e.g. LiOH), radiolysis of water and dissolved hydrogen in the fuel pellets and in the water [40]. When the absorbed hydrogen concentration exceeds the terminal solid solubility, hydrogen precipitates as zirconium hydrides.

There is little agreement on the exact pick up mechanism for hydrogen in zirconium alloys [41]–[43]. To reach the metal, hydrogen must pass through the oxide layer of the alloy. A perfect, defect-free oxide is impermeable to hydrogen, however real oxides contain defects such as grain boundaries [44]. The transport of hydrogen through the oxide occurs as a result of the presence of these defects.

Rudling and Wikmark proposed a mechanism for Zircaloy-2 using inverse rate constants called 'reaction resistances' (RR) that are related to each step in the corrosion and hydriding process (Figure 2.10) [45]. The rate-limiting parameters will have the highest RR value and control the overall reaction rate. The authors suggest two routes for hydrogen pick up in Zircaloy alloys that are dependent on the oxide thickness. When the oxide layer is thin, H transport occurs directly through the oxide and through the second phase particles (SPPs) when the oxide thickens. $RR_{H,\ init,\ barrier}$ increases as the pre-oxide transition regime progresses.

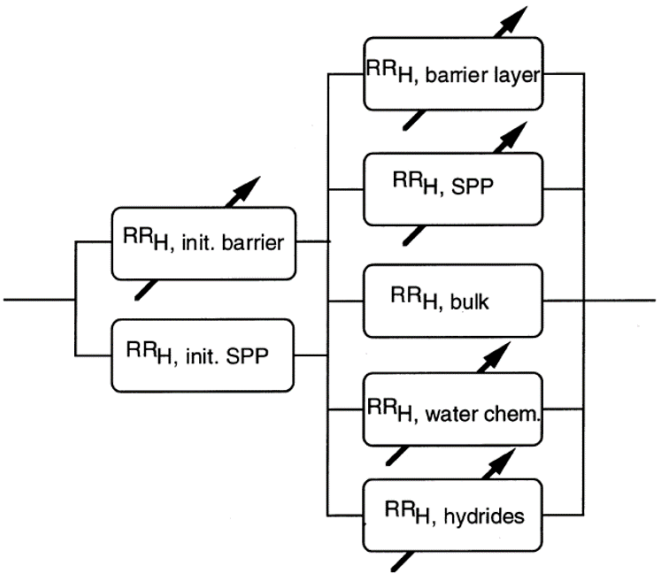


Figure 2.10: Schematic showing the reaction resistance (RR, inverse rate constant) based hydrogen pick up mechanism. In this mechanism the rate limiting process has the largest RR value and is dependent on the oxide thickness. The arrows indicate where the RR value is variable [45].

Ramasubramanian et al. studied hydrogen transport in the oxide layer and hydrogen pick up in Zr-2.5Nb pressure tube material using fourier transform infrared (FTIR) spectroscopy and secondary ion mass spectrometry (SIMS) [46]. The authors proposed that the sharp decreasing SIMS depth profiles for deuterium in the oxide layer of the material was not a diffusion profile but as a result of different densities of crystallite boundary pathways in the oxide layer. A schematic of this is shown in Figure 2.11. The authors suggest a hydrogen pick up mechanism where hydrogen exists near and in the oxide surface as hydroxyls and adsorbed water molecules and crystallite boundaries act as hydrated pathways. In this model, hydrogen is transported through the oxide by fast proton transfer along the hydrated pathways [46]. Hydrogen enters the oxide via randomly generated pathway openings at the oxide-environment interface. Entry into the alloy is controlled by the thin oxide layer at the end of the pathways, by providing a physical barrier and an electrical one due to ionised anion vacancies at the oxide-alloy interface [46]. The existance of -OH bonds on the oxide surface has been shown using X-ray photoelectron

spectroscopy (XPS) [47], however Chen et al. argue that the presence of O-H bonds in the oxide act as a barrier to hydrogen diffusion rather than aid it. This mechanism could be the hydrogen entry route where the oxide is thin and travel through the oxide crystallite boundaries is possible, in the mechanism suggested by Rudling and Wikmark.

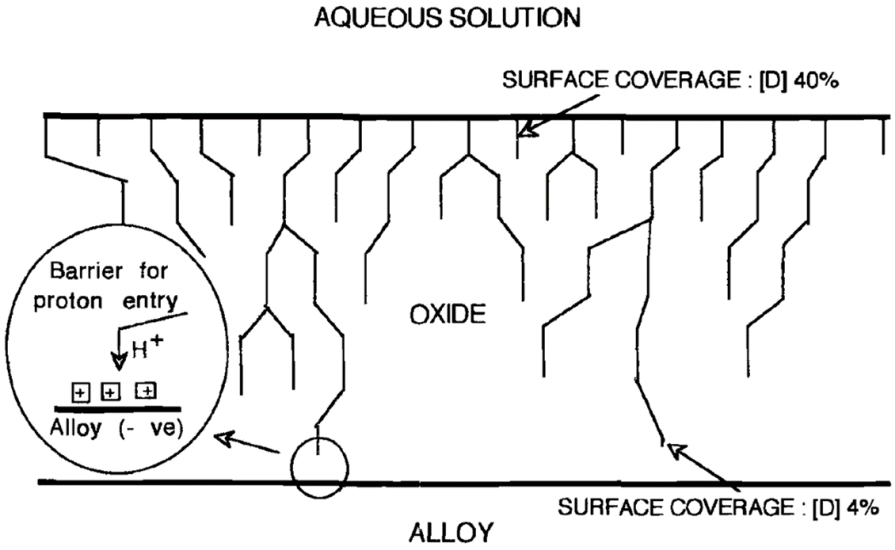


Figure 2.11: Schematic of the hydrogen pick up mechanism where hydrogen is transported through the oxide along the crystallite boundaries [46].

In a review paper by Motta et al, several observations were made regarding hydrogen pick up in Zr alloys [10]. One of these was that hydrogen enters the oxide as a proton [43]. This is in alignment with the mechanism proposed by Ramasubramanian et al. where the hydrogen moves through the oxide via fast proton transfer.

The ratio of hydrogen absorbed to the ratio of hydrogen generated during corrosion is known as the hydrogen pick up fraction, f_H.

$$f_H = \frac{H_{\text{absorbed}}}{H_{\text{generated}}} \tag{2.2}$$

The instantaneous hydrogen pick up fraction (f^i_H) varies with oxide thickness, as shown in Figure 2.12 [10]. It increases rapidly and plateaus when the oxide thickness reaches 30-70% of the transition thickness. f^i_H increases significantly before decreasing

just before transition [10]. It has an inverse relation with the corrosion rate. This coincides with the mechanism Rudling and Wikmark proposed as the changing oxide thickness will affect the strength of the barrier it causes.

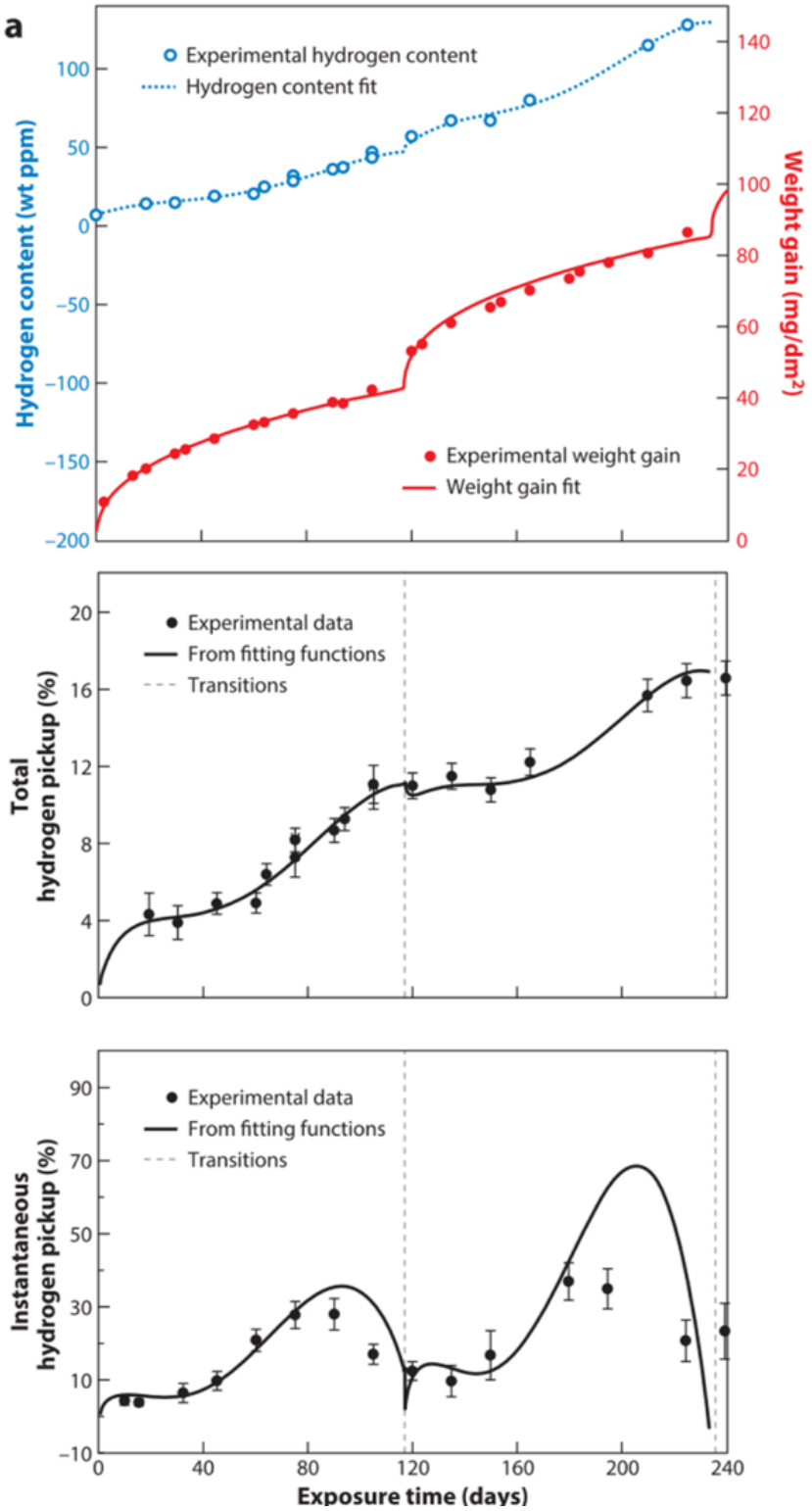


Figure 2.12: Graphs showing the variation in total hydrogen pick up fraction and the instantaneous hydrogen pick up fraction with time, hydrogen contents were measured using cold neutron prompt gamma activation analysis. The vertical dotted line represents a transition in the corrosion regime [10].

Tupin et al. used secondary ion mass spectrometry (SIMS) to examine hydrogen diffusion in the oxide layer of Zircaloy-4 [48]. It was shown that hydrogen diffuses at different rates in the different sections of the oxide. In pre-transition samples, there were two distinct sections to the oxide, an external oxide which was a few hundred nanometres thick, and an internal one approximately 1 μm thick [48]. The external oxide was more permeable to hydrogen than the internal oxide, where the transport of hydrogen through this region was diffusion limited [48]. In post-transition samples, a third, intermediate layer was observed between the internal and external oxide, which had constant hydrogen concentration. This is in agreement with earlier work by Harada and Wakamatsu [49].

The hydrogen concentration of the cladding is known to affect the corrosion behaviour [15]. Figure 2.12 shows the relation between hydrogen pick up and oxide thickness. As these two phenomena are so closely related, a better understanding of the mechanisms of zirconium alloy corrosion and hydrogen pick up should be developed.

2.5.3 Factors affecting Hydrogen Pick Up

The hydrogen quantity generated during corrosion of zirconium alloys is alloy dependent, as is the amount of hydrogen absorbed [37]. The amount of hydrogen picked up is also known to depend on the alloying elements [50], [51], alloy microstructure and microchemistry [52], [53] and the corrosion conditions [10], [54].

The addition of alloying elements generally decreases hydrogen pick up, with two exceptions, Ni increases hydrogen pick up, whereas the effect of Sn additions remains a topic of debate [10], [55]. Alloying elements tend to destabilise hydrides if they are incorporated, leading to reduced formation [55].

Rajasekhara et al. looked at the effect of alloy composition on the thickness of the hydride layer formed using Zircaloy-2, Zircaloy-4 and ZIRLO [56]. It was observed that ZIRLO had an oxide layer thickness an order of magnitude lower than either of the Zircaloys, this is shown in Figure 2.13 [56]. All of the alloys contained the δ-hydride phase with an orientation relationship of $\langle 111 \rangle_{\delta\text{-}ZrH_{1.6}} // \langle 0001 \rangle_{\alpha\text{-}Zr}$ [56]. This demonstrated that the

hydride phase that forms and the orientation relation between the hydride and the alloy are independent of alloy composition.

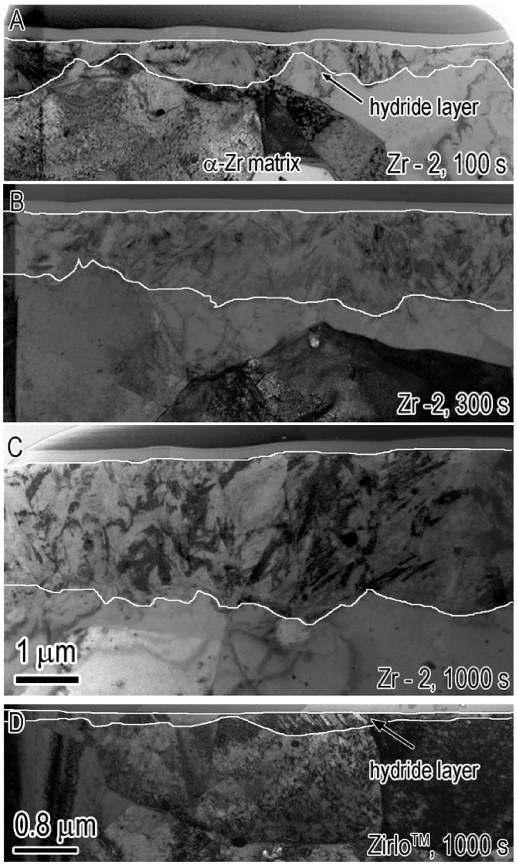


Figure 2.13: Bright field transmission electron microscopy (TEM) image of hydride layers formed in zirconium alloys. The difference in the thickness of the hydride layers formed in different alloys is clearly seen between images C and D [56].

Christensen et al. undertook density functional theory calculations to investigate the effects of alloying elements on hydrogen-containing α-Zr and zirconium hydrides [55]. It was found that the incorporation of hydrogen atoms is energetically favoured by chromium, iron and nickel and unfavoured by tin and niobium [55]. The predicted interaction of Nb with hydrogen is in agreement with experimental work by Couet et al. [15]. The authors calculated that each chromium atom could trap two hydrogen atoms, however most of the chromium is found in second phase particles (SPPs) which removes this effect [55].

The solubility of most alloying elements in α-Zr is low so the elements precipitate

as intermetallic SPPs. The effect of second phase particles on hydrogen pick up is not yet understood and it is unclear whether the SPPs are hydrogen traps, act as nucleation sites for hydrides or provide a transport path through the oxide layer [43],[57]. However it is known that the hydrogen pick up fraction is dependent on the composition, size, distribution and morphology of these particles [42], [58]. Alloys with finer precipitates exhibit higher pick up fractions than those alloys with coarse precipitates [42]. This was observed for $Zr(Fe,Cr)_2$ precipitates [15], [59].

Burr et al. used density functional theory (DFT) to calculate the enthalpy of solution of hydrogen in the intermetallic phases in the binary SPPs and in pure Nb and Zr [60]. The ternary SPPs found in Zircaloy-4, $Zr(Cr,Fe)_2$ were predicted to have an unfavourable enthalpy of solution for H and are not expected to accommodate it. In ZIRLO, the affinity of H to the $Zr(Nb,Fe)_2$ is anticipated to have strong variation with the Nb/Fe ratio; SPPs with high Nb content are expected to trap H while those with high Fe content are expected to reject it. Jones et al. used nanoscale secondary ion mass spectrometry (nanoSIMS) to provide experimental evidence of hydrogen trapping to SPPs in Zircaloy-2 and -4 as well as modelling that suggests the trap site is the boundary between the SPP and the α-Zr matrix [61]. Tuli, Claisse and Burr investigated the solubility of H in Zr-Nb alloys, in β-(Zr, Nb) using DFT . They found that increasing Nb concentration decreases hydrogen solubility but noted that the compositional changes caused by neutron irradiation would increase hydrogen solubility and strength of the trapping site [62]. This demonstrates that the effect of SPPs on hydrogen transport through the metal and oxide is alloy and precipitate dependent as only the precipitates that do not trap hydrogen will be useful in this instance. Tejland et al. showed that the distribution of SPPs is broad, therefore even if the SPPs are able to provide a shortcut through the oxide, other mechanisms will have a greater influence on the transport of hydrogen through this layer [63].

Many mechanisms for the transport of hydrogen through the oxide layer of zirconium alloys have been suggested but there is little direct experimental evidence to support these claims. We do not yet understand the influence of the alloy composition or microstructure

on hydrogen pick up [64]. The role of second phase particles in the transport of hydrogen through the oxide layer is not fully understood, or if these particles can act as a trapping site for hydrogen or the nature of the trapping behaviour. In order to further our understanding of hydrogen pick up, the interaction of hydrogen with microstructural features such as grain boundaries and second phase particles should be studied. For this to occur, techniques need to be developed to image hydrogen at the atomic scale in zirconium alloys.

2.5.4 Growth and Nucleation of Hydrides

Hydrogen is mobile in the cladding, diffusing up stress gradients to regions of tensile stress and down temperature gradients, hence local changes in stress and temperature can lead to the formation of hydrides [7], [65]. Hydrides can nucleate both under and in the absence of an applied stress. Without an applied stress, the most commonly observed hydride phase at low temperature is the face centred cubic (fcc) δ-phase. The precipitation of the δ-phase causes strain in the material as a result of the differing crystal structures and a volume expansion of 17% [66], [67]. This stress results in the hydrides forming a disc shape parallel to the basal plane [65]. It also leads to the formation of dislocation loops surrounding the hydride to accommodate the strain as seen in Figure 2.14. These loops act as nucleation sites for additional hydrides. This process repeats and the nano-hydrides arranged in stacks to form a meso-scale hydride [65]. This grouping of the hydrides is platelet shaped and is orientated in the circumferential direction in the tube. At low magnifications, these successive nucleation events look like a large hydride. Other hydride nucleation sites include grain boundaries, twin boundaries and between the twins [68].

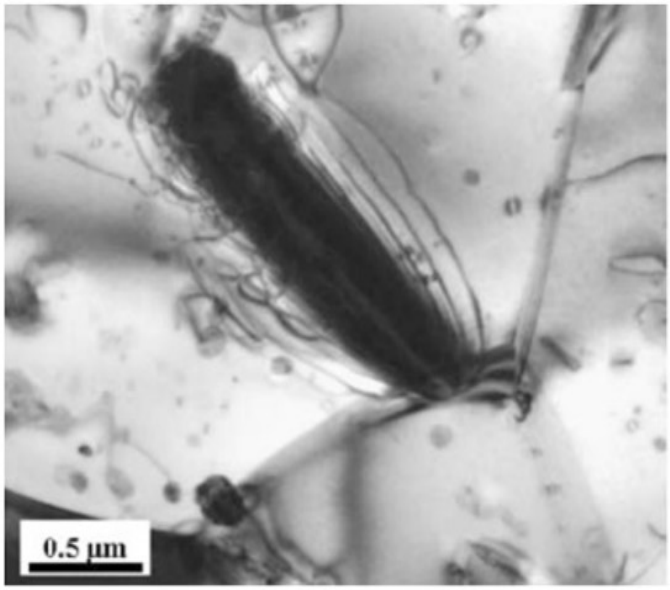


Figure 2.14: TEM micrograph showing an array of misfit dislocations surrounding a hydride particle in a Zircaloy-4 plate. Adapted from [69].

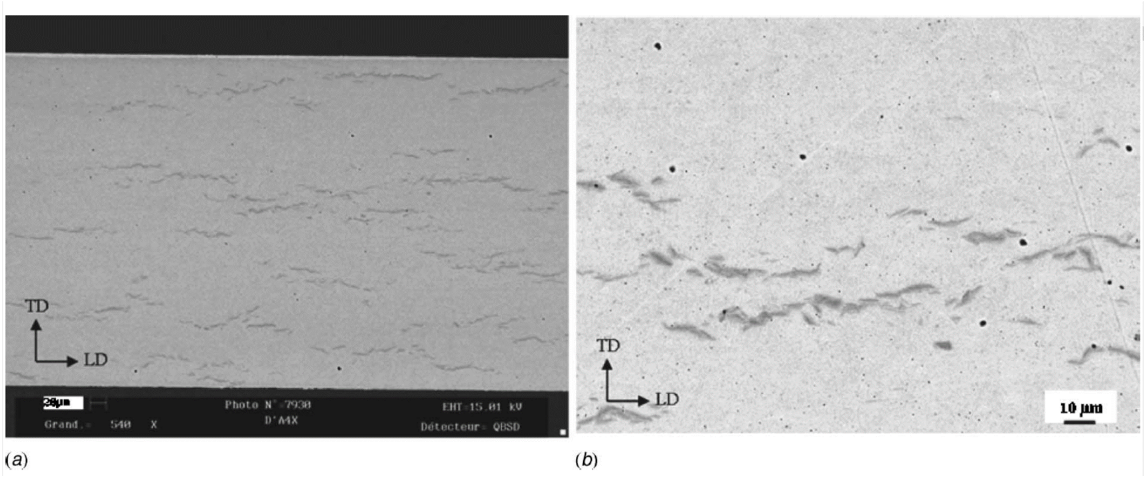


Figure 2.15: SEM image of hydrides. Image a) shows the hydrides on a macroscopic scale, with the long string orientated in the longitudinal direction. b) is a high magnification image of a hydride strings where the individual hydrides that make up the string can be seen [69].

Under the influence of an applied stress, hydrides nucleate at regions of high tensile stress including ahead of a crack tip [65]. This is the basis of the delayed hydride cracking mechanism which is further discussed in Section 2.5.5. The crystallographic relationship above still applies but the orientation of the platelet is controlled by the stress field [65].

2.5.5 Effects on Mechanical Properties

These hydrides have a lath morphology with the long axis aligned perpendicularly to the direction of the greatest tensile stress [65]. Fuel cladding tubes are processed to ensure that hydrides preferentially form in the circumferential direction to minimize degradation. These hydrides are brittle leading to the decrease in ductility of the cladding. The extent to which this occurs depends on the orientation of the platelets with respect to an applied stress [35].

Zirconium hydrides are extremely brittle at all temperatures. The hydrides act to embrittle the material and degrade the mechanical properties [37]. The main effects of this are the decrease in ductility and fracture toughness and crack growth by delayed hydride cracking. Delayed hydride cracking occurs through hydrides, therefore the extent of the degradation is due to the number, distribution and the morphology of the hydride particles.

Delayed hydride cracking is a sub-critical crack growth mechanism where hydride phases form at the tip of a crack and the failure of the hydride leads to the crack extending [70]. A schematic of this is shown in Figure 2.16. Hydrogen diffuses to tensile strained areas such as the tip of a crack, when the terminal solid solubility limit is reached hydrogen precipitates as a hydride. If the conditions for fracture are reached in the hydride, the hydride fractures and the crack arrests in the matrix. This new crack becomes the local region of high stress concentration and the process can repeat itself. The time-scale this process occurs on is dependent on the diffusion of hydrogen and the growth of the precipitate [65].

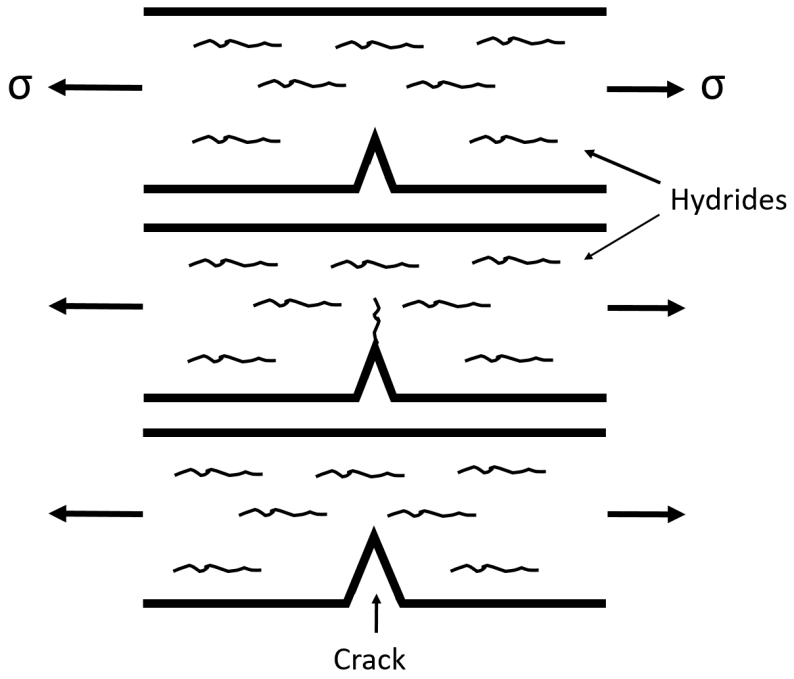


Figure 2.16: Schematic diagram of the delayed hydride cracking mechanism. Hydrogen diffuses to the crack tip and forms a hydride. When the conditions for fracture are reached, fracture occurs through the hydride advancing the crack further into the matrix. This process can repeat at the tip of the extended crack. Reproduced from [70].



Figure 2.17: Hydride precipitation ahead of a crack tip [65].

The orientation of a hydride affects the extent of the degradation it causes. It has

been shown that if hydrides are orientated unfavourably with respect to the stress state, a decrease in ductility can occur [71]. A tube, such as the fuel cladding, subjected to a hoop stress is likely to fail at lower stress levels if the hydrides are orientated such that their habit planes are orientated in the radial direction. The hydride-matrix interface provides an easy crack path leading to a lower fracture toughness.

The diffusion of hydrogen in response to stress can cause stress induced re-orientation of hydrides as illustrated in Figure 2.18. The underlying reason for the re-orientation of the hydrides or the role of stress in their re-orientation are not currently understood [65]. However, the orientation of the hydride particles influences the failure mechanism of the cladding material [65]. As such it is essential to investigate the nature of these hydrides.

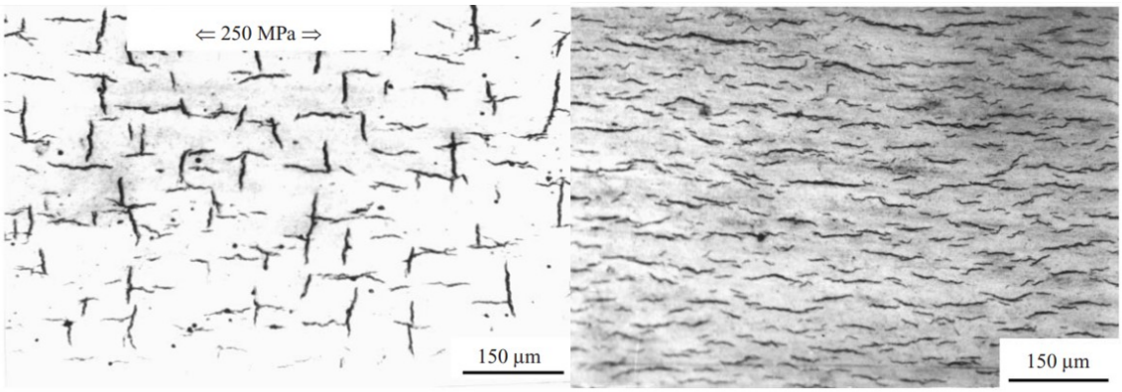


Figure 2.18: Micrograph showing the reorientation of hydride precipitates under an applied stress. The left-hand image shows the random hydride distribution and the magnitude and direction of the stress that will be applied. The right-hand image shows the re-orientated hydrides with their long axis in the direction of the applied tensile stress. Reproduced from [7].

At low temperatures, the failure mechanisms for cladding containing circumferential and radial hydrides are different. The radial hydrides can lead to the initiation of long cracks under load, causing failure by brittle fracture. In cladding containing circumferential hydrides, deformation results in the formation of voids along the hydrides. This causes failure via a damage accumulation type ductile fracture where the voids undergo strain-induced growth and coalescence [72]–[74].

The distribution of hydrides in the cladding also influences the overall ductility of the material. Unfavourable hydride features such as hydride rims or blisters can result in brittle fracture from cracks that initiate at such microstructural features [75], [76]. The thickness of these hydride features influences failure, there is evidence that the failure strain decreases as the thickness of the hydride rim increases [75].

Hydrogen influences the mechanical properties of zirconium alloys as a hydride and in solution [77]. Mechanisms for hydrogen embrittlement such as delayed hydride cracking have been proposed. However, it is not understood how hydrogen behaves at the nanoscale due to the difficulties of characterising hydrogen at the atomic level [77], [78].

2.6 Imaging and Detection of Hydrogen

Common analysis techniques, including x-ray and electron diffraction methods, struggle or fail to analyse hydrogen in material microstructure. The electron cloud surrounding the nucleus is too small for the interaction of hydrogen and radiation to be analysed as there are no outer shell electrons [79]. As result, hydrogen has a low electron and x ray cross section meaning that is almost transparent to electron and x-ray radiation [80]. These are some of the difficulties in detecting hydrogen which has led to a lack of understanding of hydrogen related phenomena.

Transmission electron microscopy (TEM) has been used to image hydrogen but only under very specific circumstances such as adatoms in graphene membrane and in columns in VH_2 and YH_2 [81]. To date, TEM has not been used to image atomic hydrogen in a commercial alloy [82]. TEM is readily used however, to image hydrogen as a hydride in a variety of materials [80]. An example of this is Figure 2.14, where a zirconium hydride is shown.

Nuclear reaction analysis (NRA) can be used to quantitatively determine the variation in concentration with depth of light elements in the near surface region of materials; for hydrogen this can be done using the $^{1}H(^{15}N,\alpha\,\gamma)^{12}C$ reaction [83]. It has high sensitivity for hydrogen and depth resolution to a few nm [84]. However it requires comparison

to a standard of known hydrogen concentration which can be difficult to obtain. This technique has been used to look at the segregation of hydrogen on the Zr(0001) and Zr($10\bar{1}0$) surfaces [85].

NanoSIMS (nanoscale secondary ion mass spectrometry) is a high spatial resolution mass spectrometer and can be used to generate a hydrogen depth profile but it does not give atomic scale imaging resolution. NanoSIMS operates under an ultra-high vacuum (UHV) and hydrogen contamination of the analysis chamber is an issue. One cannot obtain an accurate measurement of the quantity of hydrogen in the sample as it is impossible to distinguish between hydrogen originating from the sample and that from the analysis chamber itself. Hence a means of unambiguously observing the behaviour of hydrogen within a material is to charge the sample with deuterium. The deuterium isotope has a natural abundance of 0.0155% [86], therefore one can assume that any deuterium found in the mass spectra must have originated from the sample. Cathodic and gaseous hydrogen charging routes have been used to charge zirconium alloy samples with hydrogen and deuterium [87], [88].

Li et al. have used NanoSIMS to gain a 3D distribution of the hydrogen (using deuterium doping) in the oxide layer of Zircaloy-4 to investigate the mechanisms of hydrogen penetration through the oxide layer [41]. The authors showed that the deuterium was highly concentrated in the oxide near the water/oxide interface and the deuterium signal decreases in the denser oxide by the oxide-metal interface. There are abrupt peaks in the $^{2}D^{+}$ that are evidence for the existence of trapping sites such as small cracks or porosity, as seen in [24], [46]. These are linked by diffusion pathways through which deuterium can pass through to reach the metal. This work also demonstrates that SIMS can be used to analyse the distribution of hydrogen in nuclear cladding materials. It cannot however give the atomic scale resolution needed to get chemical information at this scale.

Atom probe tomography has high spatial resolution and chemical sensitivity. APT has similar problems to SIMS with hydrogen contamination as it is also an UHV technique. The reconstructed data allows the elemental identity of atoms to be studied and the

three-dimensional position in the material to be characterised with sub-nm resolution [89]. Sundell et al. have shown hydrogen to be the most abundant gas in the analysis chamber of an atom probe [90]. Using isotopic tracing with deuterium, we can use atom probe tomography to image the deuterium. The works of Takahashi, Gemma, Takamizawa, Haley and Chen have all shown that hydrogen imaging in APT is achievable in a range of materials systems provided that the deuterium content is sufficiently high [78], [91]–[94].

2.7 Atom Probe Tomography

2.7.1 APT of Zirconium Alloys

Zirconium alloys were first examined via one dimensional atom probe (1DAP) by Wadman et al. and Kruger et al. to measure the solute concentration in the zirconium alloy matrix [95], [96]. Atom Probe Tomography (APT) studies have previously been conducted on the alloying element distributions in zirconium alloy cladding and on the oxide and on the effects of irradiation. Dong et al. examined the alloying distribution of the elements in the oxide and demonstrated that Sn and Fe segregate to grain boundaries in Zircaloy-4 metal [97]. This segregation to grain boundaries has also been observed by Hudson et al. [98]. Segregation of Fe to grain boundaries was observed in ZIRLO in a study conducted by the same author, however no statistically significant Sn segregation was found [99].

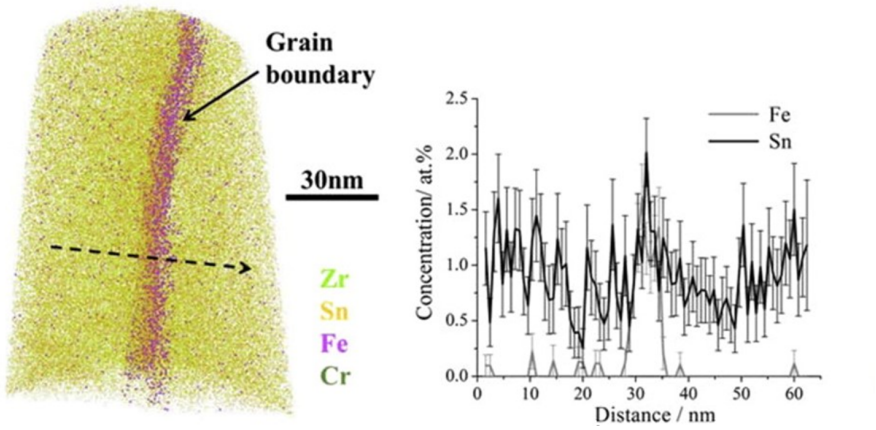


Figure 2.19: Reconstruction showing the Fe and Sn segregation to grain boundary and a profile taken in the direction indicated by the arrow. Adapted from [97].

Several studies on the metal, metal oxide and the interface between these phases have been conducted. Hudson showed the existence of ZrO in the oxide layer as shown in Figure 2.20. Hudson's PhD thesis focused on using APT to investigate the oxidation of different zirconium alloy samples at the atomic scale [100]. The nano-scale chemistry of the metal-oxide interface at different stages in the corrosion cycle of ZIRLO was studied.

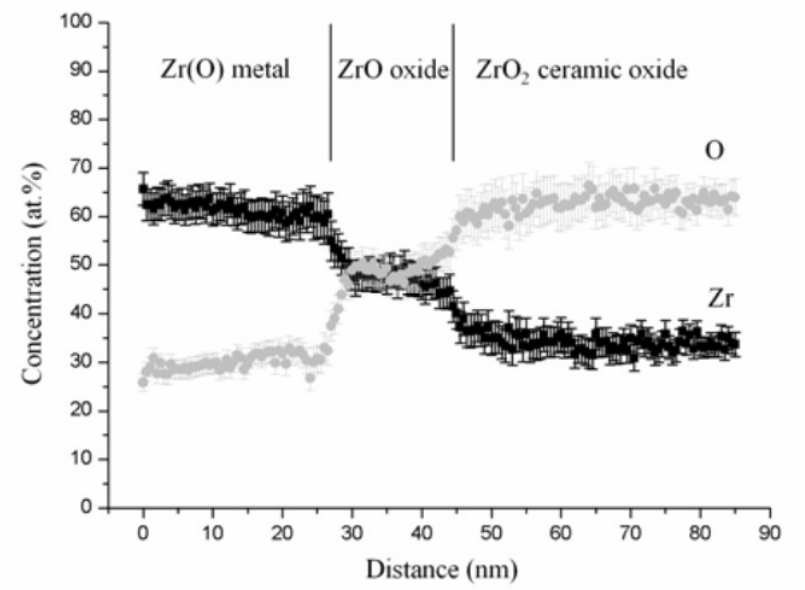


Figure 2.20: APT concentration profile taken across the metal-oxide interface of Zircaloy-4 after oxidation for 90 days at 360°C [98].

Setiadinata's PhD thesis investigated the mechanisms behind corrosion and hydrogen pick up in zirconium alloys. In particular, hydroxylation of crystallite boundaries in the oxide layer was observed as was porosity in the oxide [101]. These have both been proposed as pathways for hydrogen transport through the oxide layer by other authors [46], [102].

APT has also been used to investigate Zr alloys post neutron irradiation [103]–[106]. The ordered clustering of Fe and Cr on parallel planes the α-Zr matrix has been shown. This is thought to be caused by aligned <a>-type loops. These loops also cause the striped 'corduroy contrast' readily visible by TEM [103], [106]. Sundell also showed Fe segregation to grain boundaries and dislocation loops. Correlative TEM and APT by Jenkins and Haley have observed these phenomena, showing that the Fe is associated with <a>-loops [107].

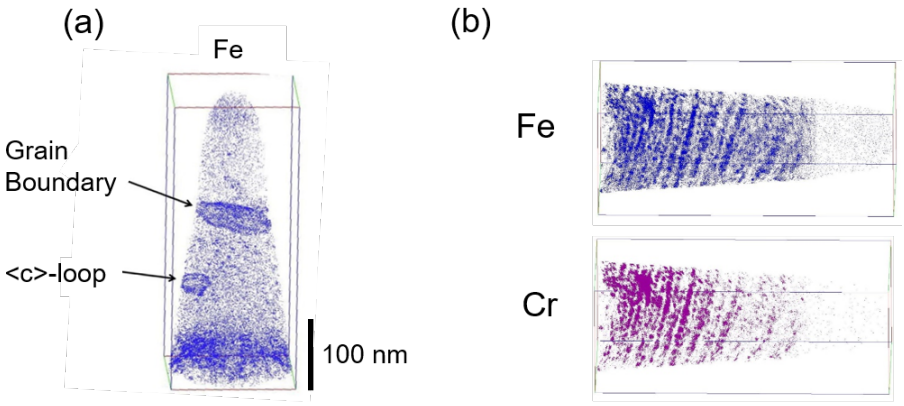


Figure 2.21: APT reconstructions of Zircaloy-2 cladding showing (a) Fe segregation to a grain boundary and dislocation loop and (b) corduroy contrast. Adapted from [103].

2.7.2 Imaging of Hydrogen using APT

Hydrogen and hydrides have been analysed using Atom Probe Tomography in a variety of materials. Gemma et al. used APT to analyse deuterium loaded Fe/V multilayered films that were gaseously charged [92], [108], [109]. Gemma showed that the analysis temperature can lead to deuterium diffusion on the surface of the APT sample during the experiment which affects the accuracy of deuterium concentration profiles [108]. At an analysis temperature of 60K deuterium migration was an issue, at 30K the surface diffusion

was no longer a problem. However a low temperature lead to reduced sample yield as a result of the decrease in ductility. This highlights the importance of appropriate analysis conditions when using APT to analyse hydrogen charged samples. The authors observed a hydrogen depleted layer, as seen in Figure 2.22. Hydrogen depleted layers have been shown to exist in other multi-layer systems [110], [111].The work by Gemma highlights the capacity of atom probe tomography to investigate hydrogen distributions providing appropriate analysis conditions are used.

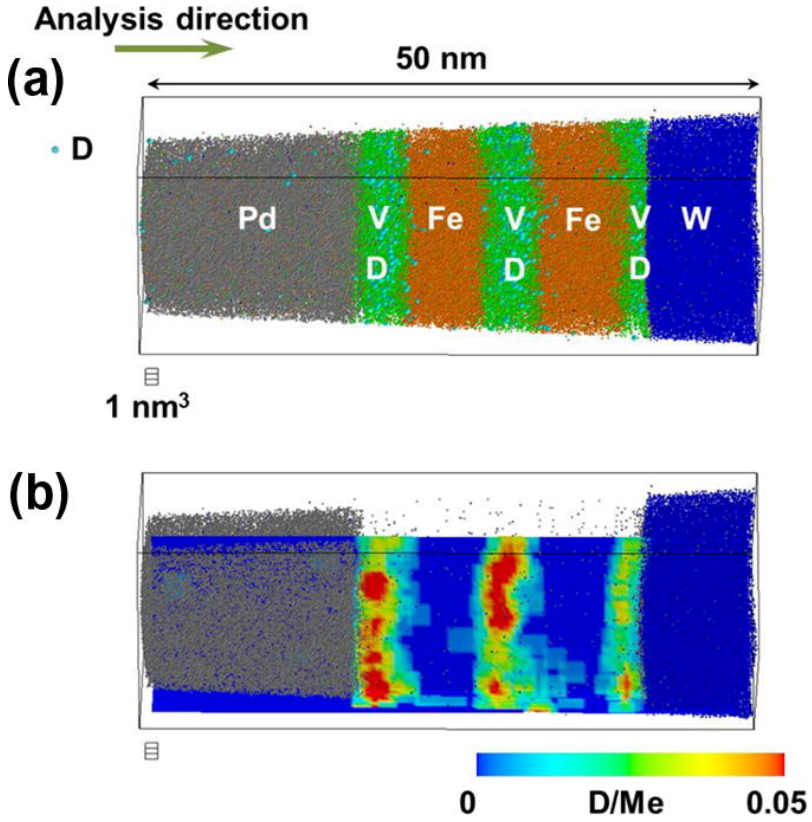


Figure 2.22: APT reconstruction showing the segregation of hydrogen (seen as deuterium) to V layers in a Fe/V multilayer film. No deuterium is seen in the Fe deuterium depleted layer. a) Reconstruction of all of the data. b) Isoconcentration surfaces for deuterium concentration using the reconstruction in a) [92].

Atom probe tomography has been used to detect and image atomic hydrogen in steels that have been gaseously and electrolytically charged with deuterium [78], [94], [112]. Takahashi et al. used a modified atom probe with a deuterium charging cell to charge TiC precipitation hardened steels [112]. Deuterium was seen to segregate to the surface of

the TiC precipitates providing experimental evidence that these precipitates are hydrogen trapping sites in this steel. However, this study could not show whether the hydrogen gets trapped inside the carbide or at the surface of it due to limited deuterium in the data.

Electrolytic charging methods can lead to increased deuterium concentrations and do not require alteration of existing equipment to carry out the experiment. Haley et al. electrolytically charged a high Mn containing steel demonstrating that deuterium could be detected using APT in these samples [94]. The work also highlighted the need to quench the samples after hydrogen charging to prevent deuterium diffusing from the steel sample.

Chen et al. observed segregation of deuterium to vanadium carbides in ferritic steels [78]. Samples were transferred from the electrolytic charging cell to the atom probe using cryogenic transfer, the transfer at cryogenic temperatures was used to prevent deuterium diffusion essentially freezing the deuterium in place.

Martin et al. conducted atom probe analyses of uranium exposed to light and heavy water vapour [113]. A hydride layer between the uranium metal and oxide was observed in the light water vapour exposed sample, and additional evidence for this feature obtained by exposure of the uranium to heavy water vapour. This was seen by the detection of uranium deuteride peaks, the corresponding ions of which were UD^{2+}, in the mass spectrum that were located in the same region as the reconstructed dataset as in the light water case.

Few studies on the distribution of hydrogen or hydrides in zirconium have been conducted using APT. Sundell et al. have studied the hydrogen and deuterium distribution in oxides of Zircaloy-2 and Zr-2.5Nb tube [114]. By corroding a sample from the Zr-2.5Nb tube in a heavy water autoclave, they were able to charge the sample with deuterium whilst forming an oxide layer. They observed the enrichment of deuterium to grain boundaries as OD^{+} which provides some support for hydrogen pick up mechanisms where hydrogen is transported via the grain boundaries. This was confirmed by a second study by the same author in which a higher concentration of OD^{+} ions were observed along a grain boundary [115]. Setiadinata also observed this in a Zr-2.5Nb alloy sample that had been deuterated using a heavy water autoclave also [101].

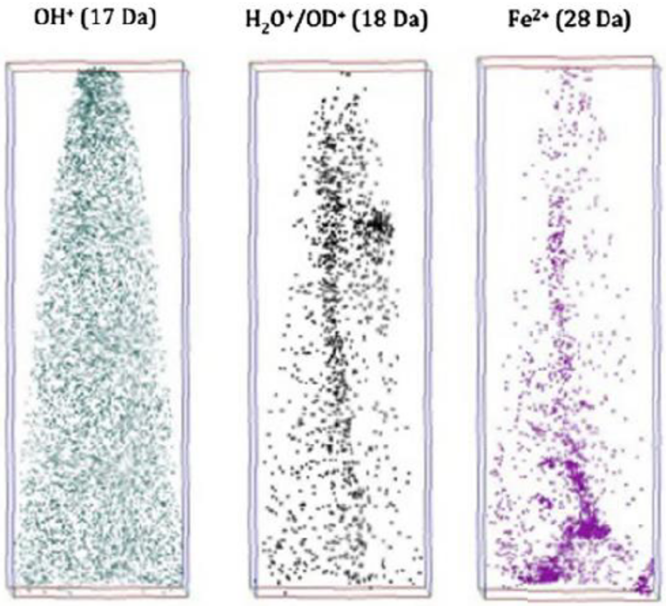


Figure 2.23: APT reconstruction showing the segregation of OD species to a grain boundary in Zr-2.5Nb oxide as indicated by the Fe distribution [101].

Breen et al. have investigated the growth front of a grain boundary using APT, TEM and electron back scattered diffraction (EBSD) [116]. The authors observed that deuterides preferentially precipitated on grain boundaries. It was also observed that Sn is rejected from the deuteride and segregates to the deuteride reaction front. An enrichment of Sn of approximately 2 at%. was observed at the interface. This segregation is shown by the concentration profile in Figure 2.24 d).

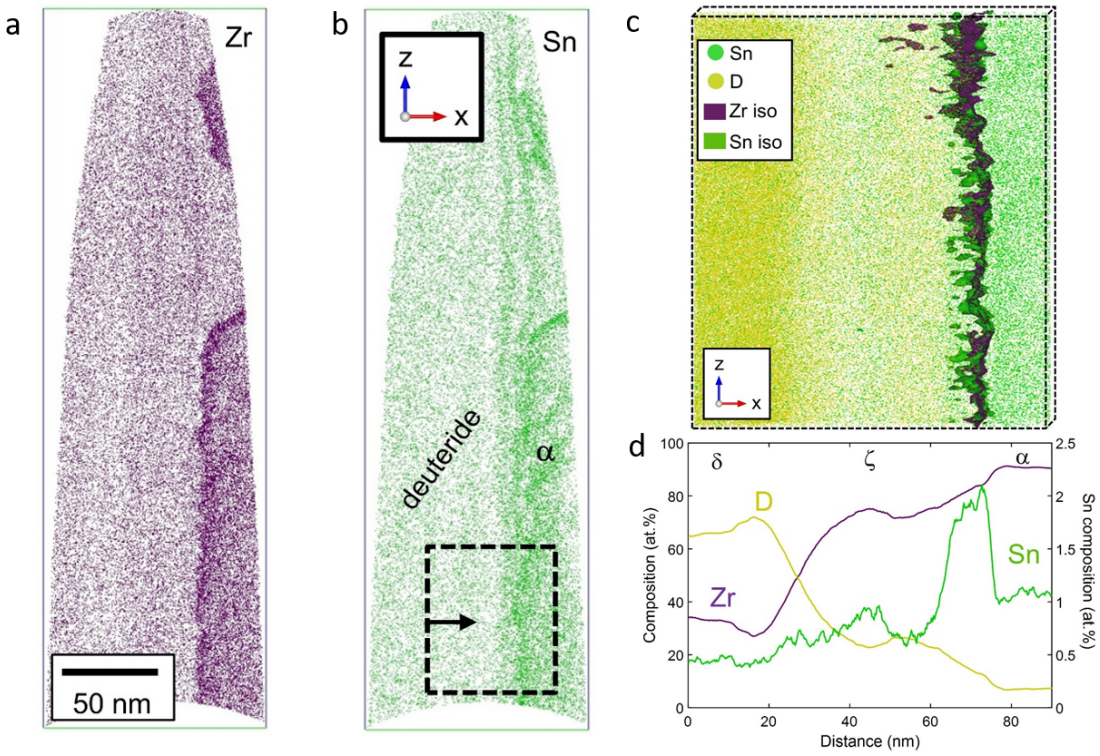


Figure 2.24: (a) and (b) APT reconstructions showing the Zr and Sn ions to show the location of the deuteride. (c) is a close up of the dotted region in (b) with Sn and Zr isoconcentration surfaces at 85 at.% and 1.9 at.% respectively, used to highlight the interface. (d) is a composition profile taken in the x direction. Figure is reproduced from [116]

Focused ion beam (FIB) techniques can used in APT studies to prepare samples from specific sites in the sample [117]. FIB milling is known to induce hydrides in zirconium alloys and similar materials [118], [119]. It is thought that interactions between the ion beam and hydrocarbons in the chamber and on the sample surface were responsible for this, although this has not been confirmed [118]. Cryogenic FIB techniques have been developed which have been shown to significantly reduce this effect [77]. FIB techniques were employed by Breen et al. to analyse the deuteride growth front, however according to the text this did not affect the deuterium concentrations in the sample [116]. No study has proven this, however.

Atom probe tomography has been shown to be able to image hydrogen in a variety

of materials systems. In zirconium alloys, APT has been used to investigate segregation to grain boundaries in the oxide layer and the growth front of a deuteride. The published work focuses on situations where the deuterium concentration is higher. Hydrogen ions (e.g. H_2^+) and hydrogen containing ions have overlapping signals with deuterium and deuterium containing ions, so it is difficult to ensure that no hydrogen is identified as deuterium when hydrogen concentrations are low. To date, no work has been published on the distribution of hydrogen in irradiated zirconium alloys or on the study of hydrogen trapping sites using APT.

The main issues surrounding hydrogen imaging with APT are as follows, firstly the background hydrogen which precludes the positive identification of hydrogen that originated from the sample. The problem of identifying hydrogen that is from the sample material, and not the analysis chamber is partly solved by using deuterium-charged samples. However, this causes uncertainty in deuterium concentrations from overlaps in the mass spectrum between -H_2 and -D containing ions as the signals cannot be easily separated in the mass spectrum. It is also necessary to be able to produce samples that are representative of the bulk and that our methods of preparing samples do not artificially change the hydrogen (or deuterium) concentration in the materials. Steps towards solving these problems must be taken in order to gain the necessary experimental data we need to understand hydrogen pick up and embrittlement.

2.8 Summary

Zirconium alloys are used as the fuel cladding for light water nuclear fission reactors. These alloys have a low neutron cross section, good corrosion resistance and adequate mechanical properties under the operating conditions. In their working environment, these alloys are exposed to irradiation and a corrosive environment. There are numerous hydrogen sources leading to hydrogen pick up and the formation of zirconium hydrides. The waterside corrosion of zirconium alloys leads to the formation of an oxide layer, through which the hydrogen has to pass to reach the metal. There is no agreed mechanism for

this process as a result of the difficulties of imaging hydrogen which has led to a lack of experimental data. Other processes such as delayed hydride cracking and hydride reorientation are not fully understood for this same reason.

Techniques have been developed to image hydrogen, as deuterium, in a variety of materials using atom probe tomography but there is limited data currently available. Few studies have been conducted on hydrogen distributions and hydrides in zirconium alloys using APT. Advancements in techniques to image hydrogen at the atomic-scale would enable the study of hydrogen interactions with microstructural features, including dislocations, grain boundaries and second phase particles, to further our understanding of hydrogen embrittlement. This information will facilitate the development of cladding alloys that are more resistant to hydrogen embrittlement.

Chapter 3

Experimental Methods

The following chapter provides information on the materials used and experimental details of the work completed in this thesis.

3.1 Materials

Zirconium alloys are the main materials investigated in this thesis. The majority of samples are of the Zircaloy series, as these are currently in use in the UK nuclear industry. Cold worked Zircaloy-4 samples were used to develop a deuterium charging protocol for Zr alloys and to study the interaction of hydrogen with materials defects. Pure Zr wire was used as we developed methods to charge these samples, as it is more likely to pick up hydrogen than Zircaloy-4. Finally, irradiated Zircaloy-2 samples were used to investigate the interaction of hydrogen with 'real' irradiation induced defects.

3.1.1 Cold Worked Zircaloy-4

Cold worked samples were obtained from the National Nuclear Laboratory that had been cross rolled to cold work levels of 30%, 60% and 80% as well as as-received material from the same stock. The cold worked samples were studied as a surrogate for irradiation induced damage in order to investigate the interaction of hydrogen with dislocations. The

nominal composition of Zircaloy-4 is shown in Table 3.1. The exact composition of the samples cannot be listed due to proprietary reasons.

Table 3.1: Nominal composition of the cold worked Zircaloy-4 samples. [120]

Element	Zr	Sn	Fe	Cr
Composition (wt.%)	Balance	1.2-1.7	0.18-0.24	0.07-0.123

3.1.2 Zirconium Wire

Pure zirconium wire of 99.95% purity (excluding Hf, Hf nominal composition 0.25%) and 0.125 mm diameter obtained from Alfa Aesar was used in the development of a deuterium charging protocol for Zr alloys.

3.1.3 Deuterated Zircaloy-4

A deuterated Zircaloy-4 sample that had been deuterated to 119 ppm wt. deuterium using heavy water was also analysed in this work, and obtained from the National Nuclear Laboratory. The hydrogen content of these samples was determined by weight gain. This material is of the same stock as the cold worked materials and has the same nominal composition.

3.1.4 Neutron-Irradiated Zircaloy-2 samples

Neutron-irradiated materials from the BOR-60 reactor were obtained from Westinghouse Electric Corporation as part of the UKRI MIDAS research consortium to investigate the interaction of hydrogen with irradiation induced defects. A standard Zircaloy-2 sheet was used and the nominal composition given in Table 3.2.

Table 3.2: Nominal composition of the neutron-irradiated Zircaloy-2 sample

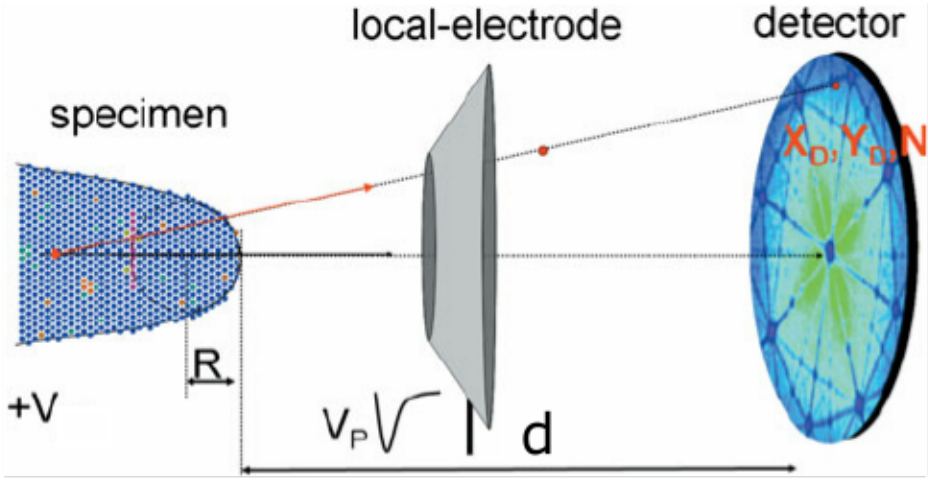
Sample	Dose (dpa)	Composition (at.%)							
		Zr	Sn	Fe	Cr	Ni	O	Si	Impurities
Standard	23.1	balance	1.02	0.27	0.18	0.10	0.67	0.01	max. 370 ppm wt

3.2 Atom Probe Tomography

Atom Probe Tomography (APT) has been used in this study to investigate the interaction of hydrogen with defects in a material's microstructure. APT has nanometre level spatial resolution and high chemical sensitivity. It is also equally sensitive to all chemical elements [117] making it well suited to imaging hydrogen in zirconium alloys [78], [108], [116] .

3.2.1 Basic Principles

APT uses highly controlled field evaporation of ions from the apex of a sharp needle-shaped sample (<100 nm radius). These ions are accelerated towards a position sensitive time-of-flight detector. The basic layout of an atom probe can be seen in Figure 3.1.



Whole system is under ultra high vacuum and cryogenic conditions

Figure 3.1: Schematic showing the main parts of an atom probe operating in voltage-pulsing mode, adapted from [121].

A high voltage is used to generate a high electric field at the surface of the specimen. The electric field, F, of a needle shaped specimen with radius of curvature, R that is subjected to a high voltage, V, can be estimated using a modification of the idealised expression for a charged sphere (Equation 3.1) where k_f is the 'field factor' and accounts for the non-spherical tip shape and the electrostatic environment [122].

$$F = \frac{V}{k_f R} \tag{3.1}$$

The electric field at the tip causes the atoms at the surface to become polarised. The energy state of an atom that is subjected to a strong electric field can be deformed such that there is a reduced energy barrier for an atom to be ionised and leave the sample. This process is known as field evaporation. The electric field penetration is extremely small for metals so only atoms at the surface of the sample are affected by the field evaporation process. In non-metallic specimens, the field penetrates further into the sample and can lead to the evaporation of complex ions (ions containing more than one atom) as more than one atomic layer is affected by the field [123]. Once an ion is field evaporated, it will

it will be projected by the highly diverging electric field away from the specimen surface towards the detector. Ions can dissociate into fragments or ionise further whilst the ion is accelerating through the high field near the samples surface leading to ions being present in multiple charge states [124].

Pulsed field evaporation is used to precisely control the evaporation event, meaning that the time of the ion's departure from the sample surface is known. Two modes of time controlled field evaporation are used: HV-pulsing (high voltage) and laser or thermal pulsing modes. The effect of these pulsing modes to overcome the barrier for field evaporation can be seen in Figure 3.2. Once the ion has been accelerated by the electric field, it passes through an aperture in the local electrode and travels a known distance, d, to the position sensitive detector. The different pulsing modes have an effect on the data, in a reflectron instrument laser pulsing is known to have a lower mass resolution as compared to voltage pulsing, as 'thermal tails' are produced in the data [117].

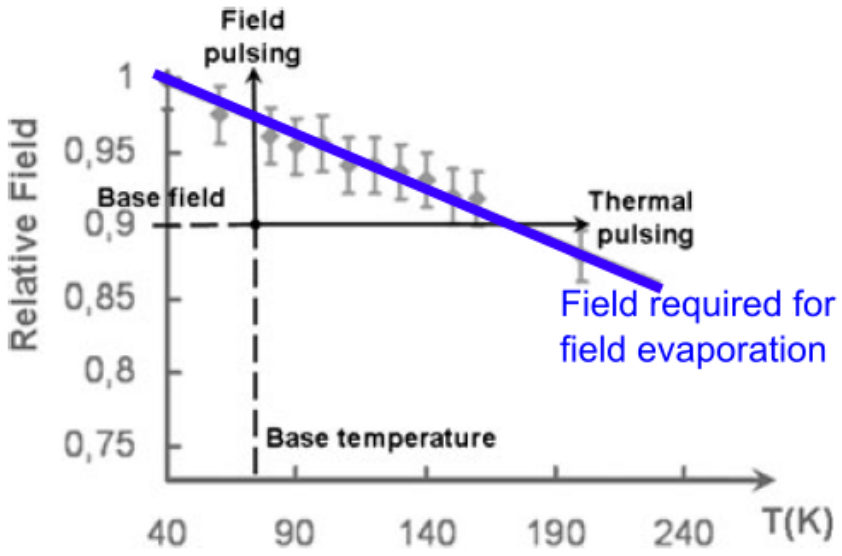


Figure 3.2: Graph showing how the application of a voltage (field) or a laser (thermal) pulse can be used to overcome the barrier for field evaporation, adapted from [117]

The time-of-flight, t, is taken to be the time delay between the application of the voltage or laser pulse and when a hit is recorded at the detector. The mass-to-charge state

ratio, m/n, can be calculated by assuming that all of the potential energy of the ion in the electric field, neV, is converted into kinetic energy $1/2 \cdot m \cdot (d/t)^2$. The relationship is as follows

$$\frac{m}{n} = 2eV\frac{t^2}{d^2} \tag{3.2}$$

where m is the mass of the ion, n is the charge state, e is the elementary charge constant, V is the applied voltage between the specimen and the local electrode, t is the time-of-flight and d is the distance between the specimen apex and electrode.

The detector is position sensitive so the impact position of the ions is recorded and a reverse-projection algorithm, based on the assumption that the specimen shape takes the form of a hemisphere on a cone, is used (by software) to estimate the location in the tip where the ion originated from [117]. Having both the mass-to-charge-state ratio and its original location in the sample, it allows for a virtual representation of the original needle to be produced, called a reconstruction, where the identity and location of each ion can be analysed. IVAS 3.8.8 was used to produce the reconstructions shown in this thesis. The initial radius of the reconstruction was calculated using the voltage curve.

A LEAP 3000X HR and a LEAP 5000 XR instruments were used for the experiments contained in this thesis unless otherwise stated. The 3000X HR instrument has a flight path of 382 mm and a laser wavelength of 532 nm. The 5000 XR instrument has a flight path of 382 mm and a laser wavelength of 355 nm.

3.2.2 Composition Calculations

Underpinning all APT analyses is our interpretation of the mass spectrum, a plot of count vs mass-to-charge-state ratio. The mass spectrum consists of mass peaks on top of a background signal. Different ionic species can have the same mass-to-charge-state ratio, known as a peak overlap. Figure 3.3 is a typical mass spectrum of Zircaloy-4 with the ionic species contributing to each peak labelled and its location on the mass spectrum indicated by the bold coloured lines. We can see peak overlaps between Zr and Zr hydride ions in

the 2+ and 1+ charge states. Peaks are detected for each isotope of an ion.

Peak overlaps occur where the peaks corresponding to the detection of more than one type of ion directly overlap in the mass spectrum, in a ‘direct’ peak overlap, or where a smaller peak overlaps with the tail of the preceding peak, a ‘tail overlap’ [125]. Figure 3.4 illustrates both types of overlap. In order to accurately calculate the composition of a mass spectrum where direct peak overlaps occur, we need to estimate the number of counts each ionic species contributes to a peak, termed peak overlap solving.

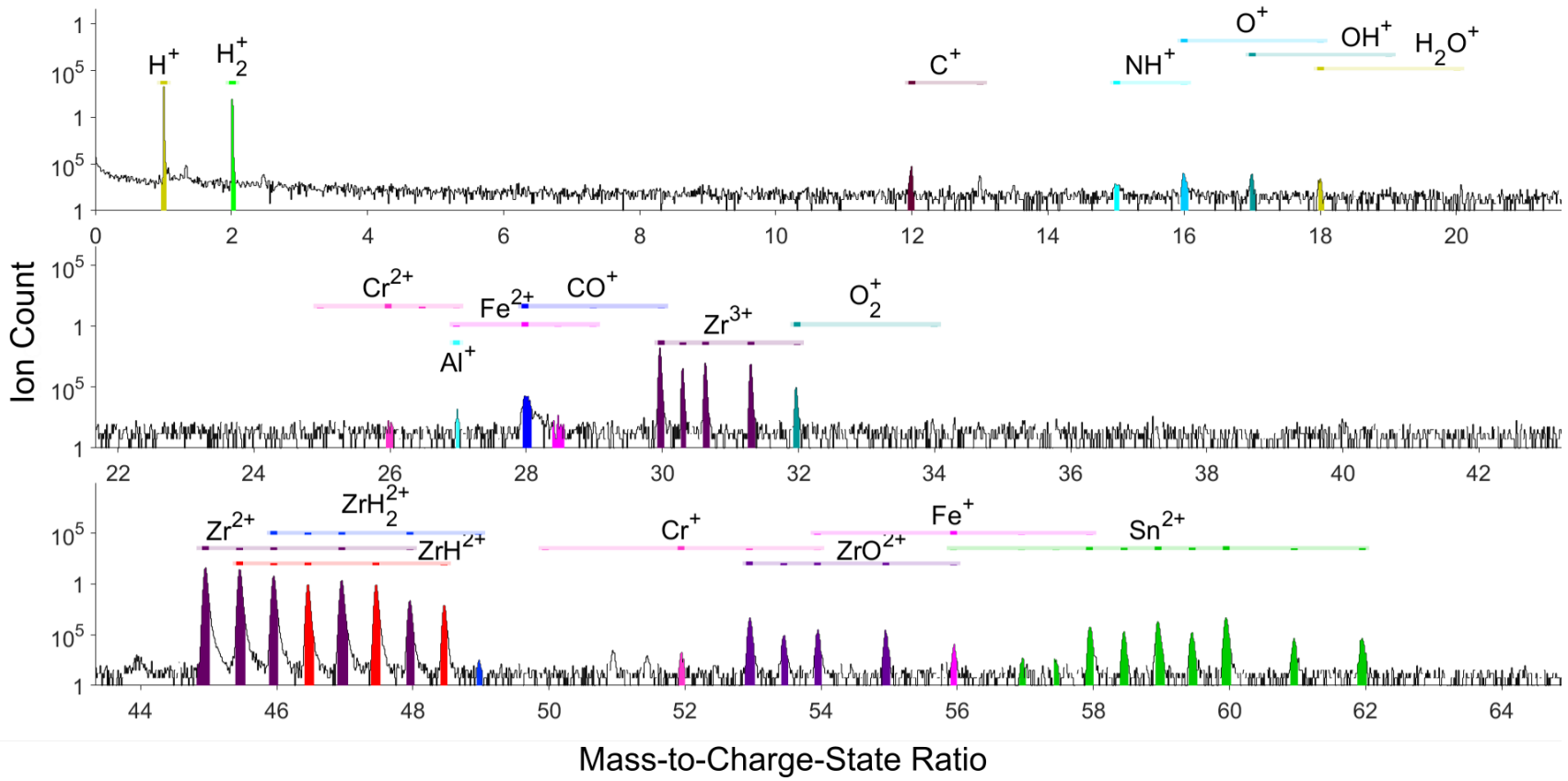


Figure 3.3: Mass spectrum of Zircaloy-4 with ionic species labelled. The bars show the mass-to-charge-state ratio of the ionic species and their height is proportional to the isotopic abundance.

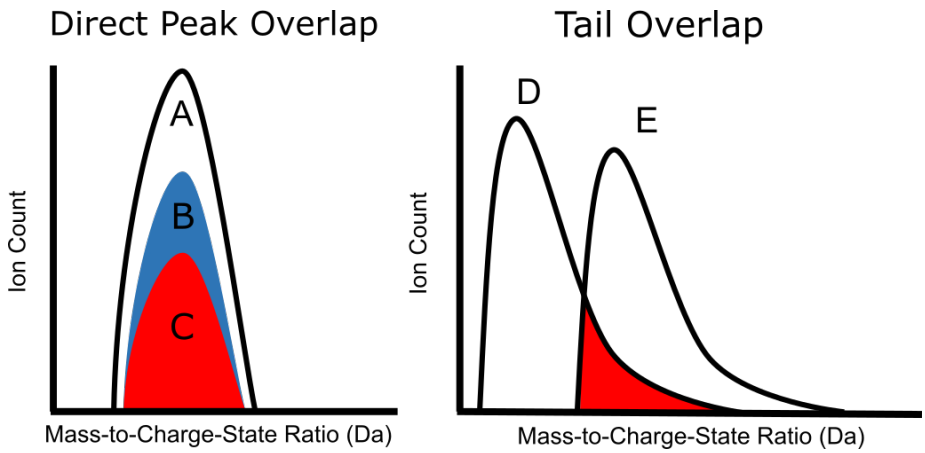


Figure 3.4: Sketch showing the types of overlaps found in APT mass spectra. A direct peak overlap occurs where two ionic species have the same (indistinguishable by APT) mass-to-charge state ratio. Peaks B (blue) and C (red) have a direct overlap, resulting in peak A being generated for the global mass spectrum. A tail overlap occurs where a peak overlaps with the tail of the proceeding peak such as peaks D and E, giving rise to a tail overlap (red region).

We are able to solve peak overlaps into their respective components where the group of peaks which contain overlaps has at least as many peaks as there are ions in the overlap problem. The different ions can be the same ion type but different isotopes of the elements in said ion, e.g. $^{90}Zr^{2+}$ and $^{91}Zr^{2+}$ are two different ions. Otherwise we are unable to solve this because the equations for the overlap problem are deemed rank deficient. We use the number of counts in each of the peaks and the expected natural abundance of each isotope of the respective ions to calculate how many counts each ion should contribute to each peak. A re-occurring problem in this thesis is extracting compositions from mass spectra that contain complex peak overlap problems and those that are not solvable. The most frequently encountered is the overlap between molecular protium ($^{1}H_2^{+}$) and deuterium (^{2}H) at 2 Da. Both of these ions exist in one peak only. Thus here we explain in detail the types of peak overlap that we solve and the process by which it is undertaken.

Figure 3.5 highlights the peaks between 45 Da and 49.5 Da from Figure 3.3, where peak overlaps occur between Zr^{2+}, ZrH^{2+} and ZrH_2^{2+}. These peak overlaps are shown in graphical form in Figure 3.6. Equation 3.3 is the mathematical expression for the overlap problem; where ^{n}N is the number of ionic counts (N) in the peak at n Da, A_x is the expected

natural isotopic abundance of isotope x and N_y is the number of counts of ion y in the overlap problem. This overlap problem has been set up to exclude naturally occurring deuterium as the abundance is so low (0.015%), so the only isotope of naturally occurring hydrogen being considered is protium. Equation 3.3 is an over-determined set of linear equations and the solution can be found numerically [126].

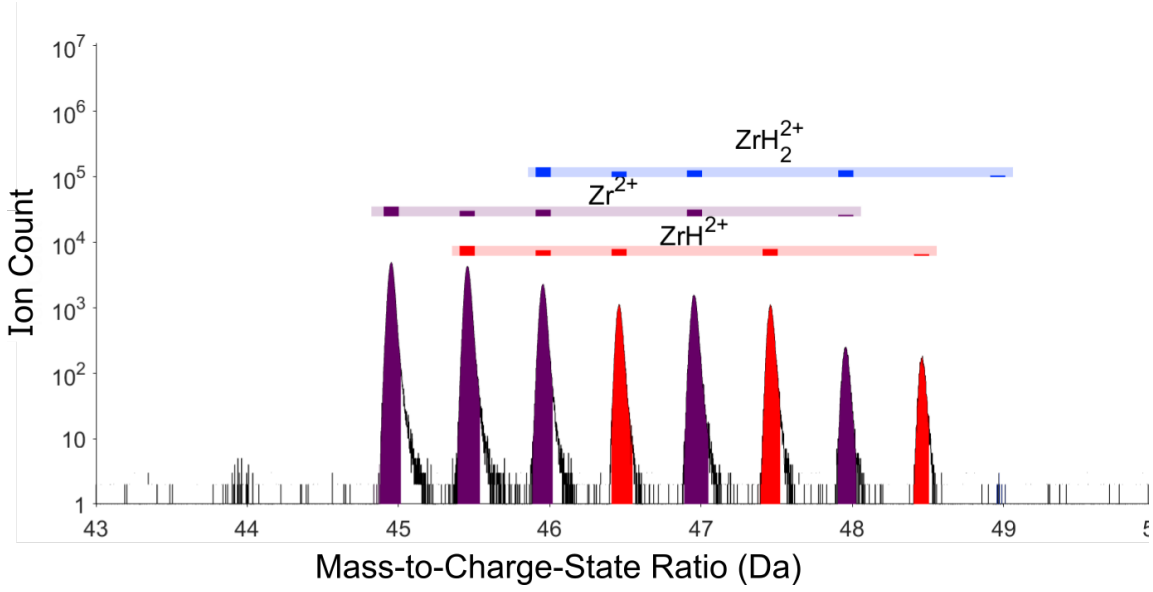


Figure 3.5: Mass spectrum of Zr^{2+} charge state peaks of Zircaloy-4 with ionic species labelled. The bars show the mass-to-charge-state ratio of the ionic species and their width is proportional to the isotopic abundance of the ion.

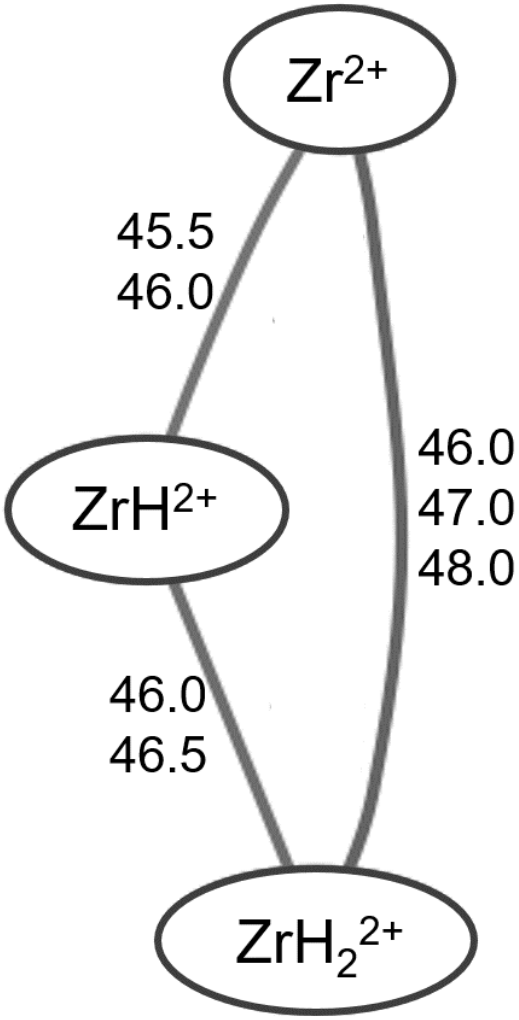


Figure 3.6: Overlap map showing peak overlaps between Zr^{2+}, ZrH^{2+} and $ZrH_2{}^{2+}$. The lines between the circles show where a peak overlap occurs and the numbers to the side of the lines provide the mass-to-charge-state ratio at which the overlaps occur.

$$\begin{bmatrix} {}^{45}N \\ {}^{45.5}N \\ {}^{46}N \\ {}^{46.5}N \\ {}^{47}N \\ {}^{47.5}N \\ {}^{48}N \\ {}^{48.5}N \\ {}^{49}N \end{bmatrix} = \begin{bmatrix} A_{^{90}\mathrm{Zr}} & 0 & 0 \\ A_{^{91}\mathrm{Zr}} & A_{^{90}\mathrm{Zr}} & 0 \\ A_{^{92}\mathrm{Zr}} & A_{^{91}\mathrm{Zr}} & A_{^{90}\mathrm{Zr}} \\ 0 & A_{^{92}\mathrm{Zr}} & A_{^{91}\mathrm{Zr}} \\ A_{^{94}\mathrm{Zr}} & 0 & A_{^{92}\mathrm{Zr}} \\ 0 & A_{^{94}\mathrm{Zr}} & 0 \\ A_{^{96}\mathrm{Zr}} & 0 & A_{^{94}\mathrm{Zr}} \\ 0 & A_{^{96}\mathrm{Zr}} & 0 \\ 0 & 0 & A_{^{96}\mathrm{Zr}} \end{bmatrix} \begin{bmatrix} N_{\mathrm{Zr}^{2+}} \\ N_{\mathrm{ZrH}^{2+}} \\ N_{\mathrm{ZrH_2}^{2+}} \end{bmatrix} \tag{3.3}$$

In this work, peak overlaps were solved using the maximum likelihood estimation through the use of AtomProbeLab (software) unless otherwise stated. This code is an implementation of the method described by London et al. [125] (`https://sourceforge.net/projects/atomprobelab/`). This code was in active development throughout this work and, as such, the most up-to-date version of the code was used for the analysis (version 0.2.3).

One of the biggest causes of the error in compositional measurements in APT is the mislabelling of peaks in the mass spectrum [127]; in order to ensure that the compositions were accurate, several programs and scripts were used to aid this process which are shown in Table 3.3.

Table 3.3: Scripts and softwares used to improve composition measurements.

Software	Purpose
Weights.exe (31.01.2018)	Identify ionic species contributing to a peak
ionFitTester.m (AtomProbeLab v0.2.3)	Ensure all counts in the mass spectra are accounted for correctly
rangeCheck.exe (04.11.2016)	Check for errors in 'range files' by checking the range identity, range width and ionic charge states

3.2.3 APT Analysis Conditions

In this work, most APT experiments were conducted using laser-pulsing evaporation mode to increase sample yield. Zirconium alloy samples are susceptible to the mechanical stresses induced by voltage-pulsing and have a tendency to fracture [95]. Temperatures below 45K are not beneficial to specimen viability [95]. However, higher temperatures are known to decrease spatial resolution due to increased ionisation of residual gases in the analysis chamber [117] and may lead to increased surface migration of certain solute atoms during an experiment. To balance these two effects, an analysis temperature of 55K was used for most experiments.

To confirm the laser conditions to most accurately quantify the amount of D, prior experiments by this author were re-analysed, with most deuterium found in the peak at 2 Da [128]. However, there is a peak overlap between molecular hydrogen (H_2^+) and D^+ at 2 Da which is rank deficient. To mitigate this, a laser energy optimisation experiment conducted by Hudson on ZIRLO was re-analysed, using AtomProbeLab, to find the experimental conditions in which the least amount of H_2^+ is present in the mass spectrum and how the total hydrogen concentration varied with laser energy (peak overlaps are explained in Section 3.2.2 and a detailed discussion of the H_2^+-D^+ overlap in Section 6.3.1) [100]. Figures 3.7 and 3.8 present the result from this experiment and show that for the LEAP 3000X HR, the minimum H_2:H ratio is found at laser energies greater than 0.45 nJ. This minimises the amount of H_2^+ at 2 Da, making the peak overlap easier to solve. At high laser energies, the total quantity of hydrogen detected decreases. The reason for this is not fully understood, so we cannot guarantee that the mechanism by which we appear to be losing hydrogen by, does not affect deuterium. To maximise the amount of deuterium we detect, we do not want this to occur, therefore 'medium' laser energies should be used. On the LEAP 3000X HR, a laser energy of 0.35 nJ was used. On the LEAP 5000 XR instrument a laser energy of 50 pJ was used because a rough estimate of the comparison of laser energy between the lasers on the two different atom probes is thought to be approximately a factor of 10, a 0.35 nJ laser energy on the LEAP

3000 is equivalent to 0.035 nJ (or 35 pJ). When trialling laser energies, the sample yield was low when 35 pJ, 40 pJ and 45 pJ were used and most samples fractured in the oxide layer. At 50 pJ, the samples yielded sensible APT data and were therefore used in the work completed on the LEAP 5000 XR.

It is noted that the hydrogen concentrations in Figure 3.8 appear to be high (varying between approximately 15-25 at.%). The sample used in this study was a focused ion beam (FIB) sharpened, electropolished needle. Zircaloy-4 samples prepared in the same manner also exhibited high hydrogen concentrations up to 47 at.% H, but most were in the region of 20 at.%, which aligns with the results of Hudson indicating that although the H concentration is high it is not unexpectedly high.

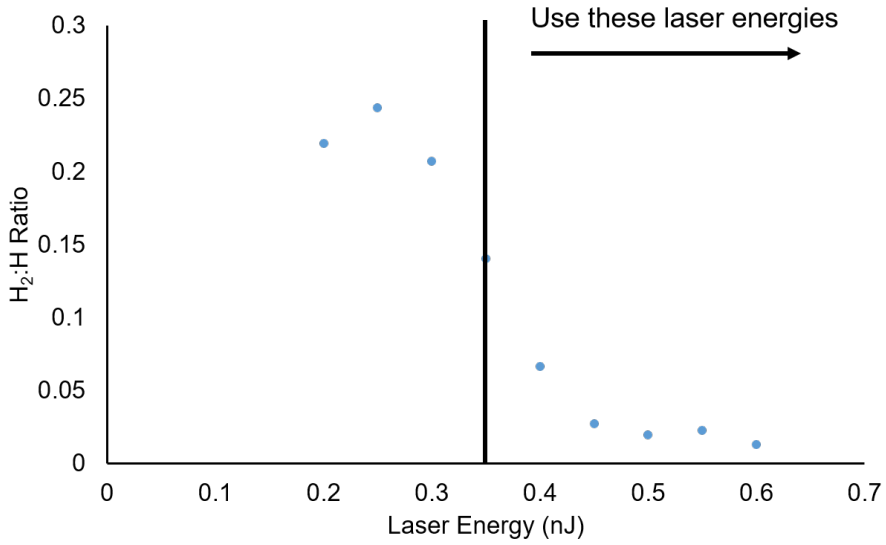


Figure 3.7: Variation in the ratio of H_2:H with laser energy for a ZIRLO sample. Data taken from [100]

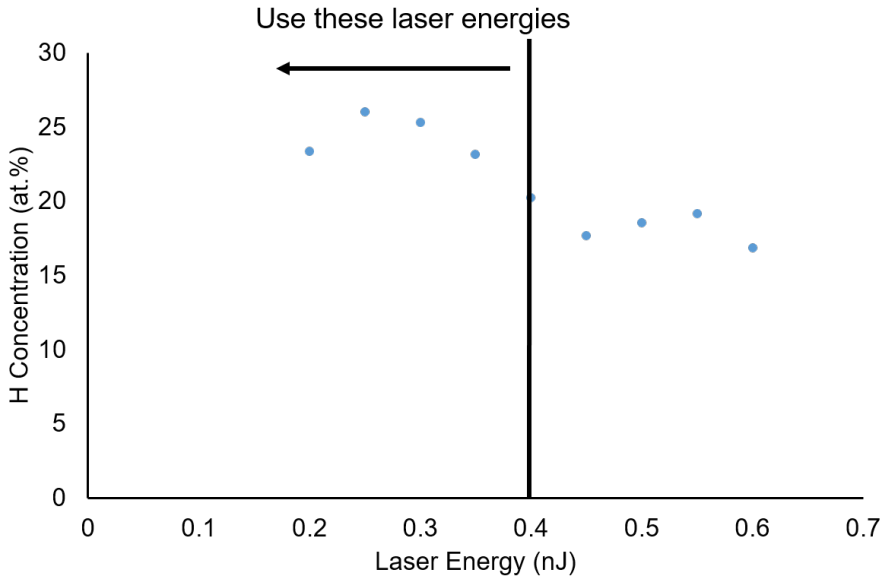


Figure 3.8: Variation in the hydrogen concentration with laser energy for a ZIRLO sample. Data taken from [100].

Another APT experimental parameter to consider is the pulse frequency. The pulse frequency controls the time between laser (or voltage) pulses and it is known that increasing the time between pulses (decreasing the pulse rate) leads to an increase in contaminant hydrogen detected, as there is a greater time between pulses during which H from the chamber can adsorb onto the surface of the specimen [90], [129]. To minimise contaminant hydrogen, as high a pulse frequency as possible should be used. However, because increasing the pulse frequency decreases the time between pulses, it decreases the maximum time any single ion can take to hit the detector after evaporation before the next pulse is applied, resetting the time of flight clock. This means that for a given voltage, there is a maximum mass-to-charge-state ratio that can be detected, as given by Equation 3.2. The metal region of a zirconium sample, does not tend to result in the evaporation of any ions with a mass-to-charge-state ratio of higher than 110 Da on the LEAP 3000X HR mass spectra or 80 Da on the LEAP 5000 XR instrument. Electropolished samples tended to start evaporating at specimen voltages of 3-4 kV and focused ion beam prepared samples between 2 and 3 kV. There is a maximum mass-to-charge-state ratio that can be detected

at any voltage for a given laser pulse frequency. The laser pulse frequency that allows for all ions to be detected in this voltage range is 200 kHz [130].

The final experimental parameter to discuss is the detection or evaporation rate. The detection rate defines the number of ions detected per pulse that the atom probe will aim to detect, for instance a detection rate of 1% equates to 0.01 ion being detected per pulse or 1 ion every 100 pulses. Meier et al. have shown that at a theoretical infinite detection rate, no contaminant hydrogen is detected in APT data and it follows that any detected hydrogen has originated from the sample [131]. For this study, suppressing any contaminant hydrogen signal is of benefit because of the peak overlaps (discussed in detail in Chapter 6) with deuterium so the highest possible (achievable) detection rate should be used. This also has the added benefit of increasing the speed of data collection. From experience, a detection rate of 0.5% yielded the most reliable results and was used. It is acknowledged that from a hydrogen contamination perspective, a higher detection rate should be used but it is better to have poorer quality data than no data.

Unless otherwise stated, atom probe conditions for all experiments were an analysis temperature of 55 K, a laser pulse frequency of 200 kHz and a laser pulse energy of 50 pJ for the LEAP 5000 XR experiments. A detection rate of 0.5% was used throughout this work.

3.3 Sample Preparation

Samples for APT analysis were prepared by one of three methods: electropolishing, electropolishing and then sharpened using a focused ion beam (FIB) or a full FIB lift out procedure.

3.3.1 Scanning Electron Microscopy

Samples were prepared for scanning electron imaging (SEM) using the following method:

- Mounted onto a brass polishing holder using Crystalbond 509
- Grind sample for 2 minutes using 800 grit
- Grind sample for 4 minutes using 1200 grit
- Grind sample for 6 minutes using 2500 grit
- Diamond polish using 6 μm diamond suspension solution and cloth for 10 minutes
- Diamond polish using 1 μm diamond suspension solution and cloth for 10 minutes
- Colloidal silica polish for 15 minutes on MD-Chem cloth
- Polish using water for 15 minutes on an MD-Chem cloth

Samples were cleaned with ethanol between each grinding stage and each polishing stage. Between each grinding step, the sample was rotated 90 degrees.

3.3.2 Atom Probe Tomography: Electropolishing

Samples were cut into ‘matchsticks’ with dimensions 20 mm x 0.5 mm x 0.5 mm using a Buehler Isomet 4000 precision saw. These were electrolytically polished down to APT needles by a two-stage polishing process (Table 3.4 and Figure 3.9).

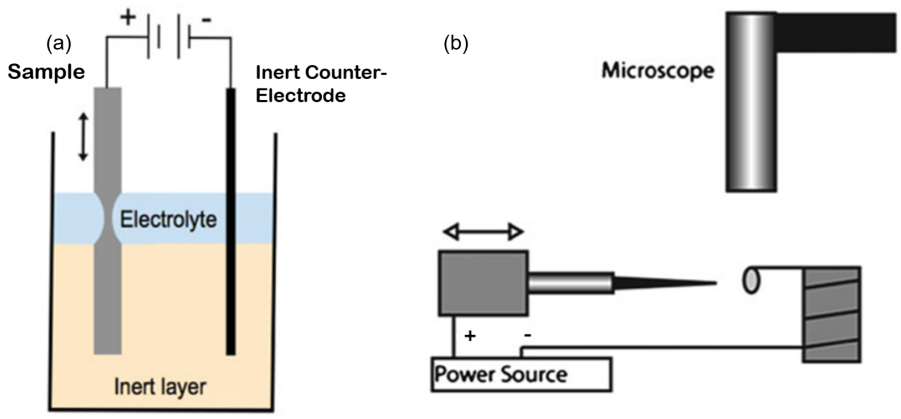


Figure 3.9: Set up used to electropolish samples for analysis in the atom probe. Diagram (a) is for the first stage of electropolishing and (b) for the second. Reproduced from [117].

The first stage of polishing involves taking the matchstick and moving the centre half up and down in a layer of acid, resting on a layer of Galden (an inert perfluoropolyether fluorinated fluid), until the cross-section of the matchstick decreases and a neck forms. This set up is shown in Figure 3.9 (a). The up/down motion is used to control the cross sectional area of the neck. This motion is continued until the sample breaks in two, yielding two usable samples. Samples were cleaned using ethanol and then isopropanol, dried with nitrogen gas or compressed air and mounted in thin-walled copper or stainless steel tubes with an outer diameter of 1.75 mm. The final stage of polishing uses the set up shown in Figure 3.9 (b). The electrolyte is suspended in a gold loop and the sample is run through this until the tip becomes sufficiently sharp. This process is monitored using an optical microscope. Cleaning was repeated, before loading into the atom probe. Fractured APT specimens were re-sharpened for APT analysis using the final polishing stage only.

Table 3.4: Conditions used to electropolish zirconium alloy samples adapted from [100].

Stage		Electrolyte	Voltage (V)	Time (Minutes)
1	Start	25% perchloric acid (60%) in 75% acetic acid (100%)	20	3
	Middle		10	3
	End		5	3
2		2% perchloric acid (60%) in 98% 2-butoxyethanol (100%)	10	10

3.3.3 Atom Probe Tomography: Focused Ion Beam

Site specific lift-outs were performed to select specific regions of the sample for atom probe analysis. This method was used to produce specimens containing grain boundaries and second phase particles. The lift-outs were peformed using a Zeiss NVision-40 dual beam FIB-SEM or a Zeiss Crossbeam 540 Analytical FIB-SEM via the method described in [132] and shown in Figures 3.10 and 3.11. The FIB accelerating voltages and currents are shown in Tables 3.5 and 3.6 for the milling of the cantilever and the sharpening stages respectively.

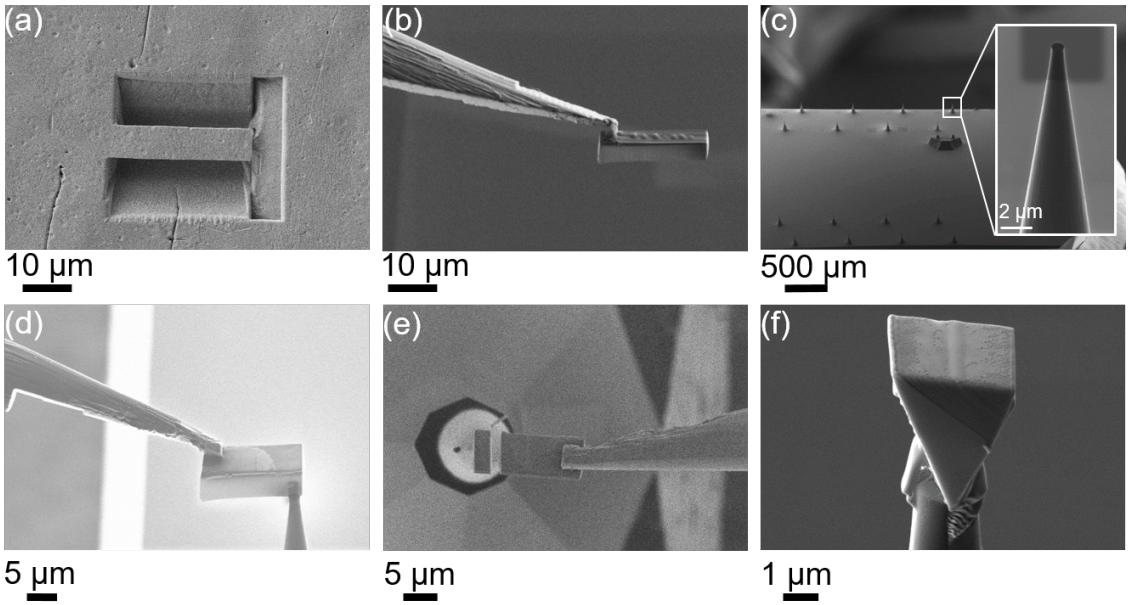


Figure 3.10: Images showing the lift-out procedure used to produce APT samples. (a) Cantilever after it has been milled. (b) Cantilever attached to the manipulator during the lift-out. (c) Array of Si micro-posts onto which samples are mounted. A higher magnification image of one of these posts is shown, also. (d) Section of material being mounted onto a micro-post. (e) A slice of the lift-out bar remains on the post. (f) A 'lift-out' mounted onto a Si micro-post using a tungsten or platinum weld.

Table 3.5: Conditions used to mill cantilever

Stage	FIB		Time (Minutes)
	Voltage (kV)	Current (nA)	
Milling Trench	30	6.5	10 (per side)
Milling Cantilever	30	3	5 (per side)
Undercutting Cantilever	30	0.7	10 (per side)
Freeing Cantilever	30	3	5

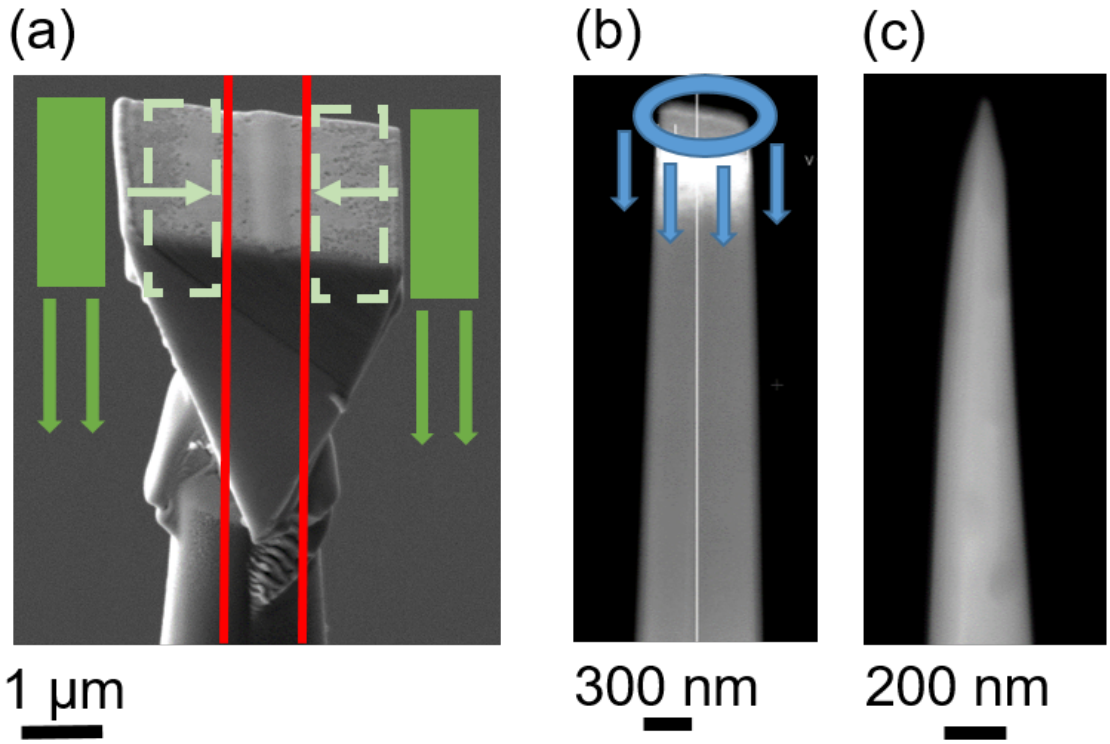


Figure 3.11: Images showing the sharpening and polishing procedure used to make APT needles from a lift-out. (a) Samples are thinned to a width of approximately 1 μm. (b) An annular mill is used to shape the sample into a needle and sharpen until the end radius is approximately 100 nm. (c) Needle after the final polish where a low kV ion beam is used to remove the 300 nm of material at the apex of the sample.

Table 3.6: Conditions used to sharpen and polish APT needles by focused ion beam. Sample diameter refers to the width of the sample.

Stage	Sample Diameter (nm)	FIB Conditions	
		Voltage (kV)	Current (pA)
Sharpening	1000	30	700
	500	30	300
	100	30	80
Polish	100	5	200

3.3.4 Sample Preparation Observations

Throughout this work several observations regarding these samples were made; firstly the likelihood of a successful APT experiment for an electropolished needle was best for samples the first time they had been prepared (Table 3.7). In this section, a successful APT experiment is defined as an experiment in which the oxide has been removed from the sample and 500,000 ions of metal were analysed. All samples were stored in ultra-high vacuum (UHV) if they could not be immediately placed into the atom probe and any electropolished samples left out of vacuum for more than 1.5 hours were often no longer viable due to sample oxidation. Samples that were prepared by electropolishing and then sharpened via focused ion beam had a better success rate. It was also noted that samples prepared in this manner tended to see a higher hydrogen concentration than those that were electropolished only which is likely due to hydride formation during sample preparation [77], [133]. The best yield of viable specimens were samples that were prepared entirely via focused ion beam methods, where almost all samples were successfully analysed.

Table 3.7: APT needle sample preparation methods and their relative success rate.

Sample Preparation Method		Success Rate
Electropolishing	First polish	1 in 4
	Subsequent polishes	1 in 9
Electropolish and FIB sharpen		1 in 2
FIB lift-out and polish		$\sim$100%

3.3.5 Samples for Transmission Kikuchi Diffraction

During sample preparation, transmission kikuchi diffraction (TKD) was used to ensure that the lift outs prepared for APT analysis contained the desired features. The TKD map was used to guide the location of the final tip to ensure it contained a grain boundary or other region of interest. TKD was not undertaken after the final milling stages in order to

prevent carbon contamination of the specimen from the SEM beam. Samples for TKD analysis were prepared using the method developed in [134]. Figure 3.12 contains images showing this process and the final TKD scan. Samples were thinned for TKD using 30kV/300 pA probe.

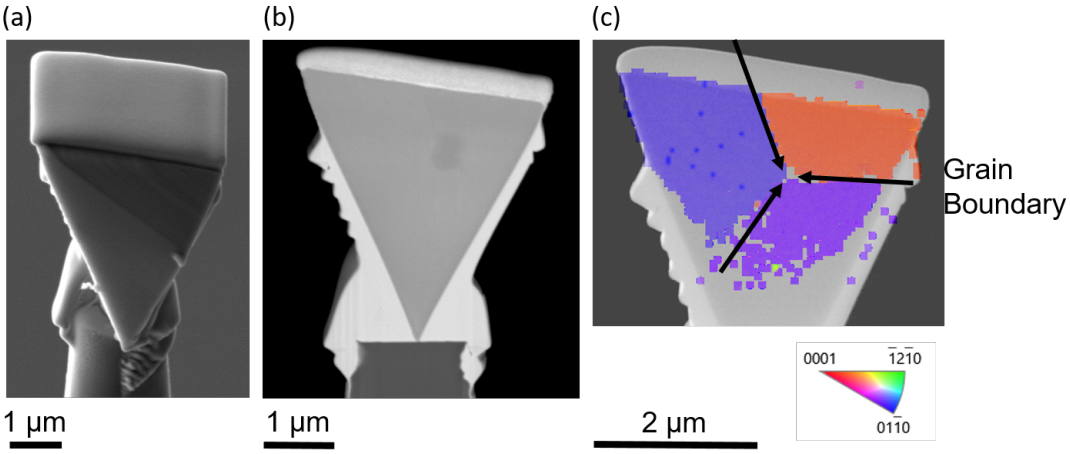


Figure 3.12: Images showing the thinning procedure used to produce samples for TKD. (a) Lift-out wedge mounted on a Si post. (b) Lift-out wedge after it has been thinned from both side to around 200-300 nm. (c) TKD scan of the lift out wedge showing the existence of a triple-point in the sample.

3.4 Deuterium Charging

Hydrogen is a common contaminant in APT data and originates from both the sample and the chamber. During data analysis, it is not normally possible to distinguish between the two [135], [136]. Samples are deuterium charged to enable the positive identification of hydrogen originating from the sample, as the natural relative abundance of deuterium is sufficiently low (0.015%). The scarcity of naturally occurring deuterium means that any deuterium detected in APT data can be assumed to have been introduced into the sample during the charging process and not during the APT analysis. In this work, samples were deuterium charged via gaseous and electrolytical methods.

3.4.1 Reaction Cell

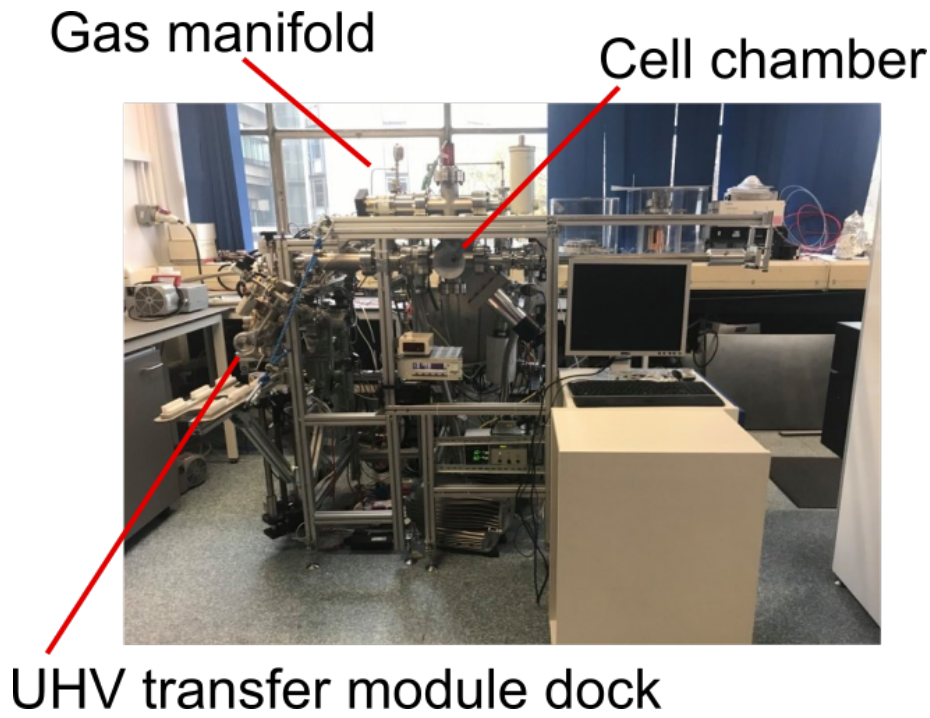


Figure 3.13: Photograph of the reaction cell in its current form as a stand-alone piece of equipment.

A reaction cell, designed and manufactured in Oxford was used to expose the sample to deuterium gas, shown in Figure 3.13 [137]. The cell allows for samples to be transferred between the LEAP to the reaction cell without air exposure, under ultra-high vacuum, using a vacuum cryo transfer module (VCTM, Figure 3.14 (a)). Typically, the transfer between the reaction cell and the analysis chamber of the LEAP is 15 minutes. The cell is able to expose samples to gas at temperatures between room temperature and 450 °C, at pressures between 1 mbar and atmospheric pressure. The temperature measurements are made using a Type K thermocouple, which located underneath the stage, approximately 1.5 cm from the sample. Pressure measurements are taken using a variety of pressure gauges; in the exchange chamber a high vacuum gauge is used to measure pressures between 400 mbar and 10^{-4} bar. In the cell, a CERAVAC pressure gauge measures the pressure.

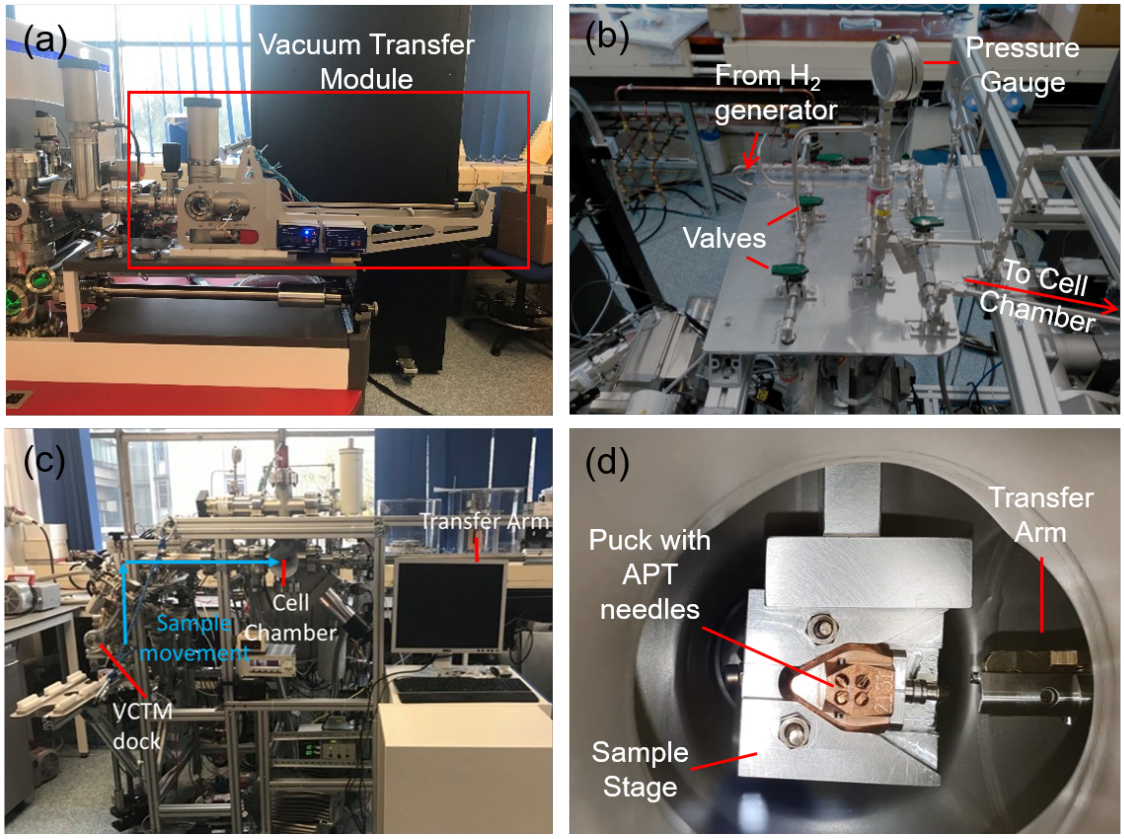


Figure 3.14: Labelled images showing the key features of the reaction cell. (a) Vacuum cryo transfer module (VCTM) docked onto the LEAP XS. (b) Top down view of the gas manifold of the reaction cell. (c) Front view of reaction cell, dock for the VCTM in (a) is labelled. (d) Sample stage for the reaction cell, that is drawn back into the cell chamber.

The deuterium gas is produced using a SRI Instruments H2-100 unit, which electrolyses heavy water producing deuterium and oxygen. The deuterium gas is dried to remove moisture before being allowed to flow into the reaction chamber. The oxygen is vented out at the point of generation. A water vapour and an oxygen trap were added into the gas line as part of this work in order to minimise levels of oxygen introduced to the cell during charging. The sample is then inserted into the cell chamber and is exposed to the gas. Once the charging has been completed, the samples can be moved into the LEAP for analysis. A residual gas analyser is attached to the reaction cell to measure the mass spectrum of the residual gas left after deuterium exposure.

3.4.2 Hydrogen Charging Protocol

The exact deuterium charging protocol used was experiment dependent, a generalised protocol is as follows :

- Analyse sample in LEAP to remove oxide film formed after sample preparation and provide a reference mass spectrum of the metal
- Transfer sample under UHV from the LEAP to the reaction cell using the VCTM
- Charge sample in cell chamber of the reaction cell
- Transfer sample under UHV from the reaction cell to the LEAP using the VCTM
- Analyse sample in the atom probe under the same analysis conditions as done previously.

This is shown schematically in Figure 3.15.

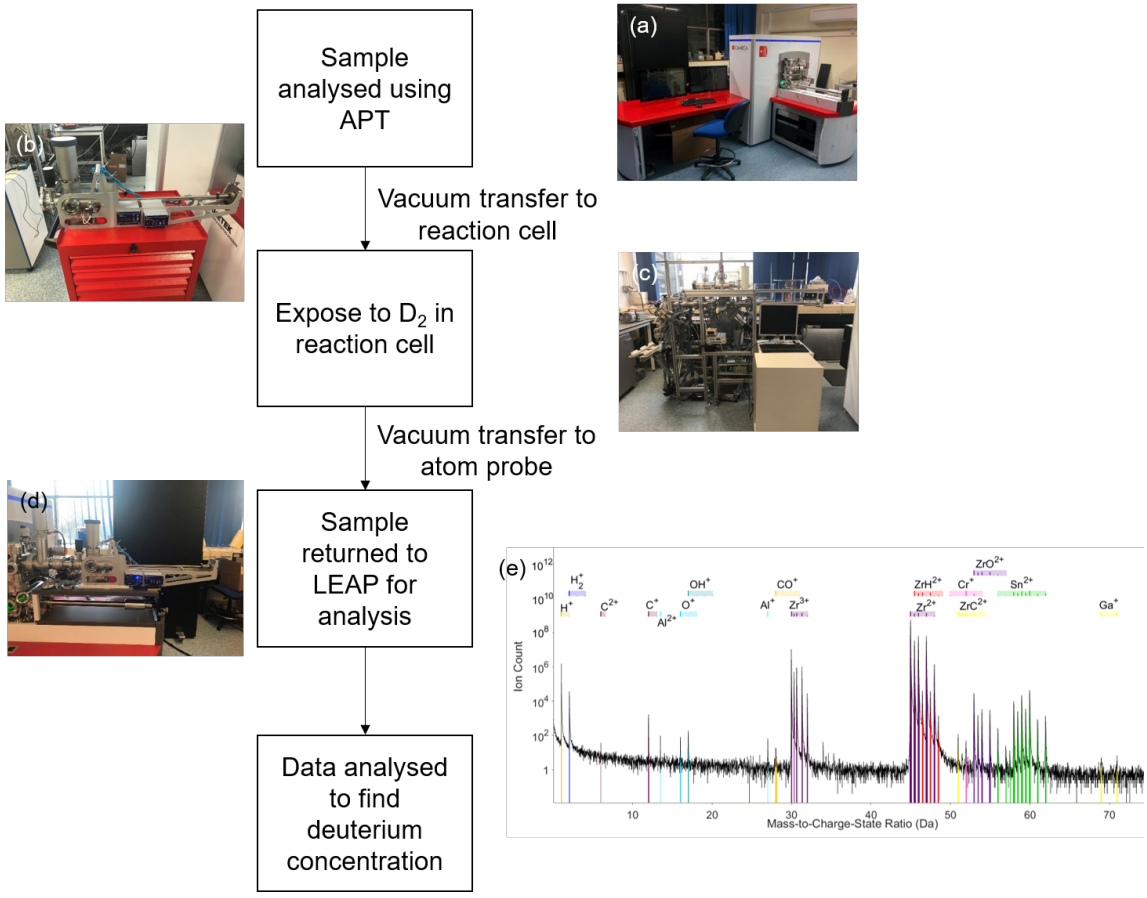


Figure 3.15: Deuterium charging protocol schematic. (a) Cameca LEAP 5000 XR atom probe. (b) Vacuum Cryo Transfer Module used to move samples between LEAP and reaction cell. (c) Reaction cell used to deuterium charge samples. (d) Vacuum transfer module docked onto an atom probe. (e) Zircaloy-4 mass spectrum.

In this work Zircaloy-4 and pure zirconium wire samples were deuterium charged. A full list of the experiments conducted can be found in Section 3.5.

3.5 Developing deuterium charging protocols

To develop appropriate deuterium charging protocols Zircaloy-4 and pure zirconium wire samples were deuterium charged using the gas reaction cell detailed in Section 3.4. Tables 3.8 and 3.9 give the parameters of the deuterium charging experiments that were undertaken. In these tables, the temperature listed is the set point for the heater and the temperature of the thermocouple. The heating tape refers to tape, that was heated to

180 °C and was wrapped around the cell chamber to help maintain a constant temperature throughout the cell. The gas purification column gives which gas traps were in operation during the charge. The cooling method indicates how the samples were cooled; 'in vacuum' means that the D_2 gas was pumped out and the sample allowed to cool under vacuum, the cell heater was turned off and the cell left to cool. 'In D_2 gas' means that the sample and gas were left to cool, by turning off the heater and letting the system cool down, until T=100 °C before the gas was pumped out of the cell chamber and the sample removed. 'In cold D_2 gas,' the hot D_2 gas was pumped out and replaced with D_2 gas at room temperature in order to cool the system. Gas was added and pumped out until T=50 °C.

Table 3.8: Table of deuterium charging conditions used for Zircaloy-4 experiments in this work. The temperatures listed refer to the set point of the cell heater. 'Y' means yes and 'N' means no in the table.

Temperature (°C)	Pressure (mbar)	Time (min)	Heating Tape	Gas Purification		Cooling Method
				Water Vapour Trap	Oxygen Scrubber	
300	1000	15	N	N	N	In vacuum
300	1000	15	Y	Y	N	In vacuum
300	1000	15	Y	Y	N	In D_2 gas
320	1000	90	Y	Y	Y	In D_2 gas
320	1000	180	Y	Y	N	In cold D_2 gas

Table 3.9: Table of deuterium charging conditions used for the zirconium wire experiments in this work. The temperatures listed refer to the set point of the cell heater. 'Y' means yes and 'N' means no in the table.

Temperature (°C)	Pressure (mbar)	Time (min)	Heating Tape	Gas Purification		Cooling Method
				Water Vapour Trap	Oxygen Scrubber	
300	1000	90	Y	Y	N	In D_2 gas

3.6 Cryogenic focused ion beam sample preparation

Cryogenic sample preparation methods were trialled to find a method to prepare site-specific lift-outs of APT samples where the deuterium trapping is unaffected by the focused ion beam and to prevent hydride formation [133]. Hydride formation is known to occur in the FIB sample preparation of Zr alloys and the majority occurs in the final stages of ion beam milling where the sample is thinnest [82], [133].

Lift-outs from the as-recieved and deuterated Zircaloy-4 samples were produced in Oxford using the Zeiss NVision-40 and Crossbeam-540 dual FIB-SEM instruments. These mounted 'lift-outs' (image (f) in Figure 3.10) were sent under vacuum, using an Oxford Atomic low vacuum transport holder, to the University of Nottingham where the samples were sharpened at a temperature of -150 °C using a Zeiss Crossbeam 550 FIB-SEM instrument equipped with a Quorum PP3010 cryo-FIB/SEM preparation system. The FIB probe voltage and currents used to sharpen the sample are the same as those listed in Table 3.6.

3.7 APT of Cold Worked Zircaloy-4

To investigate the interaction of hydrogen with dislocations, cold worked materials were prepared for APT analysis using electropolishing and then FIB sharpening. Samples containing grain boundaries and second phase particles were produced from the as-received Zircaloy-4 sample using the lift-out method described previously.

3.8 APT of Irradiated Zircaloy-2

Irradiated Zircaloy-2 samples were deuterium charged to investigate the interaction of hydrogen with irradiation induced defects. The sample preparation and secondary ion mass spectrometry (SIMS) acquisition was undertaken at the National Nuclear Laboratory's Central Laboratory.

3.8.0.1 Deuterium Charging

The samples were ground and polished down to an EBSD finish using the method in Section 3.3.1. To remove the surface oxide prior to deuterium charging, the samples were electropolished at 5 °C in a 5 vol.% perchloric acid in acetic acid solution. The samples were polished for 10 minutes with the current limited to 800 mA, 600 mA, 400 mA and 200 mA. The samples were then cleaned with ethanol and immediately charged. The samples were deuterium charged using an electrochemical charging cell similar to that in [138], purchased from DEK Research. The samples were charged using a current density of 2 kAm^{-2} in solution of 1.5 wt. % D_2SO_4 in D_2O at 65 °C for 4 hours. This method was adapted from [116] and [139].

3.8.0.2 SIMS

Secondary ion mass spectrometry (SIMS) data was acquired using a Tescan XEIA plasma FIB/SEM with TOF-SIMS to aid the production of deuterated APT samples. SIMS maps were obtained using 30 kV/ 10 nA and 30 kV/ 100 nA in order to map out the peak at 2 Da, corresponding to the H_2^+-D^+ overlap.

3.8.0.3 APT Sample Preparation

24 samples from the 4 samples were taken (one lift-out per sample in the deuterated and as-recieved state). The lift-out and sharpening procedure followed the method in Section 3.3.3. The lift-out procedure was conducted at room temperature and the final shaping and sharpening stages at -90 °C.

Chapter 4

Deuterium Charging Protocol Development

4.1 Introduction

In order to investigate the interaction of hydrogen with material defects in zirconium alloy fuel claddings using APT, it is necessary to prepare Zr APT samples that are deuterium charged. The deuterium acts as an isotopic tracer, enabling the identification of hydrogen in the resulting APT data. We can achieve a deuterated APT needle in two ways, firstly by deuterium charging a bulk Zr sample and producing needle shaped specimens from this or by deuterium charging a pre-prepared APT needle. In the literature, both methods have been used to analyse deuterides and deuterium segregation and trapping in a range of materials using APT. Breen et al. and Mouton et al. have electrolytically charged a bulk Zircaloy-4 sample to analyse the growth front ahead of a deuteride and hydride formation at grain boundaries respectively [116], [140]. In comparison, Chen et al. used electrolytic charging of electropolished APT needles to investigate deuterium segregation to carbides, dislocations and grain boundaries in ferritic and martensitic steels [78], [141].

Deuterium charging a bulk sample allows for complementary analysis techniques to be used on the deuterated sample prior to producing site-specific lift-outs for APT

analysis. These techniques include secondary ion mass spectrometry (SIMS), for larger scale chemical information or electron back scatter diffraction (EBSD). However, it is known that Zr alloy samples are prone to picking up large amounts of hydrogen during sample preparation. This could cause the implantation of environmental hydrogen and/ or the loss of deuterium; both of these would limit the sensitivity to deuterium in APT measurements. To the authors knowledge there are no studies currently available which have systematically examined the effect of FIB milling on hydrogen trapping in deuterium-charged samples. Hanlon et al. have shown that hydriding is severly reduced when the final stages of TEM sample thinning are completed under cryogenic conditions [133]. However, as the hydriding is reduced and not removed, it is not clear what the effect on any atom probe samples prepared in this manner may be. This will be discussed further in Chapter 5 which addresses the use of cryogenic focused ion beam methods to produce APT needles.

An alternative to using bulk samples is to prepare APT needles and deuterium charge them prior to analysis. This has the advantage of not needing FIB access and enables a reference mass spectrum from the uncharged sample which can aid data analysis (i.e. the same needle before and after deuteration). For a FIB prepared specimen a needle from the bulk prior to deuteration could be obtained but it is not the exact same sample as the charged one. The deuterium charge itself can take place via gaseous and electrolytic routes [91], [94]. In previous studies in the literature, Zr alloys have been hydrogen charged in both ways (in the literature) but due to the likelihood of the Zr APT needle corroding during an electrolytic charge, gaseous hydrogen charging was used in this study. Gas charging is a known method for hydrogen charging zirconium samples , but this has not yet been used to successfully deuterium charge zirconium alloy APT samples to analysis the atomic scale behaviour of hydrogen [87], [88], [142]. A gas reaction cell was used to charge Zr alloy samples with deuterium [137]. The aim of this work was to develop a method to deuterium charge Zr alloy APT needles that could be use for further investigations.

Previous investigations by this author have analysed as-received and cold worked Zircaloy-4 APT samples that were deuterium charged using the same set up [128]. One of

the conclusions from this work was that the gaseous charging methods could be used to charge Zircaloy-4 samples despite the current methods introducing oxygen into the sample. Diffusion of hydrogen through the oxide of Zr is the rate limiting step in hydrogen pick up [143]. In post-charging APT analyses, deuterium was found to be at highest levels in the oxide layer but little or none was observed to be present in the metal (Figure 4.1 (b)). Future avenues for research should therefore start with maximising deuterium uptake by altering the charging parameters and limiting the oxidation occurring during the charge as this will also aid deuterium uptake.

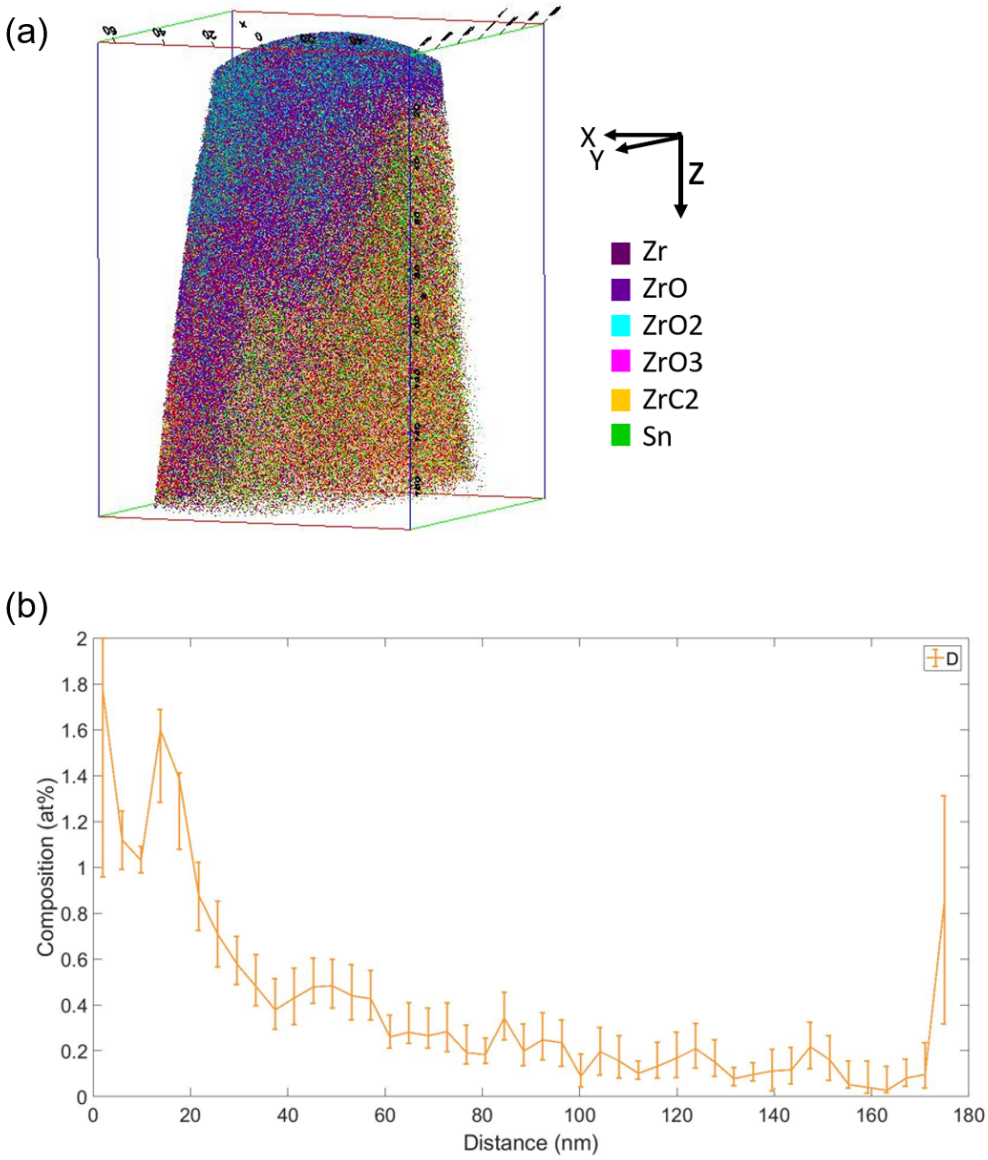


Figure 4.1: (a) Reconstruction from a deuterium-charged Zircaloy-4 sample. (b) Concentration line profile down the length of the reconstruction (Z direction). Adapted from [128].

4.2 Preventing sample oxidation during D_2 charging

4.2.1 Experimental Methods

To conduct a deuterium charging experiment, 3 pieces of equipment are needed. Firstly, the atom probe (Figure 4.2 (a)) is required to 'clean' the samples prior to the deuterium charge, provide a reference mass spectrum and analyse the deuterium-charged sample. Secondly, the gas reaction cell (Figure 4.2 (c)) is necessary to conduct the deuterium charge. Finally the Vacuum Cryo Transfer Module (VCTM, Figure 4.2 (b)) which is used to move the samples between the atom probe and reaction cell (as these are separate pieces of equipment). The use of the VCTM is necessary to move the samples, under vacuum, between the cell and atom probe in order to prevent sample oxidation and to keep the specimens clean. Both the reaction cell and the atom probe have suitable docks to attach the VCTM to so the transfer can be completed.

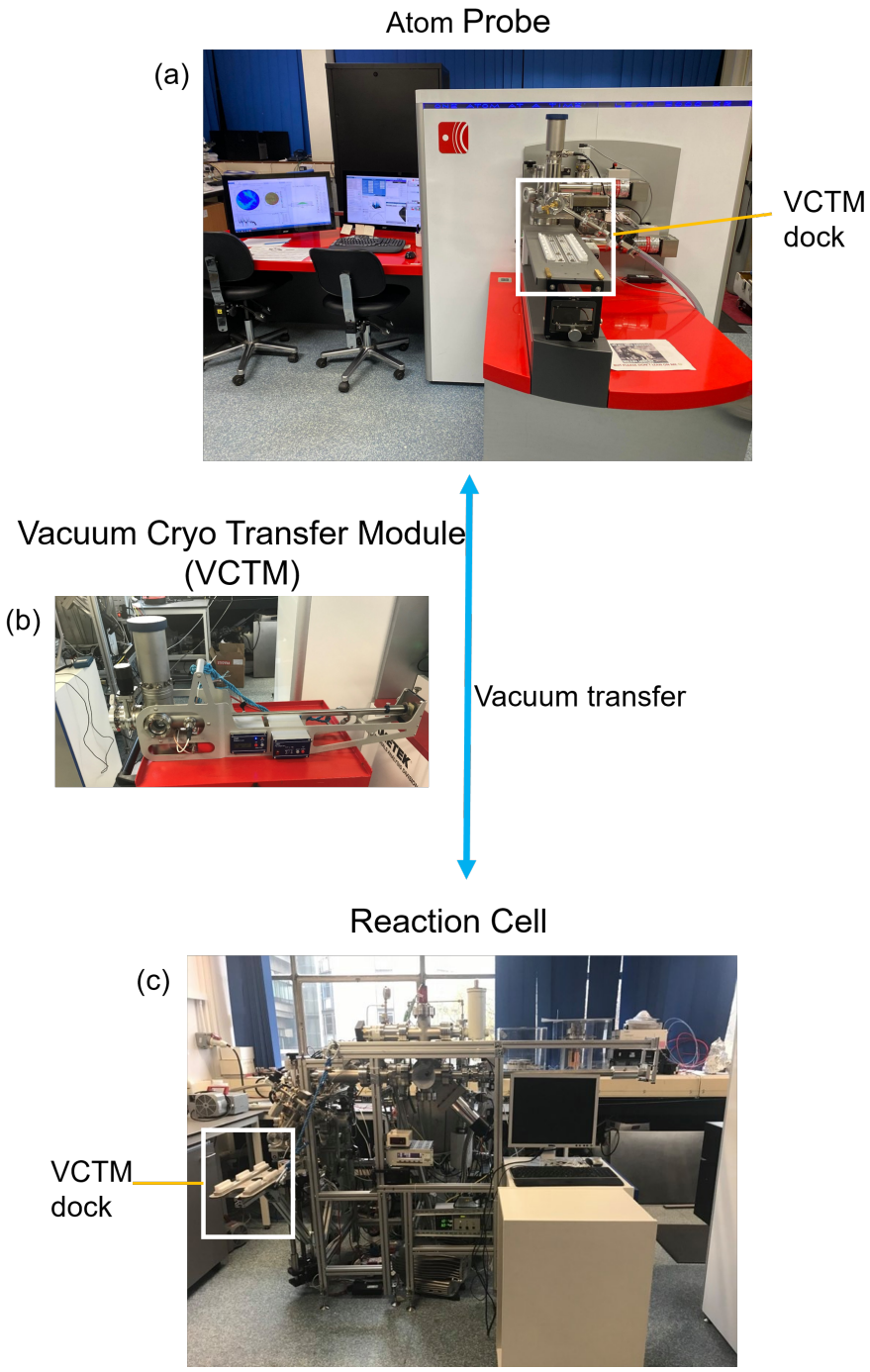


Figure 4.2: Equipment used in deuterium charging experiments. (a) Atom probe used to analyse the samples. (b) VCTM use for the transfer. (c) Reaction cell used to conduct the gas charge.

4.2.2 Oxidation sources

In previous work, deuterium charging samples showed that during the charging process, the Zr samples oxidise [128]. This is undesirable because zirconium oxide is a barrier to hydrogen ingress and as samples tend to fracture during analysis of the oxide layer it is better for data yield if we do not have this layer present. Figure 4.3 shows representative APT reconstructions from the previous study highlighting the oxide layer formed during the charging protocol.

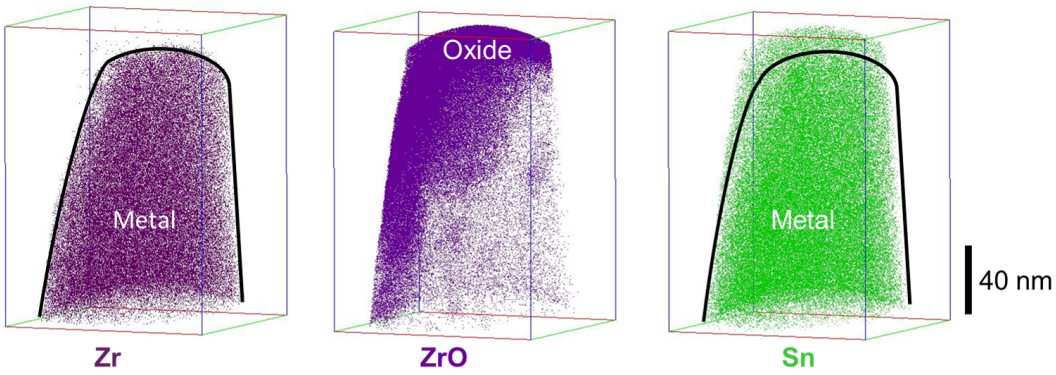


Figure 4.3: Reconstructions of APT needle after a deuterium charge. An oxide can be seen on the sample by the location of ZrO ions. The Zr and Sn ions are also included to highlight where the metal region of the sample is. Figure adapted from [128].

The hydrogen charging protocol we followed in the current investigation contains a number of processes in which the samples could be oxidised. Figure 4.4 is a schematic of the protocol and identifies that there are points in the protocol where oxidation could occur: during the time between the initial, reference APT analysis and the deuterium charge, and the charge and the final APT analysis where the sample is held under vacuum; during the transfer between LEAP and reaction cell and from the gas in the charge itself. It was necessary to identify where in the deuterium charging protocol the sample was oxidising and how significant it was so we could work to prevent it (Table 4.1).

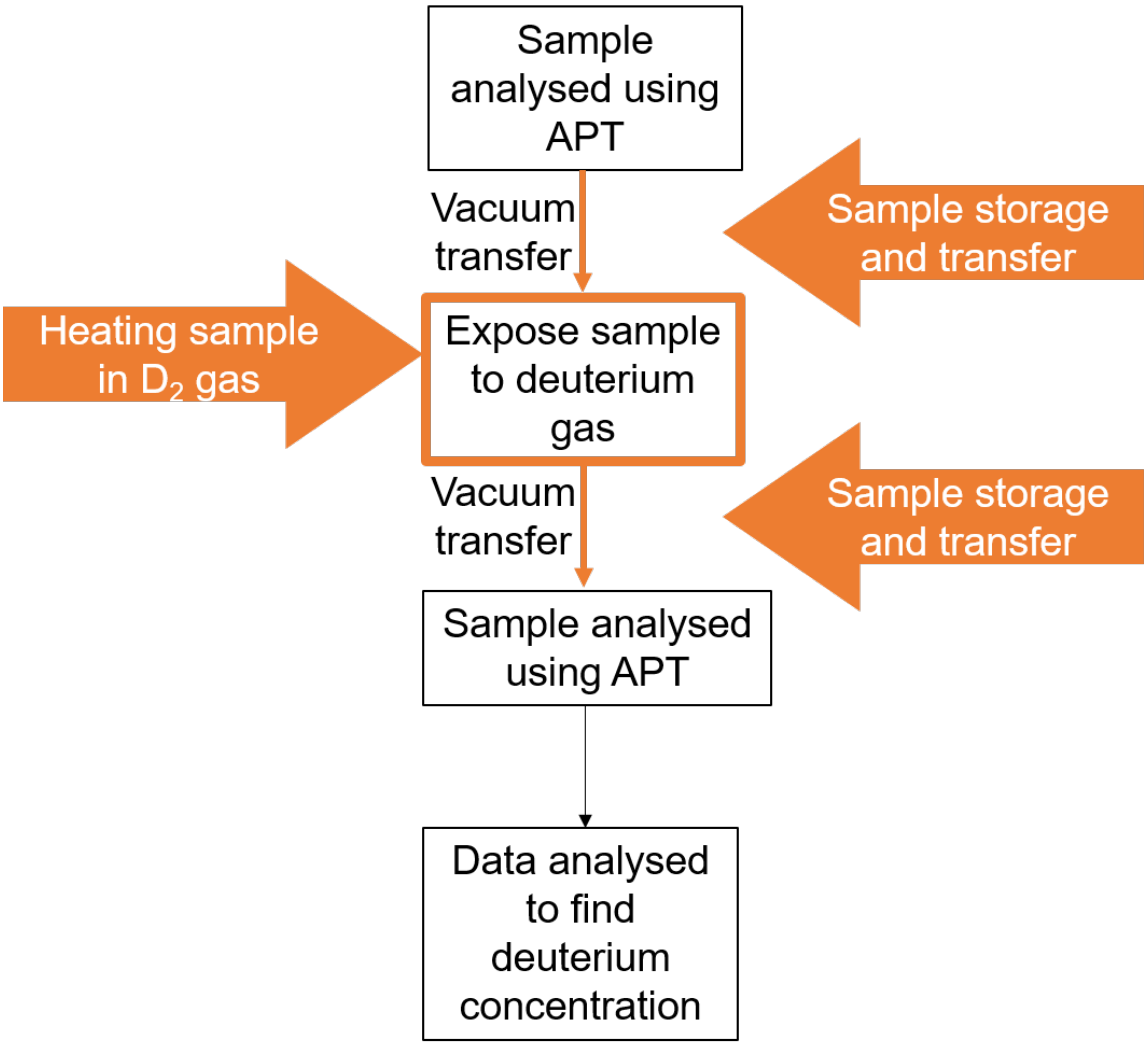


Figure 4.4: Schematic of the charging protocol with the points in the protocol where the sample could be prone to oxidation are labelled with the orange arrows.

Table 4.1: Potential solutions to the problem of the oxidation of the Zr alloy samples during analysis.

Oxidation Place	Potential Prevention Method
Storing sample	Take and return sample immediately to analysis chamber
Vacuum transfer	Transfer under cryogenic conditions
Gas	Gas purification

Due to experimental constraints, there was often a period of time for which samples

were left in the buffer chamber of the atom probe under UHV. Typical pressures in the buffer vacuum are 10^{-8}- 10^{-9} Torr. To test whether oxidation occurs in this stage, we analysed a sample in the atom probe to remove the oxide and gain a reference mass spectrum of the metal and left it in the buffer of the atom probe for approximately 6 weeks (Figure 4.5 (c)). Subsequent APT analysis showed that a thin but complete layer of oxide had formed on the sample after this, showing that samples will develop an oxide film if they are left in the buffer for extended periods of time.

Sample transfer between the reaction cell involved moving the sample through sections of pipework that are vented to atmospheric pressure. It is also possible that sample oxidation could occur during this stage, even when using the vacuum cryo-transfer module. To check for the occurrence of oxidation at this stage, we analysed a sample in the atom probe as previously and then transferred the sample from the analysis chamber of the atom probe to the reaction cell chamber and re-analysed the sample (Figure 4.5 (b)). It was found was found that a complete oxide film was found to be present on the sample, indicated by ZrO_x ions being present across the entire surface of the reconstruction. To ensure that there was no issue associated with the transfer specifically to and from the reaction cell, a sample was transferred between two atom probes (Figure 4.5 (d)). This sample also had a complete oxide film on it, showing that during a vacuum transfer at ambient temperatures, we end up with an oxide film on the samples.

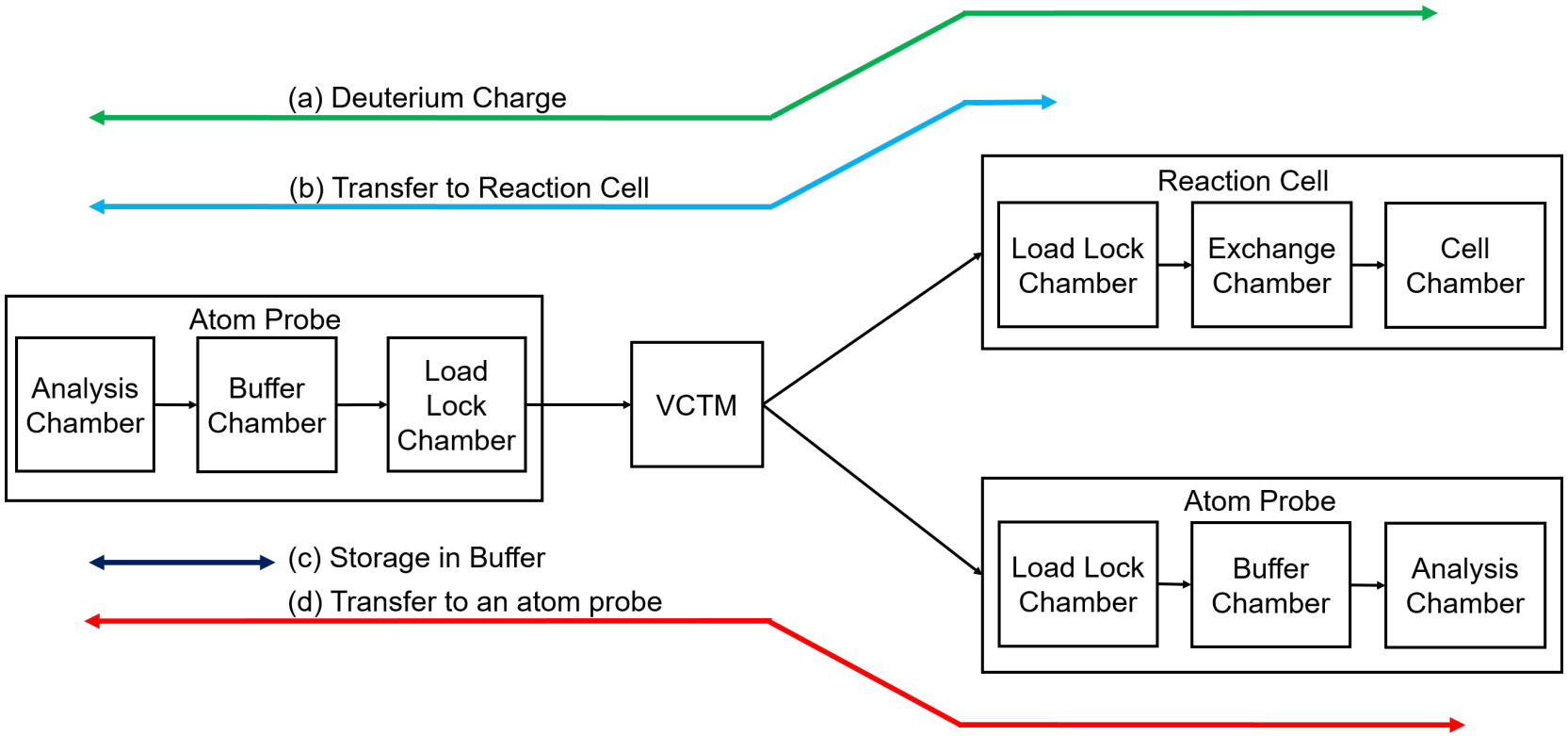


Figure 4.5: Diagram showing the different parts of the protocol and transfers investigated for the amount of oxidation. (a) Sample transfers that take place during the deuterium charging protocol. The deuterium charge itself occurs in the Cell Chamber. (b) Transfer of a sample from the analysis chamber of the atom probe to the first chamber of the Reaction Cell. (c) Sample storage in the buffer chamber of the atom probe. (d) Sample transfer from one atom probe's analysis chamber to another.

Table 4.2: Stages of the deuterium charge protocol, whether they led to oxidation or not and the relative severity of the oxidation indicated by the ranking from 1-5 where 1 is the thickest oxide and 5 the thinnest.

Stage of Protocol	Oxidation	Severity of Oxidation Types of ZrO Ions			Relative Thickness
		ZrO	ZrO_2	Zr_2O_3	
Storage in Buffer	Yes	Y	Y	N	4
Transfer to atom probe	Yes	Y	Y	N	3
Transfer to Cell	Yes	Y	Y	N	Unknown
Charge	Yes	Y	Y	Y	1
Metal	N/A	Y	N	N	N/A
Post sample preparation	N/A	Y	Y	N	2

Table 4.2 contains the results from these experiments. It was found that an oxide film forms on these Zicaloy-4 samples before they have reached the reaction cell and undergone the charge. This is important information to know because in order for the deuterium to reach the metal in the sample, it has to pass through this layer and thus its presence should be taken into account when deciding the duration of the charge as diffusion of D through an oxide in Zr is slower than that in a metal. This work also demonstrates that the samples will form an oxide film if kept in vacuum for extended periods of time so any charged samples were analysed as quickly after the charge as was feasible. More oxide appeared to form during transfer to the cell than between LEAPs indicating that there may be an issue with part of the transfer system with the cell.

The oxide formed during the different stages of the protocol that are outside of the charge itself, is insignificant compared to the oxide formed during the gas charging part of the procedure. The majority of the oxidation occurs inadvertently during the exposure to impurity oxygen that is present during the deuterium gas charge. Filtering the gas to improve the purity could decrease the oxidation that occurs by removing any oxygen containing components such as O_2 and H_2O.

This series of experiments, in which the various stages of specimen preparation, transfer, charging and analysis, show that the Zr samples are prone to forming a thin but complete oxide film during the non-charging parts of the protocol. However, this does not account for the thickness of oxide seen post-charge demonstrating that gas filtering is needed during charging.

4.2.3 Gas filtering

The reaction cell has a residual gas analyser attached to the exposure chamber which enables a measurement of a mass spectrum of the gas left over from the charge to be acquired. By analysing this mass spectrum we can determine what gases are present in the chamber post-charge, and are therefore likely to be in the deuterium gas the samples are exposed to. The gas produced by the hydrogen generator is 99.99% deuterium, according to the manufacturer SRI Instruments, however we did not confirm this and the gas has to pass through the gas manifold before reaching the chamber where the sample resides and could be contaminated after it leaves the generator. Figure 4.6 presents the mass spectrum of the residual gas after a deuterium charge. It is evident that the highest intensity peaks are recorded from 15-25 Da which corresponds to peaks for oxygen and water vapour. This leads to the question as to whether removing these components from the gas would prevent sample oxidation, thereby improving deuterium uptake.

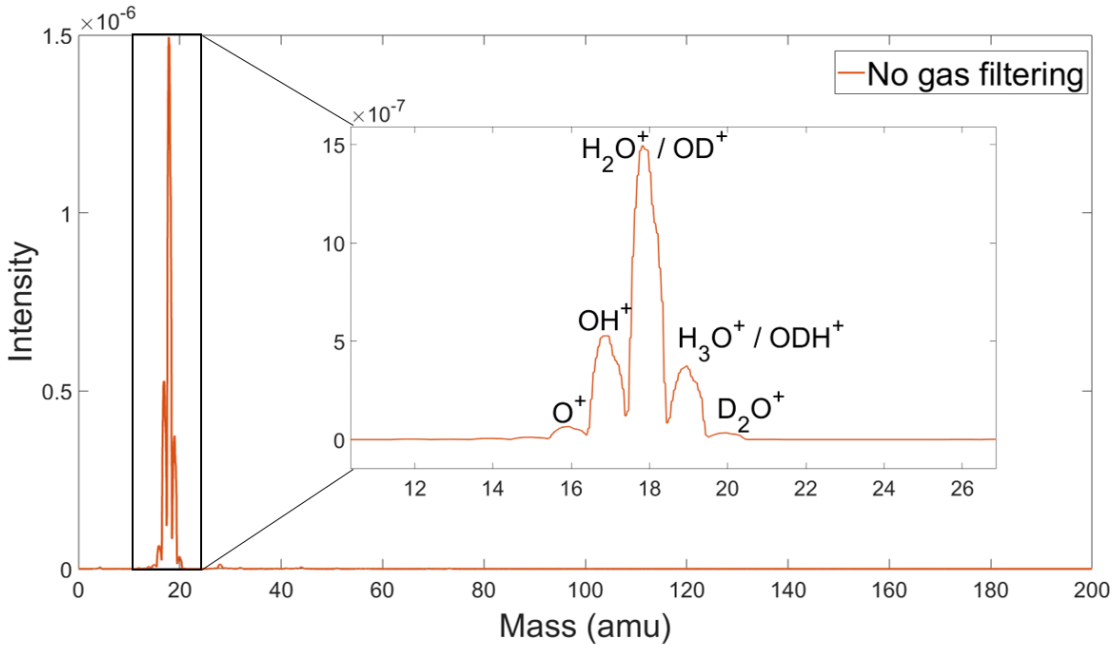


Figure 4.6: Residual gas analysis scan of the gas in reaction cell post deuterium charge at 300C for 15 minutes. The water peaks (black box) have been highlighted.

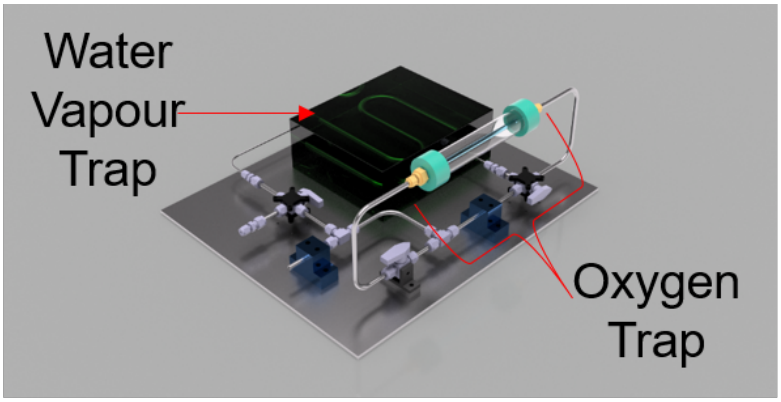


Figure 4.7: Diagram of the water vapour and oxygen traps in the gas line of the reaction cell.

A water vapour trap (Figure 4.7) was acquired (Restek rechargeable molecular sieve).This re-usable water vapour trap could be heated to remove the water vapour from it between charges. This was added into the gas line after the generator to remove water vapour, and reduce sample oxidation. A schematic of the gas flow after it is generated is presented in Figure 4.8. To test the effectiveness of the trap (Figure 4.8 c)), tungsten wires

were used as they have a higher yield during APT experiments than Zr.

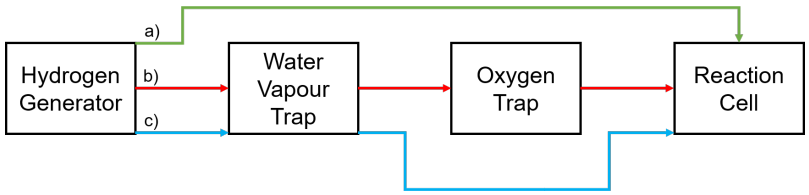


Figure 4.8: Schematic of the deuterium gas flow routes into the reaction cell, through the different filters. a) No gas filtering applied. b) Water vapour trap is used to filter the deuterium gas. c) Both the water vapour and oxygen traps are used to filter the gas.

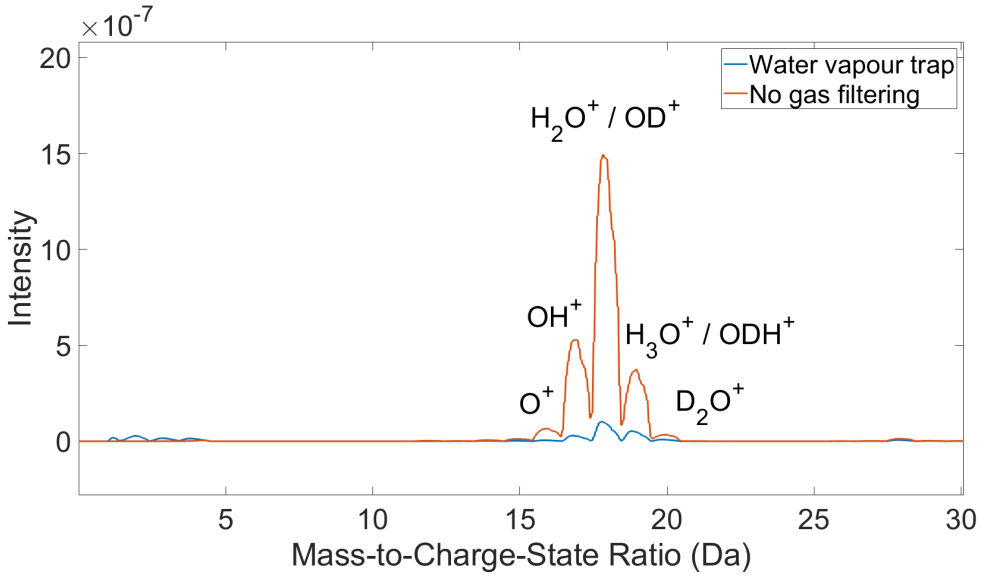


Figure 4.9: Mass spectrum of the residual gases in the cell chamber of the reaction cell after a 15 minute deuterium charge at 300°C comparing the cases in which the gas was and was not filtered by the water vapour trap. The possible identity of the ions that have caused the formation of these peaks are labelled.

Figure 4.9 provides an insight into the contents of the gas the samples were exposed to. The section of the mass spectrum shown contains the water peaks, it is evident that the use of the water vapour trap does appreciably decrease the amount of water vapour in the gas. However, it does not remove the water vapour completely. It was also necessary to repeat these experiments with Zr because it oxidises much more readily than tungsten.

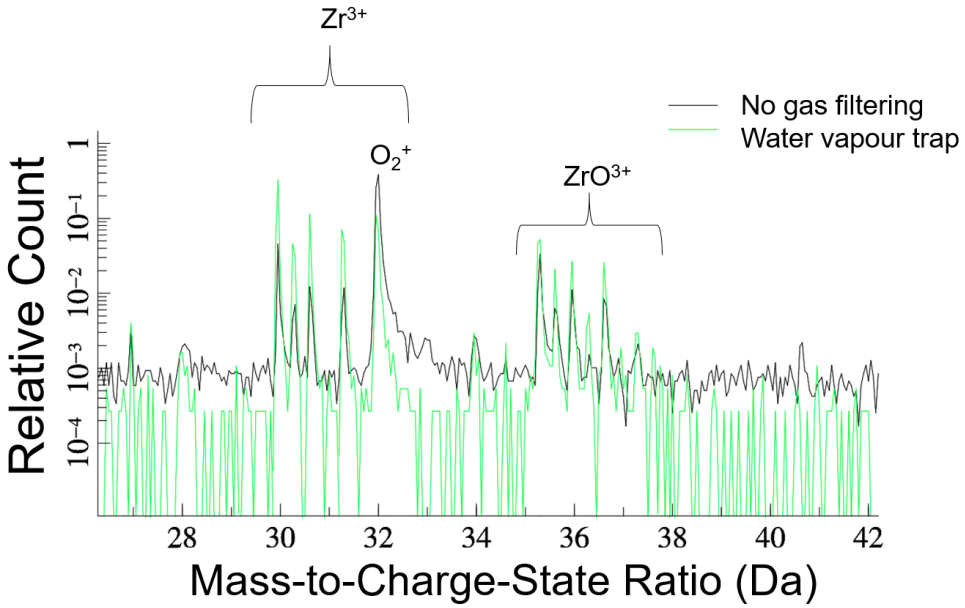


Figure 4.10: Section of an APT mass spectrum from 28-42 Da of a Zircaloy-4 sample after deuterium charges at 300°C where the water vapour trap was (green) and was not (black) implemented. All of the peak heights are scaled to the $^{90}Zr^{2+}$ peak at 45 Da.

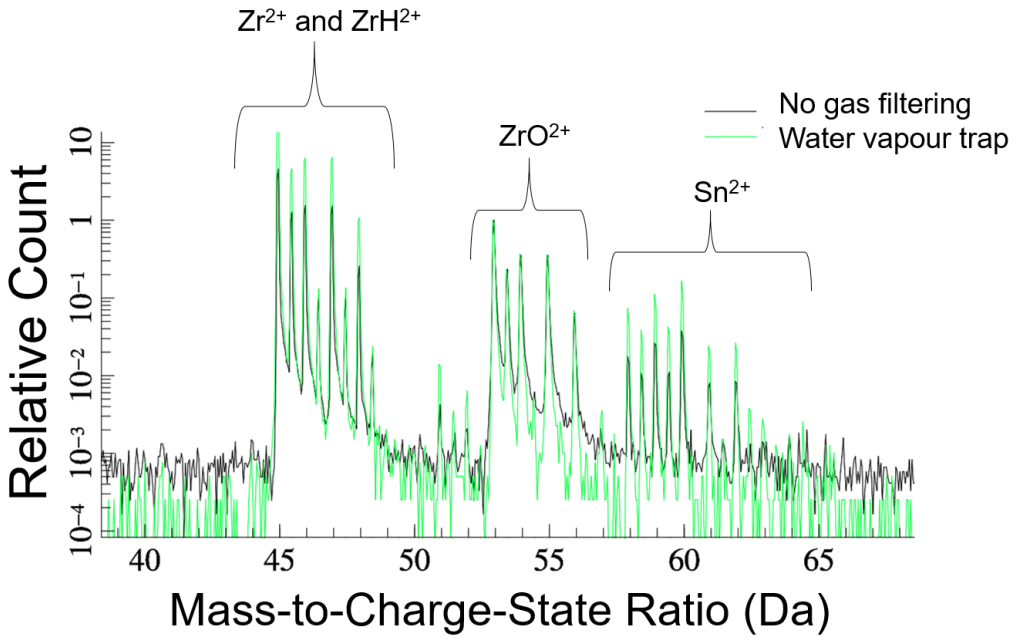


Figure 4.11: Section of an APT mass spectrum from 40-65 Da of a Zircaloy-4 sample after deuterium charges at 300°C where the water vapour trap was (green) and was not (black) implemented. All of the peak heights are scaled to the $^{90}Zr^{16}O^{2+}$ peak at 53 Da.

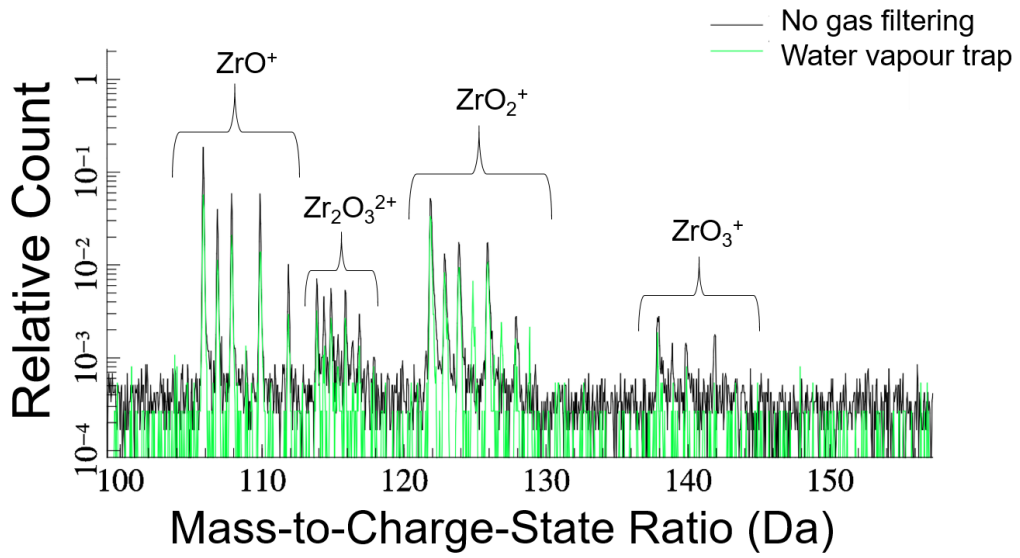


Figure 4.12: Section of a mass spectrum of a Zircaloy-4 sample after deuterium charges at 300°C where the water vapour trap was (green) and was not (black) implemented. All of the peak heights are scaled to the $^{90}Zr^{2+}$ peak at 45 Da.

Figures 4.10, 4.11 and 4.12 show the effect of the water vapour trap on the APT mass spectrum of Zircaloy-4 after deuterium charging. The mass spectra are scaled to the height of a defined peak to enable a comparison between datasets without any effect of the number of ions analysed in each dataset on the analysis. Figures 4.10 and 4.12 are normalised with respect to the $^{90}Zr^{2+}$ peak to enable a comparison of the relative amount of Zr and oxide ions. The peak corresponding to molecular oxygen (O_2^+ at 32 Da in Figure 4.10) is smaller when the trap is used. Relatively fewer counts of oxygen containing ions are detected when the water vapour trap is used, indicating that less oxidation has occurred than previously (Figure 4.12). The peaks corresponding to metal ions have a (relatively) higher intensity when the water vapour trap is used. This confirms that the water vapour trap reduces oxidation as oxidised samples contain fewer metal ions as in comparison with the more oxidised samples (Figure 4.11). The reconstructions in Figure 4.13 show this by the lack of ZrO_2 ions in the reconstruction using the water vapour trap. A lower value of x in the ZrO_x type ions indicates less oxidation [97]. These results

show that the water vapour trap did lead to reduced water vapour levels in the residual gas and less oxidation of the Zr samples. However more gas filtering would be needed to reduce the oxidation further. To this end, an oxygen trap was implemented in the gas line (after the water vapour trap).

The purpose of the oxygen vapour trap was to remove any remaining oxygen from the deuterium gas and limit oxidation. Figure 4.13 presents APT reconstructions of the ZrO and ZrO_2 ions from deuterium-charged samples after different gas filtering methods were used. It is evident that the oxidation that occurred when the oxygen trap was used is much worse than that without any gas filtering at all as indicated by the increased amount of ZrO_2 ions in the recontructions (Figure 4.13). The sample for the charge with no gas filtering was electropolished and the charge with water and oxygen traps was electropolished and FIB sharpened. The difference in sample preparation method indicates that the sample for the oxygen trap would have had a thinner oxide layer as a result of the preparation so the sample preparation could not have given rise to the oxide thickness here. Also, both samples were left in storage for similar lengths of time. The layer of oxide at the top of the reconstruction is approximately twice as thick as compared to that without gas filtering or with the water vapour trap. It is acknowledged that the thickness of the oxide layer is dependent on the tip geometry and therefore the accuracy of the reconstruction parameters. All of the reconstructions in this thesis were produced using the starting voltage of the experiment to calculate the initial radius so are equally accurate, meaning that a rough comparison between the thickness of the oxide layer of samples that have similar numbers of ions is appropriate. These results imply that the oxygen scrubber actually made the oxidation situation worse. Gas leakage through the fittings is the likely cause of the increased oxidation in this case. For future work, the oxygen trap was not used. It would be beneficial for future users to see how low the oxygen levels could be reduced to.

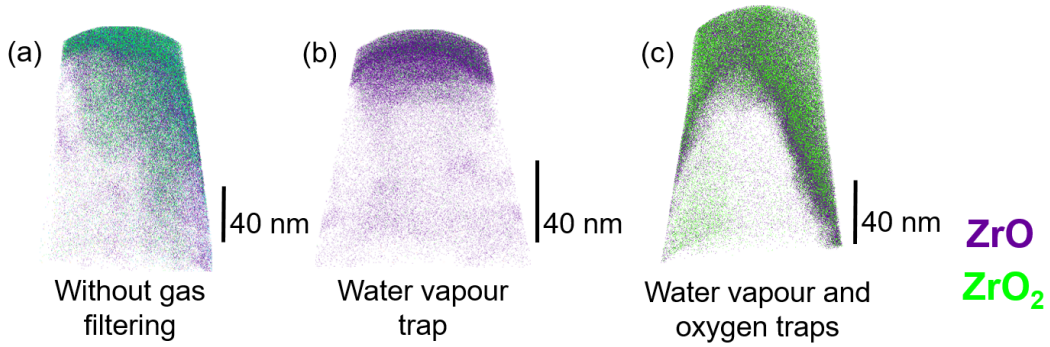


Figure 4.13: APT reconstructions of Zircaloy-4 samples after a deuterium charge where the gas (a) has not been filtered (19.3 million ions analysed), (b) has passed through the water vapour trap only (7.6 million ions analysed) and (c) water vapour and oxygen traps (16.7 million ions analysed).

4.3 Optimising deuterium charging parameters

4.3.1 Expected Data

Prior to interpreting the results, it is important to understand what an uncharged Zircaloy-4 dataset looks like and what constitutes a successful deuteration in terms of the APT data we generate.

Zircaloy-4 is a Zr-Sn alloy with small amounts of Fe and Cr. A representative mass spectrum is given in Figure 4.14. Features of note in the mass spectrum include Zr being present in the 1+, 2+ and 3+ charge state, and that the 2+ charge state is the most abundant for Zr.

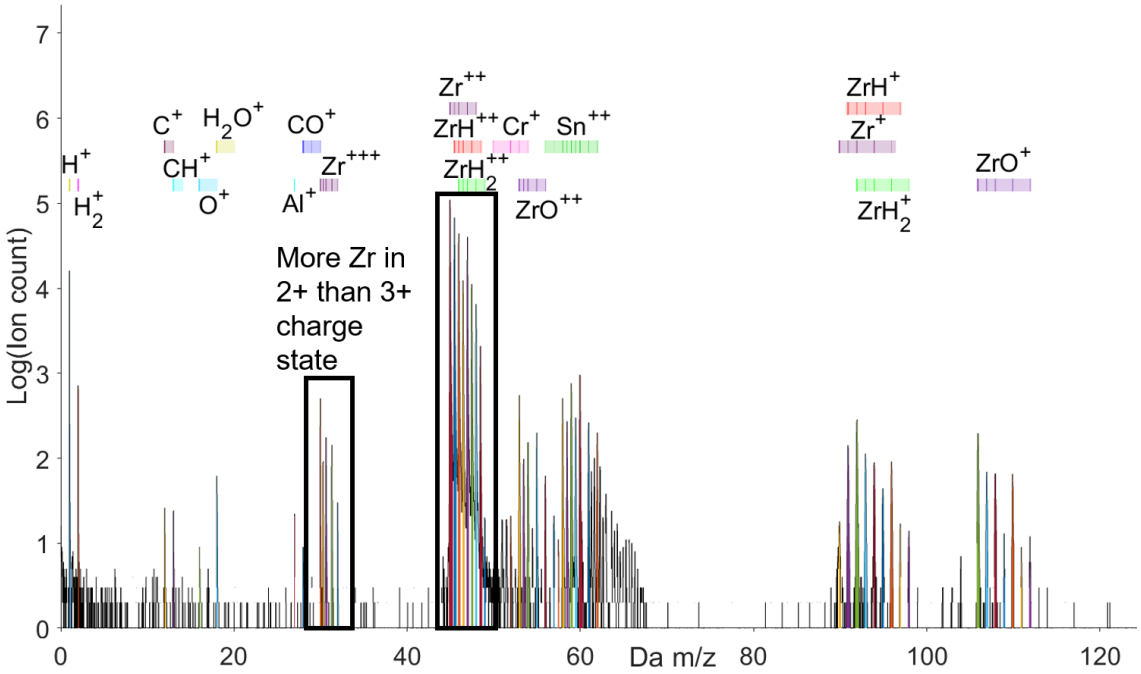


Figure 4.14: Representative mass spectrum of a Zircaloy-4 specimen, with peaks labelled. The height of the bars is related to the isotopic abundance of the ions.

A sample would be considered to have been deuterated if the mass spectrum contained peaks related to the detection of deuterated ions, namely these would be a large peak at 2 Da (D^+), at 3 Da (DH^+), 4 Da ($D_2{}^+$) and Zr deuteride ions (ZrD, ZrDH and ZrD_2). These peaks are highlighted in the close-ups in Figure 4.15. For Zircaloy-4, a peak at 3 Da is not always indicative of deuterium. In uncharged specimens, a peak at 3 Da is present in the oxide at the beginning of the APT experiment from $H_3{}^+$ ions but it is not present in the Zr metal region of the dataset. For a deuterium-charged sample, DH^+ ions also contribute to this peak. As we detect a peak at 3 Da in the oxide of an as-received specimen, this peak in an oxide region is not enough to show that deuterium is present in the sample. A peak at 3 Da in a metal region of the sample must be due to the presence of deuterium as it is not present in the as received state.

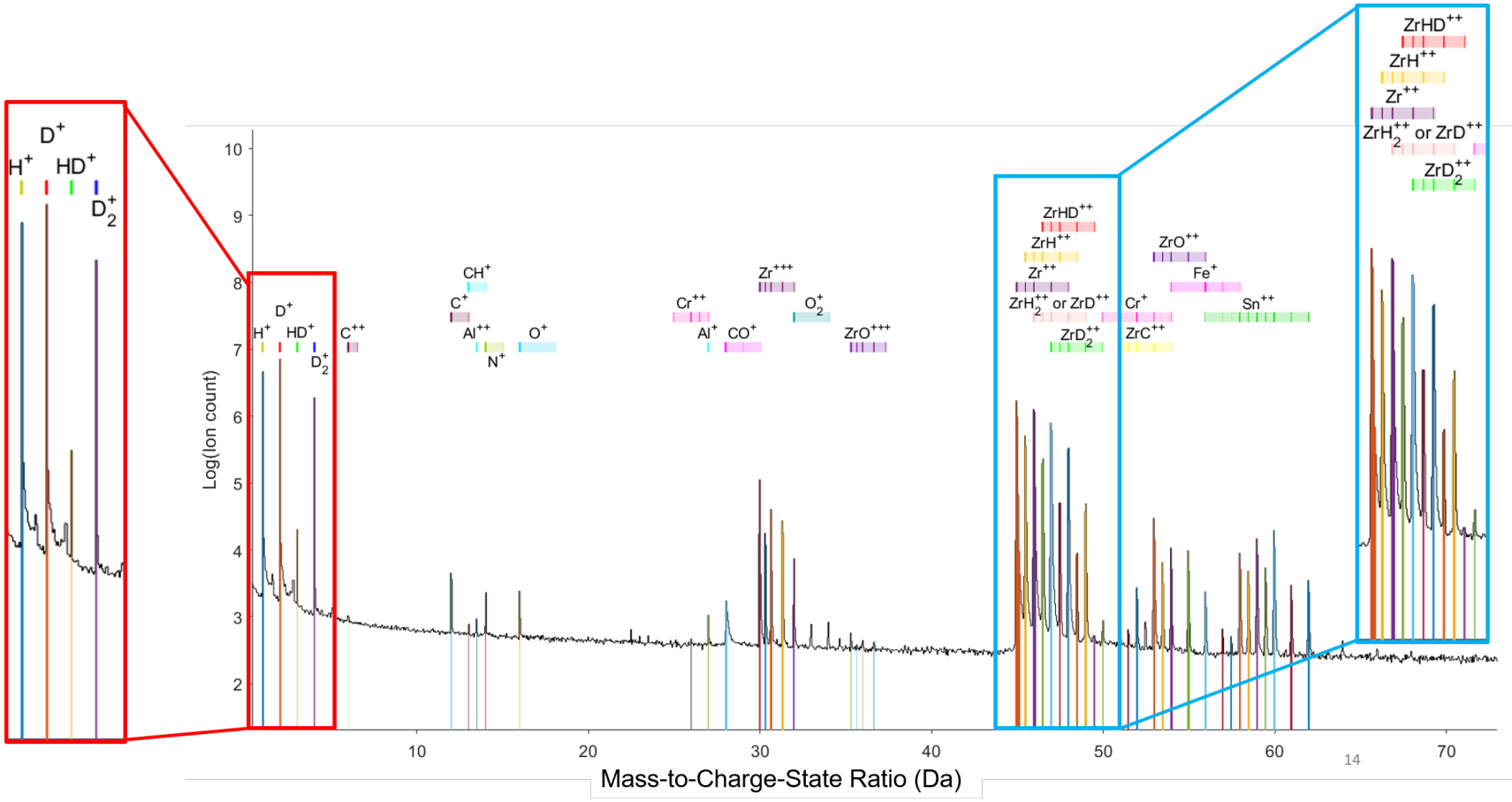


Figure 4.15: Mass spectrum taken from a deuterated Zircaloy-4 sample, the deuterium containing regions of the dataset have been highlighted and enlarged. The experimental data was from [116].

4.3.2 Charging Parameter Optimisation

The parameters of the hydrogen charging experiments are the temperature, pressure, time, post-charge cooling method, surface condition and gas purity. We have discussed the influence of gas purity in the previous section and have shown the presence of the oxide film on the sample prior to charge, which is not an ideal surface condition because Zr oxides are a known barrier to hydrogen pick up [143]. The maximum temperature achievable in the cell with 1 bar of gas was either 300 or 320 °C respectively across different parts of the project. The maximum allowed pressure in the reaction cell is 1 bar. To optimise hydrogen uptake, the pressure and temperature were kept at maximum throughout this work. A summary of the changes made throughout this work are given in Table 4.3. A full list of the experiments conducted can be found in Table 3.8 in the Experimental Methods chapter.

Table 4.3: Changes made to the deuterium charging protocol and corresponding motivation in this work to enhance deuterium uptake

Change in Protocol	Aim
Heating tape around the cell	Increase uniformity of temperature gradient in cell
Cool Sample in D_2 gas	Remove chance that we were pumping out deuterium from the sample as it cooled
Increase time	Increase deuterium uptake
Cool sample with cold D_2 gas	Quench sample in D_2 gas
Use focused ion beam sharpened samples	Increase likelihood of successful APT sample so increasing data collected

Focused ion beam (FIB) sharpened samples were used where possible because they had a higher yield of data in the atom probe and thereby increased chances of a successful experiment. Half of all FIB sharpened electropolished needles were found to be viable to hydrogen charge as opposed to a rate of 1 in 10 electropolished needles.

The cooling method was altered to try and increase deuterium uptake. The samples were cooled in gas to prevent any chance that we were removing the deuterium gas from

the sample, as we removed the gas from the reaction cell. Two methods were trialled, firstly cooling the sample in the gas and allowing the whole system to cool to 50°C before pumping out the gas. In the second, we pumped some of the deuterium gas out and replaced with gas at ambient temperature, in quick succession. This was repeated until the sample stage temperature was reduced to 50°C. 50°C was chosen because at this temperature hydrogen is approximately insoluble in Zr, hence potentially leading to the formation of hydrides [144]. Neither of these methods appeared to have a significant impact on the data collected. This is because the main issue with the lack of deuterium uptake being seen is the length of time of the charge, which is to be discussed within this chapter. Previous work undertaken by Khanchandani et al. has shown that it is possible to completely remove the deuterium from the material in the conditions created as the gas is pumped out of the reaction cell, so in future the samples should be quenched [145].

4.3.2.1 Zircaloy-4

Deuterium charges of Zircaloy-4 were successfully completed for the following lengths of time: 15 minutes, 1.5 hours and 3 hours and atom probe data was collected for all of these. There were some interesting features seen across all of the reconstructed datasets. All of the datasets had an oxide film on them which is to be expected as it was seen in previous work (Figure 4.16) [128]. The oxide film on the sample charged for 1.5 hours has the thickest oxide film due to the fact that the ineffective oxygen trap was used during this charge.

However, it was not expected that the samples would out-gas during the deuterium charge and a decrease in hydrogen concentration by approximately 100 times was observed. In the mass spectrum this was seen as a decrease in the hydrogen containing peaks, namely the zirconium hydride peaks in the 2+ charge state as shown in Figure 4.17.

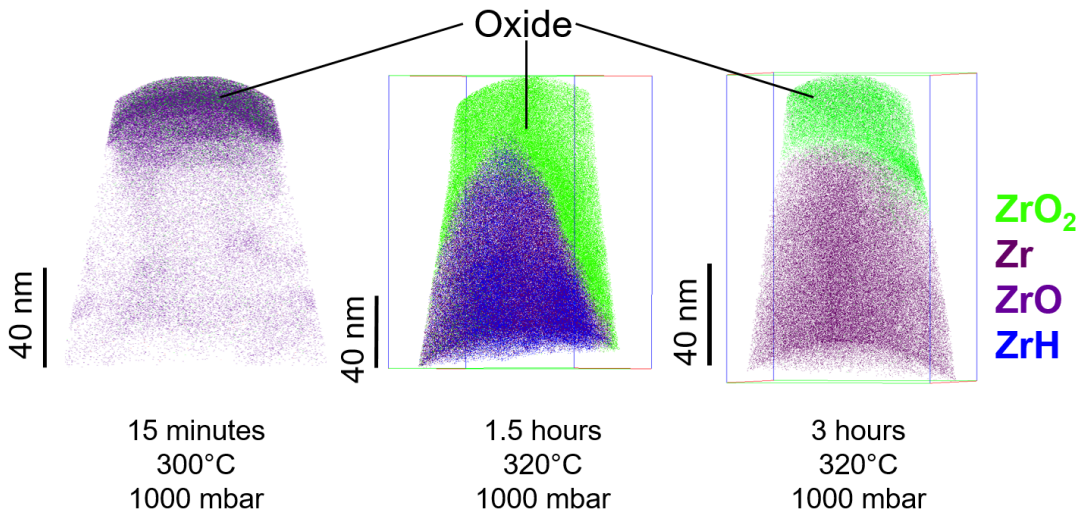
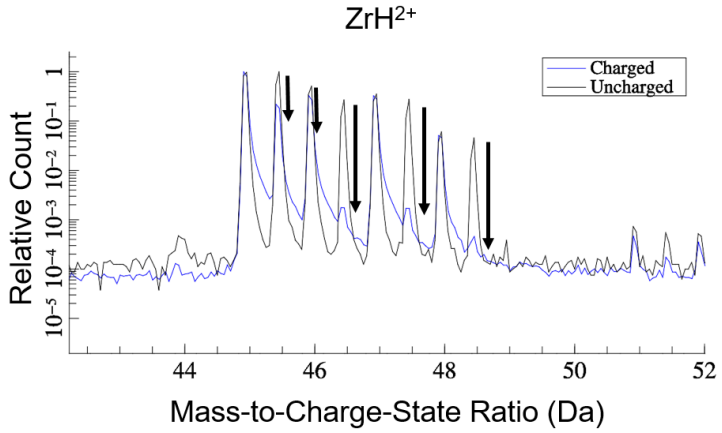


Figure 4.16: APT reconstructions of the Zircaloy-4 that was deuterium charged for 15 minutes, 1.5 hours and 3 hours. All of the samples had an oxide film on them (labelled).

(a) Deuterium charged for 3 hours



(b) Deuterium charged for 15 minutes

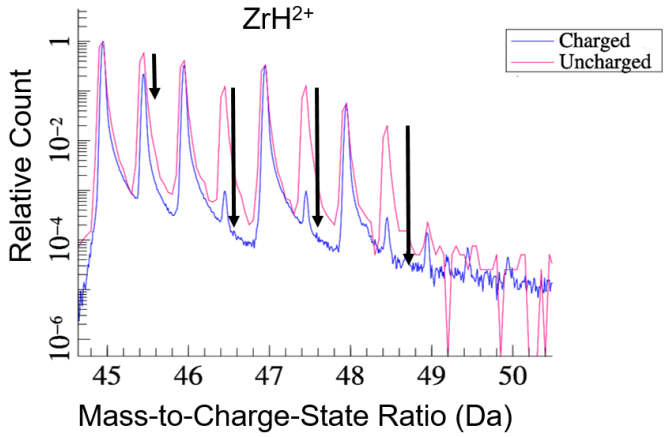


Figure 4.17: Sections of the mass spectrum containing the Zr^{2+} charge state peaks, the data has been normalised to the $^{90}Zr^{2+}$ peak at 45 Da.

None of the datasets contained deuterium in the metal regions of the sample, see Figures 4.18 and 4.19. However, evidence of deuterium was seen in the very beginning of the some of the APT experiments. For example, Figure 4.19 contains a section of the mass spectrum from the first 1 million ions collected from the sample and a peak at 4 Da is present. This indicates that the deuterium charging process is leading to deuterium uptake by the sample, but the deuterium diffusion to the metal is likely being blocked by the oxide.

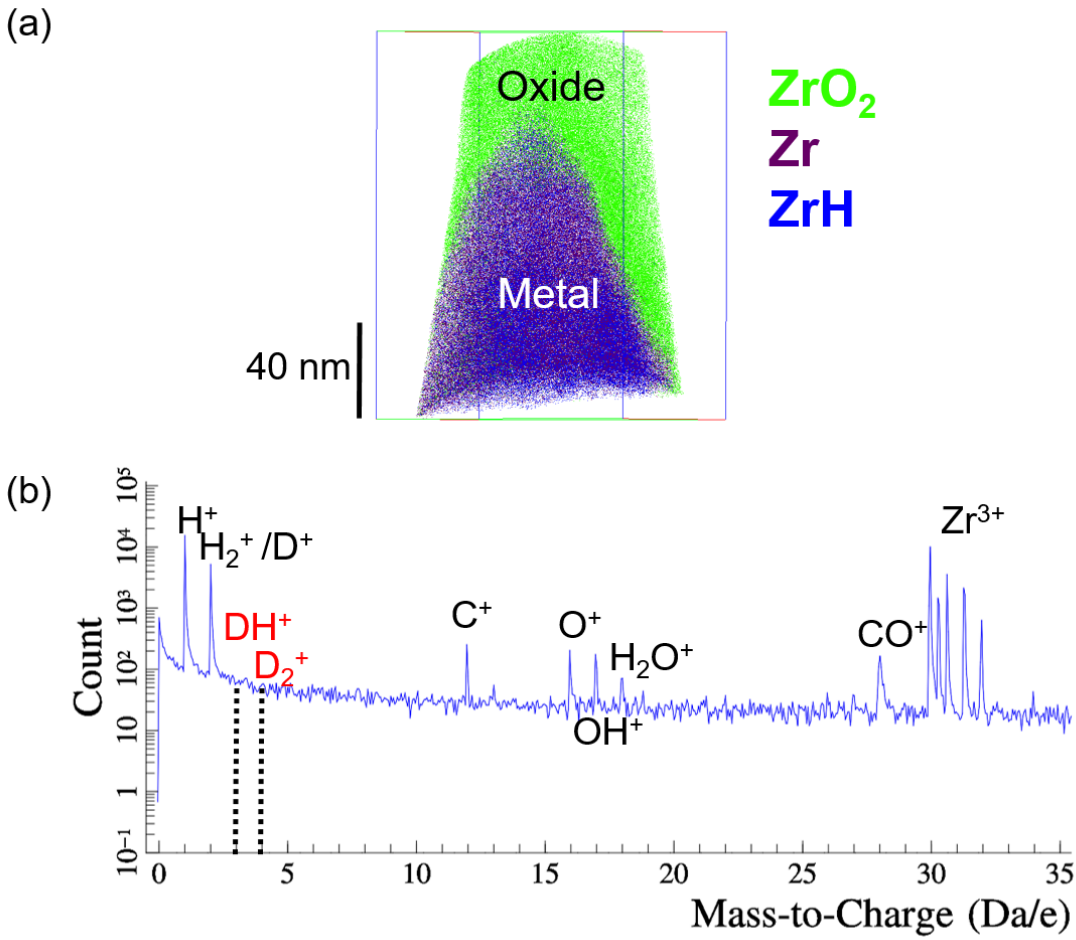


Figure 4.18: (a) APT reconstruction of the Zircaloy-4 sample deuterium charged for 1.5 hours. The metal and oxide regions of the samples are indicated. (b) Mass spectrum of the metal region of the sample, the dashed line indicate where DH^+ and D_2^+ would be present in the mass spectrum if detected.

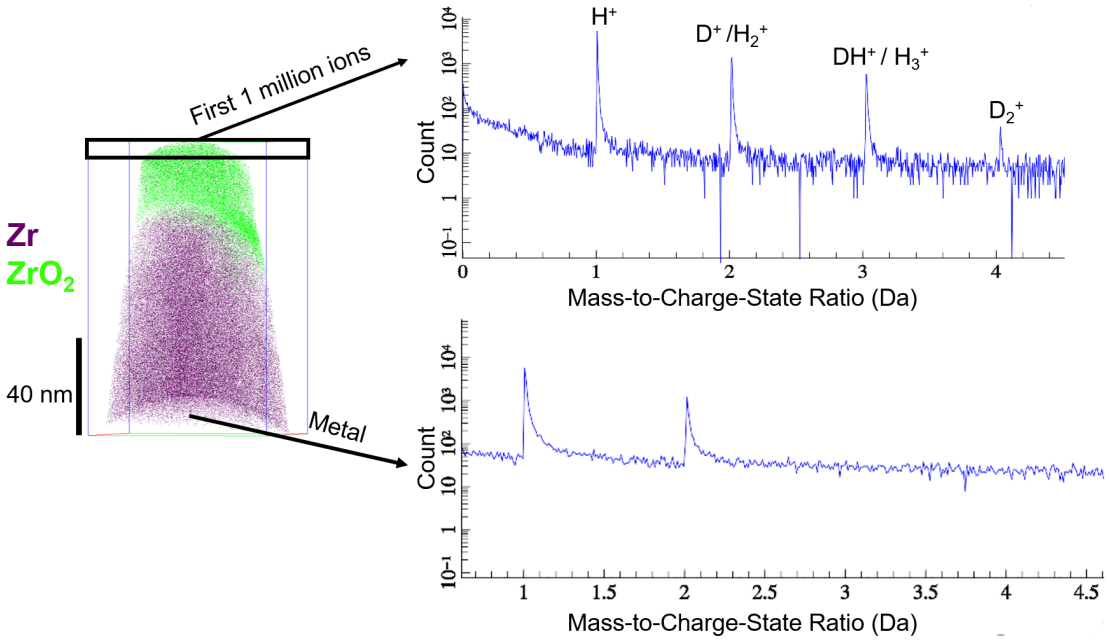


Figure 4.19: Reconstruction of the sample charged for 3 hours alongside sections of the mass spectra for the first 1 million ions collected and the metal of the sample.

Due to the limited deuterium pick up we were observing in the Zircaloy-4 samples; pure Zr wire was examined as higher H pick up was anticipated. Due to practical considerations, maximum charge times were limited to 5 hours.

4.3.2.2 Zr Wire

Previously, Maimaitiyili et al. successfully deuterium charged a pure Zr powder powder bed, we attempted to replicate this work because it is one of the few items in the literature that does not use a bulk sample and uses temperatures and pressure achievable in our equipment. This work used conditions of deuterium gas pressure of 0.5 bar and 300°C and showed that after approximately 1.35 hours Zr underwent a phase transformation into theε-hydride phase [142]. To maximise the chances of a transformation, we increased the time to 1.5 hours (Figure 4.20) and kept the temperature of the cell at 320°C as we anticipate that the true temperature of tip of the needle is lower than stated because the thermocouple is actually on the sample stage, a few cm away.

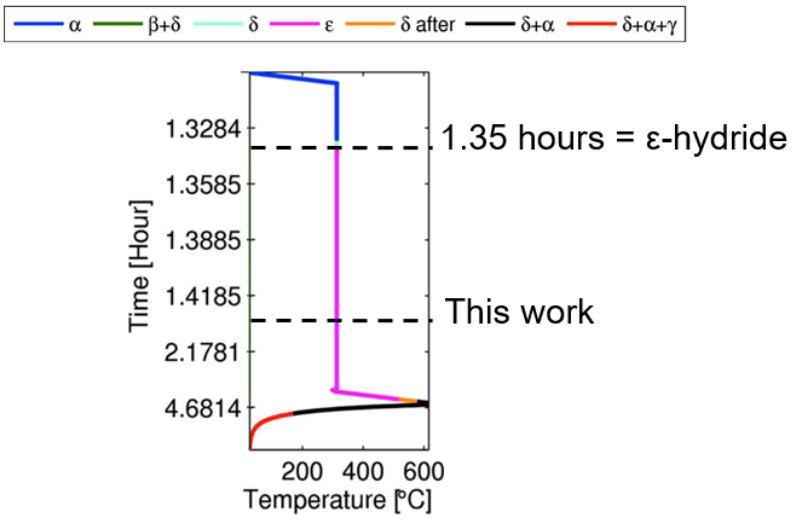


Figure 4.20: Graph showing phase changes occurring in a pure Zr powder bed underwent during heating and cooling under a D_2 atmosphere. Adapted from [142].

Figures 4.21 and 4.22 present the results from this experiment. Unfortunately, the APT sample fractured after 400,000 ions and thus limited data was available. An oxide layer is observed at the top of the reconstruction. Unfortunately, the mass spectrum does not contain any peaks at 3 or 4 Da or any additional peaks in the Zr 2+ peaks between 45 and 50 Da so it does not appear that deuterium has been picked up by the sample.

Looking more closely at the mass spectrum (Figure 4.22), it can be seen that there is a change in the ratios of the Zr ions, which was unexpected, the charged data contains more Zr^{3+} than Zr^{2+}. Figure 4.23 shows the difference between the charge and anticipated data, all of the data is scaled to the height of the $^{90}Zr^{3+}$ peak. This change in Zr^{2+}:Zr^{3+} ratio implies a change in evaporation field at the tip of the needle. This is unlikely to be as a result of the oxide layer that is seen on the sample because if this change were due to the oxide, we would see it in all of the data collected thus far and we have not. Some causes of changes in evaporation field could be due to changes in atomic bonding at the surface of the needle, which implies atomic re-arrangement. This could be attributed to the phase change we trying to cause during the charge, but seeing as there is little evidence of deuterium, this seems unlikely. In order to gain additional data, this experiment was

repeated.

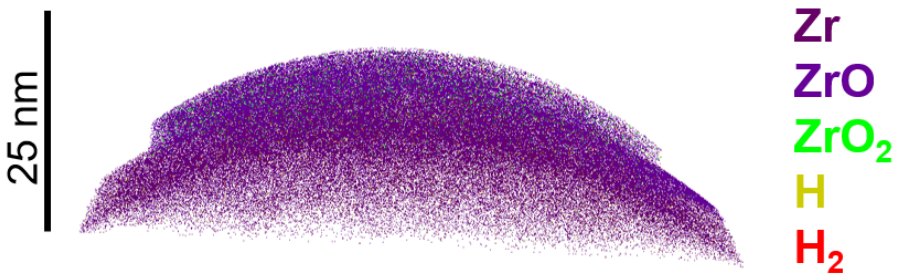


Figure 4.21: Reconstruction of a pure Zr wire deuterium charged for 1.5 hours at 300°C (Experiment 1)

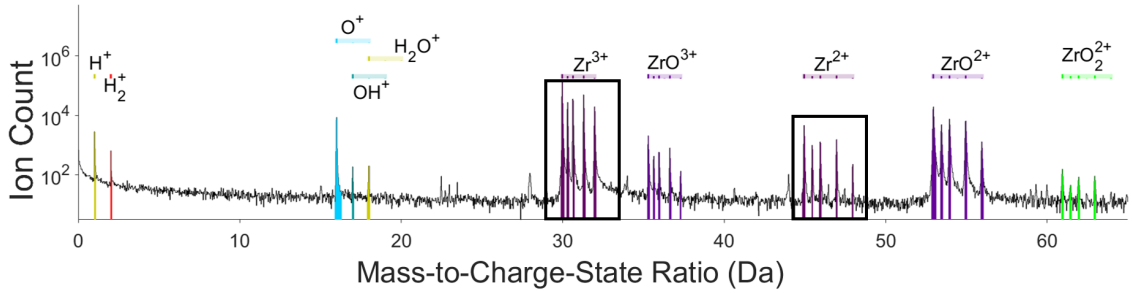


Figure 4.22: Mass spectrum of a pure Zr wire deuterium charged for 1.5 hours at 300°C (Experiment 1)

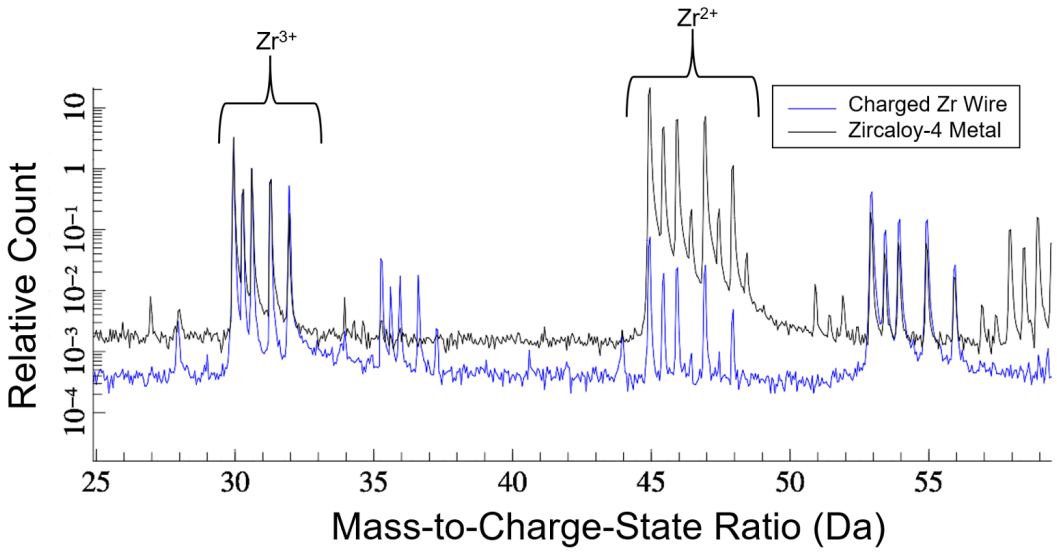


Figure 4.23: Mass spectrum of a pure Zr wire deuterium charged for 1.5 hours at 300°C (Experiment 1)

The data from the second experiment can be found in Figures 4.24 and 4.25. Again, an oxide film is present but what is more interesting is that the same swap in preferential charge state for the Zr ions is seen, implying a real and reproducible effect. In this experiment, there is evidence of deuterium in the mass spectrum, there are peaks at 3 and 4 Da. There are no additional peaks in the 2+ charge state. However, given the fact that most of the deuterium seen in the hydride containing data of Breen et al. was in the 2-4 Da peaks [116], we would expect the first signs of deuterium uptake to be in the hydrogen peaks at the start of the mass spectrum. The evidence of hydrogen pick up shows that the change in charge states could be as a result of an alpha Zr to deuteride phase change but with no data from a non-oxidised area of the sample, this cannot be confirmed. The change in charge states is unlikely to be due to the presence of an oxide layer because if this were the case we would have seen it in the other samples that have been exposed to deuterium gas in the reaction cell and at the beginning of each run and we do not. In the mass spectrum of the oxide layer from this experiment, Zr hydroxide ions were detected; this is likely due to the increased oxidation experienced by the pure Zr wire as opposed to Zircaloy-4. Some of the ions do contain multiple hydrogen atoms, such as $ZrO_2H_2^{2+}$ which

could be ZrO_2D^{2+}. This would be consistent with the Zircaloy-4 data where deuterium was seen in the oxide layer of the sample. At this time, the ranges have not included deuterium because of the insufficient evidence that the ions are deuterium containing as the peaks have been present in the mass spectra of other samples that have been oxidised.

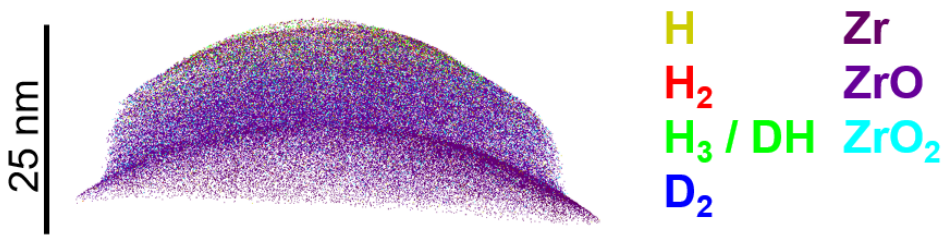


Figure 4.24: Reconstruction of the Zr wire deuterium charged for 1.5 hours at 300°C (Experiment 2)

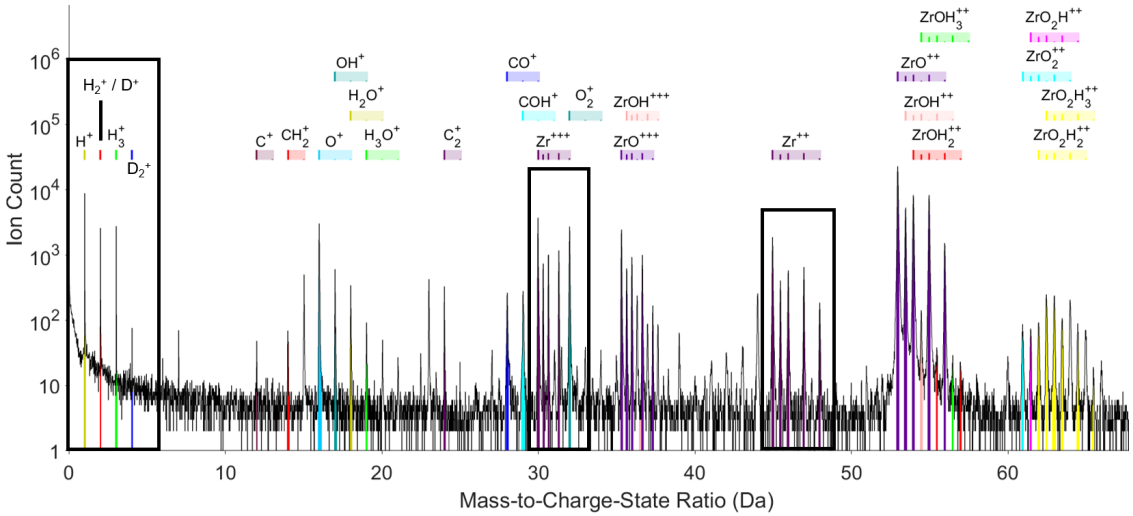


Figure 4.25: Mass spectrum of the Zr wire deuterium charged for 1.5 hours at 300°C (Experiment 2)

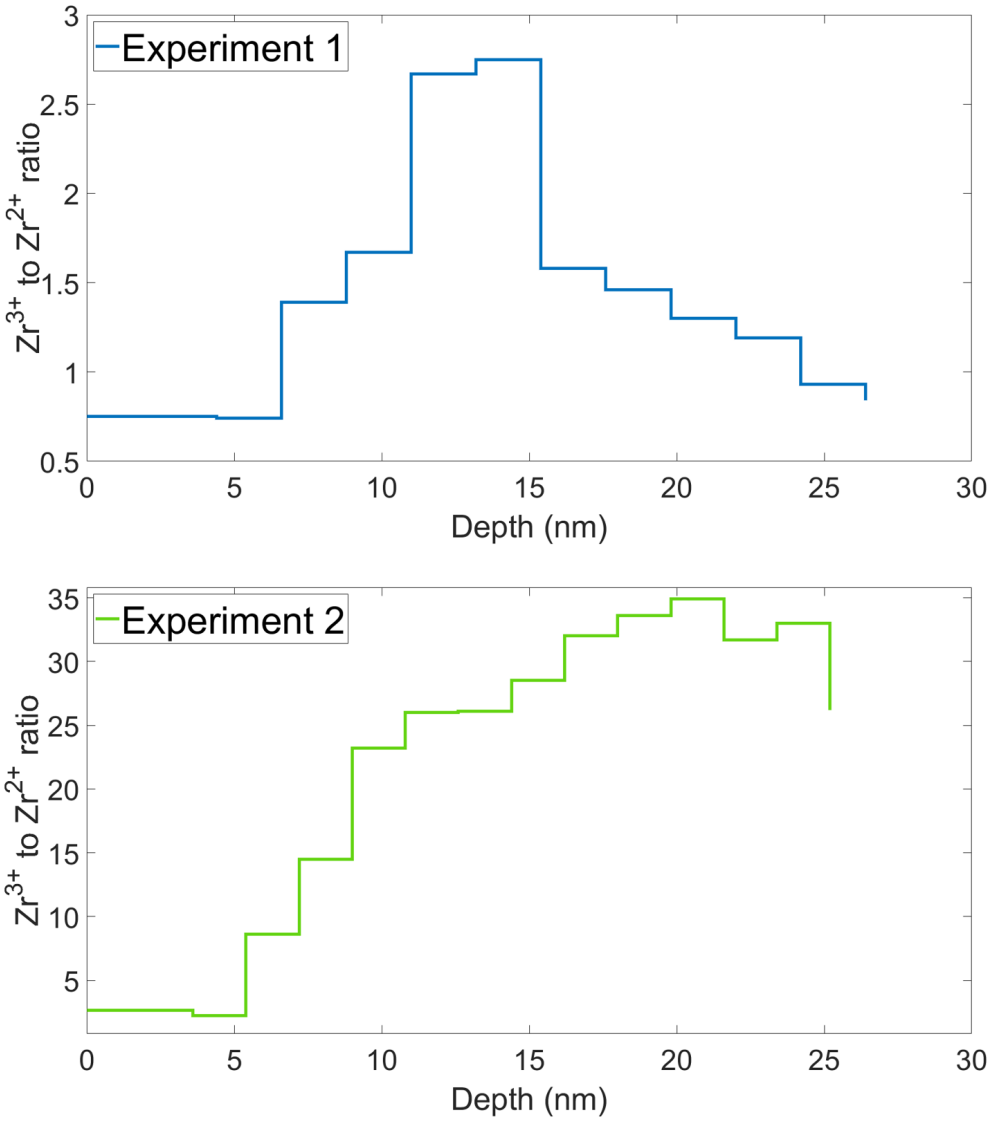


Figure 4.26: Ratio of counts of Zr^{3+} to Zr^{2+} as a function of depth into the sample in the two Zr wire deuterium charging experiments

Figure 4.26 presents the ratio of the number of ions detected as Zr^{3+} and Zr^{2+} as a function of depth. A value greater than one indicates that there were more Zr^{3+} than Zr^{2+}. A fracture can be seen in the reconstructions of both experiments (Figures 4.21 and 4.24) so it was necessary to ensure that the change in charge state ratio that was seen, was not due to the fracture of the specimens. The increase in the ratio of the ion charge states does not correlate to the fracture of either specimen. The ratio is also greater than one for

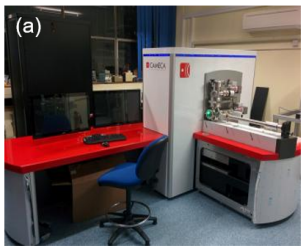
most of the data collected, showing that there was more Zr in the 3+ charge state than the 2+. Both of these indicate that the change in charge state is a real observation.

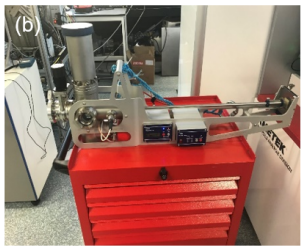
The results from these experiments on Zr wire show that the change in Zr^{3+}/Zr^{2+} is due to the sample having undergone the deuterium charging protocol. However, without additional data from a non-oxidised area of the sample it is unclear if a phase change to a deuteride occurred. This is however a positive result showing that the gas charging is still a compelling avenue for future research.

4.4 Conclusions

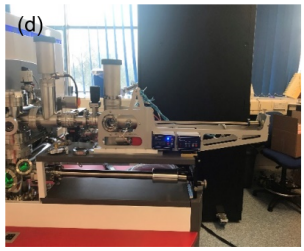
This chapter describes the work completed to develop a method to deuterium charge Zircaloy-4 samples with deuterium gas using our own gas-reaction cell. Figure 4.27 presents a schematic of the optimised protocol from this work. Although we were not successful in causing the formation of deuterides in these samples, some useful lessons were learnt that will help advance the rate of success of subsequent similar experiments. It has been shown that this experimental protocol can produce viable APT specimens. It was also demonstrated that the Zr samples will most likely have an oxide layer on them prior to the charge. The fact that the deuterium must diffuse through such a layer should be taken into account for any future work when looking at the time to charge. A 3 hour charge was sufficient to input deuterium in the oxide film but not sufficient to reach the metal. This indicates that this reaction cell can be used to deuterium charge zirconium alloy samples, provided that appropriate charging parameters can be found. The samples out-gas during the charge, and it would be worth investigating further what happens if we were to out-gas the samples (by heating in the reaction cell) prior to the charge to remove any H from the needle (picked up during sample preparation), thereby maximising the amount of D that could be absorbed. The samples should be quenched to encourage deuteride formation also. The Zr wire samples underwent some change during the charge which led to the change in charge state of Zr. However there is insufficient evidence to determine whether the charging induced the intended hydride phase change. The Zr wire results provide

further evidence of the potential of this method producing deuterated Zr alloy samples for APT analysis.









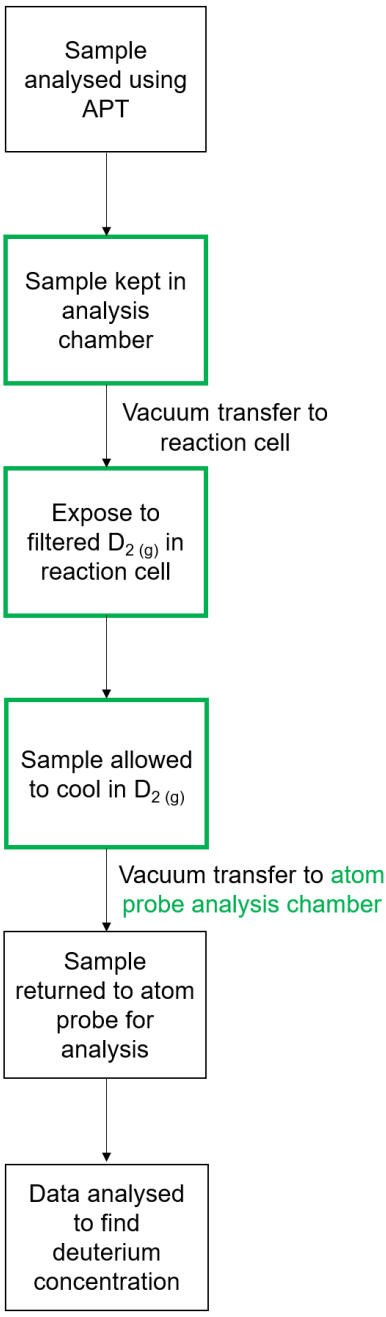


Figure 4.27: Schematic of the optimised deuterium charging protocol. The boxes in green have been implemented or improved upon as part of this work. (a) Cameca LEAP 5000 XR atom probe. (b) Vacuum Cryo Transfer Module used to move samples between the atom probe and reaction cell. (c) Reaction cell used to deuterium charge samples. (d) Vacuum transfer module docked onto an atom probe.

Chapter 5

Cryogenic Focused Ion Beam Sample Preparation

5.1 Introduction

Focused ion beam (FIB) based methods are used in atom probe tomography (APT) to produce site specific lift-outs from samples, enabling the analysis of grain boundaries, and specific phases in a multi-phase sample. However, producing samples via this method is known to cause hydrogen ingress into certain materials such as Ti and Zr [118], [146]. This could prevent deuterium uptake if the sample is already effectively hydrogen charged. The hydrogen levels introduced into these samples by FIB-based preparation are sufficiently high such that precipitation of hydrides is routinely observed.

FIB methods have been used by Breen et al. [116] and Mouton et al. [140] to successfully lift-out APT needles from deuterated zirconium alloy samples. Breen states that there was no effect from the FIB beam on the deuterium present in the data [116], however this author has not found a study supporting this assertion in the literature.

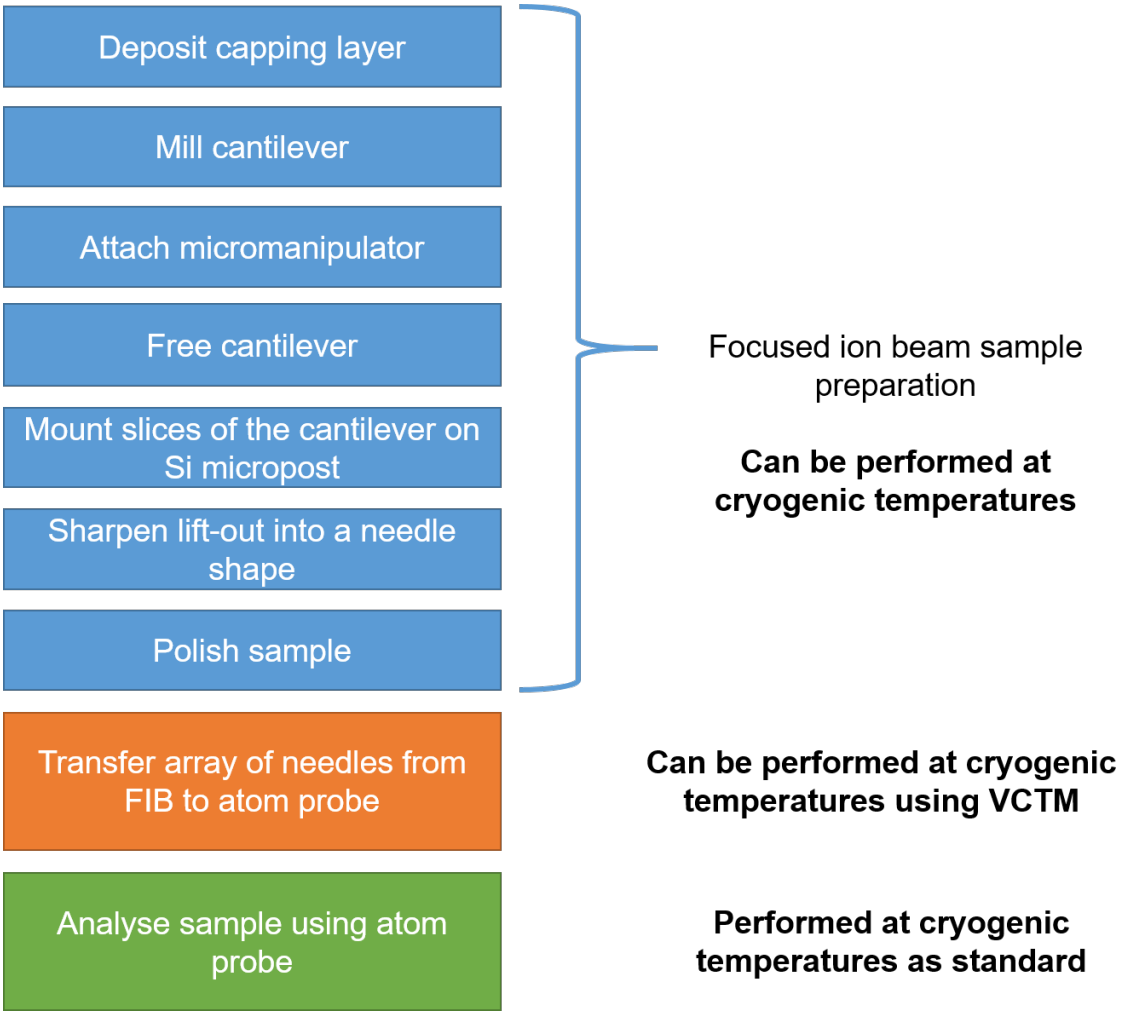


Figure 5.1: Focused ion beam sample preparation work flow

It is possible to prepare APT samples via a full cryo-chain (Figure 5.1), where the sample is kept under cryogenic conditions from sample preparation in the FIB/SEM to the atom probe. Milling at cryogenic temperatures does not pose any issues, but the gas deposition is difficult at cryogenic temperatures and will condense all across the exposed surface of sample. Tungsten and platinum are typically used as the protective capping layer and to attach slices of the cantilever to the micro-posts. Using a vacuum cryo-transfer module (VCTM) (Section 3.4), the samples can be transported under vacuum and cryogenic conditions to the atom probe for analysis. In order for this to occur, the VCTM has to be able to dock to both the atom probe and the FIB instrument. The VCTM is commercially

available but has not been designed to be used with all FIB instruments. Producing APT needles via a full cryogenic chain would be time consuming and experimentally difficult. There has been no evidence yet presented that it is needed at present.

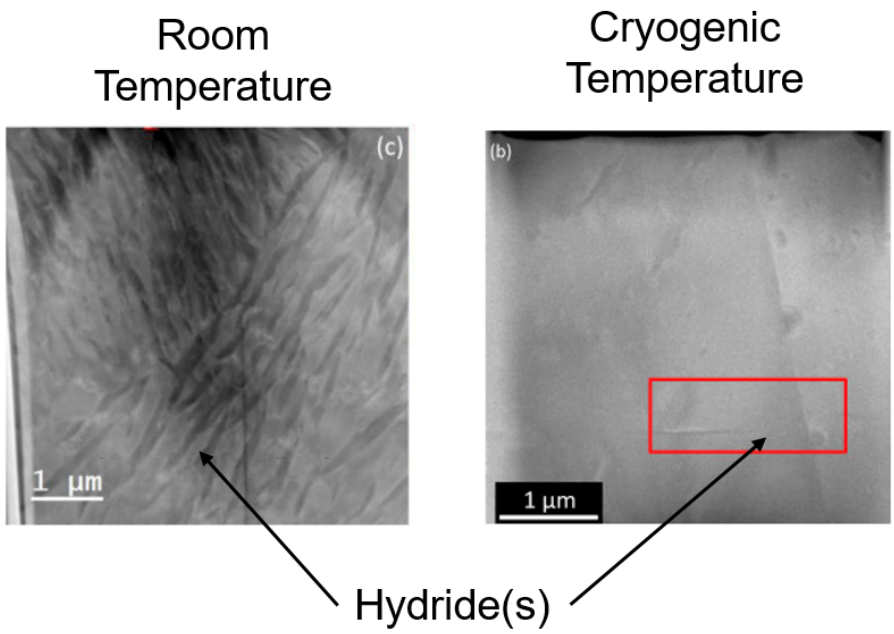


Figure 5.2: TEM images showing that performing the final lamellae thinning at cryogenic temperatures reduces hydride formation in Zr alloy TEM samples. Adapted from citeHanlon2019.

Hanlon et al. have shown that by undertaking the final thinning stages of TEM samples at cryogenic temperatures, it greatly reduces the amount of hydrogen pick up which is implied by the reduced hydride formation (Figure 5.2) [133]. However, this decrease in hydrogen pick up as a result of a cryo-sample preparation route has not been quantified. In relation to APT needles, this work hypothesises that the primary damage is induced during the final shaping and sharpening stages and that performing these stages at cryogenic temperatures could further reduce hydrogen pick up. If it can be demonstrated that to limit hydrogen pick-up, cryogenic temperatures are only necessary at the final tip sharpening stage of the the FIB lift-out process, then it could mean that we could avoid having to do the entire sample preparation and transfer under cryogenic conditions.

If we are to more accurately study the behaviour of H in Zr alloys then it is imperative to know whether the use of cryogenic FIB techniques for APT needle sharpening reduces hydrogen pick up in Zr alloy APT samples and if so, to what extent. It is also essential to understand how the FIB beam interacts with deuterium present in the sample and how it influences the results. It may be that the current approaches can be greatly simplified, making the method more accessible for both research and industrial use.

5.2 Results and Discussion

5.2.1 Effect of cryogenic FIB methods on hydrogen pick up in Zircaloy-4 APT samples

To investigate the effect of cryogenic focused ion beam methods (cryo-FIB) on the hydrogen content in APT data from the analysis of Zircaloy-4, the hydrogen concentration of as-received Zircaloy-4 samples prepared at cryogenic temperatures and ambient temperatures, respectively, was calculated (Figure 5.3). The mean hydrogen concentration was observed to decrease by approximately 2.5 times from 4.33 to 1.76 at.% (excluding the outliers). The outliers are likely due to the samples having a hydride in them as a result of the sample preparation, and as a result have a vastly higher hydrogen concentration than the other samples. The cryogenic FIB method introduced less hydrogen into the samples; therefore it is less likely that the hydrogen concentration exceeds the solubility limit and precipitate out as a hydride. This explains the results of Hanlon et al., where the hydride formation is reduced but not eliminated entirely [133]; hydrides are present in the TEM data prepared at cryogenic temperatures in Figure 5.2 but we can see there are much fewer than in the sample prepared at room temperature.

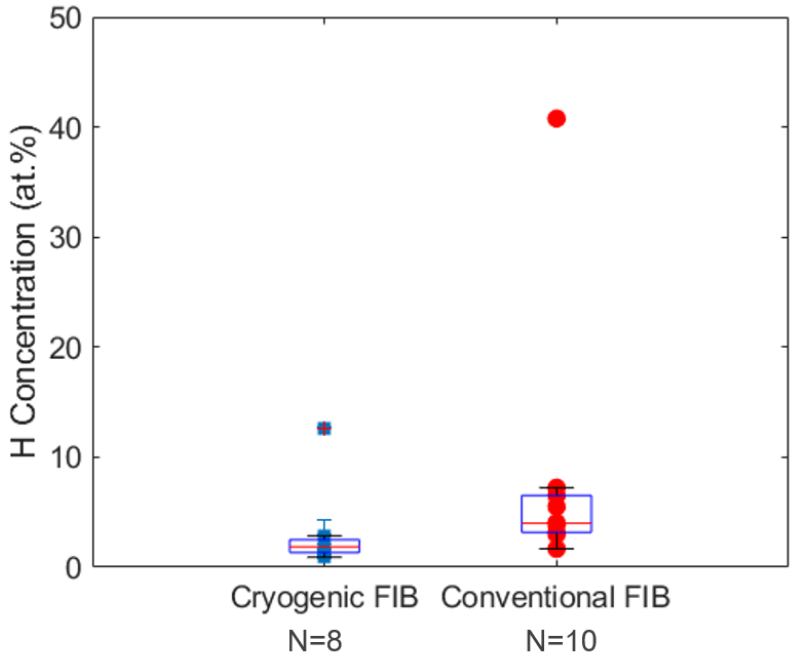


Figure 5.3: Measured H concentration decreases when Zircaloy-4 APT samples are sharpened and polished at cryogenic (Cryogenic FIB) as compared to ambient temperatures (Conventional FIB). A reduction in detected hydrogen concentration is observed under cryogenic conditions.

The observed scatter for the hydrogen concentration measurement is also reduced as a result of sharpening the samples at cryogenic temperatures (Figure 5.3). This is beneficial for deuterium analysis because if the amount of hydrogen in the data is more reproducible it could aid in improving the accuracy of the quantification of deuterium in the sample.

The hydrogen concentration is not reduced to zero for any of the samples prepared at low temperatures, the measured minimum is 0.91 at.%. The hydrogen detected in this material is likely to have resulted from a combination of the steps of the FIB protocol that were undertaken at ambient temperatures, from the material itself and the analysis chamber of the atom probe [147].

These results demonstrate that the use of cryoFIB to sharpen APT needles does reduce the amount of hydrogen picked up. However, it is highly unlikely to have eliminated

it entirely.

5.2.2 Use of cryogenic FIB techniques to prepare APT samples from deuterated Zircaloy-4

The second part of this work looks at the effect of the FIB process on the deuterium already present in the samples. It is important to establish whether we can still detect deuterium in the deuterium charged Zr samples sharpened at cryogenic temperatures as it remains unclear whether the remaining hydrogen that we observe with cryogenically prepared samples is intrinsic to the sample, independently of the preparation method, or whether the preparation method itself has introduced foreign hydrogen. To determine this, deuterated samples are investigated, in conjunction with cryogenic preparation.

From the set of 5 deuterated samples investigated, all of the samples successfully yielded APT data (metal region of the needle was analysed) which is comparable to as-received samples prepared by FIB methods at ambient temperatures. Only one of the datasets showed evidence of deuterium (Figures 5.4 (a) and 5.5). Peaks at 3 and 4 Da caused by DH^+ and $D_2{}^+$, and additional deuterium-related peaks in the Zr^{2+} charge state were found in some of the data, Figure 5.4 (b). The deuterium in the data shows that we can still detect deuterium in the samples after exposure to a FIB beam at ambient temperatures.

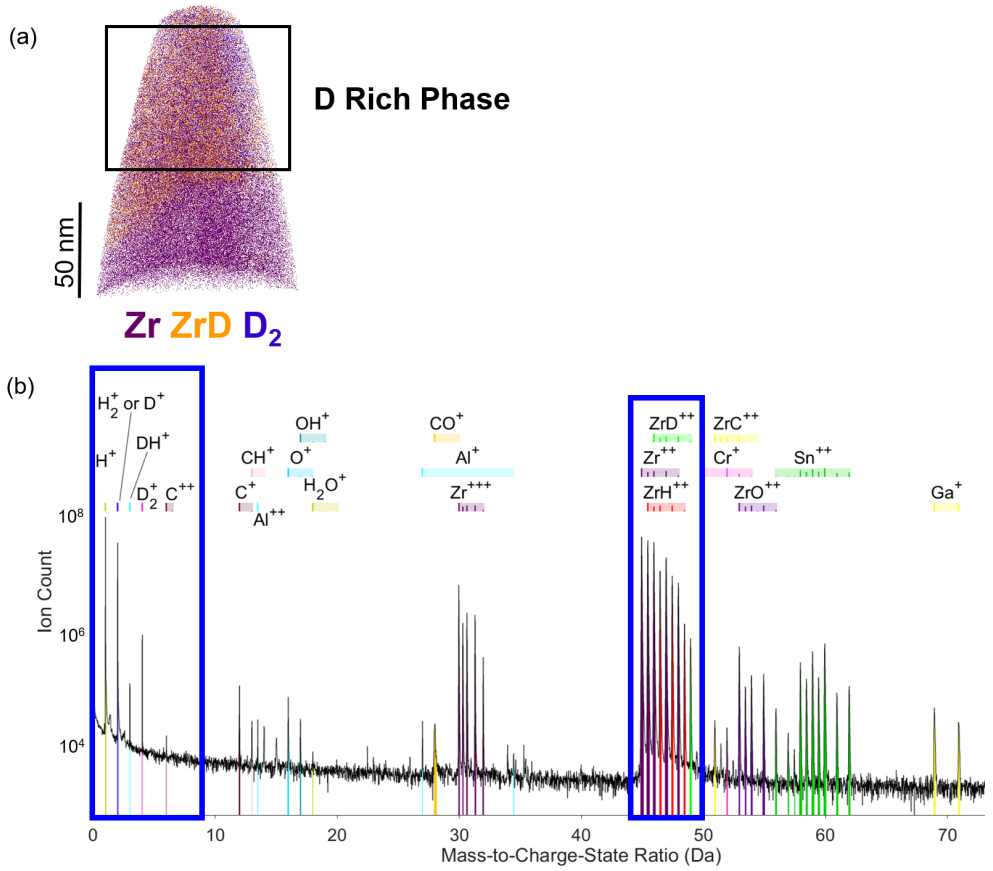


Figure 5.4: (a) APT reconstruction of a deuterated Zircaloy-4 sample. (b) Mass spectrum taken from the deuterium rich region highlighted in (a). The boxes indicate peaks where deuterium is seen. The ionic species are labelled above the peaks and the bold coloured bars beneath show the relative isotopic ratio of the ions.

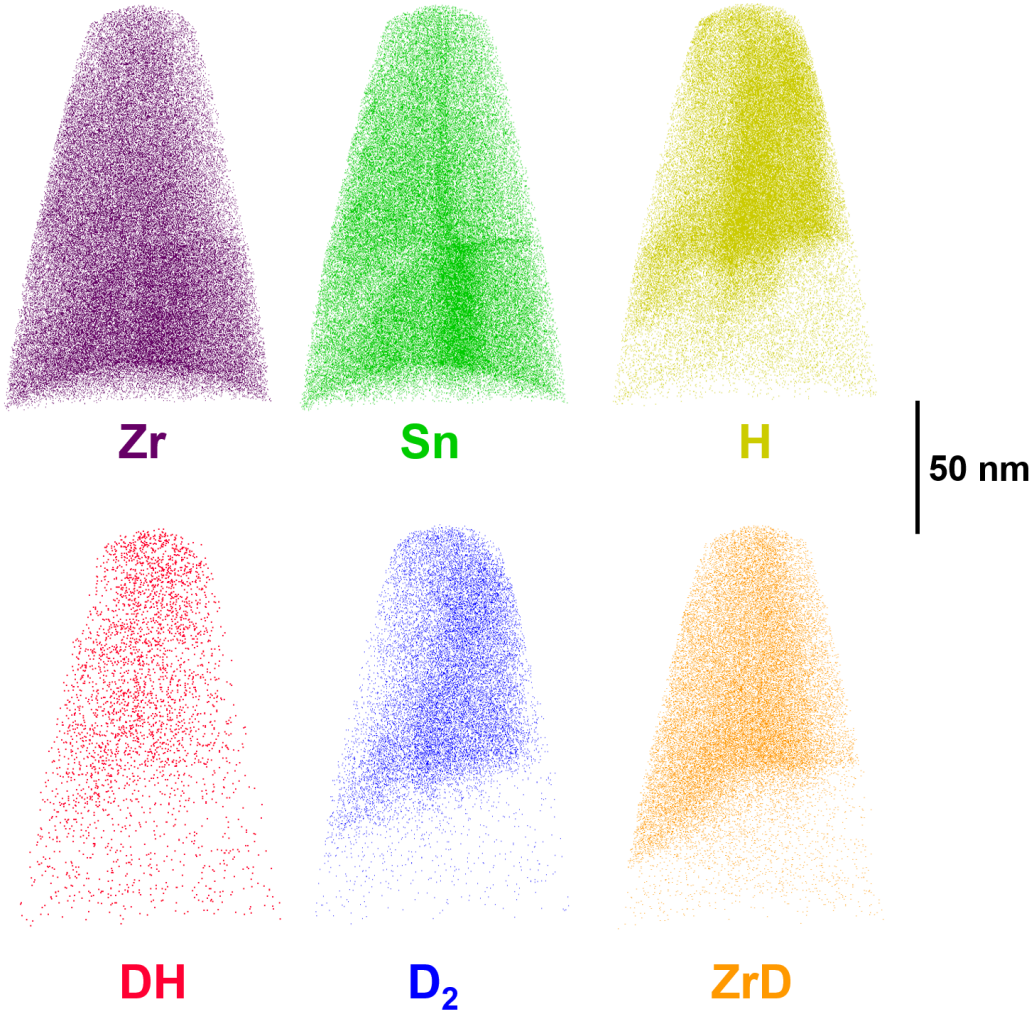


Figure 5.5: Deuterated Zircaloy-4 sample prepared at cryogenic temperatures. Reconstructions are of the same data as in Figure 5.4

In the APT reconstruction of this specimen presented in Figure 5.5, Sn shows evidence of segregation to crystallographic poles, in line with previous studies [114], [128]. This is visible in the reconstruction as the vertical dense line of Sn ions, the line appears to bend as it crosses from the deuterium rich region into the Zr metal.

The ability to produce a deuterium containing sample is significant, however, we also need accurately obtain the chemical information so as to better understand hydrogen pick up at the atomic scale. The deuterium concentration was calculated using the method

developed and described in Section 6.3, where all non-deuterium containing peak overlaps are solved as per Chapter 3 and the deuterium containing peaks are solved separately. All counts that could be ZrH_2 or ZrD are assumed to be ZrD and the overlap at 2 Da between H_2^+ and D^+ using the ratio of H_2^+ to H^+ in an uncharged sample to calculate the counts of H_2^+ in the peak. The deuterium concentration in the deuterium rich region of this sample was calculated to be between 10 and 13 at.%. This value is not consistent with the D concentration for any known hydride phase. The measured hydrogen concentration is between 28 and 32 at.%; even if the deuterium and hydrogen concentrations are combined the total could range from 41-42 at.%. The stable hydride phases of $ZrH_{1.6}$ and ZrH_2 (δ- and ε-hydride phases) contain 62 and 67 at.% H and the meta-stable γ-phase 50 at.%. indicating that this is more likely to be a super saturated solid solution than a hydride phase. The hydrogen concentration is unusually high for this material as it is on average 4.3 at.% for Zircaloy-4 samples prepared at ambient temperatures. This could indicate a that deuterium is being exchanged for hydrogen in this material.

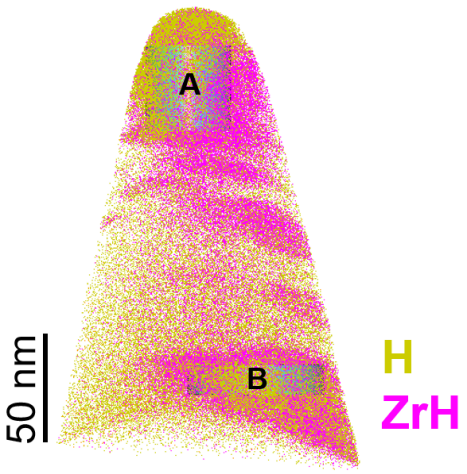


Figure 5.6: Deuterated Zircaloy-4 sample prepared at cryogenic temperatures. A and B are regions of interest used to calculate the local hydrogen concentration.

It is notable that the APT reconstructions of the deuterated samples prepared by cryo-FIB did contain varying amounts of hydrogen. Some of the samples contained no

deuterium and low levels of hydrogen and some samples contained no deuterium and high levels of hydrogen. This variation was observed across specimens generated from both of the lift-out cantilevers made so it is not likely to be due to problems with the samples. Figure 5.6 is an example of the possible variation in measured hydrogen content, the volume contained in the two regions of interest (A and B) were 38.99 and 30.62 at.% hydrogen. Possible explanations for this increase in hydrogen concentration could be due to the crystal orientation of the lift-out with respect to beam exposure during sample preparation or there exists an actual inhomogenous H/D distribution. The latter is most likely to be the case as the sample was deuterated and annealed to re-distribute the deuterium and form a uniform distribution of the deuterides. It is thus assumed that the deuterium distribution is therefore inhomogenous within the microstructure. Figure 5.7 (b) shows how, due to the relatively small sampling volume in each cantilever it would be possible to produce APT needles from the deuterated bulk samples that contain differing amounts of deuterium. The samples produced from lift-out 'X' would contain little deuterium because the cantilever does not incorporate a deuteride, whereas some of the samples in 'Y' would contain some of the deuteride and have a higher deuterium concentration. The samples that do not contain the deuteride, should contain a deuterium concentration of the terminal solid solubility at the temperature when the charging was conducted. Further more when producing the samples we assumed that the deuterium distribution would be homogeneous throughout the matrix of Zircaloy-4 metal, which is possibly not the case, indicated by the data. This assumption was made because it can be difficult to image individual hydrides using a SEM due to lack of imaging contrast caused by the similar masses of Zr and its associated hydride phases.

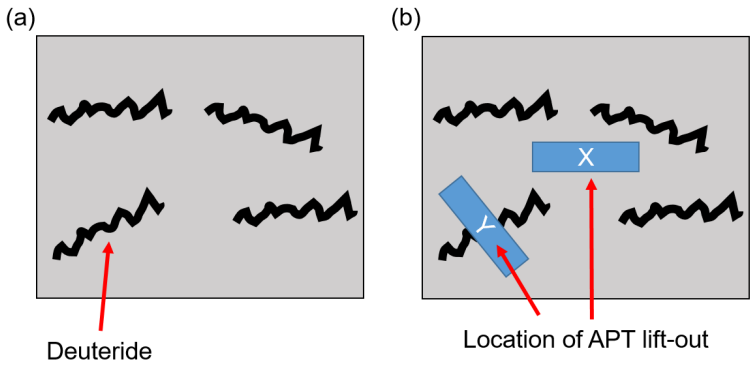


Figure 5.7: (a) Sketch of deuterides in a Zr sample. (b) Potential location of two APT lift-outs and sets of samples.

5.3 Conclusions

This study demonstrates that the use of cryogenic FIB to sharpen atom probe samples does reduce the amount of hydrogen picked up during sample preparation, explaining the results of Hanlon et al. [133]. It has been shown that deuterium can be detected in Zr alloy samples prepared in this manner, demonstrating the viability of using cryogenic FIB methods to produce APT needles from deuterated specimens. However, it is important to note that the inhomogeneity in the hydrogen (and deuterium) concentrations across the samples means that multiple samples must be prepared to guarantee that a deuterium containing sample is analysed. The approach used here presents a simpler approach than prior full-cryogenic chains, making it simpler to examine D contents within Zr alloys. However, it remains to be seen whether the residual hydrogen content can be further suppressed without resorting to a full-cryogenic chain solution.

Further work where more of the steps in the FIB sample preparation are conducted at cryogenic temperatures, could potentially reduce this further. For instance, it would not be significantly more difficult to produce the cantilever at cryogenic temperatures, perform the lift-out at ambient temperatures and sharpen the samples at cryogenic temperatures as we have done in this work.

Chapter 6

Improving the Data Analysis of Deuterated Zr Alloy APT Data

6.1 Introduction

Previous works have highlighted problems with quantifying deuterium concentrations using APT, as a result of the complex peak overlaps that are present in the mass spectrum between ions containing molecular hydrogen and atomic deuterium (H_2 and D) [126], [131]. In this chapter, quantification of deuterium is optimised in historic and simulated atom probe data by applying new data analysis methods using pre-existing tools. The optimised method developed in this study was used to re-analyse a previously published Zircaloy-4 dataset in which the deuterium concentration was quantified in a concentration line profile across an α-Zr/ deuteride interface. A technique to find the likely chemical identity of individual ions contained in a peak overlap has also been investigated to improve understanding of the spatial distribution of deuterium. Improving the quantification and understanding of the distribution of deuterium in APT data will enable us to investigate hydrogen trapping and embrittlement at the atomic scale.

6.1.1 Key Terms

The goals of this chapter are to ensure that the data processing done by different softwares provide consistent composition measurements for APT data and are not dependent on the software in use; to reduce bias and variability in APT compositions and to develop a standardised protocol for analysing these datasets. Throughout this work, it will be necessary to distinguish between different mass-interference phenomena, hence a set of terms for commonly encountered spectral features are needed. To the author's knowledge, the APT community does not have standard terms for describing the processes involved in calculating the composition from a mass spectrum where peak overlaps occur or the different types of peak overlaps that arise in APT mass spectra. As such, the following terms will be used in this chapter (and thesis) and their definitions are below.

Direct Peak Overlap Peaks in the mass spectrum with mass-to-charge-state ratios so similar that the peaks cannot individually be resolved (see Figure 3.4) [125].

Peak Tail Overlap Peak that overlaps with the tail of the preceding peak (see Figure 3.4) [125].

Peak Overlap Solving estimating the number of counts each type of ion contributes to an overlapped peak [125].

Deconvolution Method to enhance the signal from recorded data by removing the effect of blurring. In terms of peak overlap solving, this would refer to separating the signals of two peaks involved in a peak tail overlap.

D will be used as a chemical symbol for deuterium. Hydrogen (H) is assumed to be mono-isotopic and hydrogen refers to ^{1}H only.

6.1.2 Motivation

A number of steps are required to calculate a composition measurement from atom probe data, as outlined in Figure 6.1. Inaccurate compositions can arise from a

number of places in the data analysis workflow. Firstly, correct labelling of mass spectrum peaks is necessary to ensure that the correct overlap problem is being solved. Accurate quantification of the counts contributing to each peak is essential, as this is the input to the peak overlap solver. Ranging is the process of giving a peak its ionic identity and assigning the peak a width. The analysis software, RangeCheck [148] was used to check each range file for errors in width and ion identity. A detailed investigation into the effect of range widths on the composition was outside the scope of this work. In addition, the solving of peak overlaps must be performed accurately. The workflow for calculating a composition shown in Figure 6.1. The two processes under investigation in this study are indicated by the blue arrows.

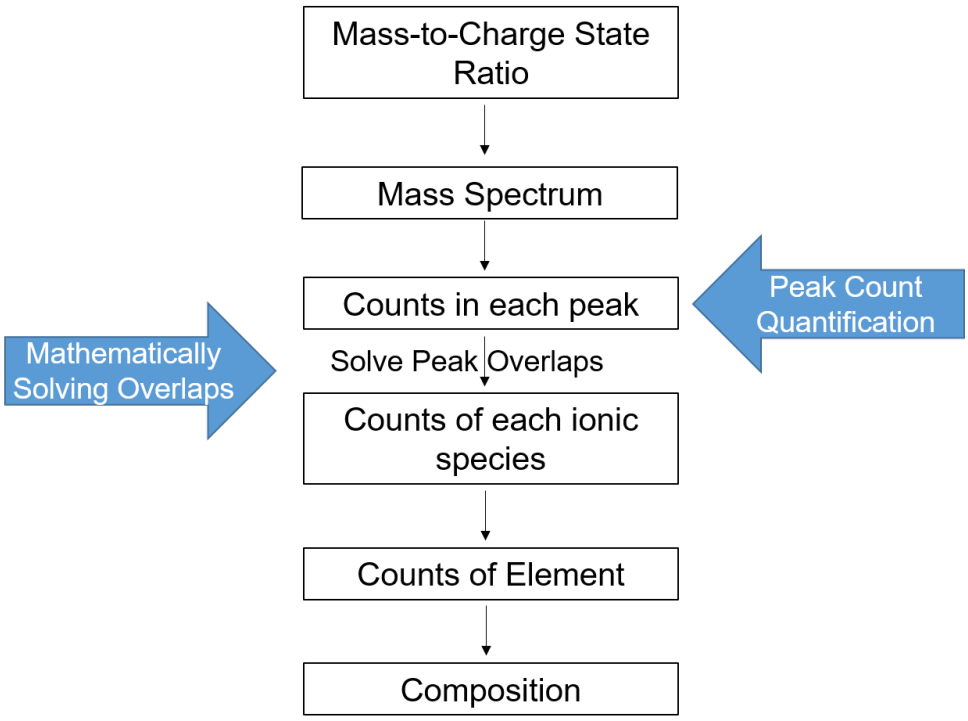


Figure 6.1: Schematic showing the steps taken to calculate a composition in APT data. Errors can arise from ranging (ionic species and range width), quantifying the number of counts in each peak and solving the overlaps.

The subtraction of background noise from the mass spectrum is not investigated in this study directly but is important when quantifying the counts in a specific peak. Prior to peak overlap solving, the background is subtracted from the ranged counts. There are

many contributors to the background signal, including from residual gas in the chamber or contaminants on the specimen surface, and from the atom probe itself [117]. However, some components to the background are correlated to the mass peaks. Noise from the atom probe and the residual gases tend to be constant in time-of-flight (TOF) space, meaning that in mass-to-charge space (in which the mass spectrum is plotted) it decreases across the mass spectrum. The hydrogen and deuterium peaks have low mass-to-charge-state ratios, so be subject to large amounts of background noise. The background due to random events can be removed by a global background subtraction, where the background is estimated and subtracted from the counts in the range. AtomProbeLab removes the global background by using a fixed mass window at the beginning of the mass spectrum and the local background by fitting an exponential function in TOF space.

Optimisation of composition calculations results in the accurate chemical information on the nano-scale. To improve our understanding of hydrogen embrittlement, it is necessary to obtain accurate chemical information on the nano-scale and to this end, the composition calculations were optimised. Confirming that we were addressing the correct overlap problem (i.e. potentially overlapping ions correctly identified) was done using the tools described in Table 3.3. To check that our peak overlap solving tool of choice, AtomProbeLab, was producing accurate results we compared its output to that of IVAS in Section 6.2. This section analyses the quantification of counts in the peaks and the mathematical peak overlap solving. The most accurate method of solving the peak overlaps is found. Deuterated samples contain complex peak overlaps and a method of solving a peak overlap between -D and -H_2 is discussed in Section 6.3, as this peak overlap cannot be solved using information from this mass spectrum alone. The optimised peak overlap solving method is applied to data from the literature. Finally, a method to solve peak overlaps on the local scale to more accurate analyse the spatial distributions of ions contained in peak overlaps is investigated.

6.2 Nb Composition Verification

Niobium containing zirconium alloys are used in structural components of nuclear fission reactors; these alloys include ZIRLO and Zr-2.5 Nb. APT analysis of these samples is becoming more routine so it is necessary to know that we can accurately calculate the compositions of APT data from samples of these alloys [107], [149]–[153]

6.2.1 Nb composition verification between software packages

This section re-utilises data originally collected by Hudson [100]. Hudson collected this data for a study on ZIRLO to investigate the effects of the energy of the applied laser pulsing in an APT experiment on composition measurement. The experimental data has been re-analysed in this work using both IVAS and AtomProbeLab (these are explained in Section 3.2.2) in order to investigate any potential differences in the composition determined between the softwares. The experiments were conducted on a LEAP 3000X HR and used analysis conditions of 60K and a 200 kHz laser pulse frequency. Hudson varied the laser energy between 0.2 nJ and 0.6 nJ at 0.05 nJ intervals and 1 million ions were collected at each laser energy [100].

Re-analysis of Hudson's data using AtomProbeLab gave similar results to those originally published IVAS-calculated compositions for all elements except Nb. In his PhD thesis, Hudson observed no clear trend but when the data was analysed using AtomProbeLab, the Nb concentration was found to increase with laser energy, as seen in Figure 6.2 [100]. This is surprising because if operating correctly, it would be expected that both of the softwares would generate the same answer. This motivated further investigation to find the underlying causes for the observed differences because this indicates that one or both softwares are not calculating the composition accurately.

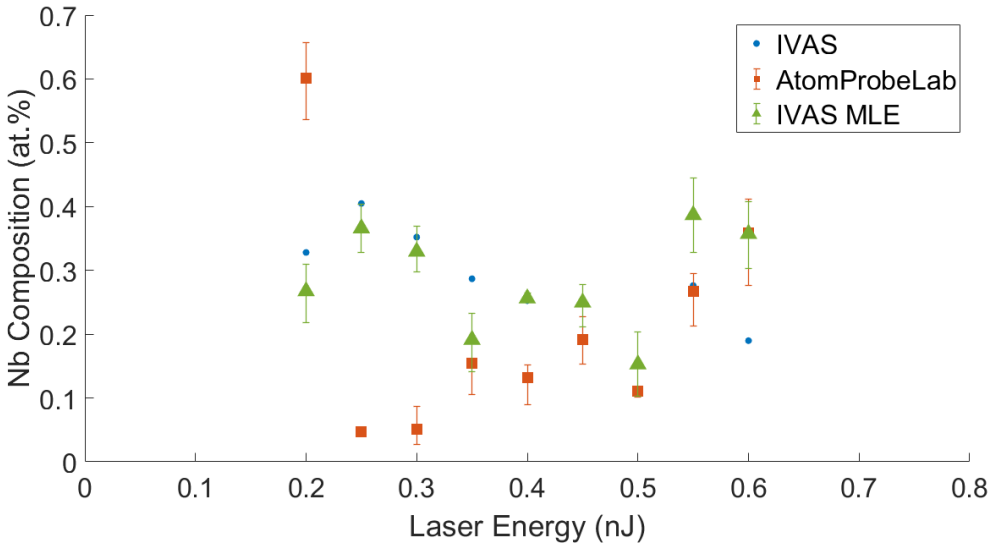


Figure 6.2: Comparison of measured Nb in ZIRLO as a function of laser energy, as calculated by IVAS, AtomProbeLab and IVAS combined with the maximum likelihood estimation (MLE)

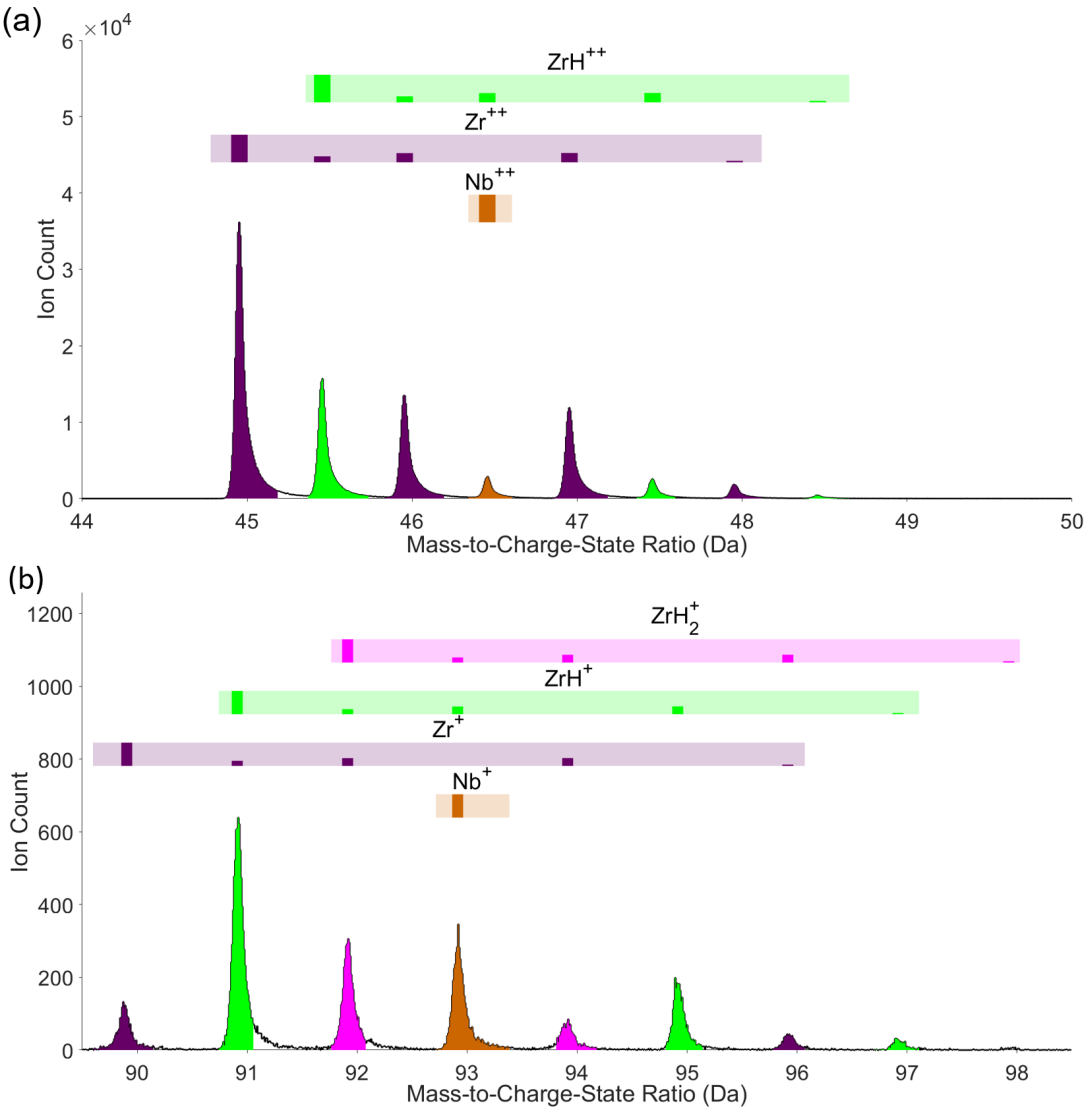


Figure 6.3: Sections of the mass spectrum of ZIRLO where Nb overlaps with ZrH ions, (a) 2+ charge state and (b) 1+ charge state. The bold bars show where each peak for an ionic species occurs and their height corresponds to their relative isotopic abundance.

Upon examining the mass spectrum for this sample, it was found that Nb is present in the 1+, 2+ and 3+ charge states. In the 2+ and 1+ charge states, there are peak overlaps with ZrH ions, shown in Figure 6.3. With Nb being the main alloying element in ZIRLO, it is important to be able to find the correct solution for these overlap groups so that accurate Nb compositions can be reported. Hudson used IVAS in his analysis [100] so there could

be some discrepancy between the methods employed by AtomProbeLab and IVAS. To pinpoint where the issue is coming from, the same input masses and ranges were used to calculate the AtomProbeLab and IVAS data points in Figure 6.2. This eliminates any error introduced by the difference in ranging between this study and Hudson's, meaning that any differences must be caused by the processing done by each software.

Figure 6.2 presents the Nb compositions as a function of laser energy in the APT experiment. It can be seen that IVAS and AtomProbeLab do not calculate the same concentrations at all of the laser energies, leading to a different trend in the data. The IVAS results give no trend in laser energy, agreeing with Hudson's observation whereas the AtomProbeLab compositions give an increasing trend in Nb composition with laser energy.

To look further into these differences, the IVAS-MLE data points were calculated using the peak count information from IVAS and the peak overlaps were solved using the MLE approach (see Section 3.2.2 for more information on MLE). The IVAS peak count quantification was solved using MLE to remove any effect from the different software's input into the mass solver on the overall composition. Figure 6.4 contains a flow chart showing the relationship between the different datasets.

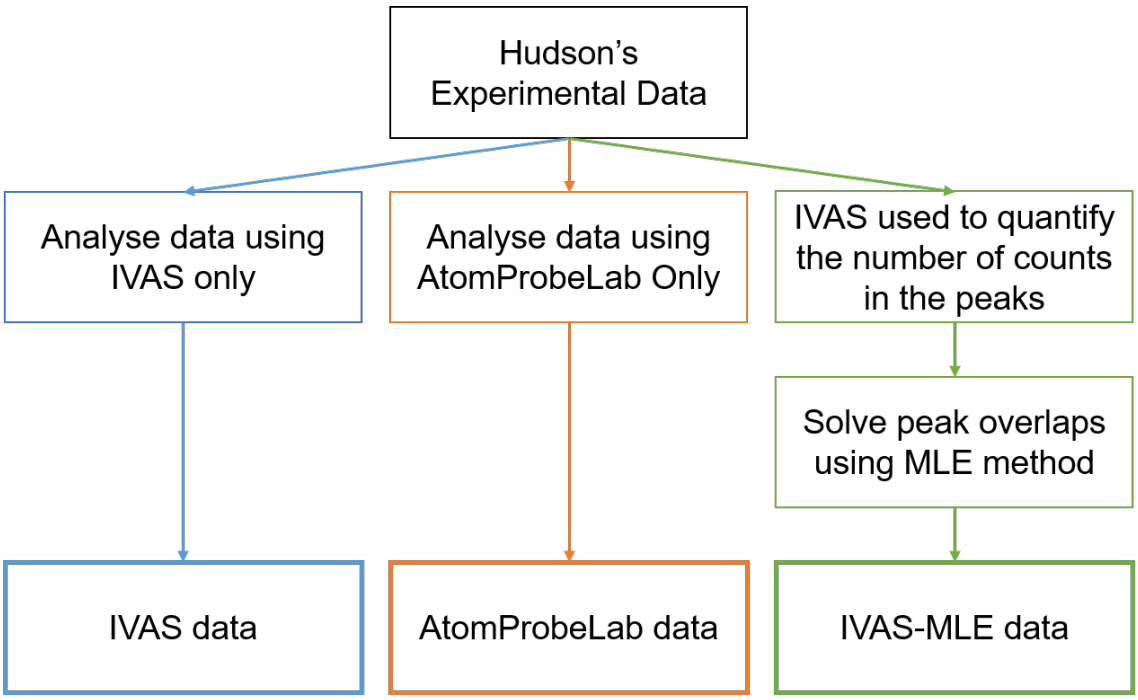


Figure 6.4: Data analysis work flow for the IVAS, AtomProbeLab and IVAS-MLE datasets.

The resulting compositions from the IVAS-MLE route do not give a difference in Nb composition with laser energy, agreeing with Hudson's findings. It also shows that the difference in apparent trend in Nb composition is likely a result of the counts inputted into the peak overlap solvers, as opposed to the actual peak overlap solving. This is because when the IVAS count quantification is used to calculate the Nb composition for all of the laser energies, no trend in Nb concentration with laser energy is found, regardless of the software used. Notably, the mass spectrum in Figure 6.3 contains peak tail overlaps between adjacent peaks. If the data in these peaks are not handled correctly, the quantification of counts in the peaks could be inaccurate. This issue will be addressed in the proceeding section.

6.2.2 Peak Count Quantification

Accurate quantification of counts in the peaks of APT data is important because it is used during the peak overlap solving in the first step so if we are unable to calculate the

number of counts correctly, it will be very difficult to accurately calculate a composition. One method of doing this is to find the number of counts in a given range. This assumes that all of the counts in the defined range correspond to a single peak. However where peak tail overlaps occur, this may not be the case demonstrated by the sketch in Figure 6.5.

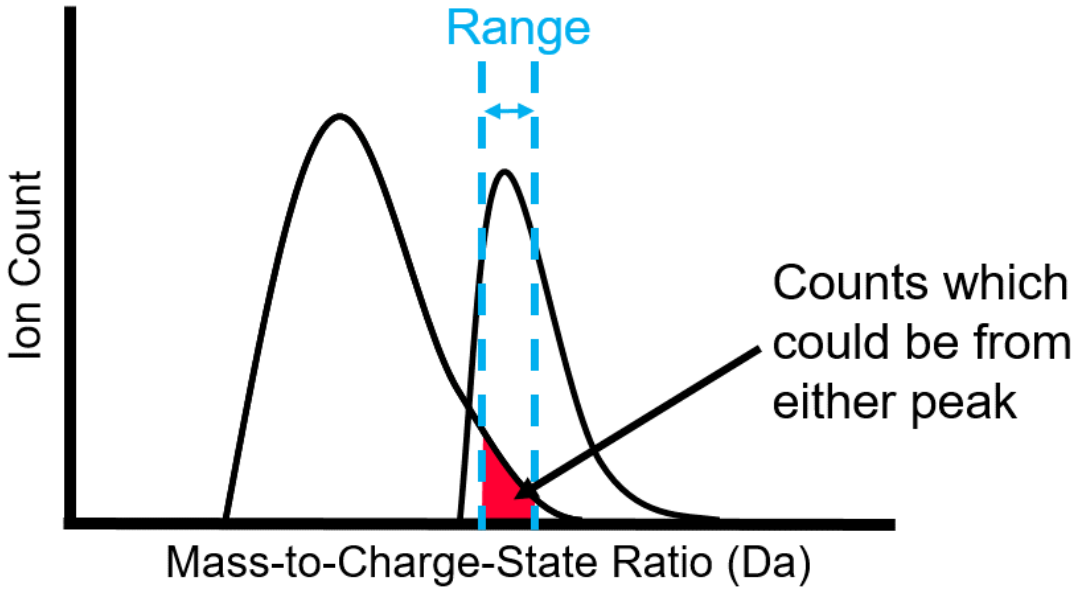


Figure 6.5: Sketch of a peak tail overlap in an APT mass spectrum where a range contains counts from two peaks.

This section utilises simulated APT-like mass spectra data. The fact that the simulated data has a known composition to enable us to probe discrepancies between IVAS' and AtomProbeLab's calculated compositions found during the analysis described in Section 6.2.1. The peaks in the simulated mass spectrum were generated so as to more realistically recreate the effect of peak tail overlaps in experimental data to check the quantification of counts in the peaks. The composition of the data was modelled on experimental data, taken from Hudson's laser energy optimisation study, for the part of the run at 0.6 nJ [100]. Data with a realistic peak shape that was based on real experimental data and data with Gaussian-shaped peaks were used. Peak overlap analysis was performed on these

datasets and compared.

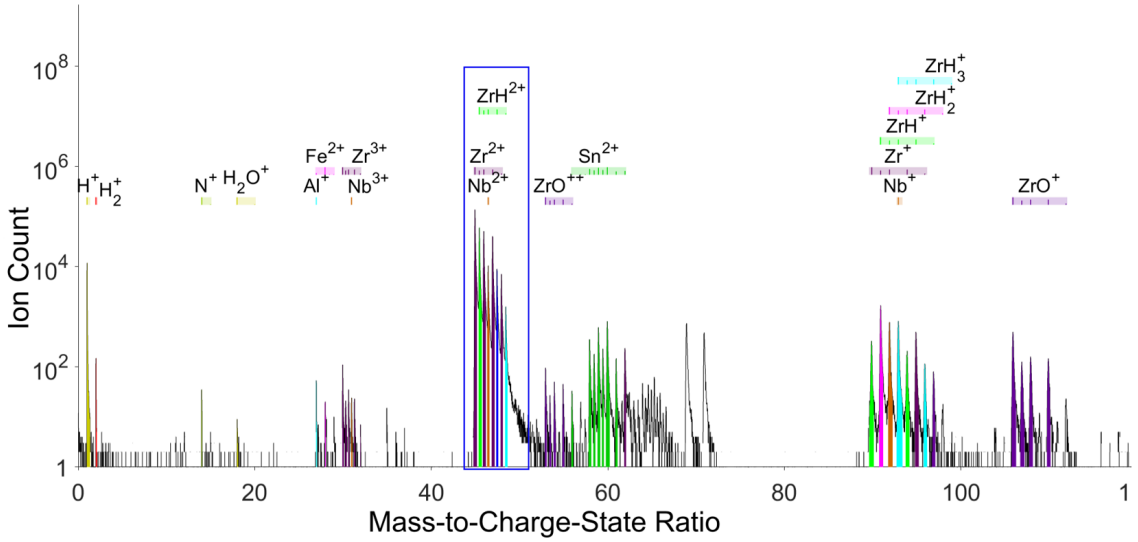


Figure 6.6: Mass spectrum of ZIRLO needle. The Zr^{2+} charge state peaks are highlighted in blue as the simulated data was based on these peaks.

An entire ZIRLO mass spectrum was simulated with a realistic peak shape and a Gaussian-peak shape; these modelled situations where peak tail overlaps did not and did occur. The mass spectrum from Hudson's data is shown in Figure 6.6. Two simulated datasets for the entire mass spectrum were produced containing 1 million ions. The distribution of the masses of the ions were generated to produce shapes that mimicked experimental mass spectra data, and Gaussian-shaped peaks that had a full-width half-maximum of 0.06 Da (in mass-to-charge-state ratio space). The overall composition of the dataset and the ionic composition (input for the mass spectrum simulator script) are shown in Tables 6.1 and 6.2.

Table 6.1: Composition of the ZIRLO dataset for the whole mass spectrum. This data is modelled on the 0.6 nJ section from the laser energy optimisation experiment of Hudson [100].

Element	Zr	H	Nb	Sn	Al	Fe
Composition (at.%)	82.53	16.34	0.34	0.77	0.01	<0.01

Table 6.2: Ionic input for mass spectrum simulation used for overlap solving verification.

Ion	Composition (Ionic %)	Proportion of ion in each charge state		
		1+	2+	3+
Zr	balance	0.004	0.995	0.001
ZrH	17.180	0.080	0.920	0.000
Nb	0.400	0.330	0.660	0.020
H	2.000	1.000	0.000	0.000
H_2	0.027	1.000	0.000	0.000
Sn	0.900	0.000	1.000	0.000
Fe	0.006	1.000	0.000	0.000
Al	0.010	1.000	0.000	0.000

Peak tail overlaps occur when a peak overlaps with the tail of the preceding peak [125]. These peak tails are artefacts due to the evaporation process within the atom probe experiment, for example delayed evaporation in laser evaporation mode experiments or an energy deficit in voltage mode experiments [117]. There was some discrepancy in the calculated compositions of the simulated data, Table 6.3. Looking closer at the data, we can see that for the Gaussian-shaped peaks, we can calculate the correct composition using both AtomProbeLab and IVAS. In the realistic peak model, neither software was able to calculate the correct composition, due to ineffective handling of the peak tail overlaps (Figure 6.7). The values provided by IVAS are, however, closer to the simulated values.

Table 6.3: Compositions calculated by each software package for real and Gaussian peak shapes

Element	Composition (at.%)								
	Simulated (True)	Real Peak Shape				Gaussian Peak Shape			
		AtomProbeLab	Deviation From Simulated	IVAS	Deviation From Simulated	AtomProbeLab	Deviation From Simulated	IVAS	Deviation From Simulated
Zr	82.53	82.27	**-0.26**	82.54	**+0.01**	82.57	**+0.04**	82.56	**+0.03**
H	16.34	16.56	**+0.22**	16.28	**-0.06**	16.34	**-0.03**	16.31	**-0.03**
Nb	0.34	0.40	+0.06	0.39	+0.05	0.34	0.00	0.34	0.00
Fe	0.01	0.00	-0.01	0.02	+0.01	0.00	-0.01	0.00	-0.01
Al	0.01	0.01	0.00	0.01	0.00	0.01	0.00	0.01	0.00
Sn	0.077	0.77	0.00	0.76	-0.01	0.77	0.00	0.76	-0.01

Most of the Zr, Nb and ZrH ions are present in the 2+ charge state hence a second simulated dataset was produced containing these peaks only using a Gaussian peak shape. These datasets were used to investigate the peak counting and how the presence of peak tails affected this. The ionic composition of the dataset was modelled on the experimental data from Figure 6.3 (a).; which is also the same data in the blue box of Figure 6.6. The composition of the datasets and ionic input are given in Tables 6.4 and 6.5. Two different peak widths were used to simulate situations where peak tail overlaps do and do not occur, FWHM of 0.28 and 0.263 Da, respectively, Figures 6.7 (a) and (b). A Gaussian curve was fitted to the peaks in both situations, as shown. Figures 6.7 (c) and (d) shows the fraction of the total quantified counts that each software has calculated to be in the peak and those calculated from the fitted curve.

Table 6.4: Composition of the ZIRLO data for the Zr 2+ peaks only. This data is modelled on the 0.6 nJ section from the laser energy optimisation study by Hudson [100].

Element	Zr	H	Nb
Composition (at.%)	85.50	14.26	0.24

Table 6.5: Ionic input to generate the simulated ZIRLO mass spectrum for the Zr 2+ charge state peaks only.

Ion	Composition (Ionic %)
Zr	83.00
ZrH	16.72
Nb	0.28

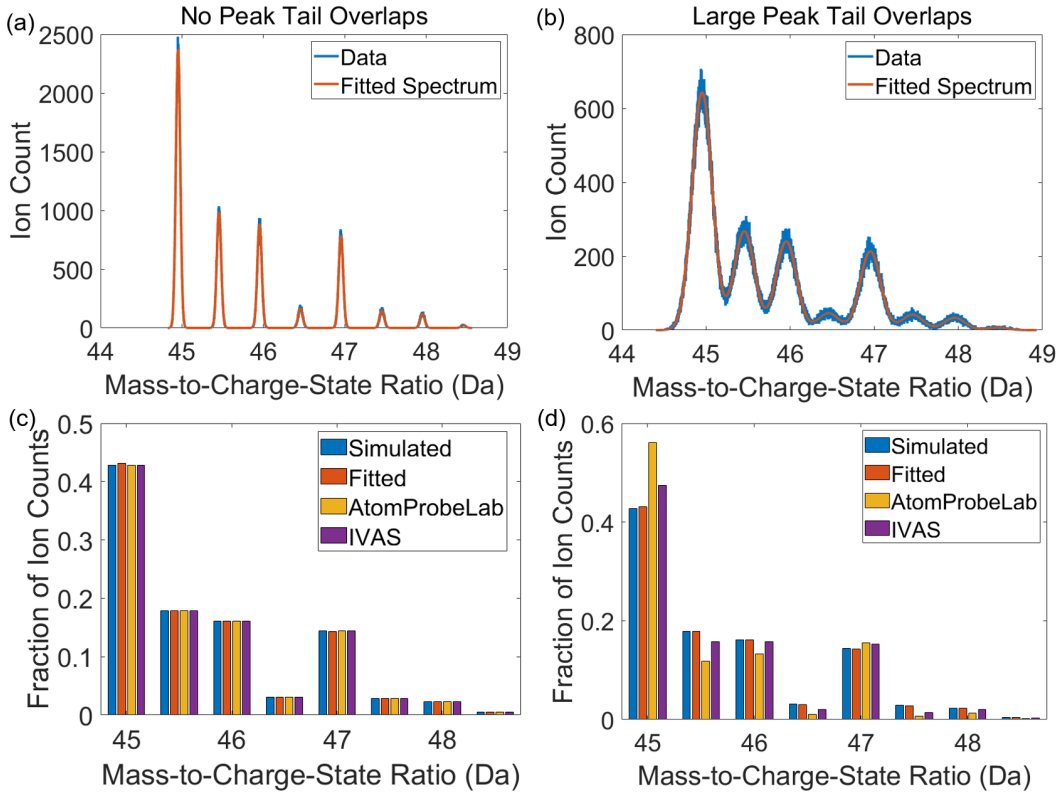


Figure 6.7: Simulated mass spectra with Gaussian-shaped peaks of different widths. (a) and (b) are the mass spectra with Gaussian curves fitted. (c) and (d) are bar charts giving the fraction of counts in each peak as calculated using the fitted spectra, AtomProbeLab and IVAS.

Figure 6.7 (c) shows that where peak tails do not overlap, the number of counts in each peak can be calculated accurately. However, where tail overlaps occur, the estimation of the number of counts that AtomProbeLab and IVAS give are less accurate (Figure 6.7 (d)).

The composition that IVAS calculated for the simulated data is closer to the simulated value because the number of counts in the peaks is closer to the simulated value, as shown in Figure 6.7. The reason for this observation is unclear; IVAS is a commercial software and CAMECA did not provide any more detailed information regarding the specific algorithm used. In situations where peak overlaps do not occur, both IVAS and AtomProbeLab can calculate the correct composition, see Table 6.3, which demonstrates that the peak overlaps

themselves are being solved correctly. Neither software handles the occurrence of peak tails correctly and the inaccurate count quantification leads to an incorrect composition. These analyses demonstrate that if we could improve the way each software package handles the peak tail overlaps, both IVAS and AtomProbeLab would be able to calculate a more accurate composition. However, in order to do this, the APT community would need to improve the understanding of the shapes of the the mass-to-charge state ratio peaks that occur within in the APT data. Methods such as those developed by Johnson et al. and Meisenkothen et al. could potentially be implemented for this purpose [154], [155].

The results in this section show that without including peak fitting as part of the analysis, the most accurate composition for Zr-NB alloys is obtained by using IVAS to provide the count information. The maximum likelihood estimation is a good method to solve the peak overlaps where there are few counts [156]; therefore the best method to solve this overlap group is to use the AtomProbeLab MLE algorithm to solve the count quantification obtained from IVAS. This approach has been used in the following section to analyse data from reference [116].

6.3 Improving the analysis of deuterated Zircaloy-4 APT data

6.3.1 Improving the quantification of deuterium in Zircaloy-4 APT data

Producing accurate compositions of deuterium is essential in getting quantitative information about hydrogen embrittlement on the nano-scale. Having completed the previous work to optimise solving peak overlaps for Zr samples, this method is now applied to previously published analyses to improve the quantification of deuterium. This section re-uses data from the literature and historic datasets, acquired within the Atom Probe Research Group at the University of Oxford, to quantify deuterium levels in a deuterated Zircaloy-4 APT dataset from MPIE (Max-Planck-Institut für Eisenforschung).

The deuterated Zircaloy-4 data was originally presented in work by Breen et al. [116]. A site-specific lift-out was taken from a grain boundary deuteride in an electrochemically

charged Zircaloy-4 sample (Zr-1.5Sn-0.2Fe-0.1Cr wt.%). The APT data was collected using a LEAP 5000 XR instrument using analysis conditions of a 60 pJ laser energy, 250 kHz pulse frequency and an analysis temperature of 60K.

In the mass spectrum of deuterated zirconium samples, deuterium is detected as the following ions: D^+, DH^+, D_2^+ and deuteride ions such as ZrD, ZrDH and ZrD_2 ions. The addition of these ions to the mass spectrum leads to the formation of complex peak overlap problems. There are direct peak overlaps between any ion that contains D or H_2, these are D^+ and H_2^+ and ZrD and ZrH_2 in both the 2+ and 1+ charge states. These overlap problems are not solvable using the usual peak overlap solving methods. A map showing the overlaps is in Figure 6.8, and the corresponding sections of the mass spectrum are shown in Figures 6.9 and 6.10.

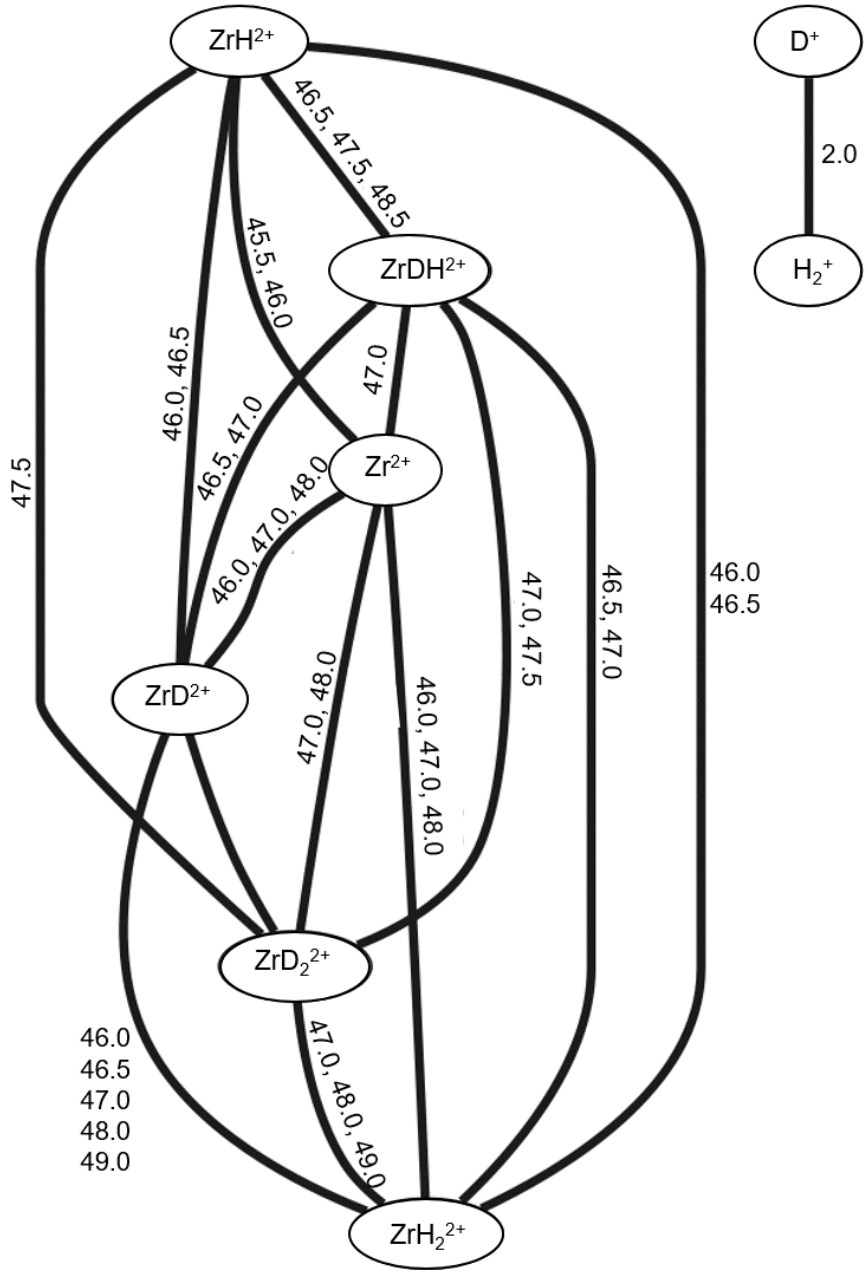


Figure 6.8: Overlap maps for the H_2^+-D+ and Zr^{2+} ions. There is one circle for each ion and the peak overlaps are represented by lines between each ion. The mass-to-charge-state ratio where the overlap occurs written to the side of the lines.

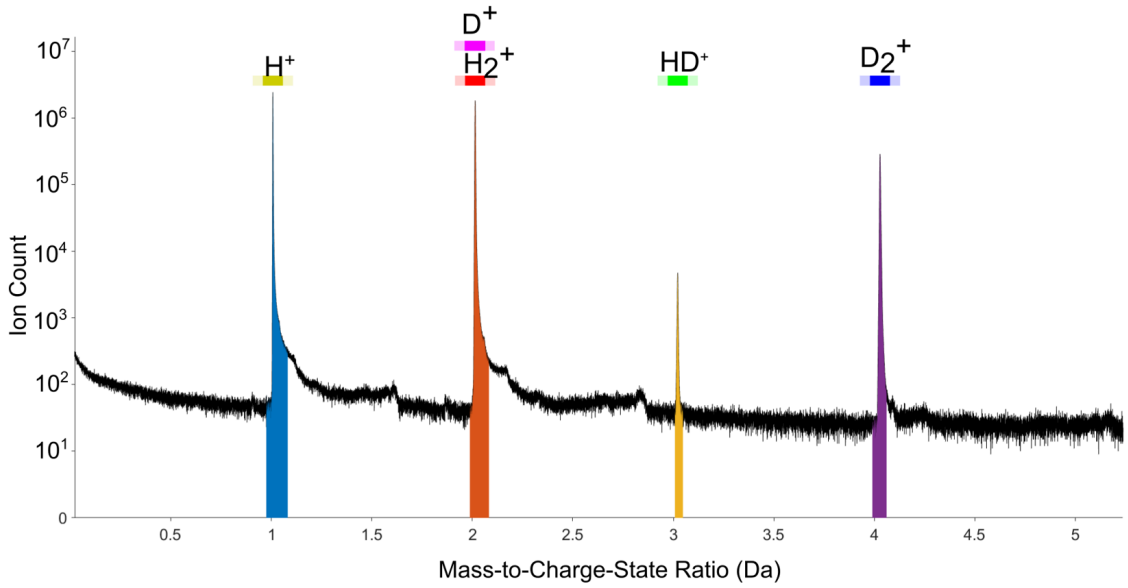


Figure 6.9: Section of a mass spectrum of deuterated Zircaloy-4 sample with the hydrogen and deuterium peaks labelled. The bars show the mass-to-charge-state ratio of the ionic species and their height is proportional to the isotopic abundance of the ion. All of these ions are monoisotopic.

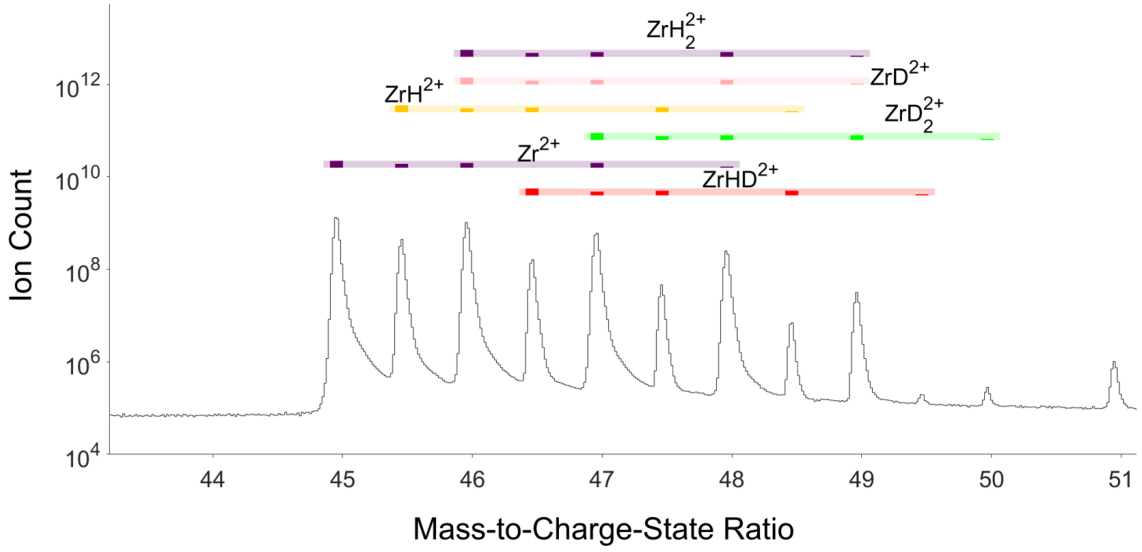


Figure 6.10: Section of a mass spectrum of deuterated Zr sample with the Zr, Zr hydride and Zr deuteride peaks labelled. The bars show the mass-to-charge-state ratio of the ionic species and their height is proportional to the isotopic abundance of the ion.

These overlap problems are rank deficient (insufficient information in the mass

spectrum to solve the problem) and therefore cannot be directly solved using conventional methods. In the original work, Breen et al. solved the rank deficient peak overlaps by making several assumptions. To solve the overlap between H_2^+ and D^+ at 2 Da, it was assumed that all counts of this peak were D^+ [116], [126]. The ZrH_2^{2+}-ZrD^{2+} peak overlap was solved by assuming that any counts that could be ZrH^{2+} or ZrD^{2+} were all ZrD^{2+}. Both of these assumptions overestimate the number of counts of deuterium containing ions and therefore the deuterium concentration in the sample. The authors state that the deuterium concentration calculations are an overestimate but they were unable to give an indication of by how much [116].

As there are negligible counts of ZrH_2 in the data from the uncharged sample, it was assumed that any counts that could be either ZrH_2 or ZrD were all ZrD. Both of these assumptions ignore the contributions of H_2 to the composition and will have the effect of overestimating the deuterium concentration, as acknowledged in the prior studies [116], [126]. In the deuterium-charged Zircaloy-4 data, there are few counts of ZrH_2 and the assumption that there are no counts of ZrH_2 in the data has little effect on the overall composition. However, for the peak overlap at 2 Da, the situation is not as straightforward. The H_2:H ratio is non-negligible, so some of the counts in the peak will be H_2^+. Including the contribution of hydrogen to this peak improves the accuracy of the deuterium concentration over the previous work [116].

A key source of error in solving the H_2^+-D^+ peak overlap at 2 Da is the H_2^+:H^+ ratio. Instead of the assumption above, this ratio can be used to calculate the number of counts in the peak at 2 Da that corresponds to molecular protium, meaning that the other counts in the peak are D^+ ions. To underpin this approach a paired experiment can be used; by analysing the sample before deuteration, we can calculate this ratio in the uncharged (deuterium free) state and assume that this ratio is unchanged by the charging process. For the dataset acquired by Breen et al., we did not have this information, so to estimate this ratio we used historic APT data from the Oxford Atom Probe Research Group. The Zr alloy datasets were a mixture of Zircaloy-4, Zr-0.2Nb, Zr-0.8Nb and Zr-2.5Nb alloys. All

samples were prepared using the lift-out method of Thompson et al. [132] using either a FEI Helios dual-beam plasma focused ion beam, a Zeiss NVision dual-beam Ga focused ion beam or Zeiss Crossbeam dual-beam Ga focused ion beam. The APT experimental conditions used for these samples used laser pulse energies between 40 and 100 pJ, laser pulse frequencies of either 200 or 250 kHz and temperatures between 50 and 60 K. All experiments were conducted using a LEAP 5000 XR instrument. Appendix A.4 contains the Experiment ID dataset used here.

Twenty four zirconium alloy datasets were analysed to find the H_2:H ratio in each respective environment. These ratios gave bounds of 0.11 and 0.71 ($\mu \pm 2\sigma$). These bounds were used to calculate the maximum and minimum contribution of deuterium in the peak at 2 Da and therefore the overall deuterium concentration. We have used this information to solve the peak overlaps across a concentration line profile and provide a quantitative deuterium concentration across an α-Zr/deuteride boundary. These datasets were a mixture of Zr alloys at different analysis conditions due to a limited number of Zircaloy-4 datasets being available at the time this analysis took place. The width of the bounds is therefore likely to be larger than if we were to have used the same material analysed under the same analysis conditions. It is also noted that as part of another piece of work a Zircaloy-4 needle was analysed in two different LEAP 5000 XR (transfer between these was completed under vacuum) and the H_2:H ratios for each instrument were 0.39 and 0.69, respectively, so it is feasible that there is significant intra-sample variation.

By splitting a dataset up into sections along a certain direction, and finding the composition of each subsection, we can compute composition line profiles across grain boundaries and interfaces in the APT data. Breen et al. used a composition line profile to look at interfacial segregation to a deuteride. A peak overlap solved composition line profile was produced for a similar region of the dataset to the previous work [116] (Figure 6.11) producing a similar line profile, which is shown in Figure 6.12.

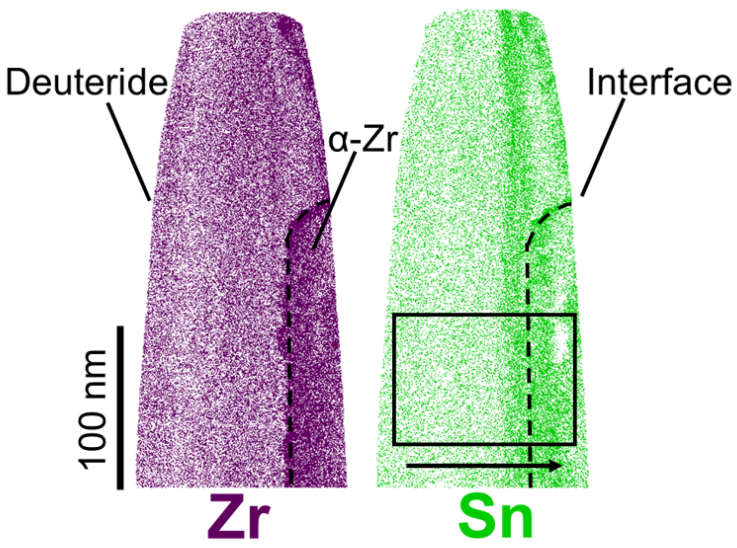


Figure 6.11: APT reconstruction showing the location of the metal and the area over which the line profile was calculated. The dashed line shows the α-Zr/deuteride interface and the arrow shows the direction in which the line profile was taken.

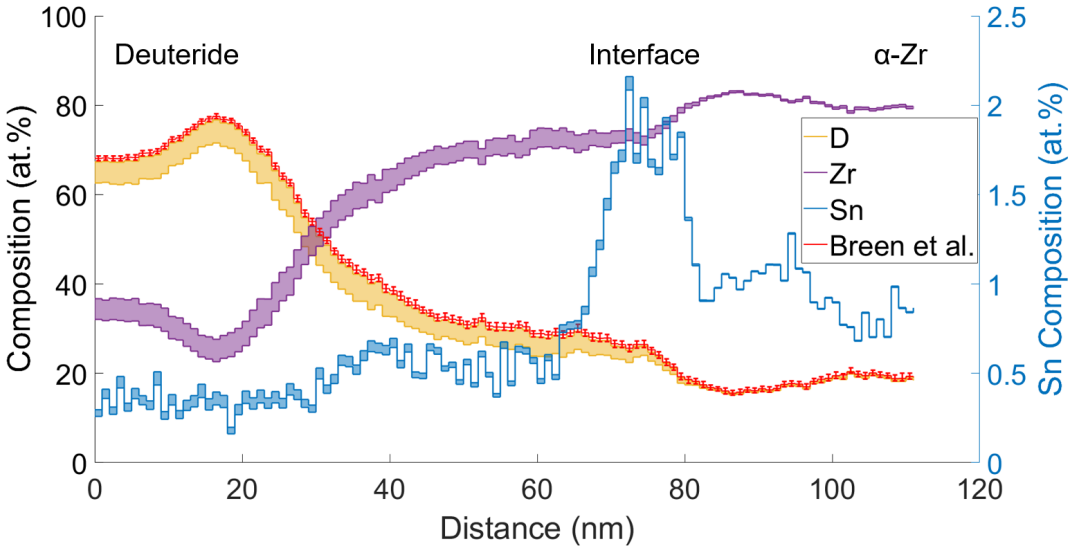


Figure 6.12: Peak overlapped solved line profile across a zirconium matrix-deuteride interface. The upper and lower bounds of the concentrations were calculated using the upper and lower bounds of the H_2:H ratio ($\mu \pm 2\sigma$) of 0.11-0.71.

Figure 6.12 confirms that Sn is segregating to similar levels to the previous work;

this is expected as Sn is not present in a peak overlap system that contains D. If we look at the deuterium line profile calculated with the same assumptions as the previous work (Breen et al.), we can see that it is in good agreement with the upper bound of the deuterium concentration. This shows that the values previous calculated were a reasonable overestimate of the composition.

The method described in this section can be used to produce upper and lower limits for the deuterium concentration in laser mode APT data. The assumptions made by Breen and co-workers meant that the reported concentrations were an overestimate, this work produced a more accurate quantitative concentration line profile for the deuterium concentration.

6.3.2 Spatially localised peak overlap solving

In the APT mass spectrum of Zircaloy-4, many peak overlaps are present (as seen in Figure 6.6). As well as affecting composition measurements, peak overlaps also make analysing the spatial location of mass-overlapped ions in the reconstruction difficult. This is because, to display the ions in 3D on an atom map, the ions contained within each defined range of mass-to-charge-state ratios must be assigned a single identity, whereas in reality, multiple ionic species may be contributing to the ions within the range if there is a peak overlap. Therefore by looking at the location of the ions originating from an overlapping range in the mass spectrum, we are actually looking at the spatial locations of multiple ions. This can make unambiguously discerning the spatial location of minor elements from the rest of the peak difficult.

Addressing this problem is relevant to the current study because it is of scientific interest to investigate the trapping of hydrogen to irradiation-induced defects. However, deuterium is present in several peak overlaps, as shown in Figures 6.9 and 6.10. Figure 6.13 demonstrates the need to be able to discriminate the respective position of different types of ion contributing to the same overlapping peak. The ranges highlighted in red in the mass spectrum contain the counts of ZrDH. These peaks also contain Zr and ZrH which

combined, contribute the strongest signal to the overall peak count. The reconstruction below shows all counts that could be ZrDH is actually showing mostly Zr and ZrH which means it is not possible to unambiguously characterise the spatial distribution of ZrDH ions alone.

To analyse the spatial location of deuterium in our APT data, we need to be able to discriminate the different types of ions in peak overlaps. To this end, the single ion deconvolution method of London et al. [125] has been trialled to see if it can provide us with the spatial information for deuterium containing ions.

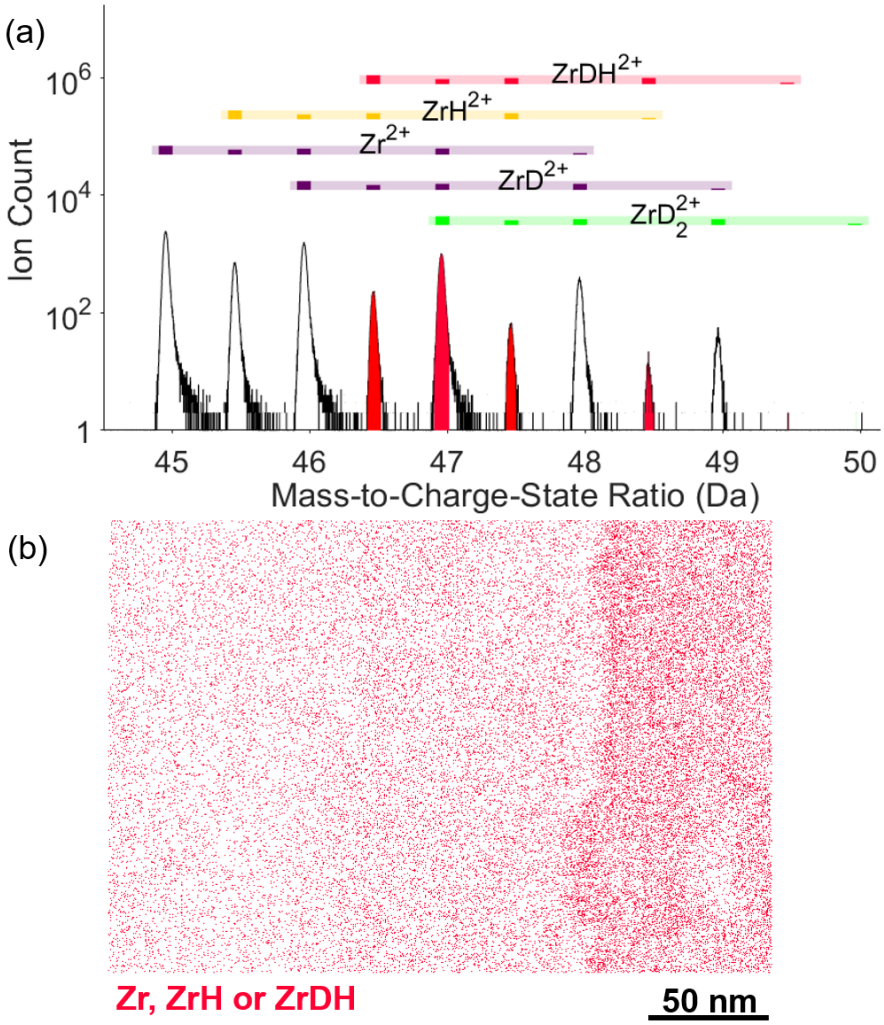


Figure 6.13: (a) Section of a mass spectrum from a deuterated Zircaloy-4 sample where the peaks containing some ZrDH ions are highlighted in red. (b) Reconstruction containing ions in the ranges previously described.

The method devised by London et al. defines a local volume around each ion in the reconstruction that is associated to the overlapping peak, using a sphere of size defined by either a radius or a minimum number of nearest neighbours. The mass spectrum for this local volume is analysed and the peak overlaps are solved to provide a measurement of local composition around each of these ions. The central ions that are contained in peak overlaps then have their chemical identities re-assigned probabilistically, where the local ionic composition is used as the probability of each ion being assigned a specific

identity [125]. An example of this can be found in Figure 6.14. This method was initially designed for the analysis of clustered ions in APT data.

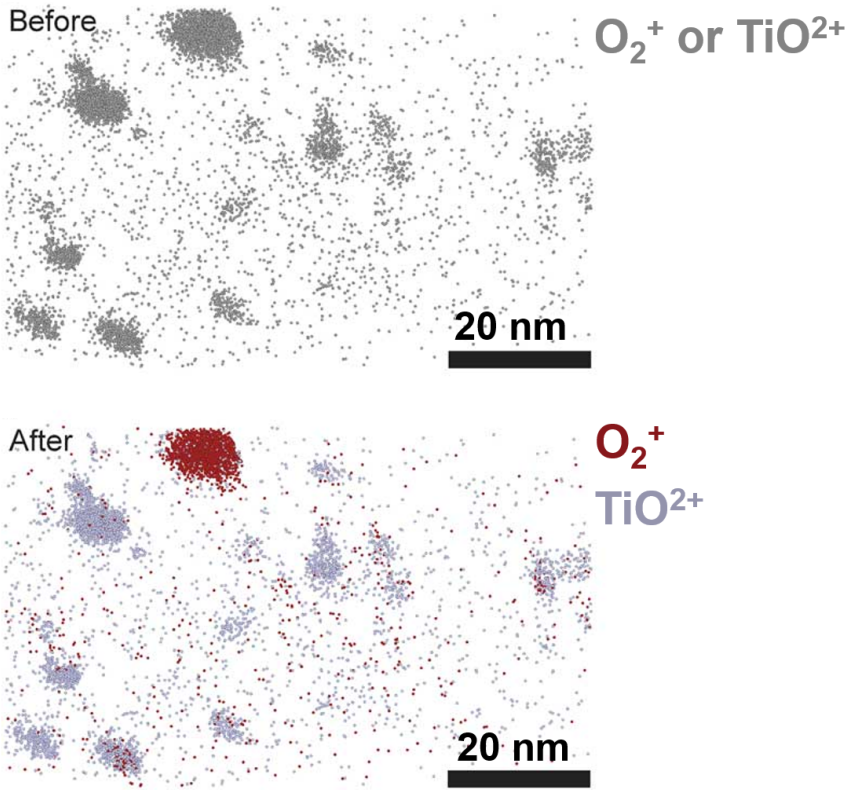


Figure 6.14: Example of the ion by ion deconvolution of the peak overlap between O_2^+ and TiO2+ at 32 Da in the APT analysis of an ODS steel. After the ion by ion deconvolution, the data shows an oxygen-rich cluster of ions. Reproduced from [125]

Peak deconvoluted datasets were produced for a 1 nm thick slice of the interface region shown in Figure 6.15 (a). Figure 6.15 does not contain ZrDH or ZrD_2 ions because they contribute too little counts to the mass spectrum (0.08% and 0.0002% of the total counts respectively), so showing the ranges in which these ions are present, in a reconstruction would mostly be caused by the other ions in the range, not the ions of interest. A 1 nm slice of the interface was used to limit computational cost of the single ion deconvolution calculations.

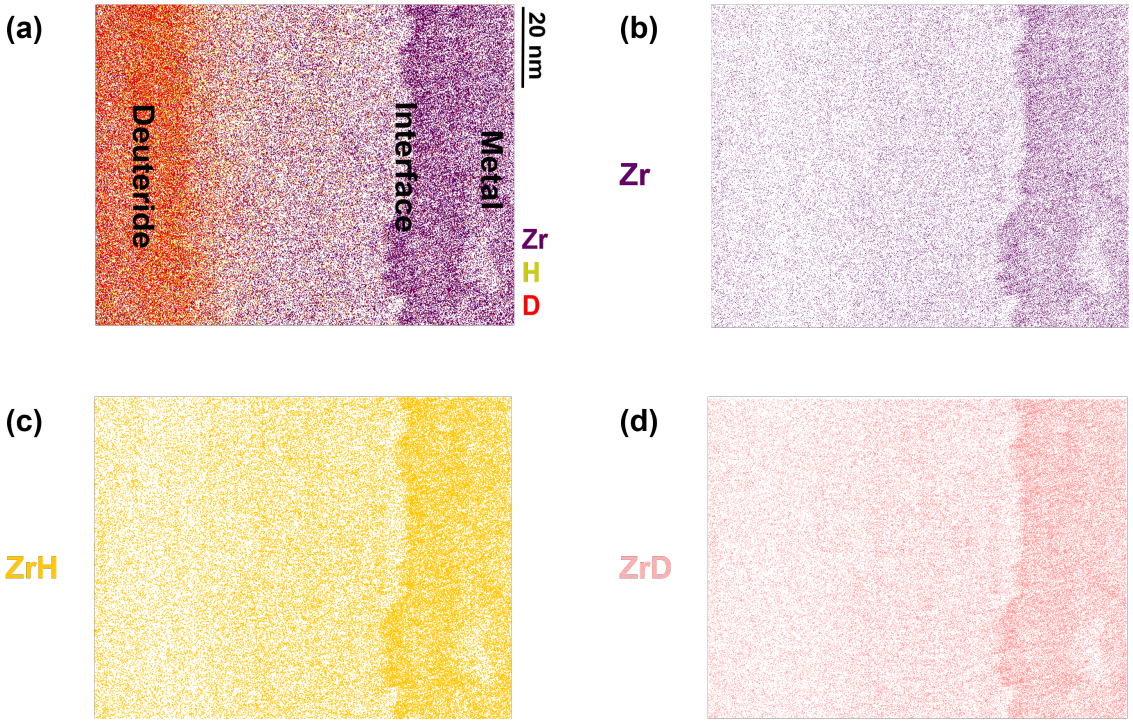


Figure 6.15: 1 nm slice of the line profile from the previous section where the data underwent localised peak overlap solving to improve the spatial accuracy of ions in the peak overlaps. (a) Slice showing all ions that could be Zr, H and D. (b) All ions that could be Zr. (c) All ions that could be ZrH. (d) All ions that could be ZrD. (b)-(d) are to act as a comparison for the relabelled data.

Datasets where the overlapping ion identities were relabelled were produced using the single ion peak deconvolution algorithm incorporating a spherical-shaped local environment with radii of 2, 5, 10, 20 and 50 nm, respectively. All ions in the mass spectrum were considered in the analysis but the following text focuses on Zr, ZrH, ZrDH and ZrD_2 as these were of the most interest. Figure 6.16 shows the ions contained in the Zr^{2+} problem after peak overlap solving.

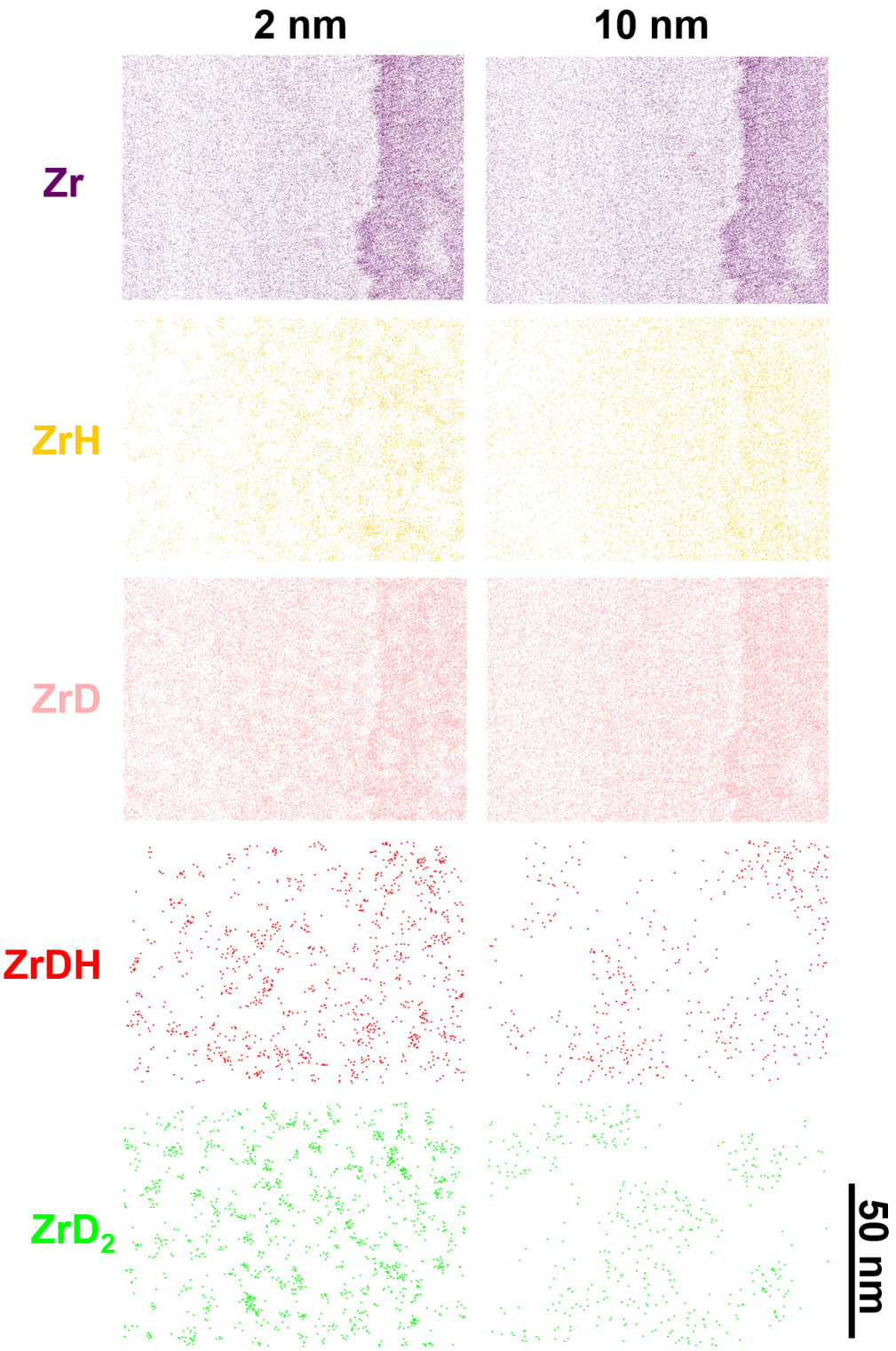


Figure 6.16: Reconstructions of Zr, ZrH, ZrDH and ZrD_2 ions after relabelling using spherical local environments, where the sphere radius used was 2 nm and 10 nm respectively.

Figure 6.16 shows the location of the Zr ions after the local decomposition. It can be seen that the Zr ions remain mostly unchanged after the relabelling procedure. The ZrH ions appear to have formed clusters post local peak overlap solving, as have the ZrD ions but to a less pronounced extent. ZrDH and ZrD_2 ions have also formed what appear to be clusters using both the 2 and 10 nm local environments. The clusters in the 2 nm radii data for these ions are smaller and more defined.

Experimental APT data contains two types of clusters, those that are random (i.e. due to statistical fluctuations) and those that are surplus to the statistically expected random case. An APT dataset is considered to have clusters if it can be shown that there are more than would be expected in the random case. The nearest neighbour (NN) distribution curves give a distribution of the distance between an ion (considered to be the centre of the cluster) and its kth nearest neighbour. One statistical test is to examine the inter-atomic distances, and its deviation from the random case. To check if the clusters are due to random fluctuations, we compare the NN distributions of the experimental dataset, to those of the same dataset that has been randomised (randomised experimental data). The randomised dataset does not contain any non-random clusters and will have a known nearest neighbour distribution. In the case where an experimental dataset contains only random clusters, both NN distributions will overlay. A shift between the distributions from the experimental data and the randomised experimental data indicates that there is a significant change in the experimental data and there are non random clusters.

The statistical test mentioned above will show whether the clusters seen in the data are due to statistical fluctuations or not. As we have processed the data, it is also necessary to check that any non-random clusters were not caused by the data processing (i.e. were caused by the single ion deconvolution and are not present in the original data). To check that the code did not create the clusters, we created a ‘shuffled’ dataset where the ion identities were randomly shuffled. The shuffled dataset contains random clusters only. The single ion deconvolution was performed on this shuffled dataset and analysed for any clustering. The processed shuffled data will only contain non-random clusters if

the clusters are as a result of the processing because we know there are no non-random clusters in the shuffled data.

The following text compares a number of different datasets given below and their relation to one another is shown in Figure 6.17.

- **2 nm relabelled data** is the original experimental data after having undergone the local peak overlap solving using a 2 nm spherical local environment.
- **randomised 2 nm relabelled data** is the 2 nm relabelled data where the ion identities have been randomised.
- **shuffled dataset** refers to the original experimental data where the ion identity has been randomised.
- **2 nm relabelled shuffled data** is the shuffled dataset after it has undergone the local peak overlap solving using a 2 nm sized spherical local environment.
- **randomised 2 nm relabelled shuffled data** is the 2 nm relabelled shuffled dataset after all of the ion identities have been randomised.

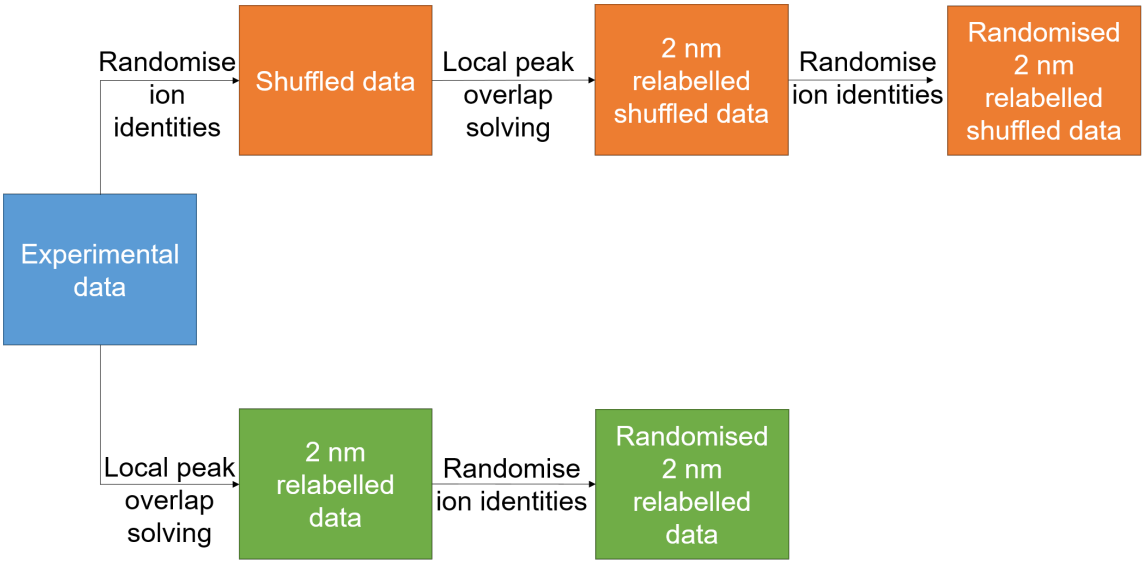


Figure 6.17: Diagram showing the relationship between the five datasets used in this section.

By computing nearest neighbour curves for the 2 nm relabelled data and randomised 2 nm relabelled data, a shift between the nearest neighbour distributions for the ZrDH ions can be seen (Figure 6.18). This indicates that the clusters are non-random, meaning that clusters are present in the data. A similar shift was observed for the Zr, ZrH, ZrD and ZrD_2 ions.

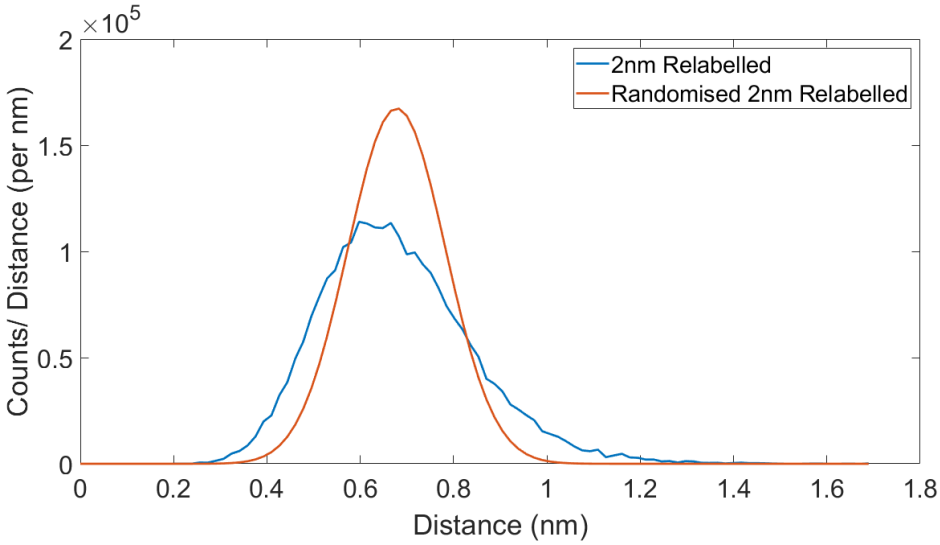


Figure 6.18: 5th nearest neighbour curves for the ZrDH ions from 2 nm relabelled data and the same data after it has been randomised.

If real, the existence of clusters in the Zr deuteride ions (ZrD, ZrDH and ZrD_2) would be interesting and has not been shown in the literature. However before any further analysis is done, it is necessary to ensure that these clusters are truly present in the data and are not an artefact of the single ion peak overlap solving analysis.

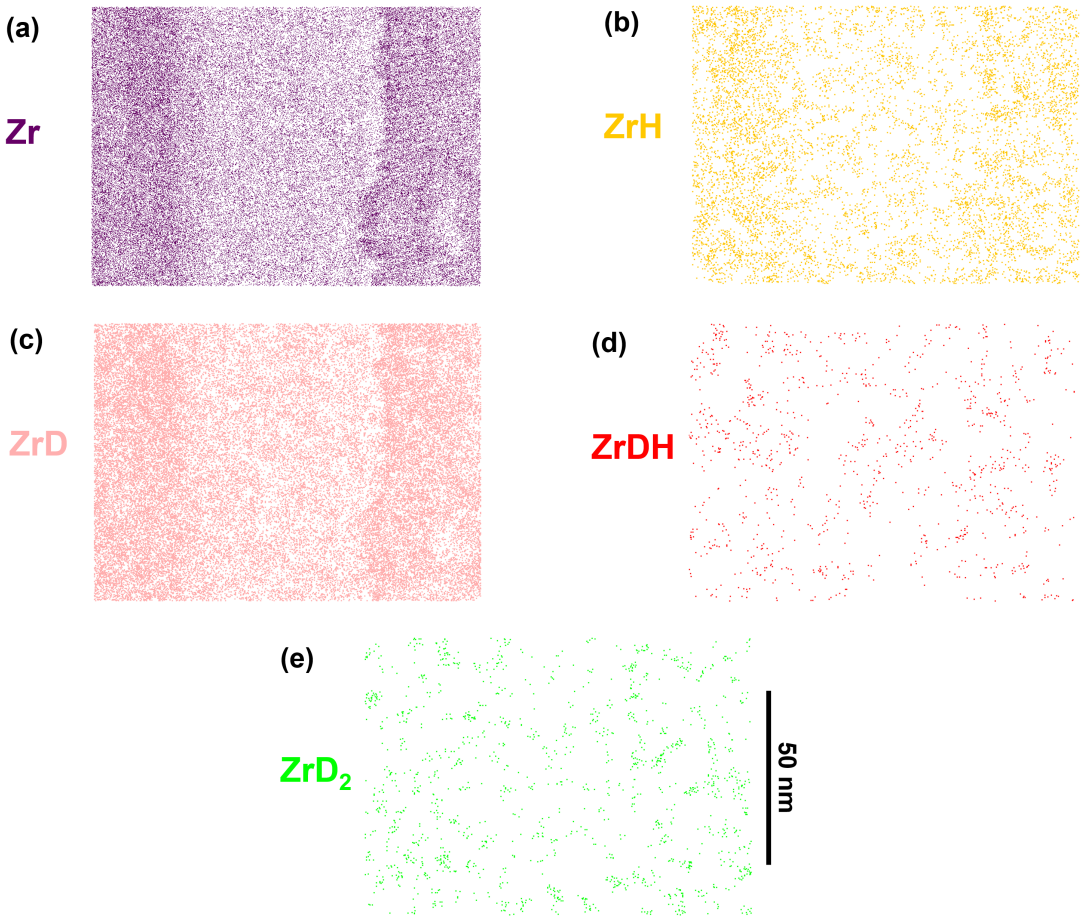


Figure 6.19: Shuffled data after the local peak overlap solving using a 2 nm spherical local environment. The (a) Zr, (b) ZrH, (c) ZrD, (d) ZrDH and (e) ZrD_2 ions are shown here.

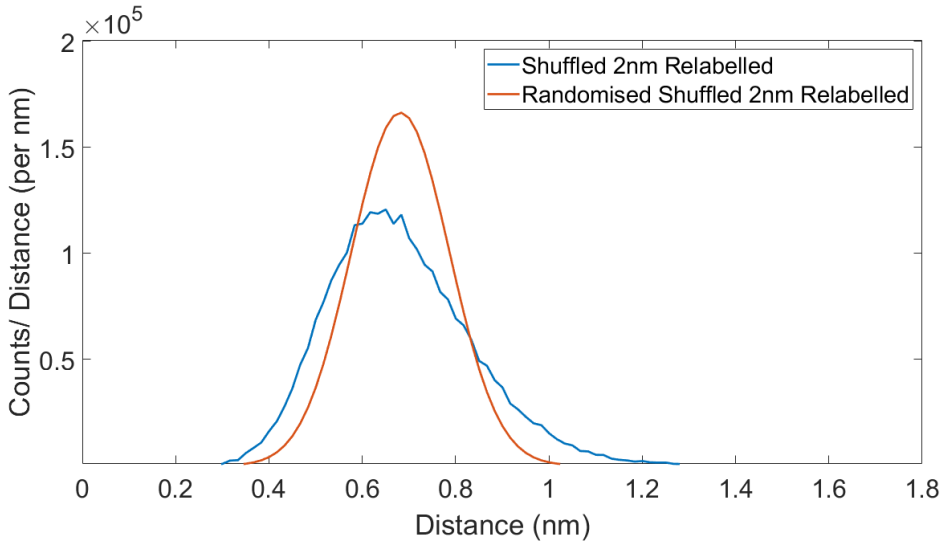


Figure 6.20: 5th nearest neighbour curves for the ZrDH ions for the shuffled data relabelled using a 2 nm spherical local environment and a randomised version of said data.

Figure 6.19 is the shuffled dataset post-analysis. It is concerning that even visually, clusters of ions can be seen in the reconstructions, this is quite distinct in Figures 6.19 (b), (d) and (e). By repeating the nearest neighbour analysis as before, the nearest neighbour curves for the ZrDH ions are contained in Figure 6.20. The shift in distributions indicates that the clusters in Figure 6.19 are not random. The presence of clusters in Figure 6.19 indicates that the clustering seen in the previous figures in this section are unlikely to be real and are an artefact of the data analysis method.

The likely cause of this clustering effect is the way in which the code used for this analysis works. Peak overlapped ions are found in the dataset and a k-d tree is produced after a nearest neighbour search on the overlapped ions. On an ion-by-ion basis, the surrounding atoms are found and the composition calculated. After this, the ions are relabelled probabilistically, with a probability based on the ionic composition. This means that the composition for the local environment surrounding a deuterium containing ion will have a higher deuterium concentration and will increase the chance that during the relabelling step a deuterium containing ion is chosen. The region around the atom included in the composition uses user-defined parameters (number of nearest neighbours

or distance) which is why the clusters in the 2 nm data appear to be smaller than that in the 10 nm data.

Limitations in the tool led to slow computational speeds. It is also worth noting that the overlap problem, in this data, that contained Zr and Zr deuteride ions was large and would have hindered this process. The overlap diagram is shown in Figure 6.8. Due to limited performance of this specific implementation (e.g. complexity of the overlap problem), a 1 nm slice of the interface was chosen. Future analyses could revisit this method but more advanced software may be required, which was outside the scope of this work.

The need to use such a small volume of data has meant that the spheres used to define the local environment are in fact discs which probably affects the spatial accuracy of this method. The clusters in the 10 nm local environment in Figure 6.16 appear stretched in the direction of the long edge of the reconstruction (across the width of the page).

In summary, the local decomposition method used by London et al. can produce a locally peak overlap solved dataset for bulk data but some considerations should be taken into account before using it to ensure it handles the data correctly. Several issues with this method were found including problems with the handling large quantities of data (more than a few hundred thousand ions) and if the script could process the data, it was slow. Once the data was relabelled the data processing was found to have induced the formation of artificial clusters in the Zr alloy data. Before applying this method to other bulk APT data, the problems previously listed should be considered. It can however be used for the data from extracted clusters, where the number of ions analysed is smaller and therefore can be processed within reasonable timescales.

6.4 Conclusions

This chapter follows efforts to improve the data analysis of deuterated zirconium alloy datasets by improving the accuracy of composition estimations and location of ions that exist in peak overlaps.

The influence of peak tails on the solving of peak overlaps is often overlooked,

however it was shown in this chapter that it has significant influence. The mishandling of peak tail overlaps meant that an increasing trend in Nb concentration with laser energy was found when in fact the Nb concentration is invariant with respect to laser energy. The count quantification of IVAS was found to be more accurate than AtomProbeLab. It has been shown that the most accurate method for solving peak overlaps in Zr alloy, using already available software, is to use IVAS to quantify the counts and the maximum likelihood estimation from AtomProbeLab to solve the peak overlaps. However, peak counting processes must be developed that take the shape of the peak into account and the extent of the overlap in mass-to-charge-state ratio or incorrect composition estimations of the data will continue to be made. The optimised peak overlap solving approach was used to analyse data from the literature and quantify deuterium concentrations in Zr alloy APT data for the first time. A method that relabels peaks based on the local composition to improve the spatial accuracy of deuterium was trialled. It was demonstrated that the algorithm introduced artificial clustering into the re-labelled data as a result of the logic used in the re-labelling.

Chapter 7

Atom Probe Tomography of Cold Worked Zircaloy-4

7.1 Introduction

APT cannot be used to directly image dislocations in the same way that transmission electron microscopy (TEM) can but it is possible to infer the presence of decorated dislocations in a sample by the segregation of solute elements. For example, iron has been observed to segregate to dislocations in Zircaloy-4 [97], [157]. Hence, there exist the potential to image dislocations as hydrogen trapping sites, identifiable by the co-segregation of iron and the implanted deuterium. An example of Fe segregation to dislocations in APT data of an autoclaved Zircaloy-4 sample is given in Figure 7.1. Furthermore, from a previous study, Figure 7.2 provides evidence of deuterium segregation to dislocations in a martensitic steel by the co-segregation of carbon and deuterium . These works demonstrate that it should be possible to image the co-segregation of Fe and D to dislocations in Zr alloy samples. As long as deuterium does segregate to dislocations within Zr alloy microstructure it should be possible to identify and characterise these features with APT data.

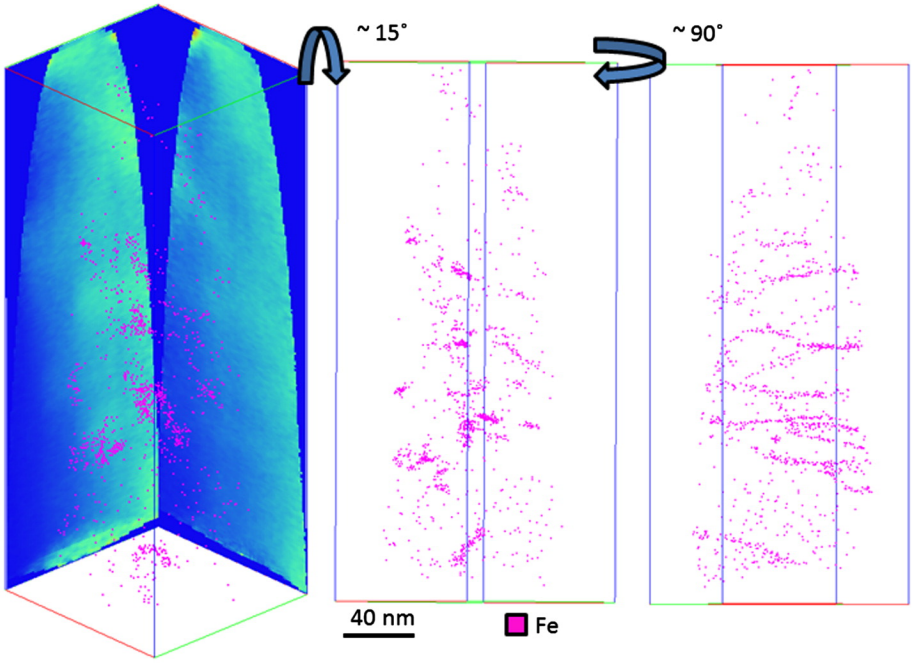


Figure 7.1: APT reconstruction showing Fe segregation to dislocations in Zr [157].

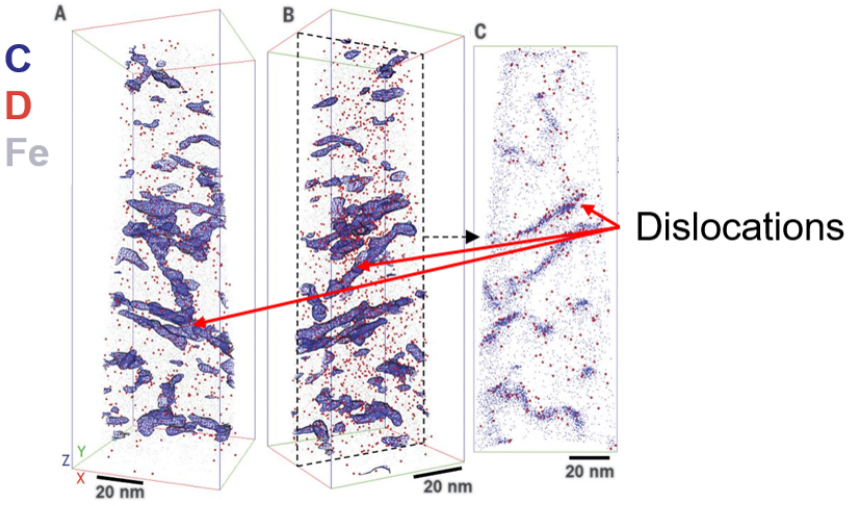


Figure 7.2: APT reconstruction of a martensitic steel, the blue 2% carbon iso-concentration surfaces are used to highlight the dislocations. The red circles indicate the distribution of deuterium atoms. Adapted from [141].

In this study, cold worked materials were investigated for use as surrogate for irradiation as straining a material also induces dislocations. These samples had been

cross rolled and cold work levels of 30%, 60% and 80% were produced. Cross rolling has been used as they are significantly less expensive surrogate for irradiated samples as they are easier (and safer) to handle and perform experiments on. However, the dislocation types and structures will differ between a cold worked and irradiated sample. Dislocations in irradiated materials take the form of loops, whereas dislocations induced by straining the material are line dislocations [28], [158]. The density of dislocations within the material will depend on the irradiation dose received as this will change the amount of atomic displacement or the amount of cold working the material has undergone [31], [158] . If the use of cold worked samples for such analyses can be shown to be a viable alternative it would enable us to more easily develop a method to image deuterium in Zircaloy-4 using APT before looking at irradiated materials.

This chapter investigates the APT analysis of the as-received and cold worked Zircaloy-4 samples used to develop a deuterium charging protocol.

7.2 Results and Discussion

Prior to commencing work to develop an optimised approach to deuterium charge these samples, it was necessary to understand what the APT data from an uncharged, as-received and cold worked sample normally looks like. In this way, we aim to distinguish between features in the data that are due to the cold working and the subsequent changes due to the deuterium charge accurately. There are two major aspects of APT data: the mass spectrum (which is used to generate compositional information) and the reconstruction.

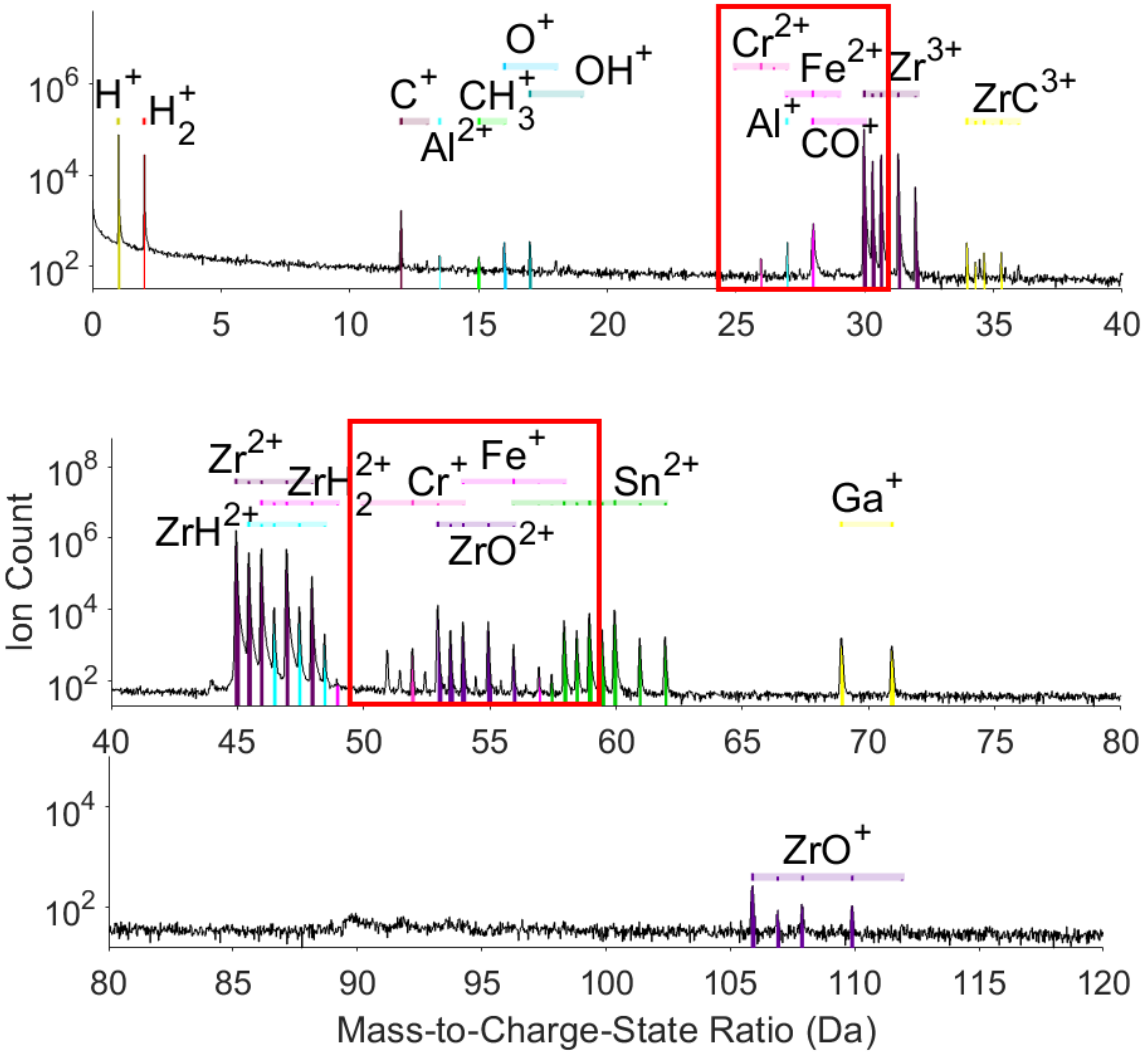


Figure 7.3: Representative mass spectrum of an as-recieved Zircaloy-4 sample. Red boxes highlight where peaks due to the detection of Cr and Fe are present.

In the mass spectrum of Zircaloy-4, the alloying elements are seen in the following charge states; Fe and Cr are seen predominantly in the 2+ charge state and in small quantities in the 1+ charge state (Figure 7.3). Sn is detected as 2+ charge state only. Fe is contained in peak overlaps with CO^+ at 28 and 29 Da, ZrO_2^{2+} at 53.9 Da and 55.9 Da, and Sn $^{2+}$ at 55.9, 56.9 and 57.9 Da. A challenge with this analysis is the fact that Fe^{2+} is only detected in the peak at 28 Da ($^{56}Fe^{2+}$), where it overlaps with CO^+. The complexity of

this peak overlap is increased by the trace quantities of Fe that are present in this alloy. To image dislocations in the data, there will need to be sufficient segregation of the ions from the peak at 28 Da.

The average composition as measured by APT is presented in Table 7.1. The measured composition of the samples does not vary with cold worked level which is expected as cold working a material is not going to cause a change in composition on the macroscale. The composition given is comparatively low in Fe and Cr compared to the standard bulk compositions quoted for Zircaloy-4 which are 0.30-0.39 and 0.12-0.23 at.% respectively [120]. This is because the solubility limits of these alloying elements are low in the α-Zr matrix so most of the Fe and Cr exist in second phase particles (SPP's), which were not encapsulated in any of the volumes analysed by APT.

Table 7.1: Average composition of the Zircaloy-4 samples. The error is the standard deviation across 18 samples.

Element	Composition (at. %)	Error
Zr	97.07	1.97
Sn	1.31	0.28
Fe	0.02	0.07
Cr	0.04	0.07
Al	0.01	0.01
C	0.23	0.54
O	1.28	1.31
N	0.02	0.08

As previously discussed, the APT analysis conditions will affect the apparent composition measured and this is a recurring issue for the APT community [90], [117], [159] The justification for the analysis conditions can be found in Section 3.2.3 and were chose to maximise deuterium detection. Based upon Hudson's laser energy optimisation study, it is apparent that the use of the low laser energy pulses in the atom probe experiment is likely

to have resulted more counts H_2^+ in the peak at 2 Da, a higher hydrogen concentration (as compared to high laser energies) and not have altered the amount of Sn or O [100]. There is too little Fe or Cr in the matrix to make a meaningful statement regarding the effects of the experimental conditions on the measurement of these elements.

All of the samples whose analysis were incorporated into Table 7.1 were analysed with a LEAP 5000 XR using a laser pulse energy of 50 pJ, laser pulse frequency of 200 kHz, a temperature of 55 K and a detection rate of 0.5%. The 80% cold worked material was analysed with a LEAP 3000X HR, with approximately equivalent conditions which were the same as previously stated but with a laser pulse energy of 0.35 nJ.

There are several important features of the reconstructions. The spatial distribution of Sn is inhomogeneous, likely as a result of Sn migrating on the surface to crystallographic poles. Samples have been analysed in laser-evaporation mode and Sn has a higher evaporation field than the Zr matrix which leads to Sn being retained on the needle during analysis and diffuses to areas of high electric field, such as the crystallographic poles [95].

Statistically, the as-received samples should not contain any dislocations, second phase particles or grain boundaries. These exist in the bulk material but do not have sufficient density to be sampled in the very small volume of an APT dataset without intentionally selecting site specific regions of interest during sample preparation (i.e. intentionally putting them in the samples). Therefore, the Fe should be distributed homogeneously and is confirmed by Figure 7.4.

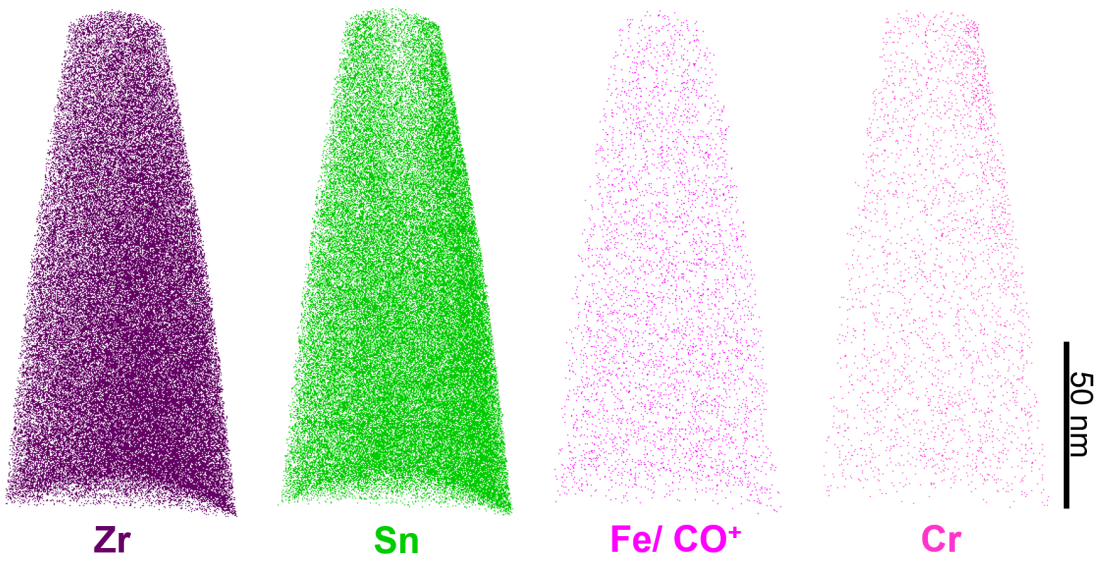


Figure 7.4: Representative reconstructions of an as-received Zircaloy-4 showing the respective distributions of Zr, Sn, Fe and Cr.

In contrast, the cold worked materials should contain a high number density of dislocations and hence it was expected that we were statistically likely to randomly sample such features in an APT analysis and that they would be apparent in the reconstruction by the segregation of Fe atoms. This means that there should be visible segregation of the peak at 28 Da (Fe^{2+}/CO^{+}) in the samples. However, this was not the case for any of the cold worked materials (Figures 7.5 - 7.7).

Upon examining the 28 Da peak, the most likely signal to enable identification of Fe, it does not appear to be segregating to any specific features in the sample, for the cold worked samples (Figures 7.5 - 7.7) implying that there are no dislocations in these reconstructions or segregation of Fe to dislocations in these systems is below a level detectable by the APT analysis. It is known that straining a material induces dislocations and the dislocation density in the 80% cold worked samples is expected to be in the region of $10^{15}m^{-2}$ which indicates that we should be able to have dislocations in a randomly electropolished sample of [160]. This is based on the cross-sectional area of any point down the needle being in the order of $10^{-15}m^{-2}$; this is calculated by assuming that the

cross section of the needle is approximately circular and that the smallest cross section is at the needle apex of radius 25 nm. The area of a circle is πr^2, giving an area of 2 x 10^{-15} m^{-2}. This means that there should be 2 dislocations (minimum) at any cross section of the needle. Therefore, it is likely that the samples do have dislocations in them but investigating the spatial distribution of ions associated to the 28 Da peak is not viable to provide evidence of the presence of dislocations in these APT reconstructions.

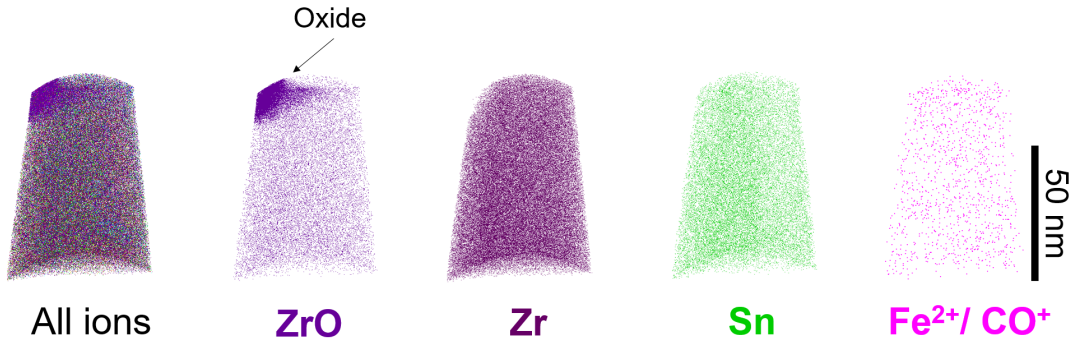


Figure 7.5: APT reconstruction of a 30% cold worked Zircaloy-4 sample.

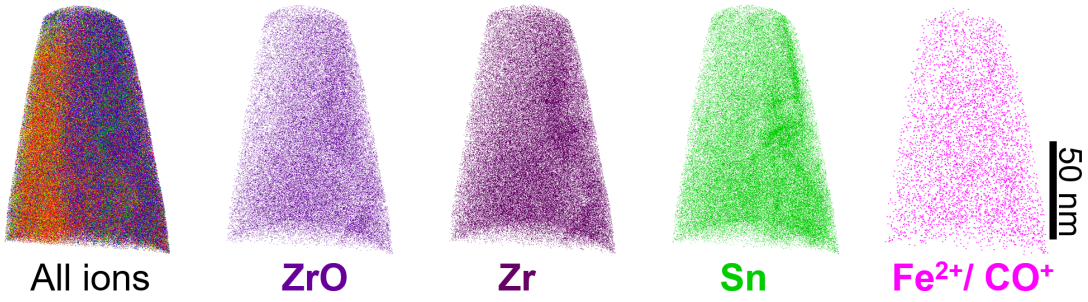


Figure 7.6: APT reconstruction of a 60% cold worked Zircaloy-4 sample.

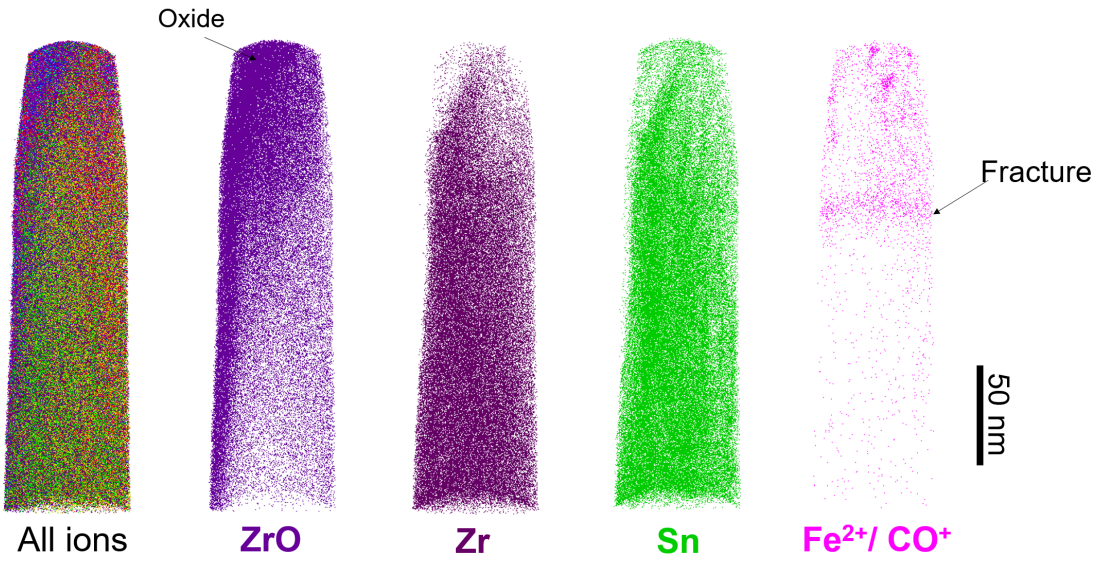


Figure 7.7: APT reconstruction of a 80% cold worked Zircaloy-4 sample.

Previously, Hudson used only the leading edge of the peak at 28 Da to investigate the Fe distribution in some of the samples in his PhD thesis as $^{56}Fe^{2+}$ has a slightly lower mass-to-charge-state ratio that $^{12}C^{16}O^{+}$ [100]. However, this method did not yield useful results for these samples. Figure 7.8 displays the data from the 60% cold worked samples when this method is applied and there is still no segregation due to ions contributing to the leading edge of this peak visible in the reconstruction.

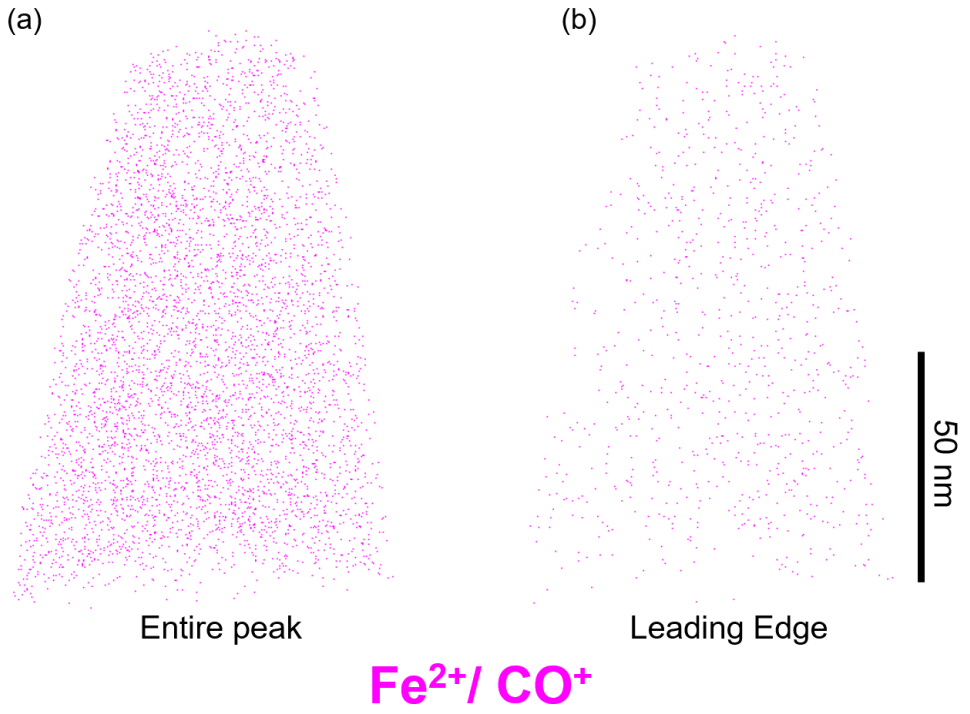


Figure 7.8: APT reconstruction of the 60% cold worked Zircaloy-4 sample, only the ions contributing to the 28 Da peak is shown. (a) Reconstruction where the entire peak is ranged. (b) Reconstruction where only the leading edge of the peak is ranged.

Figure 7.7 on first glance appears to have some segregation due to ions associated to the peak in question but this is due to the increased oxidation cause by the sample being electropolished (the 30% and 60% samples were also FIB sharpened post- electropolishing so would have less oxide on it). The occurrence of a micro-fracture of the needle during the atom probe experiment likely caused the feature seen in the reconstruction. The sudden decrease in voltage in Figure 7.9 indicates that a small fracture occurred, where the tip of the needle fractured but what remained was still analysable via APT. This fracture would have temporarily altered the shape of the specimen, increasing the amount of gas that would adsorb to the surface until the needle has had time to reform the hemispherical tip-apex shape present during the steady-state emission of ions. In the reconstruction, this is visible as the feature in Figure 7.7.

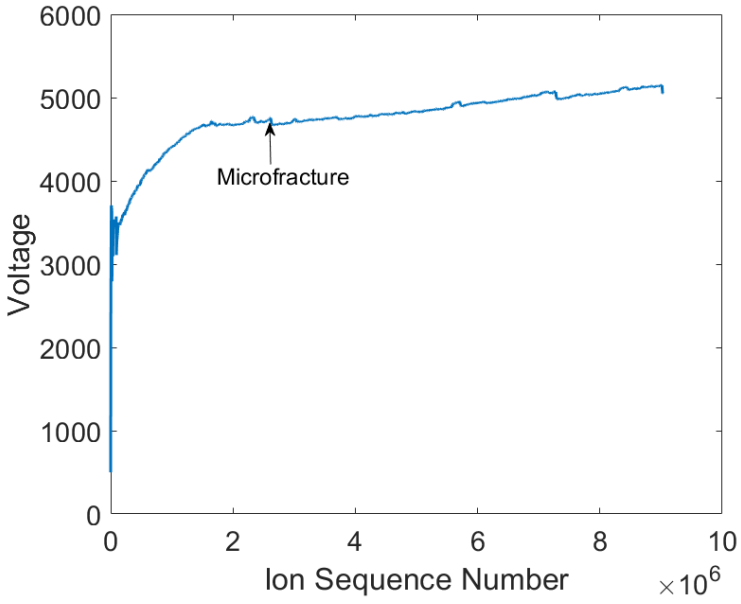


Figure 7.9: Voltage history of the 80% cold worked sample in Figure 7.7.

There are several possible reasons that may contribute to why these samples did not show any Fe segregation:

- The samples did not contain the quantities of Fe expected.
- The samples were not worked sufficiently so do not contain a sufficient number density of dislocations
- The samples do have dislocations in them but there is insufficient Fe segregating to the dislocations for it to be visible in the APT reconstruction (i.e. there are dislocations but we cannot see Fe at them).

Hence, to ensure that Fe is segregating to precipitates and interfaces as expected in the materials, site-specific lift-outs of samples containing grain boundaries and second phase particles (SPP) were prepared. Figures 7.10 and 7.11 are examples of these analyses. Figure 7.10 contains a SPP which was measured to contain 32.87 at.% Zr, 42.85 at.% Fe and 24.10 at.% Cr, implying that it is a laves phase of the $Zr(Fe_x,Cr_{1-x})_2$ type, where x=0.65. The associated mass spectrum shows Cr and Fe in the 2+ charge state.

Figure 7.11 contains a reconstruction containing a grain boundary and section of the mass spectrum where Fe^{2+} ions are seen. These two datasets demonstrate that in situations where there is sufficient Fe segregation, it is possible to visualise where Fe sits in the data; this means that it is potentially possible to look at the co-segregation of deuterium and Fe using APT.

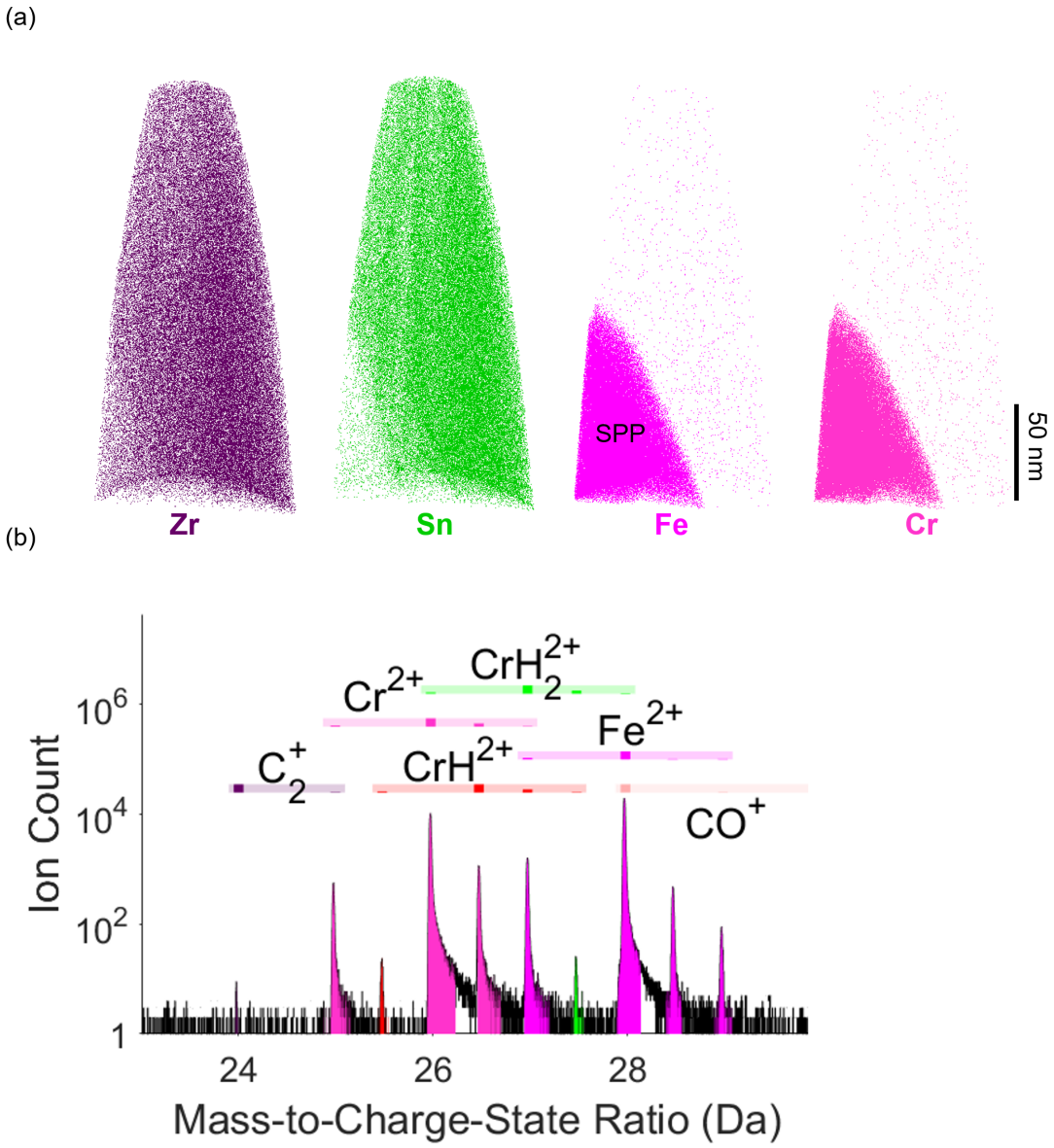


Figure 7.10: (a) Reconstruction of a needle containing part of a second phase particle (SPP). The SPP is Fe and Cr rich and a close up of their signals in the mass spectrum are shown in (b).

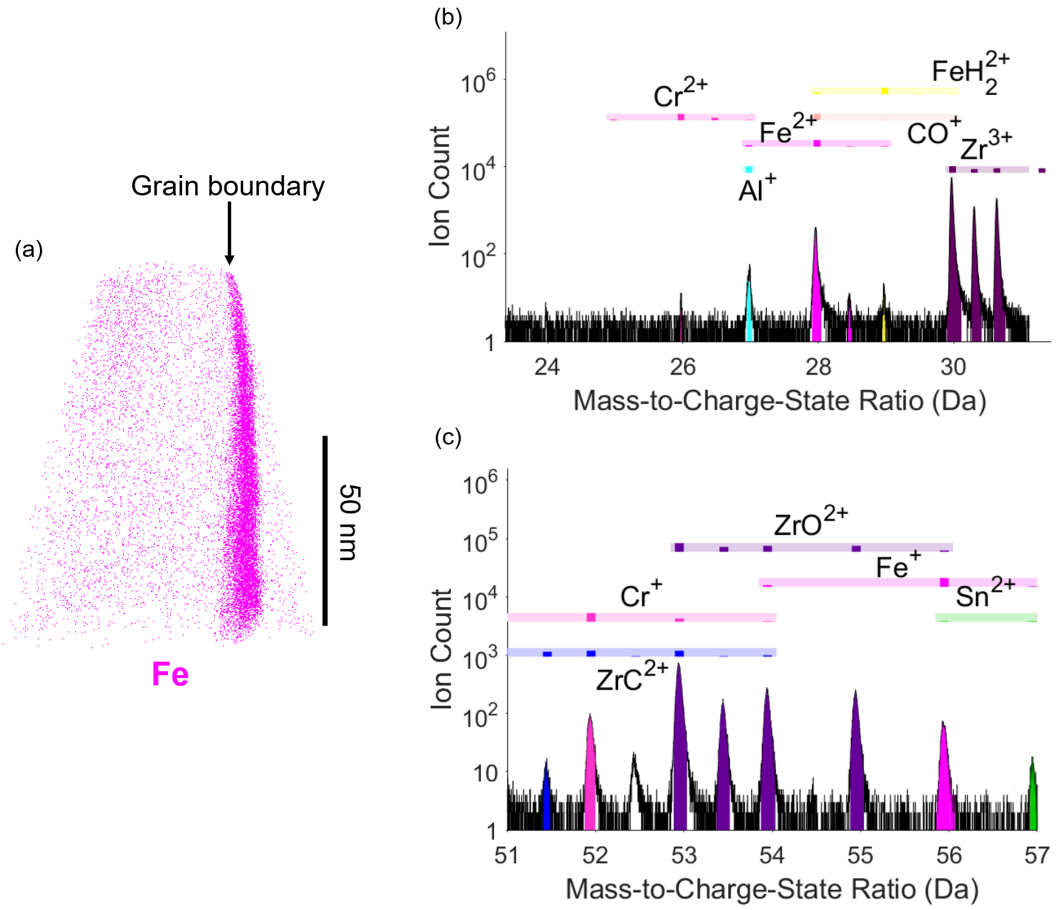


Figure 7.11: (a) APT reconstruction of a grain boundary in the as-received Zircaloy-4 sample. The location of the boundary is indicated by the location of the Fe ions. (b) and (c) are the sections of the mass spectrum where Fe is detected.

Transmission electron microscopy (TEM) was used to characterise the distribution of dislocations in the 30 and 80% cold worked samples to confirm their presence and to aid our understanding of why we are unable to see them in the APT data. Figure 7.12 contains micrographs of the dislocations in the sample. The red boxes are the approximate volume of an APT dataset, dislocations are encompassed by this box, regardless of where it is located. This indicates that the dislocation density is high enough such that an electropolished sample should contain some dislocations.

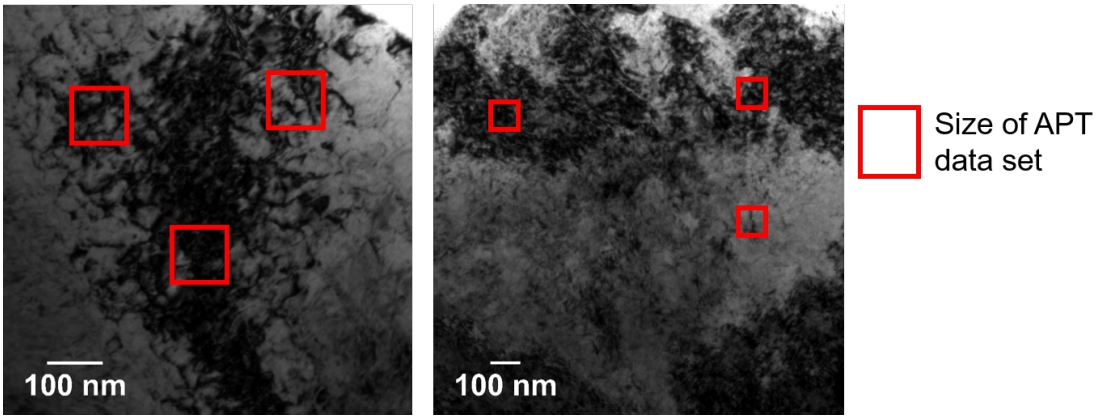


Figure 7.12: TEM micrographs of 30% cold worked Zr-4 samples. The red boxes are the approximate volume encompassed by an APT dataset. Images produced by D. Tweddle and Z. Shen

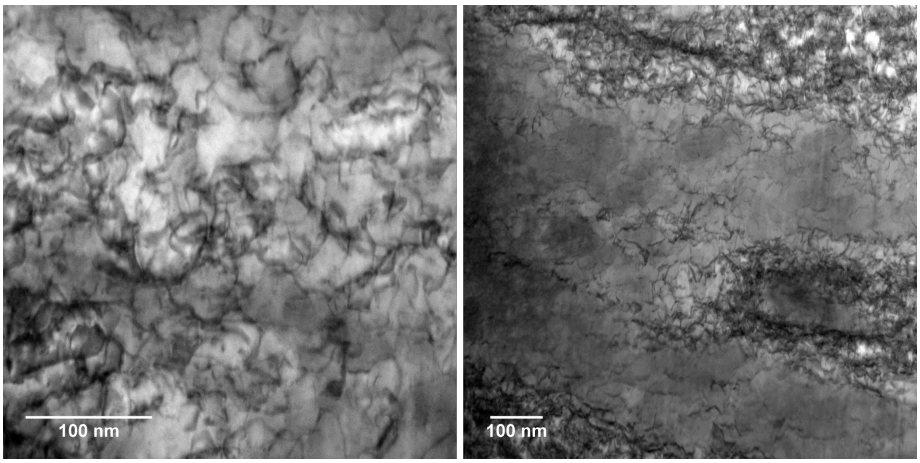


Figure 7.13: TEM micrographs of 80% cold worked Zr-4 samples. Images produced by J. Haley

The observations from the TEM data from the 80% cold worked samples agree with the 30% samples in that a randomly selected volume of the microstructure sampled by APT analysis we can expect to find a dislocation. This means that all of the datasets most likely have at least one dislocation in them and the fact they are not visible is likely due to a lack of Fe segregation. The TEM data proves that the volume of material analysed to produce the reconstructions shown, most likely did contain some length of dislocation line but there was insufficient Fe segregation for this to be visible.

The samples were subsequently annealed after the cold working to re-crystallise

the material. The conditions of the anneal were not provided by the National Nuclear Laboratory. However, it was confirmed by the company that there should have been sufficient time for the Fe to diffuse to the dislocations. Providing this is assertion is true, this means that we cannot see the Fe segregation in the samples because of the overlap of Fe and CO at the peak at 28 Da being compounded by the low levels of Fe present in the material. It is apparent that this peak mostly originates due to the detection of CO^+ and unless more Fe segregates to the dislocations or an approach to better extract the Fe data is developed, we will continue to struggle to see the Fe segregation to dislocations in these samples.

The little segregation is either a result of limited Fe in the matrix or 'too many dislocations' in each volume (i.e. the small amount of Fe is spread across too much area so the signal is not readily visible). To address this issue, a lower cold work level could be used as these samples would have a decreased dislocation density.

7.3 Conclusions

This chapter contains the work to characterise cold worked Zircaloy-4 samples. Figure 7.14 depicts the process of experimental work required to image hydrogen segregation to dislocations, the boxes in green are the work completed as part of this chapter. The remaining pieces of work (blue boxes) have been investigated in previous chapters.

In this work, it has been demonstrated that the cold work materials analysed here, Fe segregation to dislocations was not visible using APT. Fe levels in the matrix of Zircaloy-4 are low so there are few Fe ions to segregate to dislocations. Most Fe ions are detected as $^{56}Fe^{2+}$ which overlaps with CO^+ in the mass spectrum at 28 Da. The peak overlap issue is exacerbated by the small quantities of Fe in the Zr matrix. The TEM data provides evidence of dislocations and indicates that the dislocation densities in these samples were not suitable to image the Fe segregation that was desired.

As the dislocations are not visible in the APT data, we cannot use Fe segregation in these samples to show dislocations which would make it difficult to unambiguously confirm

in the deuterated samples that any deuterium segregation is due to dislocations. We also cannot be sure that we would have the same lack of segregation for the hydrogen (i.e. deuterium does segregate but the levels are not visible in APT). Therefore these cold worked levels are not suitable to be used to image hydrogen segregation to dislocations. Lower cold rolled samples should be used for future investigations (of less than 10%). Even though the results are inconclusive, the analyses undertaken in this study are helping to refine the experiments that would make the use of cold worked materials as a surrogate for irradiation viable.

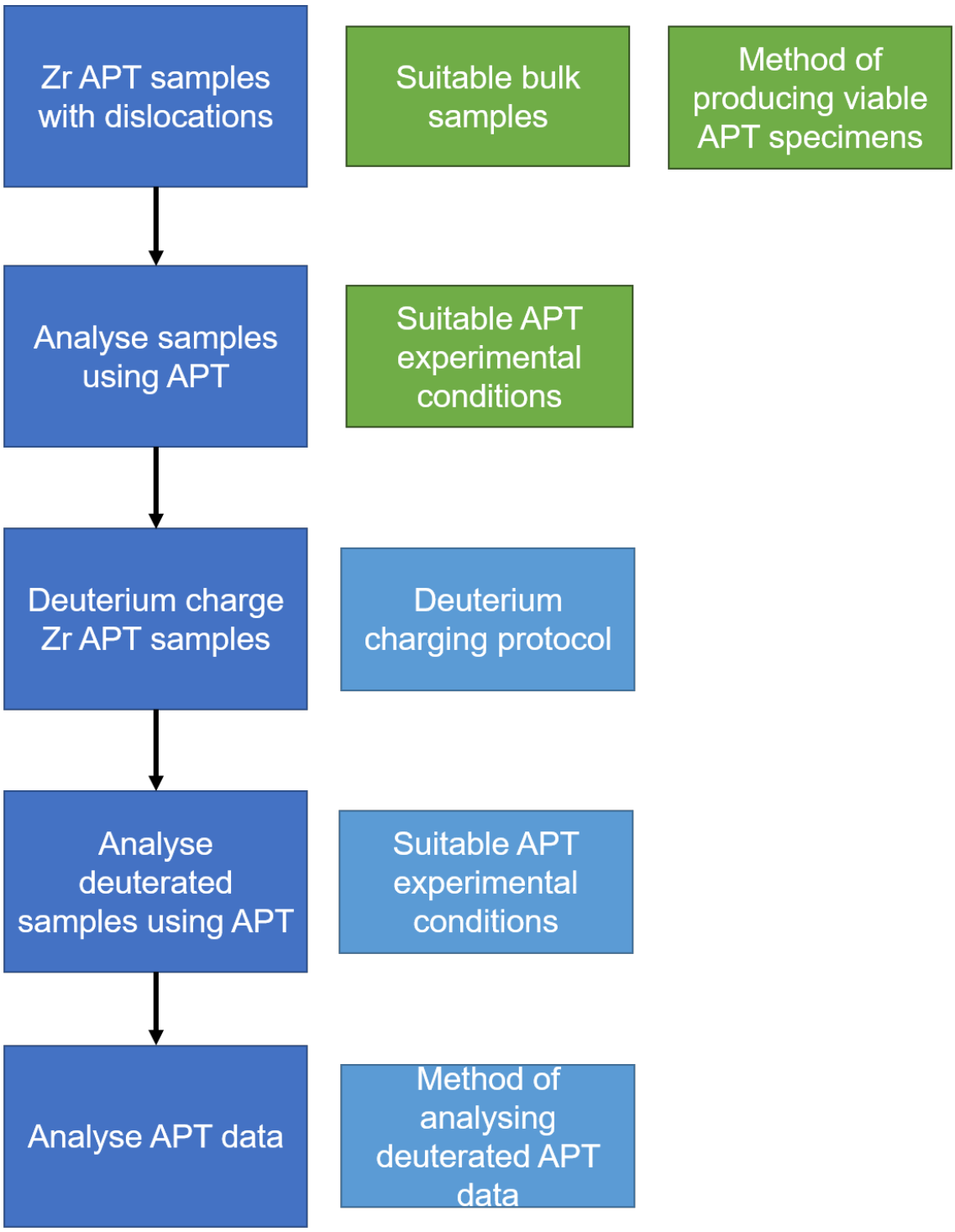


Figure 7.14: Flow chart of proposed method to image hydrogen segregation to dislocations using APT. The boxes green were covered in this chapter, and those in blue in other chapters.

Chapter 8

Atom Probe Tomography of Irradiated Zircaloy-2

8.1 Introduction

The work in the previous chapter investigates the viability of using a cold worked specimen as a surrogate for irradiation induced damage. The work demonstrated in the cases studied, the Fe segregation that was expected to indicate the presence of dislocations in the samples was insufficient to be used as evidence of dislocations. It was proposed that this was due to the very high number density of dislocations introduced by the levels of cold work and the limited amount of Fe available to decorate them. Also, cold work induces dislocation networks as opposed to dislocation loops which is likely to affect the trapping behaviour of hydrogen. As such, it is desirable to also look at neutron-irradiated materials which contain the defects which are known to manifest during service.

8.2 Experimental Methods

The aim of this work was to investigate the interaction of hydrogen with irradiation induced defects, namely dislocations, at the atomic scale in order to further our understand-

ing of hydrogen embrittlement in Zr-based alloys and to provide a potential framework for investigations in the behaviour of hydrogen under irradiation in other materials. Zircaloy-2 samples were neutron-irradiated in the BOR-60 sodium-cooled fission reactor and are being used for materials research in the MIDAS (**M**echanistic Understanding of **I**rradiation **D**amage in Fuel **As**semblies) Research Consortium. Due to the activity levels of these samples, sample preparation and handling had to be conducted at the National Nuclear Laboratory at Sellafield Site, which has dedicated equipment and expertise to prepare APT needles from such samples.

The experimental plan was to prepare APT needles from a paired deuterated and as-received neutron-irradiated Zircaloy-2 sample set. The as-received samples were prepared for the FIB/SEM by grinding the sample down to 2500 grit and then electropolished for 10 minutes using a 5 vol.% perchloric acid in acetic acid solution. The electropolishing was completed at 5°C by cooling the acidic solution using liquid nitrogen.

The deuterated samples were prepared using the same approach but were also deuterium-charged immediately following the electropolishing procedure. The deuterium charging method was based on the work of Breen et al. where they cathodically deuterium-charged the sample using 1.5 wt.% D_2SO_4 in D_2O using a current density of 2 kAm^{-2}, at 65 °C for 24 hours [116]. A subsequent anneal was performed on their samples for 5 hours at 450°C. However, in this work, deuterium charging was limited to four hours due to working constraints in the active area at Central Laboratory. This is expected to produce a thinner hydride rim at the surface of the samples, in comparison to that observed in Breen's work but was estimated that it should still be thick enough to be detectable via APT. The experimental set up for this is presented in Figure 8.1 (image taken at the University of Oxford due to the limited photography allowed on Sellafield Site). The glass vessel and Pt electrode (mesh 10 x 10 mm) were acquired from DEK Research Instrumentation, the deuterated sulphuric acid from Merck and heavy water from Armar Isotopes. The temperature was achieved and maintained throughout the charging using a hot plate. The tin foil shield was necessary to maintain a constant temperature in the vessel due to the

updraft of the fume hood. The temperature was monitored using a thermometer (Figure 8.1 (a)) at regular intervals to ensure the temperature was maintained. The hot plate kept the sample at a constant temperature (once the liquid reached the desired temperature), and tests were conducted using the same equipment with water in the vessel to check the stability of the temperature beforehand, which led to the use of the tin foil shield.

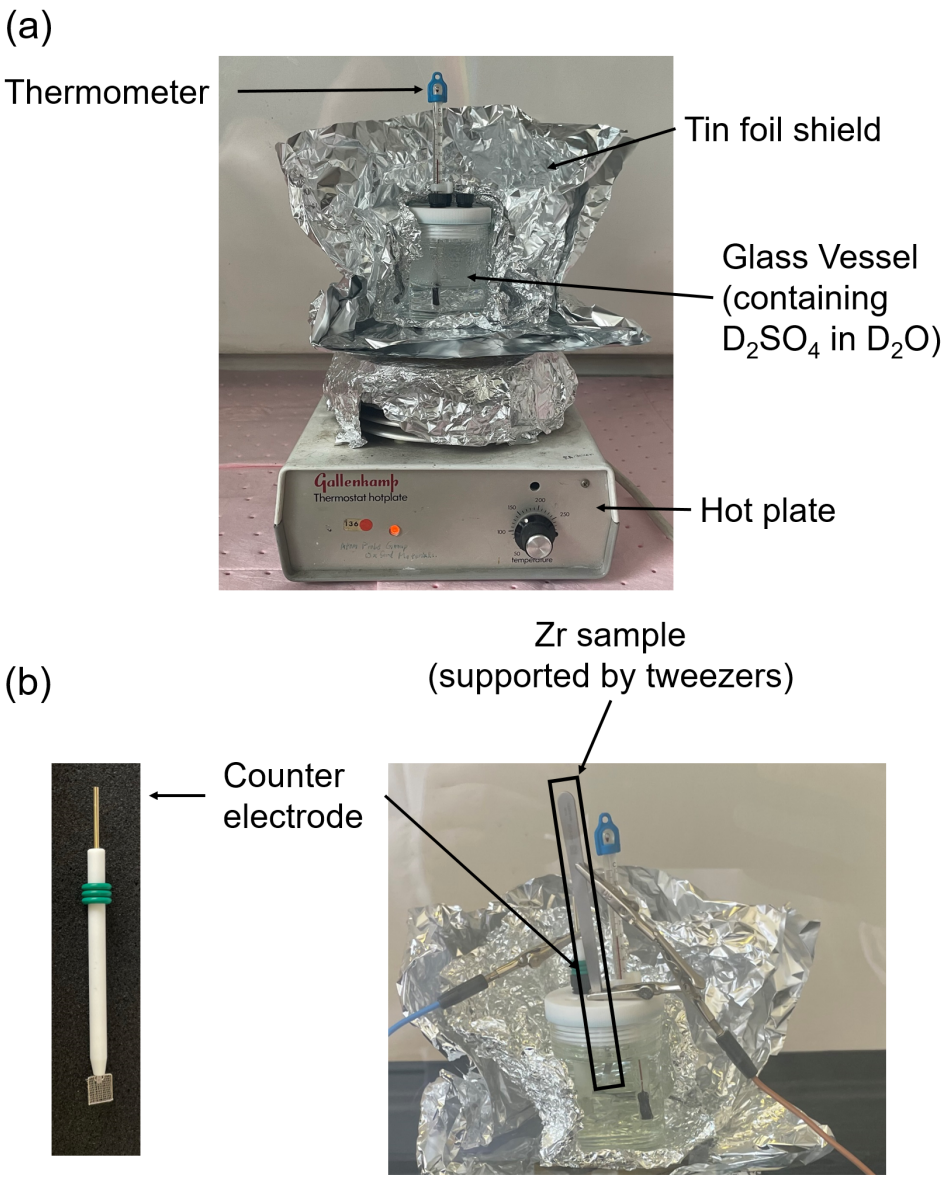


Figure 8.1: Electrolytic charging set-up used to deuterium charge the Zircaloy-2 samples using D_2SO_4 in D_2O. (a) Set up without the electrode, sample or electrical connections. (b) Vessel during a trial experiment where the sample is supported by a set of tweezers and a close up of the Pt counter electrode is seen.

In this study, the samples were not heat treated to re-distribute the deuterium because the temperature necessary to do this (after charging) would have likely also annealed out the irradiation induced dislocation loops that we wanted to have in our samples. Breen chose to do this to re-distribute the deuterium to form hydrides in the bulk [116]. An

approximation to Fick's first law can be used to estimate diffusion distances. We estimated that, using the conditions above, the deuterium would have diffused a sufficient distance into the sample to be analysed by APT. Deuterium would be expected to diffuse 1 μm in pure Zr and 55 nm in pure zirconia, using diffusion co-efficient as calculated from references [161] and [162]. The charged sample would be a thin layer of sub-stoichiometric oxide and Zircaloy-2 so the actual diffusion distance in the experiment would be between these two values, but closer to that of pure Zr. The sample was electropolished immediately before the charge to limit the formation of a ZrO_2 oxide. An APT dataset is unlikely to be longer than 500 nm in depth, so we would expect to see deuterium in the APT data without the need to heat treat and re-distribute the deuterium.

Once deuterium-charged, the sample was analysed via Secondary Ion Mass Spectrometry (SIMS) to guide selection of sites from which to extract APT specimen to maximise the chances of visualising deuterium/deuterides in this material. SIMS was acquired using a Tescan XEIA3 PFIB-SEM at ambient temperatures. The aim was to produce maps of the highest 2 Da :1 Da peak ratios (D^+: H^+) and use these to select regions for APT analysis.

APT samples were produced for analysis via the standard lift-out procedure but the samples were sharpened and polished at a temperature of -90°C. The samples were warmed to room temperature under vacuum to prevent condensation from forming on the needles, oxidising the samples. The samples were transferred to the atom probe at atmospheric pressure and ambient temperatures. Atom probe analyses were performed using a 50 pJ laser energy and 200 kHz pulse frequency and a temperature of 55K.

8.3 Results and Discussion

Prior to the analysis of deuterated material, it is necessary to characterise the as-received material to provide reference data. Figure 8.2 presents a typical APT dataset from the as-received irradiated Zircaloy-2 samples. It is evident that there are Fe and Cr containing clusters, but not all of the clusters are Cr rich. The ordered clustering of Fe and Cr on parallel planes or 'corduroy bands' can be seen also; which is in agreement

with previous work [30], [107], [163] on similar materials. Sn is anti-correlated to the Fe rich bands. The banding of clusters is caused by the aligning of the <a> dislocation loops formed as a result of the neutron bombardment these sample underwent [30], [104].

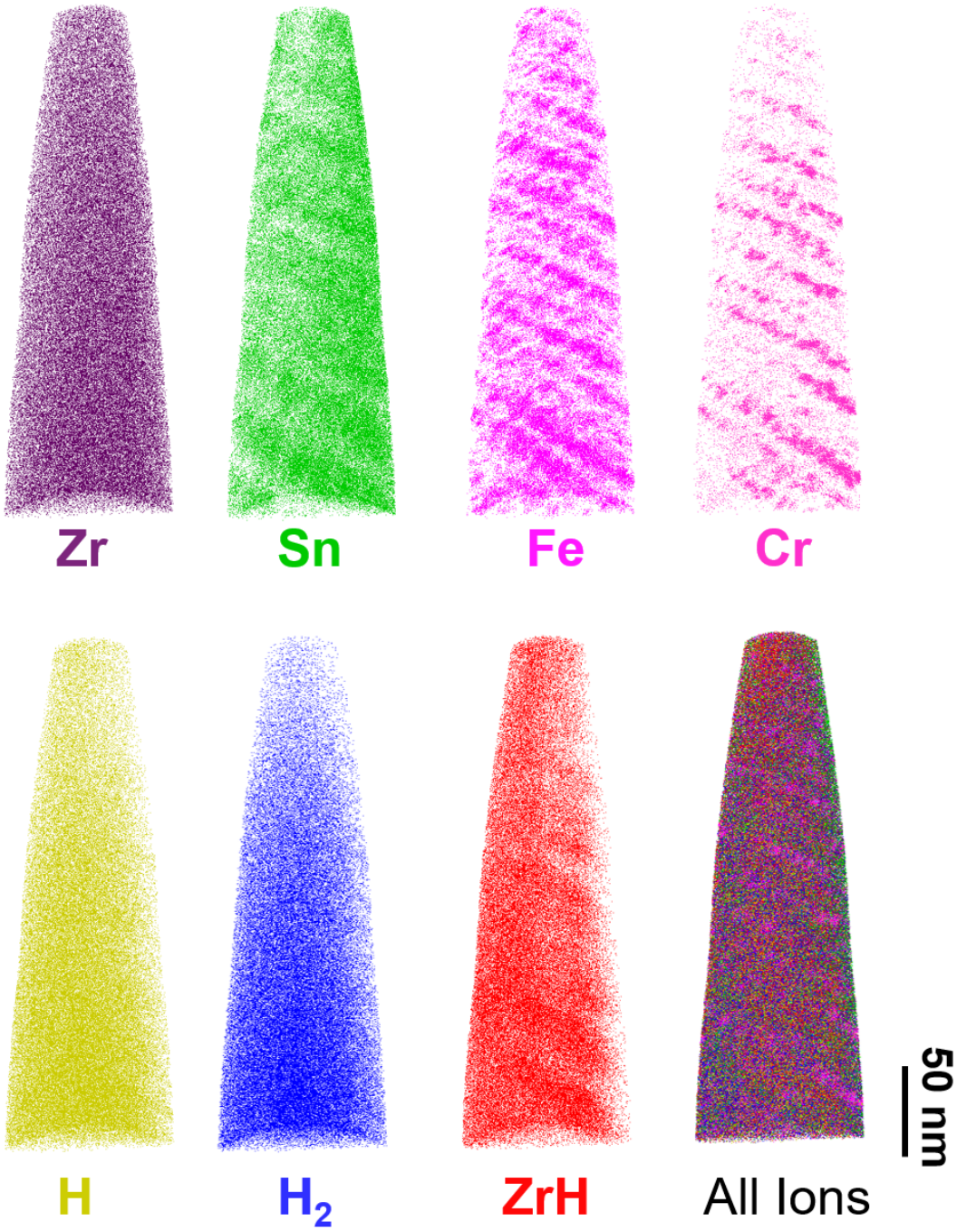


Figure 8.2: APT reconstructions of an as-received neutron-irradiated Zircaloy-2 sample.

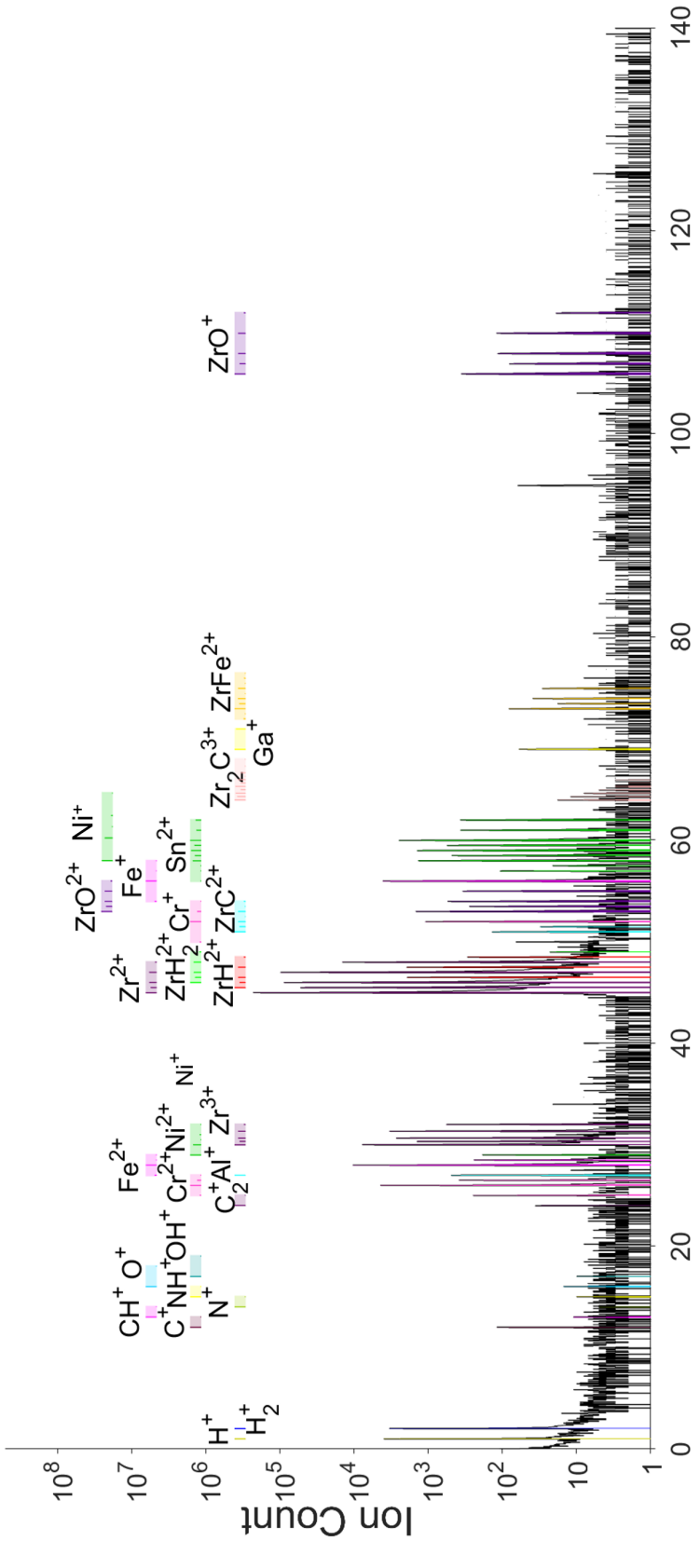


Figure 8.3: APT mass spectrum of an as-received neutron-irradiated Zircaloy-2 sample. The coloured bars indicate the ranges at which the labelled ions occur and the relative heights of the darker bars, the relative isotopic abundances of the ions.

Figure 8.3 presents a mass spectrum from the Zircaloy-2 sample. There are peaks which indicate the presence of the alloying elements of Zircaloy-2: Sn, Fe, Cr and Ni. The distribution of Ni is not shown in the reconstructions in the Figure 8.2 as it is contained in overlaps with Zr^{3+}, Fe^{2+} and Sn^{2+} where it is the minority ionic species and so determining its spatial distribution is non trivial. It is situations such as these where it would be necessary for the application of local peak overlap solving methods, as discussed in Section 6.3.2. These reconstructions contained significant amounts of the ZrH_2^{2+} ions which will need to be carefully considered when analysing and interpreting the data of the deuterated material, as they overlap in the mass spectrum with ZrD^{2+} ions.

To calculate the composition of the sample, it was necessary to divide the APT reconstruction into the clusters and remaining Zr matrix. The clusters were isolated and extracted for analysis by using a 1 at.% Fe isoconcentration surface (bound surface where the concentration is greater than or equal to 1 at.%, Figure 8.4). Once extracted, the elemental concentration of the clusters and the matrix was calculated using the peak overlap solving methods described previously (Section 3.2.2) and are presented in Table 8.1.

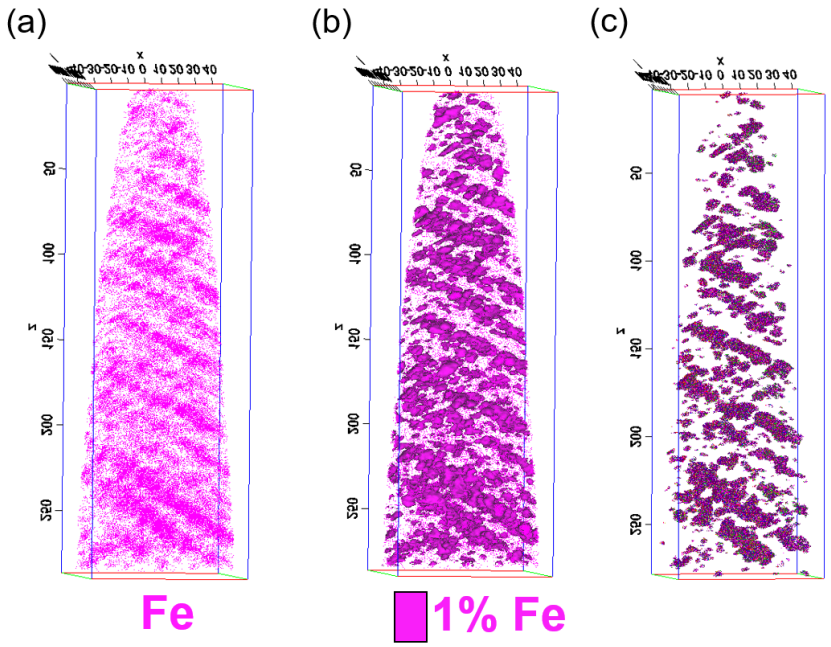


Figure 8.4: (a) Fe ions in an APT reconstruction of the as-received Zircaloy 2 sample. (b) 1% Fe isoconcentration surface used to identify clusters. (c) Clusters extracted from the APT reconstruction using the iso-surface in (b). The units of the scales on the reconstruction are in nm.

Table 8.1: APT composition of the matrix and clusters in the four as-received Zircaloy-2 samples. The error given is the standard error (2σ).

	Composition (at.%)	
	Clusters	Matrix
Zr	90.48 ±1.67	93.36 ± 0.86
H	3.90 ± 1.09	4.67 ± 0.86
O	0.71 ± 0.17	0.64 ± 0.04
Cr	0.71 ± 0.69	0.06 ± 0.05
Fe	2.59 ± 0.27	0.11 ± 0.14
Ni	0.03 ± 0.05	0.02 ± 0.05
Sn	1.40 ± 0.16	1.03 ± 0.09
C	0.18 ± 0.16	0.06 ± 0.03

The clusters are seen to be Fe rich, incorporating 2.59 at.% Fe on average, and also contain higher levels of Sn. Some of the clusters contain Cr and Ni but not all of them which has led to the high error associated with the Ni and Cr compositions. This effect is even directly observable upon visual inspection of the reconstructions and has previously been shown to occur in similar alloys [105].

In summary, the as-received Zircaloy-2 APT data contains Fe and Sn rich clusters, with varying different amounts of Cr and Ni. These clusters are seen to exhibit the 'corduroy banding' caused by the aligning of dislocation loops. Deuterium charging should not alter the clustering in the alloy so it is anticipated that the results from the deuterated material should reflect this.

After deuterium charging had been completed, Secondary Ion Mass Spectrometry (SIMS) analysis was performed (on the deuterated samples) with the aim of providing complementary data that could show regions of high deuterium and increase the chances of a successful experiment where we analyse a deuterium rich region via APT. This data is given in Figure 8.5. The data contains the peaks that would be expected for Zr (highlighted by the box) and the alloying elements. However, we did not detect any counts at 2 Da which indicates that there is no, or very little, deuterium present in the volume of material analysed. The decision was made to produce APT needles from the sample regardless because we expect the deuterium distribution to be inhomogeneous so it is feasible that we did not analyse a region containing deuterium with the SIMS. Due to time constraints for access to the NNL facility, only a finite number of regions of sample could be probed. Unfortunately this will also mean that we could feasibly not detect any deuterium in the APT data for the same region.

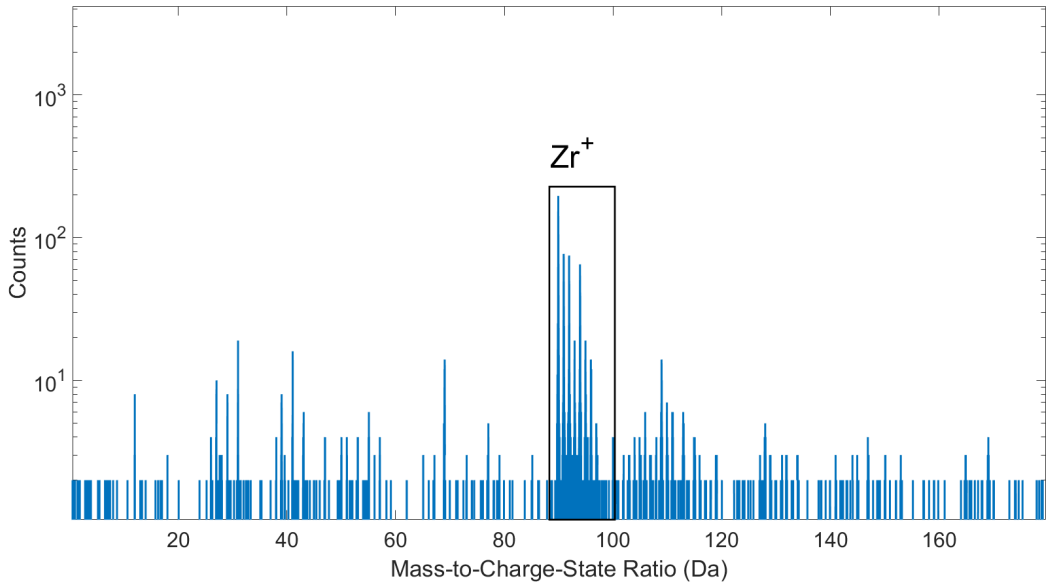


Figure 8.5: SIMS mass spectrum of a deuterium-charged neutron-irradiated Zircaloy-2 sample.

In total 5 APT samples were produced of the deuterated material and were successfully analysed. This, itself, is a significant result as it shows the validity of the experimental approach and that it is possible to reliably produce APT data from samples prepared in this manner. The samples were analysed under the same APT experimental conditions as the as-received materials.

The APT reconstructions of the deuterated material also contain Fe rich clusters, as presented in Figure 8.6. This is unsurprising as the complementary as-received material contains these clusters and this demonstrates that the deuterium charging does not affect the irradiation induced nanostructural changes. This is important for future experimental planning because it demonstrates the validity of the methods used and that this approach can be used in future work as we have shown that deuterium charging will not affect the nanostructure of the material.

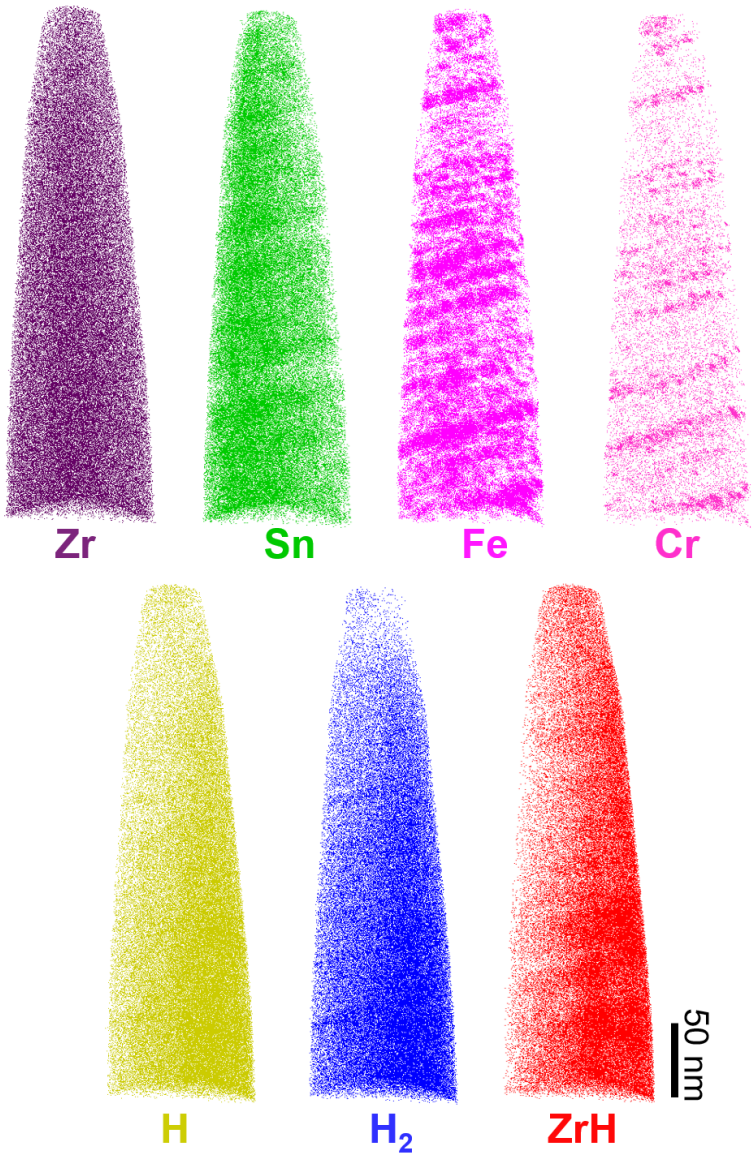


Figure 8.6: APT reconstruction of a deuterium-charged, neutron-irradiated Zircaloy-2 sample.

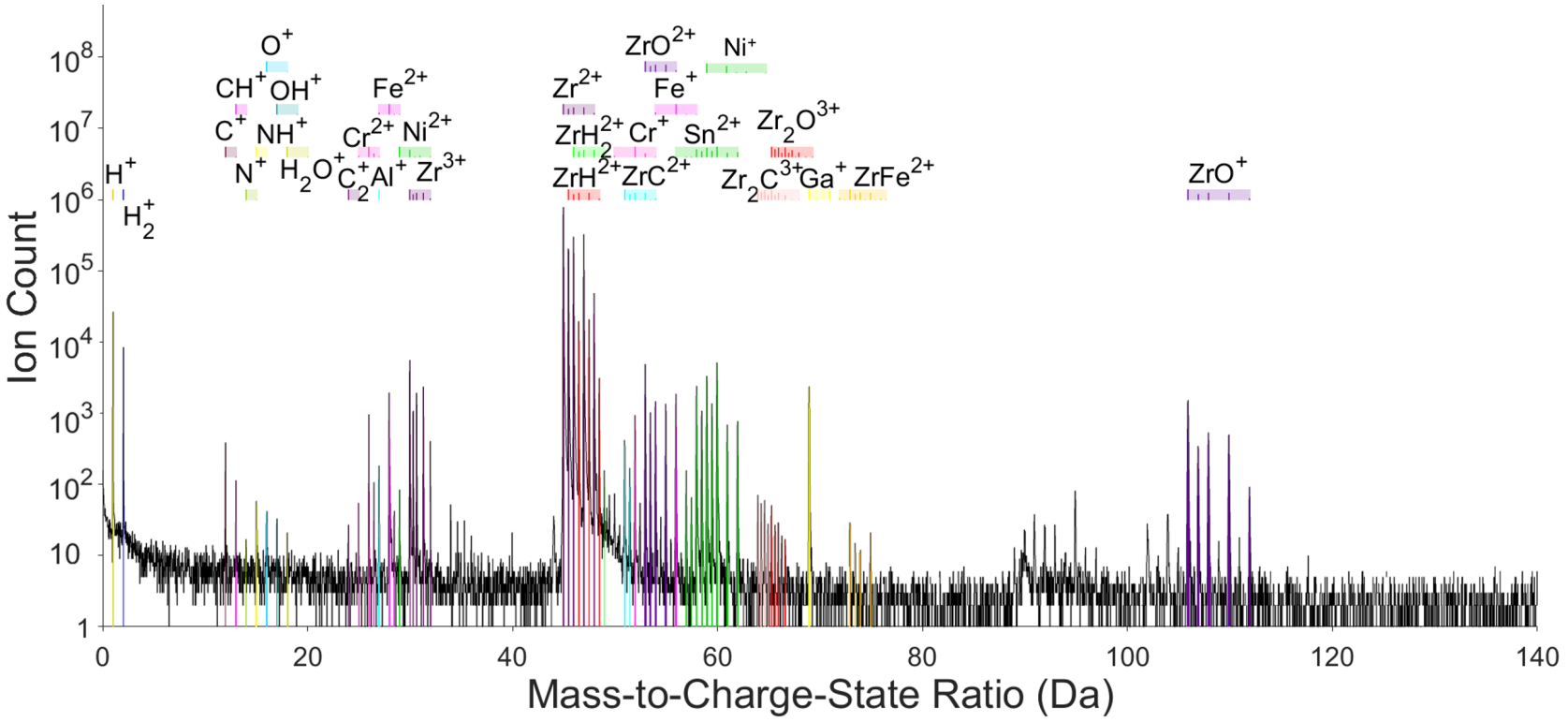


Figure 8.7: APT mass spectrum of a deuterium-charged, neutron-irradiated Zircaloy-2 sample. The coloured bars indicate the ranges at which the labelled ions occur and the relative heights of the darker bars, the relative isotopic abundances of the ions.

Figure 8.7 presents the mass spectrum of the entire APT dataset, upon first glance it is not significantly different to that of the as-received material. As anticipated, peaks corresponding to the alloying elements in Zircaloy-2 are present. Most of the deuterium in a deuterated sample, is expected to exist in the peaks at 2 and 4 Da as atomic and molecular deuterium, at 3 Da in the DH^+ ion and some will exist as ZrD type ions. The peak at 2 Da contains an overlap with molecular hydrogen, and in a deuterated sample it is possible for the peak at 2 Da to be larger than that at 1 Da due to the added deuterium (Section 6.3.1). The hydrogen peaks from 1-4 Da for the same dataset are shown in Figure 8.8 and it is evident that there are no peaks at 3 and 4 Da, and the peak at 2 Da is smaller than that at 1 Da. The fact the peaks which are expected to contain most of the detected deuterium are not present, or are not at the correct ratio for this to occur indicates that it is unlikely that deuterium was detected in the APT data. However, most of the deuterium that would be present in a reconstruction would be expected to be in the peak at 2 Da, so the final part of the data analysis was to analyse the ratio of the counts in the peaks at 1 and 2 Da to see if it is likely that there is any deuterium in the peak at 2 Da.

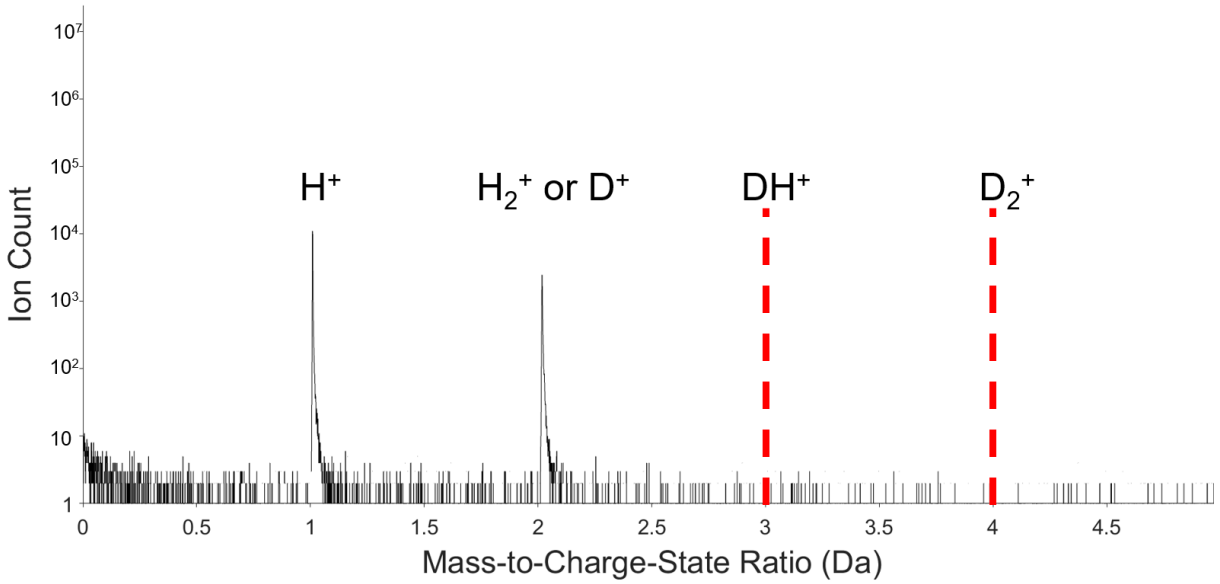


Figure 8.8: Hydrogen peaks of an APT mass spectrum of a deuterium-charged, neutron-irradiated Zircaloy-2 sample. The red dashed lines indicate where the deuterium peaks would be expected.

As discussed in Chapter 6, the ratio of the counts in the peaks at 1 and 2 Da can be used to estimate the proportion of the peak at 2 Da which is deuterium. This method can also be used to give evidence of deuteration having occurred by comparing the H_2^+: H^+ ratio of as-received and deuterated samples. The work in Chapter 6 shows that we would expect inter- and intra- sample variation and that this ratio varies from 0.11-0.71 for as-received Zr alloy samples (Zircaloy-4, Zr-0.2Nb, Zr-0.8Nb and Zr-2.5Nb). As a final check of the success of the deuterium charging, the H_2^+: H^+ ratio was calculated for the clusters and matrix of the as-received and deuterated samples, respectively (Table 8.2).

These ratios provide us with a number of observations, firstly the ratios for the as-received material are within the bounds that we would expect for this material. There is no significant difference between the ratio from the clusters and the matrix, meaning that a difference between these in the deuterated data could indicate the presence of deuterium in the data. Examining the ratios of the deuterated data, it is evident that there is no significant difference between the ratios of the cluster and the matrix, or between the as-received and deuterated material. Unfortunately, this means we were unlikely to have deuterium present in our APT data. Interestingly, there is increased spread of the ratios for the deuterated material vs the as-received material. None of the ratios for the deuterated material were outside of the bounds of 0.11 and 0.71, and only one of the as-received samples was, where the H_2^+: H ratio was 0.89.

Table 8.2: H_2^+: H ratio of the as-received and deuterated Zircaloy-2 APT data. The error given is the standard error (2σ).

	As-Received	Deuterated
Clusters	0.65 ± 0.30	0.58 ± 0.47
Matrix	0.54 ± 0.34	0.49 ± 0.39

The calculated compositions listed in Table 8.3 have assumed that there is no deuterium in the sample and no deuterium containing ions have been included in this analysis. As with the as-received material, the clusters are Fe and Sn rich and some contain Cr and Ni. The results for both the as-received and deuterium-charged materials

are similar which indicates that there was no deuterium in the APT data from the deuterated samples. This does not necessarily mean that there is no deuterium in the bulk sample because we could have produced APT samples from a region in which there was no deuterium, producing samples that do not provide any evidence of deuterium.

Table 8.3: APT composition of the matrix and clusters in the deuterium-charged Zircaloy-2 samples. The error given is the standard error (2σ).

	Composition (at.%)	
	Clusters	Matrix
Zr	88.24 ± 5.27	90.60 ± 6.95
H	6.45 ± 5.75	7.45 ± 7.04
O	0.71 ± 0.17	0.68 ± 0.12
Cr	0.40 ± 0.36	0.05 ± 0.03
Fe	2.52 ± 0.37	0.14 ± 0.00
Ni	0.03 ± 0.04	0.01 ± 0.06
Sn	1.52 ± 0.37	1.00 ± 0.20
C	0.17 ± 0.17	0.07 ± 0.03

Table 8.4 presents the average composition of the as-received and deuterated Zircaloy-2 samples. It can be noted that whilst the compositions between the two different samples are not similar, the deuterated materials on average have a higher concentration of hydrogen in both the matrix and the clusters. The deuterated samples followed the same pattern of there being more hydrogen in the matrix than the clusters and there is a greater variation in the results. The increase in hydrogen in these samples is similar to that observed in the deuterated Zircaloy-4 samples in Chapter 5. The likely causes of this increase in hydrogen concentration is as a consequence of the sample production. Other than the deuterium charging procedure, both the as-received and deuterated samples underwent the same processing indicating that the difference is a result of the deuterium charging process, for instance the deuterium being replaced by protium (^{1}H) during the

FIB lift-out procedure.

Table 8.4: APT composition of the matrix and clusters in the as-received and deuterium-charged Zircaloy-2 samples. The error given is the standard error (2σ). This table is an accumulation of Tables 8.1 and 8.3 for ease of comparison.

	Composition (at.%)			
	As-received		Deuterated	
Element	Clusters	Matrix	Clusters	Matrix
Zr	90.48 ± 1.67	93.36 ± 0.86	88.24 ± 5.27	90.60 ± 6.95
H	3.90 ± 1.09	4.67 ± 0.86	6.45 ± 5.75	7.45 ± 7.04
O	0.71 ± 0.17	0.64 ± 0.04	0.71 ± 0.17	0.68 ± 0.12
Cr	0.71 ± 0.69	0.06 ± 0.05	0.40 ± 0.36	0.05 ± 0.03
Fe	2.59 ± 0.27	0.11 ± 0.14	2.52 ± 0.37	0.14 ± 0.00
Ni	0.03 ± 0.05	0.02 ± 0.05	0.03 ± 0.04	0.01 ± 0.06
Sn	1.40 ± 0.16	1.03 ± 0.09	1.52 ± 0.37	1.00 ± 0.20
C	0.18 ± 0.16	0.06 ± 0.03	0.17 ± 0.17	0.07 ± 0.03

8.4 Conclusions

This chapter focused on using the knowledge learnt throughout this PhD project to analyse deuterium-charged, neutron-irradiated Zircaloy-2 samples. It has been demonstrated that the deuteration procedure did not alter the corduroy banding and clustering caused by neutron irradiation. A viable workflow for deuterium charging and preparing APT needles from neutron-irradiated samples has also been shown.

The ability to reliably generate APT data after the deuterium charging protocol developed in this work shows that the experimental method was viable and that future experiments with different charging conditions are a valid avenue for research. In order to improve results, deuterium charging for a longer period of time would increase the hydride rim thickness and the amount of deuterium in the sample. Figure 8.5 does not

contain a significant amount of counts because the SIMS scan was not run for long due to time constraints. It would be beneficial in future work to charge the sample for a longer period of time and to devote more time to try and detect deuterium, because of the small concentrations of deuterium likely to be present in the sample matrix. Adaptations such as these may lead to the deuterated data needed to be able to image hydrogen at the atomic scale in Zr alloys.

Chapter 9

Conclusions and Future Work

The work completed in this thesis aimed at developing methods for the atom probe tomography analysis of deuterated zirconium alloys with a view to enhancing our understanding of hydrogen embrittlement of nuclear fuel cladding. This project was approached from multiple angles, Chapters 4 and 5 look at different methods of producing a deuterated sample by using gaseous deuterium charging pre-prepared APT samples, and focused ion beam lift-out from a deuterated bulk sample. Chapter 6 optimises the post-processing of Zr alloy APT data to get the most accurate compositions from the data collected. A method to more accurately quantify deuterium concentrations is developed. Chapter 7 contains the atom probe analysis of cold worked Zircaloy-4 samples which were used as a surrogate for irradiated materials to investigate hydrogen trapping behaviour of dislocations. The final chapter investigates the hydrogen trapping to irradiation induced defects through the atom probe tomography analysis of deuterated, neutron-irradiated Zircaloy-2 samples.

9.1 Conclusions

9.1.1 Developing Deuterium Charging Protocols

The work into the development of deuterium charging protocols demonstrated that the gas reaction cell could be used to put deuterium onto the surface of a sample, however

issues with sample oxidation prevented the ingress of the deuterium into the metal region of the samples. The lessons learnt can be found in the list below:

- Zr alloy APT needles will oxidise readily, even under high vacuum conditions; this includes during storage in the atom probe and transfer to the reaction cell using the vacuum cryo-transfer module (VCTM).
- Deuterium gas produced by the hydrogen generator is not pure and should be filtered to remove components that may cause the oxidation of Zr samples.
- A 3 hour deuterium charge was sufficient for deuterium to diffuse into the oxide on the sample but not into the metal region. This demonstrates that the gas reaction cell could be used to deuterium charge further samples.
- The Zr wire samples underwent some change during the deuterium charge which led to the change in charge state of Zr where more Zr^{3+} was detected than Zr^{2+}. This change in detected charge state ratio implies an increase in the field required for evaporation (Zr^{3+} has a higher evaporation field than Zr^{2+}). Changes in the evaporation field imply changes in atomic bonding.

9.1.2 Cryogenic Focused Ion Beam Sample Preparation

The use of cryogenic focused ion beam methods were investigated in this chapter to decrease hydrogen pick up during sample production. The conclusions are as follows:

- Peforming APT needle sharpening and polishing at cryogenic temperatures produces viable APT specimens.
- Sample preparation method reduces the hydrogen detected in the Zircaloy-4 APT data.
- Deuterium containing samples were successfully produced but did contain a higher hydrogen concentration than anticipated.

9.1.3 Improving the Data Analysis of Deuterated Zr Alloy APT Data

Optimising the data analysis of a deuterated Zr sample involves finding the optimal methods of solving the peak overlaps in the mass spectrum, reconstructing the data and handling the ions contained in peak overlaps in the reconstruction. This chapter focused on the first and the final of these and the conclusions are below:

- The importance of understanding how the different data analysis tools are handling the data has been demonstrated by the fact that two different softwares could produce two different trends in the Nb concentration with laser energy, when the same data was inputted into both.
- Peak tail overlaps are not accurately being accounted for during peak counting processes by IVAS and AtomProbeLab. The mishandling of the data led to inaccurate Nb concentrations which resulted in the different trends shown in Figure 6.2.
- Using IVAS and AtomProbeLab, the most accurate method for solving the peak overlaps in Zr alloy samples is to use IVAS to quantify the counts and AtomProbeLab's Maximum Likelihood Estimation algorithm to solve the overlaps and calculate a composition.
- Analyses of a previously published Zr/ Zr-deuteride boundary have been improved upon by quantifying the deuterium concentration in a concentration line profile across the boundary (within given bounds)
- A method to solve peak overlaps on a local scale, to handle situations where we would like to analyse the location of ions contained in a peak overlap, were investigated. The method used introduced clusters into the data, as a result of the algorithm used and was not used for any further analysis as a result.

9.1.4 Atom Probe Tomography of Cold Worked Zircaloy-4

This chapter contains the work to characterise cold worked Zircaloy-4 samples via APT to use as a surrogate to irradiated samples. The aim was to analyse the Fe distribution in the samples to find evidence of dislocations and enable future work where these samples would be deuterium charged to investigate the interaction of hydrogen with dislocations by looking at the co-segregation of Fe and D.

The conclusion from this work was that the cold worked samples used in this study are not an adequate surrogate for irradiated materials as no Fe segregation to dislocations was visible in the APT data from the cold worked materials.

This has been found to be due to:

- Insufficient iron in the matrix of the Zircaloy-4 samples for any segregation to be visible.
- The small quantities of Fe meant that the Fe signal could not be discerned due to a CO^+ peak overlap at 28 Da.
- Dislocation density of the samples was not conducive to their being sufficient Fe to decorate the dislocations for it to be visible in the APT data, despite TEM data providing evidence of dislocations in the bulk samples.

9.1.5 Atom Probe Tomography of Irradiated Zircaloy-2

This chapter focused on using the knowledge learnt throughout this PhD project to analyse deuterium-charged, neutron-irradiated Zircaloy-2 samples. In conclusion, this work demonstrated that:

- The experimental protocol of electropolishing, deuterium charging, followed by a focused ion beam lift-out where the samples were sharpened at cryogenic temperatures was able to produce viable APT specimens from a deuterium charged, neutron-irradiated specimen.

- Performing the deuteration did not alter the clustering that was present after irradiation, demonstrating that the developed experimental method does not alter the material and can be safely used for future experimental work.

9.2 Future Work

- The successful deuterium uptake by the oxide of the Zircaloy-4 samples and mass spectrum changes of the data from the pure Zr wire indicate that the gas reaction cell is charging the samples with deuterium. Further work using the gas reaction cell to deuterium charge should be conducted using the Zr wire (to maximise deuterium uptake). Different APT analysis conditions should be used to maximise sample yield, such as a higher analysis temperature and a laser pulse energy to reduce the mechanical stresses on the sample during APT analysis and therefore reduce the likelihood of sample fracture. It would be of benefit to use a pure deuterium gas bottle or to establish the composition of the gas produced by the hydrogen generator to remove the deuterium gas as a source of oxidation. Methods to decreased the oxidation occurred during the transfer would also be beneficial such as increasing the time the dock for the VCTM is pumped down for on the LEAP and reaction cell to remove contaminants prior to the gas in these chambers coming into contact with the specimen.

- Performing the final stages of APT sample preparation at cryogenic temperatures reduced the amount of hydrogen detected in the APT samples. Although possible, it is very difficult to perform the entire lift-out procedure at cryogenic temperatures. To investigate if it would be possible to reduce the hydrogen detected in the APT data further, all of the milling should be conducted at cryogenic temperatures (i.e. producing the cantilever and performing the sharpening and polishing all under cryogenic conditions).

- Chapter 6 demonstrated the importance of accurately extracting counts from the mass

spectrum and that counts in peak tail overlaps are not accurately being accounted for. Separating the signals from the peaks involved in the tail overlap can be done by mathematically, by deconvoluting the signals. Processes of peak fitting have been attempted but due to the complex nature of this issue (e.g. [154], [155]) were not the universal solution the APT community needs and this area would benefit from additional work to produce a method of peak fitting that is easy to use and applicable to a wide range of materials.

- Chapters 6, 7 and 8 contain examples of APT data where it would be beneficial to be able to isolate the location of ions in the reconstruction that are detected in peak overlaps. Zr alloys are not the only materials system where peak overlaps occur and a method for peak overlap analysis on a local scale, that does not introduce clusters into the data would be useful for investigations of Zr and other alloy systems.

- Future work to investigate the interaction of hydrogen with dislocations via APT should be completed using samples of a low cold worked level (<10%) as these may act as a better surrogate for irradiated materials.

- Work by Hu et al. demonstrates that deuterium can be detected via in Zr-Nb alloys after exposure in an autoclave containing heavy water [164]. Studies of ex-service materials from heavy water reactors should be characterised via APT to investigate the interaction of hydrogen with irradiation induced defects using the data analysis techniques developed in this thesis.

Bibliography

[1] *Basics of Nuclear Fission | Definitions | nuclear-power.com*. [Online]. Available: https://www.nuclear-power.com/nuclear-power/fission/basics-of-nuclear-fission/ (visited on 11/12/2022).

[2] C. R. F. Azevedo, *Selection of fuel cladding material for nuclear fission reactors*, Dec. 2011. DOI: 10.1016/j.engfailanal.2011.06.010. [Online]. Available: https://www.sciencedirect.com/science/article/abs/pii/S1350630711001531.

[3] P. D. Wilson, *The nuclear fuel cycle : from ore to wastes*. Oxford University Press, 1996, p. 323, ISBN: 0198565402. [Online]. Available: https://www.mendeley.com/research-papers/nuclear-fuel-cycle-ore-wastes/?utm%7B%5C_%7Dsource=desktop%7B%5C&%7Dutm%7B%5C_%7Dmedium=1.17.11%7B%5C&%7Dutm%7B%5C_%7Dcampaign=open%7B%5C_%7Dcatalog%7B%5C&%7DuserDocumentId=%7B%5C%%7D7B5ca1331d-df04-4dd0-be2c-a276c9af66f5%7B%5C%%7D7D.

[4] World Nuclear Association, *Nuclear Fusion : WNA - World Nuclear Association*, 2016. [Online]. Available: http://www.world-nuclear.org/information-library/nuclear-fuel-cycle/conversion-enrichment-and-fabrication/fuel-fabrication.aspx%20http://www.world-nuclear.org/information-library/current-and-future-generation/nuclear-fusion-power.aspx (visited on 12/21/2017).

[5] FEMA Emergency Management Institute, *Fuel Rods*. [Online]. Available: https://emilms.fema.gov/IS3/FEMA%7B%5C_%7DIS/is03/REM0404050.htm (visited on 05/15/2018).

[6] D. O. Northwood, "The development and applications of zirconium alloys," *Materials and Design*, vol. 6, no. 2, pp. 58–70, 1985, ISSN: 02613069. DOI: 10.1016/0261-3069(85)90165-7.

[7] S. Banerjee, "Nuclear Applications: Zirconium Alloys," *Encyclopedia of Materials: Science and Technology (Second Edition)*, pp. 6287–6299, 2001. DOI: http://dx.doi.org/10.1016/B0-08-043152-6/01117-7. [Online]. Available: http://www.sciencedirect.com/science/article/pii/B0080431526011177%7B%5C%%7D5Cnhttp://ac.els-cdn.

[8] World Nuclear Association, *The Nuclear Fuel Cycle*, 2017. [Online]. Available: http://www.world-nuclear.org/information-library/nuclear-fuel-cycle/introduction/nuclear-fuel-cycle-overview.aspx (visited on 05/23/2019).

[9] ——, "Nuclear-Powered Ships," 2023. [Online]. Available: http://www.world-nuclear.org/information-library/non-power-nuclear-applications/transport/nuclear-powered-ships.aspx.

[10] A. T. Motta, A. Couet, and R. J. Comstock, "Corrosion of Zirconium Alloys Used for Nuclear Fuel Cladding," *Annu. Rev. Mater. Res*, vol. 45, pp. 311–43, 2015. DOI: 10.1146/annurev-matsci-070214-020951. [Online]. Available: www.annualreviews.org.

[11] International Atomic Energy Agency, "Spent fuel performance assessment and research," Tech. Rep., 1997, p. 126. [Online]. Available: https://www-pub.iaea.org/MTCD/publications/PDF/te%7B%5C_%7D1343%7B%5C_%7Dweb.pdf.

[12] R. P. Gangloff and B. P. Somerday, *Gaseous hydrogen embrittlement of materials in energy technologies. Volume 1, The problem, its characterisation and*

effects on particular alloy classes. Woodhead Publishing Ltd, 2012, p. 864, ISBN: 9780857093899.

[13] R. Dutton, K. Nuttall, M. P. Puls, and L. A. Simpson, "Mechanisms of hydrogen induced delayed cracking in hydride forming materials," *Metall Trans A*, vol. 8 A, no. 10, pp. 1553–1562, 1977, ISSN: 0360-2133. DOI: 10.1007/BF02644858. [Online]. Available: https://link.springer.com/article/10.1007/BF02644858.

[14] P. Rudling, R. Adamson, F. Garzarolli, and B. Cox, *Zr Alloy Corrosion and Hydrogen Pick Up*. Molnlycke: ANT International, 2013.

[15] A. Couet, A. T. Motta, and R. J. Comstock, "Hydrogen pickup measurements in zirconium alloys: Relation to oxidation kinetics," *Journal of Nuclear Materials*, vol. 451, no. 1-3, pp. 1–13, Aug. 2014, ISSN: 00223115. DOI: 10.1016/j.jnucmat.2014.03.001. [Online]. Available: https://www.sciencedirect.com/science/article/pii/S0022311514001081.

[16] W. Burgers, "On the process of transition of the cubic-body-centered modification into the hexagonal-close-packed modification of zirconium," *Physica*, vol. 1, no. 7-12, pp. 561–586, May 1934, ISSN: 00318914. DOI: 10.1016/S0031-8914(34)80244-3. arXiv: 0402594v3 [arXiv:cond-mat]. [Online]. Available: http://www.sciencedirect.com/science/article/pii/S0031891434802443%20http://linkinghub.elsevier.com/retrieve/pii/S0031891434802443.

[17] G. Robert Odette and S. J. Zinkle, *Structural alloys for nuclear energy applications*. Elsevier, Jan. 2019, pp. 1–655, ISBN: 9780123970466. DOI: 10.1016/C2011-0-07772-4.

[18] W. Yeniscavich, R. A. Wolfe, and R. M. Lieberman, "Hydrogen absorption by nickel enriched zircaloy-2," *Journal of Nuclear Materials*, vol. 1, no. 3, pp. 271–280, Oct. 1959, ISSN: 00223115. DOI: 10.1016/0022-3115(59)90023-6. [Online]. Available: https://www.sciencedirect.com/science/article/pii/0022311559900236.

[19] V. Shishov, A. Nikulina, V. Markelov, M. Peregud, A. Kozlov, S. Averin, S. Kolbenkov, and A. Novoselov, "Influence of Neutron Irradiation on Dislocation Structure and Phase Composition of Zr-Base Alloys," in *Zirconium in the Nuclear Industry: Eleventh International Symposium*, 100 Barr Harbor Drive, PO Box C700, West Conshohocken, PA 19428-2959: ASTM International, 1996, pp. 603–603–20. DOI: 10.1520/STP16192S. [Online]. Available: http://www.astm.org/doiLink.cgi?STP16192S.

[20] G. Sabol, G. Kilp, M. Balfour, and E. Roberts, "Development of a Cladding Alloy for High Burnup," in *Zirconium in the Nuclear Industry: Eighth International Symposium*, 100 Barr Harbor Drive, PO Box C700, West Conshohocken, PA 19428-2959: ASTM International, 2008, pp. 227–227–18. DOI: 10.1520/stp18868s. [Online]. Available: http://www.astm.org/doiLink.cgi?STP18868S.

[21] B. Cox, "Effects of irradiation on the oxidation of zirconium alloys in high temperature aqueous environments," *Journal of Nuclear Materials,*, vol. 28, no. 1, pp. 1–47, Oct. 1968, ISSN: 00223115. DOI: 10.1016/0022-3115(68)90055-X. [Online]. Available: https://www.sciencedirect.com/science/article/pii/002231156890055X.

[22] B. Cox, J. P. Pemsler, and D. Bchantillons, "Diffusion of oxygen in growing zirconia films," *Journal of Nuclear Materials*, vol. 28, no. 1, pp. 73–78, Oct. 1968, ISSN: 00223115. DOI: 10.1016/0022-3115(68)90058-5. [Online]. Available: https://www.sciencedirect.com/science/article/pii/0022311568900585.

[23] A. T. Motta and L. Q. Chen, "Hydride formation in zirconium alloys," *JOM*, vol. 64, no. 12, pp. 1403–1408, Dec. 2012, ISSN: 10474838. DOI: 10.1007/s11837-012-0479-x. [Online]. Available: http://link.springer.com/10.1007/s11837-012-0479-x.

[24] N. Ni, S. Lozano-Perez, M. L. Jenkins, C. English, G. D. Smith, J. M. Sykes, and C. R. Grovenor, "Porosity in oxides on zirconium fuel cladding alloys, and its importance in controlling oxidation rates," *Scripta Materialia*, vol. 62, no. 8, pp. 564–567, Apr. 2010,

ISSN: 13596462. DOI: 10.1016/j.scriptamat.2009.12.043. [Online]. Available: http://www.sciencedirect.com/science/article/pii/S1359646209008070.

[25] F. Garzarolli, B. Cox, and P. Rudling, "Corrosion and Hydriding," Tech. Rep. January, 2012. [Online]. Available: https://www.mendeley.com/research-papers/corrosion-hydriding/?utm%7B%5C_%7Dsource=desktop%7B%5C&%7Dutm%7B%5C_%7Dmedium=1.17.12%7B%5C&%7Dutm%7B%5C_%7Dcampaign=open%7B%5C_%7Dcatalog%7B%5C&%7DuserDocumentId=%7B%5C%%7D7Bb6ee2371-75d2-42fb-95ee-e13845b00f4a%7B%5C%%7D7D.

[26] A. T. Motta, "Waterside corrosion in zirconium alloys," *JOM*, vol. 63, no. 8, pp. 59–63, Aug. 2011, ISSN: 1047-4838. DOI: 10.1007/s11837-011-0140-0. [Online]. Available: http://link.springer.com/10.1007/s11837-011-0140-0.

[27] G. H. Kinchin and R. S. Pease, "The Displacement of Atoms in Solids by Radiation," *Reports on Progress in Physics*, vol. 18, no. 1, p. 301, Jan. 1955, ISSN: 00344885. DOI: 10.1088/0034-4885/18/1/301. [Online]. Available: https://iopscience.iop.org/article/10.1088/0034-4885/18/1/301.

[28] F. Garzarolli, R. Adamson, and K. Coleman, "Microstructure of Zirconium Alloys and Effects on Performance," *Advanced Nuclear Technology International Europe AB, ANT International*, no. November, p. 41, Nov. 2015. [Online]. Available: www.antinternational.com.

[29] W. Hoffelner, "Irradiation Damage in Nuclear Power Plants," in *Handbook of Damage Mechanics*, Springer, New York, NY, 2015, pp. 1427–1461. DOI: 10.1007/978-1-4614-5589-9_36. [Online]. Available: https://link.springer.com/referenceworkentry/10.1007/978-1-4614-5589-9%7B%5C_%7D36.

[30] A. Harte, D. Jädernäs, M. Topping, P. Frankel, C. P. Race, J. Romero, L. Hallstadius, E. C. Darby, and M. Preuss, "The effect of matrix chemistry on dislocation evolution in an irradiated Zr alloy," *Acta Materialia*, vol. 130, pp. 69–82, May 2017, ISSN: 13596454. DOI: 10.1016/j.actamat.2017.03.024.

[31] M. Griffiths, “A review of microstructure evolution in zirconium alloys during irradiation,” *Journal of Nuclear Materials*, vol. 159, no. C, pp. 190–218, 1988, ISSN: 00223115. DOI: 10.1016/0022-3115(88)90093-1.

[32] A. Boyne, C. Shen, R. Najafabadi, and Y. Wang, “Numerical simulation of irradiation hardening in Zirconium,” *Journal of Nuclear Materials*, vol. 438, no. 1-3, pp. 209–217, 2013, ISSN: 00223115. DOI: 10.1016/j.jnucmat.2013.03.035.

[33] P. Tägtstrom, M. Limbäck, M. Dahlbäck, T. Andersson, and H. Pettersson, “Effects of hydrogen pickup and second-phase particle dissolution on the in-reactor corrosion performance of BWR claddings,” in *Zirconium in the Nuclear Industry: Thirteenth International Symposium*, G. Moan and P. Rudling, Eds., West Conshohocken: American Society for Testing and Materials, 2002, pp. 96–118. DOI: 10.1520/stp11385s.

[34] C. Ells, “Hydride precipitates in zirconium alloys (A review),” *Journal of Nuclear Materials*, vol. 28, no. 2, pp. 129–151, Nov. 1968, ISSN: 00223115. DOI: 10.1016/0022-3115(68)90021-4. [Online]. Available: http://www.sciencedirect.com/science/article/pii/0022311568900214?via%7B%5C%%7D3Dihub%20http://linkinghub.elsevier.com/retrieve/pii/0022311568900214.

[35] A. Zieliński and S. Sobieszczyk, “Hydrogen-enhanced degradation and oxide effects in zirconium alloys for nuclear applications,” *International Journal of Hydrogen Energy*, vol. 36, no. 14, pp. 8619–8629, Jul. 2011, ISSN: 03603199. DOI: 10.1016/j.ijhydene.2011.04.002. [Online]. Available: http://linkinghub.elsevier.com/retrieve/pii/S0360319911008330.

[36] M. A. Louchez, R. Besson, L. Thuinet, and A. Legris, “Interfacial properties of hydrides in μ-Zr: A theoretical study,” *Journal of Physics Condensed Matter*, vol. 29, no. 41, p. 415 001, Oct. 2017, ISSN: 1361648X. DOI: 10.1088/1361-648X/aa7f8a. [Online]. Available: http://stacks.iop.org/0953-8984/29/i=41/a=415001?key=crossref.fab51a4e5984775c66703c52a02be1f6.

[37] J. Bair, M. Asle Zaeem, and M. Tonks, "A review on hydride precipitation in zirconium alloys," *Journal of Nuclear Materials*, vol. 466, pp. 12–20, Nov. 2015, ISSN: 00223115. DOI: 10.1016/j.jnucmat.2015.07.014. [Online]. Available: https://linkinghub.elsevier.com/retrieve/pii/S0022311515301008.

[38] E. Zuzek, J. Abriata, A. San-Martin, and F. Manchester, "H-Zr (Hydrogen-Zirconium)," in *Phase Diagrams of Binary Hydrogen Alloys*, F. Manchester, Ed., ASM International, 2000, pp. 309–322, ISBN: 0-87170-587-7.

[39] T. Wiss, J. P. Hiernaut, D. Roudil, J. Y. Colle, E. Maugeri, Z. Talip, A. Janssen, V. Rondinella, R. J. Konings, H. J. Matzke, and W. J. Weber, "Evolution of spent nuclear fuel in dry storage conditions for millennia and beyond," *Journal of Nuclear Materials*, vol. 451, no. 1-3, pp. 198–206, Aug. 2014, ISSN: 00223115. DOI: 10.1016/j.jnucmat.2014.03.055. [Online]. Available: https://www.sciencedirect.com/science/article/pii/S0022311514001822.

[40] J. Clayton, "Out-of-Pile Nickel Alloy-Induced Accelerated Hydriding of Zircaloy Fasteners," in *Zirconium in the Nuclear Industry*, 100 Barr Harbor Drive, PO Box C700, West Conshohocken, PA 19428-2959: ASTM International, 2008, pp. 572–572–17. DOI: 10.1520/stp34495s. [Online]. Available: http://www.astm.org/doiLink.cgi?STP34495S.

[41] K. Li, T. Aarholt, J. Liu, H. Hulme, A. Garner, M. Preuss, S. Lozano-Perez, and C. Grovenor, "3D-characterization of deuterium distributions in zirconium oxide scale using high-resolution SIMS," *Applied Surface Science*, vol. 464, pp. 311–320, Jan. 2019, ISSN: 0169-4332. DOI: 10.1016/J.APSUSC.2018.09.101. [Online]. Available: https://www.sciencedirect.com/science/article/pii/S0169433218325170.

[42] S. Suman, M. K. Khan, M. Pathak, R. Singh, and J. Chakravartty, "Hydrogen in Zircaloy: Mechanism and its impacts," *International Journal of Hydrogen Energy*, vol. 40, no. 17, pp. 5976–5994, May 2015, ISSN: 03603199. DOI: 10.1016/j.ijhydene.2015.03.049. [Online]. Available: http://linkinghub.elsevier.com/retrieve/pii/S0360319915006229.

[43] B. Cox and Y. M. Wong, “Hydrogen uptake micro-mechanism for Zr alloys,” *Journal of Nuclear Materials*, vol. 270, no. 1, pp. 134–146, Apr. 1999, ISSN: 00223115. DOI: 10.1016/S0022-3115(98)00898-8. [Online]. Available: http://www.sciencedirect.com/science/article/pii/S0022311598008988.

[44] C. Anghel, “Modified oxygen and hydrogen tranport in Zr-based oxides,” PhD, KTH Royal Institute of Technology, 2006, p. 70. [Online]. Available: http://kth.diva-portal.org/smash/record.jsf?pid=diva2%7B%5C%%7D3A10706%7B%5C&%7Ddswid=9708.

[45] P. Rudling and G. Wikmark, “A unified model of Zircaloy BWR corrosion and hydriding mechanisms,” *Journal of Nuclear Materials*, vol. 265, no. 1-2, pp. 44–59, Feb. 1999, ISSN: 00223115. DOI: 10.1016/S0022-3115(98)00613-8. [Online]. Available: https://www.sciencedirect.com/science/article/pii/S0022311598006138.

[46] N. Ramasubramanian, V. Perovic, and M. Leger, “Hydrogen Transport in the Oxide and Hydrogen Pickup by the Metal During Out- and In-Reactor Corrosion of Zr-2.5Nb Pressure Tube Material,” *Zirconium in the Nuclear Industry: Twelfth International Symposium, ASTM STP 1354*, pp. 853–876, 2000, ISSN: 10403094. DOI: 10.1520/STP14331S.

[47] W. Chen, L. Wang, and S. Lu, “Influence of oxide layer on hydrogen desorption from zirconium hydride,” *Journal of Alloys and Compounds*, vol. 469, no. 1-2, pp. 142–145, Feb. 2009, ISSN: 09258388. DOI: 10.1016/j.jallcom.2008.01.157. [Online]. Available: https://www.sciencedirect.com/science/article/pii/S0925838808002144?via%7B%5C%%7D3Dihub.

[48] M. Tupin, F. Martin, C. Bisor, R. Verlet, P. Bossis, J. Chene, F. Jomard, P. Berger, S. Pascal, and N. Nuns, “Hydrogen diffusion process in the oxides formed on zirconium alloys during corrosion in pressurized water reactor conditions,” *Corrosion Science*, vol. 116, pp. 1–13, Feb. 2017, ISSN: 0010938X. DOI: 10.1016/j.corsci.2016.10.027. [Online]. Available: https://www.sciencedirect.com/science/article/pii/S0010938X16310204.

[49] M. Harada and R. Wakamatsu, “The Effect of Hydrogen on the Transition Behavior of the Corrosion Rate of Zirconium Alloys,” in *Zirconium in the Nuclear Industry: 15th International Symposium*, 3, vol. 5, ASTM International, Mar. 2009, pp. 384–384–19. DOI: 10.1520/stp48146s. [Online]. Available: http://www.astm.org/doiLink.cgi?JAI101117.

[50] W. E. Berry, D. A. Vaughan, and E. L. White, “Hydrogen Pickup During Aqueous Corrosion Of Zirconium Alloys,” *CORROSION*, vol. 17, no. 3, 109t–117t, Mar. 1960, ISSN: 0010-9312. DOI: 10.5006/0010-9312-17.3.81. [Online]. Available: http://corrosionjournal.org/doi/10.5006/0010-9312-17.3.81.

[51] S. Kass, “Hydrogen Pickup in Various Zirconium Alloys during Corrosion Exposure in High-Temperature Water and Steam,” *Journal of The Electrochemical Society*, vol. 107, no. 7, p. 594, Jul. 1960, ISSN: 00134651. DOI: 10.1149/1.2427781. [Online]. Available: http://jes.ecsdl.org/cgi/doi/10.1149/1.2427781.

[52] S. Kass and W. Kirk, “Corrosion and hydrogen absorption properties of nickel-free Zircaloy-2 and Zircaloy-4,” *Transactions: American Society for Metals*, vol. 55, 1962.

[53] Y. Hatano, M. Sugisaki, K. Kitano, and M. Hayashi, “Role of Intermetallic Precipitates in Hydrogen Transport through Oxide Films on Zircaloy,” in *Zirconium in the Nuclear Industry: Twelfth International Symposium*, 100 Barr Harbor Drive, PO Box C700, West Conshohocken, PA 19428-2959: ASTM International, 2000, pp. 901–917, ISBN: 0066-0558. DOI: 10.1520/STP14333S. [Online]. Available: http://www.astm.org/doiLink.cgi?STP14333S.

[54] E. Hillner, “Hydrogen absoprtion in Zircaloy during aqueous corrosion, effect of environment,” Pittsburgh Pa., Tech. Rep., 1964. [Online]. Available: https://www.worldcat.org/title/hydrogen-absorption-in-zircaloy-during-aqueous-corrosion-effect-of-environment/oclc/248736373.

[55] M. Christensen, W. Wolf, C. M. Freeman, E. Wimmer, R. B. Adamson, L. Hallstadius, P. E. Cantonwine, and E. V. Mader, “Effect of alloying elements on the

properties of Zr and the Zr-H system," *Journal of Nuclear Materials*, vol. 445, no. 1-3, pp. 241–250, Feb. 2014, ISSN: 00223115. DOI: 10.1016/j.jnucmat.2013.10.040. [Online]. Available: https://www.sciencedirect.com/science/article/pii/S0022311513011902.

[56] S. Rajasekhara, P. G. Kotula, D. G. Enos, B. L. Doyle, and B. G. Clark, "Influence of Zircaloy cladding composition on hydride formation during aqueous hydrogen charging," *Journal of Nuclear Materials*, vol. 489, pp. 222–228, Jun. 2017, ISSN: 00223115. DOI: 10.1016/j.jnucmat.2016.04.055. [Online]. Available: http://linkinghub.elsevier.com/retrieve/pii/S0022311516301775.

[57] Y. Hatano, K. Isobe, R. Hitaka, and M. Sugisaki, "Role of Intermetallic Precipitates in Hydrogen Uptake of Zircaloy-2," *Journal of Nuclear Science and Technology*, vol. 33, no. 12, pp. 944–949, Dec. 1996, ISSN: 00223131. DOI: 10.1080/18811248.1996.9732036. [Online]. Available: http://www.tandfonline.com/doi/abs/10.1080/18811248.1996.9732036.

[58] A. Couet, A. T. Motta, and R. J. Comstock, "Effect of Alloying Elements on Hydrogen Pickup in Zirconium Alloys," in *Zirconium in the Nuclear Industry: 17th Volume*, 10, ASTM International, 2015, pp. 479–514, ISBN: 1543201202. DOI: 10.1520/STP154320120215. [Online]. Available: www.astm.org%20http://www.astm.org/doiLink.cgi?STP154320120215.

[59] Y. Hatano, R. Hitaka, M. Sugisaki, and M. Hayashi, "Influence of size distribution of Zr(Fe,Cr)2 precipitates on hydrogen transport through oxide film of Zircaloy-4," *Journal of Nuclear Materials*, vol. 248, pp. 311–314, Sep. 1997, ISSN: 00223115. DOI: 10.1016/S0022-3115(97)00128-1. [Online]. Available: https://www.sciencedirect.com/science/article/pii/S0022311597001281.

[60] P. A. Burr, S. T. Murphy, S. C. Lumley, M. R. Wenman, and R. W. Grimes, "Hydrogen accommodation in Zr second phase particles: Implications for H pick-up and hydriding of Zircaloy-2 and Zircaloy-4," *Corrosion Science*, vol. 69, pp. 1–4, Apr.

2013, ISSN: 0010938X. DOI: 10.1016/j.corsci.2012.11.036. [Online]. Available: https://www.sciencedirect.com/science/article/pii/S0010938X12005781.

[61] C. Jones, V. Tuli, Z. Shah, M. Gass, P. A. Burr, M. Preuss, and K. L. Moore, "Evidence of hydrogen trapping at second phase particles in zirconium alloys," *Scientific Reports*, vol. 11, no. 1, p. 4370, 2021, ISSN: 20452322. DOI: 10.1038/s41598-021-83859-w.

[62] V. Tuli, A. Claisse, and P. A. Burr, "Hydrogen solubility in Zr–Nb alloys," *Scripta Materialia*, vol. 214, Jun. 2022, ISSN: 13596462. DOI: 10.1016/j.scriptamat.2022.114652.

[63] P. Tejland, C. Langhammer, and H. O. Andrén, "On the black oxide colour of zirconium alloys," *Journal of Nuclear Materials*, vol. 400, no. 1, pp. 79–83, May 2010, ISSN: 00223115. DOI: 10.1016/j.jnucmat.2010.02.013. [Online]. Available: https://www.sciencedirect.com/science/article/pii/S0022311510000528.

[64] A. Couet, A. T. Motta, R. J. Comstock, and R. L. Paul, "Cold neutron prompt gamma activation analysis, a non-destructive technique for hydrogen level assessment in zirconium alloys," in *Journal of Nuclear Materials*, vol. 425, North-Holland, Jun. 2012, pp. 211–217. DOI: 10.1016/j.jnucmat.2011.06.044. [Online]. Available: https://www.sciencedirect.com/science/article/pii/S0022311511006398%7B%5C#%7Db0030.

[65] A. T. Motta, L. Capolungo, L. Q. Chen, M. N. Cinbiz, M. R. Daymond, D. A. Koss, E. Lacroix, G. Pastore, P. C. A. Simon, M. R. Tonks, B. D. Wirth, and M. A. Zikry, "Hydrogen in zirconium alloys: A review," *Journal of Nuclear Materials*, vol. 518, pp. 440–460, Mar. 2019, ISSN: 00223115. DOI: 10.1016/j.jnucmat.2019.02.042. [Online]. Available: https://www.sciencedirect.com/science/article/pii/S0022311518316763.

[66] R. S. Daum, Y. S. Chu, and A. T. Motta, "Identification and quantification of hydride phases in Zircaloy-4 cladding using synchrotron X-ray diffraction," *Journal of Nuclear*

Materials, vol. 392, no. 3, pp. 453–463, Aug. 2009, ISSN: 00223115. DOI: 10.1016/j.jnucmat.2009.04.004. [Online]. Available: https://www.sciencedirect.com/science/article/pii/S0022311509005467.

[67] G. J. Carpenter, "The dilatational misfit of zirconium hydrides precipitated in zirconium," *Journal of Nuclear Materials*, vol. 48, no. 3, pp. 264–266, Oct. 1973, ISSN: 00223115. DOI: 10.1016/0022-3115(73)90022-6. [Online]. Available: https://www.sciencedirect.com/science/article/pii/0022311573900226.

[68] D. O. Northwood and R. W. Gilbert, "Hydrides in zirconium-2.5 wt. % niobium alloy pressure tubing," *Journal of Nuclear Materials*, vol. 78, no. 1, pp. 112–116, Nov. 1978, ISSN: 00223115. DOI: 10.1016/0022-3115(78)90509-3. [Online]. Available: https://www.sciencedirect.com/science/article/pii/0022311578905093.

[69] Z. Zhao, M. Blat-Yrieix, J. .-P. Morniroli, A. Legris, L. Thuinet, Y. Kihn, A. Ambard, and L. Legras, "Characterization of Zirconium Hydrides and Phase Field Approach to a Mesoscopic-Scale Modeling of Their Precipitation," in *Zirconium in the Nuclear Industry: 15th International Symposium*, 100 Barr Harbor Drive, PO Box C700, West Conshohocken, PA 19428-2959: ASTM International, 2009, pp. 29–29–22. DOI: 10.1520/stp48129s. [Online]. Available: http://www.astm.org/doiLink.cgi?STP48129S.

[70] IAEA - International Atomic Energy Agency, "Delayed hydride cracking in zirconium alloys in pressure tube nuclear reactors IAEA-TECDOC-1410," *October*, no. October, p. 43, 2004. [Online]. Available: http://www-pub.iaea.org/MTCD/publications/PDF/te%7B%5C_%7D1410%7B%5C_%7Dweb.pdf.

[71] R. S. Daum, S. Majumdar, Y. Liu, and M. C. Billone, "Radial-hydride embrittlement of high-burnup zircaloy-4 fuel cladding," *Journal of Nuclear Science and Technology*, vol. 43, no. 9, pp. 1054–1067, Sep. 2006, ISSN: 00223131. DOI: 10.1080/18811248.2006.9711195. [Online]. Available: http://www.tandfonline.com/doi/abs/10.1080/18811248.2006.9711195.

[72] M. Le Saux, J. Besson, S. Carassou, C. Poussard, and X. Averty, "Behavior and failure of uniformly hydrided Zircaloy-4 fuel claddings between 25 ℃ and 480 ℃ under various stress states, including RIA loading conditions," *Engineering Failure Analysis*, vol. 17, no. 3, pp. 683–700, Apr. 2010, ISSN: 13506307. DOI: 10.1016/j.engfailanal.2009.07.001. [Online]. Available: https://www.sciencedirect.com/science/article/pii/S1350630709001940.

[73] M. Le Saux, J. Besson, and S. Carassou, "A model to describe the mechanical behavior and the ductile failure of hydrided Zircaloy-4 fuel claddings between 25℃ and 480℃," *Journal of Nuclear Materials*, vol. 466, pp. 43–55, Nov. 2015, ISSN: 00223115. DOI: 10.1016/j.jnucmat.2015.07.026. [Online]. Available: https://www.sciencedirect.com/science/article/pii/S0022311515301124.

[74] M. Le Saux, J. Besson, S. Carassou, C. Poussard, and X. Averty, "A model to describe the anisotropic viscoplastic mechanical behavior of fresh and irradiated Zircaloy-4 fuel claddings under RIA loading conditions," *Journal of Nuclear Materials*, vol. 378, no. 1, pp. 60–69, Aug. 2008, ISSN: 00223115. DOI: 10.1016/j.jnucmat.2008.04.017. [Online]. Available: https://www.sciencedirect.com/science/article/pii/S0022311508002481.

[75] R. Daum, S. Majumdar, D. Bates, A. Motta, D. Koss, and M. Billone, "On the Embrittlement of Zircaloy-4 Under RIA-Relevant Conditions," in *Zirconium in the Nuclear Industry: Thirteenth International Symposium*, 100 Barr Harbor Drive, PO Box C700, West Conshohocken, PA 19428-2959: ASTM International, 2002, pp. 702–718. DOI: 10.1520/stp11412s. [Online]. Available: http://www.astm.org/doiLink.cgi?STP11412S.

[76] V. Macdonald, D. Le Boulch, A. H. de Menibus, J. Besson, Q. Auzoux, J. Crépin, and T. Le Jolu, "Fracture of Zircaloy-4 Fuel Cladding Tubes with Hydride Blisters," *Procedia Materials Science*, vol. 3, pp. 233–238, Jan. 2014, ISSN: 22118128. DOI: 10.1016/j.mspro.2014.06.041. [Online]. Available: https://www.sciencedirect.com/science/article/pii/S221181281400042X.

[77] Y. Chang, W. Lu, J. Guénolé, L. T. Stephenson, A. Szczpaniak, P. Kontis, A. K. Ackerman, F. F. Dear, I. Mouton, X. Zhong, S. Zhang, D. Dye, C. H. Liebscher, D. Ponge, S. Korte-Kerzel, D. Raabe, and B. Gault, "Ti and its alloys as examples of cryogenic focused ion beam milling of environmentally-sensitive materials," *Nature Communications*, vol. 10, no. 1, p. 942, Dec. 2019, ISSN: 20411723. DOI: 10.1038/s41467-019-08752-7. [Online]. Available: http://www.nature.com/articles/s41467-019-08752-7.

[78] Y.-S. Chen, D. Haley, S. S. A. Gerstl, A. J. London, F. Sweeney, R. A. Wepf, W. M. Rainforth, P. A. J. Bagot, and M. P. Moody, "Direct observation of individual hydrogen atoms at trapping sites in a ferritic steel," *Science*, vol. 355, no. 6330, pp. 1196–1199, Mar. 2017, ISSN: 0036-8075. DOI: 10.1126/science.aal2418. [Online]. Available: http://www.sciencemag.org/lookup/doi/10.1126/science.aal2418.

[79] J. C. Meyer, C. O. Girit, M. F. Crommie, and A. Zettl, "Imaging and dynamics of light atoms and molecules on graphene," *Nature*, vol. 454, no. 7202, pp. 319–322, Jul. 2008, ISSN: 14764687. DOI: 10.1038/nature07094. [Online]. Available: http://www.nature.com/articles/nature07094.

[80] O. Barrera, D. Bombac, Y. Chen, T. D. Daff, E. Galindo-Nava, P. Gong, D. Haley, R. Horton, I. Katzarov, J. R. Kermode, C. Liverani, M. Stopher, and F. Sweeney, "Understanding and mitigating hydrogen embrittlement of steels: a review of experimental, modelling and design progress from atomistic to continuum," *Journal of Materials Science*, vol. 53, no. 9, pp. 6251–6290, May 2018, ISSN: 0022-2461. DOI: 10.1007/s10853-017-1978-5. [Online]. Available: http://link.springer.com/10.1007/s10853-017-1978-5.

[81] R. Ishikawa, E. Okunishi, H. Sawada, Y. Kondo, F. Hosokawa, and E. Abe, "Direct imaging of hydrogen-atom columns in a crystal by annular bright-field electron microscopy," *Nature Materials*, vol. 10, no. 4, pp. 278–281, Apr. 2011, ISSN: 14764660. DOI: 10.1038/nmat2957. [Online]. Available: http://www.nature.com/articles/nmat2957.

[82] Y. Chang, A. J. Breen, Z. Tarzimoghadam, P. Kürnsteiner, H. M. Gardner, A. Ackerman, A. Radecka, P. A. Bagot, W. Lu, T. Li, E. A. Jägle, M. Herbig, L. T. Stephenson, M. P. Moody, D. Rugg, D. Dye, D. Ponge, D. Raabe, and B. Gault, "Characterizing solute hydrogen and hydrides in pure and alloyed titanium at the atomic scale," *Acta Materialia*, vol. 150, pp. 273–280, May 2018, ISSN: 13596454. DOI: 10.1016/j.actamat.2018.02.064. [Online]. Available: https://www.sciencedirect.com/science/article/pii/S1359645418301927.

[83] M. Wilde and K. Fukutani, "Nuclear Reaction Analysis," in *Compendium of Surface and Interface Analysis*, Singapore: Springer Singapore, 2018, pp. 405–411. DOI: 10.1007/978-981-10-6156-1_67. [Online]. Available: http://link.springer.com/10.1007/978-981-10-6156-1%7B%5C_%7D67.

[84] T. P. Reinhardt, S. Akhmadaliev, D. Bemmerer, K. Stöckel, and L. Wagner, "Absolute hydrogen depth profiling using the resonant 1H(15N,$\alpha\gamma$)12C nuclear reaction," *Nuclear Instruments and Methods in Physics Research, Section B: Beam Interactions with Materials and Atoms*, vol. 381, pp. 58–66, Aug. 2016, ISSN: 0168583X. DOI: 10.1016/j.nimb.2016.05.009. [Online]. Available: https://www.sciencedirect.com/science/article/pii/S0168583X16302130.

[85] C. S. Zhang, B. Li, and P. R. Norton, "The study of hydrogen segregation on Zr(0001) and Zr(1010) surfaces by static secondary ion mass spectroscopy, work function, Auger electron spectroscopy and nuclear reaction analysis," *Journal of Alloys and Compounds*, vol. 231, no. 1-2, pp. 354–363, Dec. 1995, ISSN: 09258388. DOI: 10.1016/0925-8388(95)01847-6. [Online]. Available: https://www.sciencedirect.com/science/article/pii/0925838895018476.

[86] J. Meija, T. B. Coplen, M. Berglund, W. A. Brand, P. De Bièvre, M. Gröning, N. E. Holden, J. Irrgeher, R. D. Loss, T. Walczyk, and T. Prohaska, *Isotopic compositions of the elements 2013 (IUPAC Technical Report)*, 2016. DOI: 10.1515/pac-2015-0503. [Online]. Available: https://www.degruyter.com/downloadpdf/j/pac.2016.88.issue-3/pac-2015-0503/pac-2015-0503.pdf.

[87] G. Bertolino, G. Meyer, and J. Perez Ipiña, "Effects of hydrogen content and temperature on fracture toughness of Zircaloy-4," *Journal of Nuclear Materials*, vol. 320, no. 3, pp. 272–279, Aug. 2003, ISSN: 00223115. DOI: 10.1016/S0022-3115(03)00193-4. [Online]. Available: https://www.sciencedirect.com/science/article/pii/S0022311503001934.

[88] M. Elmoselhi and M. B., "Hydrogen uptake by oxidized zirconium alloys," *Journal of Alloys and Compounds*, vol. 231, no. 1-2, pp. 716–721, Dec. 1995, ISSN: 09258388. DOI: 10.1016/0925-8388(95)01759-3. [Online]. Available: http://linkinghub.elsevier.com/retrieve/pii/0925838895017593.

[89] T. F. Kelly, M. K. Miller, K. Rajan, and S. P. Ringer, *Atomic-scale tomography: A 2020 vision*, Jun. 2013. DOI: 10.1017/S1431927613000494. [Online]. Available: https://www.cambridge.org/core/product/identifier/S1431927613000494/type/journal%7B%5C_%7Darticle.

[90] G. Sundell, M. Thuvander, and H. O. Andrén, "Hydrogen analysis in APT: Methods to control adsorption and dissociation of H2," *Ultramicroscopy*, vol. 132, pp. 285–289, 2013, ISSN: 03043991. DOI: 10.1016/j.ultramic.2013.01.007.

[91] J. Takahashi, K. Kawakami, H. Otsuka, and H. Fujii, "Atom probe analysis of titanium hydride precipitates," *Ultramicroscopy*, vol. 109, no. 5, pp. 568–573, Apr. 2009, ISSN: 03043991. DOI: 10.1016/j.ultramic.2008.11.012. [Online]. Available: http://linkinghub.elsevier.com/retrieve/pii/S030439910800305720http://www.ncbi.nlm.nih.gov/pubmed/19136213.

[92] R. Gemma, T. Al-Kassab, R. Kirchheim, and A. Pundt, "Visualization of deuterium dead layer by atom probe tomography," *Scripta Materialia*, vol. 67, no. 11, pp. 903–906, Dec. 2012, ISSN: 13596462. DOI: 10.1016/j.scriptamat.2012.08.025. [Online]. Available: http://linkinghub.elsevier.com/retrieve/pii/S1359646212005477.

[93] H. Takamizawa, K. Hoshi, Y. Shimizu, F. Yano, K. Inoue, S. Nagata, T. Shikama, and Y. Nagai, "Three-dimensional characterization of deuterium implanted in silicon using atom probe tomography," *Applied Physics Express*, vol. 6, no. 6, pp. 4–7, 2013, ISSN: 18820778. DOI: 10.7567/APEX.6.066602. [Online]. Available: http://iopscience.iop.org/article/10.7567/APEX.6.066602/pdf.

[94] D. Haley, S. V. Merzlikin, P. Choi, and D. Raabe, "Atom probe tomography observation of hydrogen in high-Mn steel and silver charged via an electrolytic route," *International Journal of Hydrogen Energy*, vol. 39, no. 23, pp. 12 221–12 229, 2014, ISSN: 03603199. DOI: 10.1016/j.ijhydene.2014.05.169. [Online]. Available: http://dx.doi.org/10.1016/j.ijhydene.2014.05.169.

[95] B. Wadman, H.-O. Andrén, and U. Rolander, "Preferential Field Evaporation During Atom Probe Analysis of Zircaloy-4," *Journal de Physique*, vol. C6, no. 48, pp. 323–327, 1988, ISSN: 0449-1947. DOI: 10.1051/jphyscol:1988656>. [Online]. Available: https://hal.archives-ouvertes.fr/jpa-00228153.

[96] R. M. Kruger, R. B. Adamson, and S. S. Brenner, "Effects of microchemistry and precipitate size on nodular corrosion resistance of Zircaloy-2," *Journal of Nuclear Materials*, vol. 189, no. 2, pp. 193–200, 1992, ISSN: 00223115. DOI: 10.1016/0022-3115(92)90532-P. [Online]. Available: https://ac.els-cdn.com/002231159290532P/1-s2.0-002231159290532P-main.pdf?%7B%5C_%7Dtid=0af75d3c-ec8e-11e7-ac64-00000aab0f6c%7B%5C&%7Dacdnat=1514548227%7B%5C_%7Da6ef6ed1afac25a3b49e281758bb0615.

[97] Y. Dong, A. T. Motta, and E. A. Marquis, "Atom probe tomography study of alloying element distributions in Zr alloys and their oxides," *Journal of Nuclear Materials*, vol. 442, no. 1-3, pp. 270–281, 2013, ISSN: 00223115. DOI: 10.1016/j.jnucmat.2013.08.055.

[98] D. Hudson, N. Ni, S. Lozano-perez, D. Saxey, C. English, G. D. W. Smith, J. Sykes, and C. Grovenor, "The atomic-scale structure and chemistry of the Zircaloy-4 metal-

oxide interface," in *14th International Conference on Environmental Degredation of Materials in Nuclear Power Systems*, Virginia Beach, 2009, pp. 1407–1418.

[99] D. Hudson and G. D. Smith, "Initial observation of grain boundary solute segregation in a zirconium alloy (ZIRLO) by three-dimensional atom probe," *Scripta Materialia*, vol. 61, no. 4, pp. 411–414, 2009, ISSN: 13596462. DOI: 10.1016/j.scriptamat.2009.04.032.

[100] D. Hudson, "Zirconium Oxidation on the Atomic Scale," PhD Thesis, University of Oxford, 2011.

[101] S. B. Setiadinata, "Corrosion and Hydrogen Pickup Mechanisms of Zirconium Alloys," PhD Thesis, University of Oxford, 2016, p. 265.

[102] M. Lindgren, G. Sundell, I. Panas, L. Hallstadius, M. Thuvander, and H.-O. Andrén, "Toward a Comprehensive Mechanistic Understanding of Hydrogen Uptake in Zirconium Alloys by Combining Atom Probe Analysis With Electronic Structure Calculations," in *Zirconium in the Nuclear Industry: 17th Volume*, 100 Barr Harbor Drive, PO Box C700, West Conshohocken, PA 19428-2959: ASTM International, Jan. 2014, pp. 515–539. DOI: 10.1520/stp154320120164. [Online]. Available: http://www.astm.org/doiLink.cgi?STP154320120164.

[103] G. Sundell, M. Thuvander, P. Tejland, M. Dahlbäck, L. Hallstadius, and H. O. Andrén, "Redistribution of alloying elements in Zircaloy-2 after in-reactor exposure," *Journal of Nuclear Materials*, vol. 454, no. 1-3, pp. 178–185, Nov. 2014, ISSN: 00223115. DOI: 10.1016/j.jnucmat.2014.07.072.

[104] A. Harte, R. P. Babu, C. A. Hirst, T. L. Martin, P. A. Bagot, M. P. Moody, P. Frankel, J. Romero, L. Hallstadius, E. C. Darby, and M. Preuss, "Understanding irradiation-induced nanoprecipitation in zirconium alloys using parallel TEM and APT," *Journal of Nuclear Materials*, vol. 510, pp. 460–471, Nov. 2018, ISSN: 00223115. DOI: 10.1016/j.jnucmat.2018.08.033. [Online]. Available: https://www.sciencedirect.com/science/article/pii/S0022311518304963.

[105] J. Eriksson, G. Sundell, P. Tejland, H. O. Andrén, and M. Thuvander, “An atom probe tomography study of the chemistry of radiation-induced dislocation loops in Zircaloy-2 exposed to boiling water reactor operation,” *Journal of Nuclear Materials*, vol. 550, p. 152 923, Jul. 2021, ISSN: 00223115. DOI: 10.1016/j.jnucmat.2021.152923.

[106] T. Sawabe and T. Sonoda, “Evolution of nanoscopic iron clusters in irradiated zirconium alloys with different iron contents,” *Journal of Nuclear Science and Technology*, vol. 55, no. 10, pp. 1110–1118, Oct. 2018, ISSN: 00223131. DOI: 10.1080/00223131.2018.1479987. [Online]. Available: https://www.tandfonline.com/doi/abs/10.1080/00223131.2018.1479987.

[107] B. M. Jenkins, J. Haley, M. P. Moody, J. M. Hyde, and C. R. Grovenor, “APT and TEM study of behaviour of alloying elements in neutron-irradiated zirconium-based alloys,” *Scripta Materialia*, vol. 208, p. 114 323, Feb. 2022, ISSN: 13596462. DOI: 10.1016/j.scriptamat.2021.114323.

[108] R. Gemma, T. Al-Kassab, R. Kirchheim, and A. Pundt, “APT analyses of deuterium-loaded Fe/V multi-layered films,” *Ultramicroscopy*, vol. 109, no. 5, pp. 631–636, Apr. 2009, ISSN: 03043991. DOI: 10.1016/j.ultramic.2008.11.005. [Online]. Available: http://linkinghub.elsevier.com/retrieve/pii/S030439910800297 0%20http://www.ncbi.nlm.nih.gov/pubmed/19131167.

[109] R. Gemma, T. Al-Kassab, R. Kirchheim, and A. Pundt, “Analysis of deuterium in V-Fe5at.% film by atom probe tomography (APT),” in *Journal of Alloys and Compounds*, vol. 509, Sep. 2011, S872–S876, ISBN: 0925-8388. DOI: 10.1016/j.jallcom.2010.11.122. [Online]. Available: http://linkinghub.elsevier.com/retrieve/pii/S0925838810028859.

[110] S. Yamamoto, H. Naramoto, and Y. Aoki, “Analysis of hydrogen in Nb thin films and Nb/Cu multilayers, using ion beams,” *Journal of Alloys and Compounds*, vol. 253-254, no. 1-2, pp. 66–69, Dec. 1997, ISSN: 09258388. DOI: 10.1016/S0925-8388(96)03057-5. [Online]. Available: https://www.sciencedirect.com/science/article/pii/0925838895018050.

[111] D. Nagengast, J. Erxmeyer, F. Klose, C. Rehm, P. Kuschnerus, G. Dortmann, and A. Weidinger, "Hydrogen-charging of Nb/Fe multilayers," *Journal of Alloys and Compounds*, vol. 231, no. 1-2, pp. 307–309, Dec. 1995, ISSN: 09258388. DOI: 10.1016/0925-8388(95)01804-2. [Online]. Available: https://www.sciencedirect.com/science/article/pii/0925838895018042.

[112] J. Takahashi, K. Kawakami, Y. Kobayashi, and T. Tarui, "The first direct observation of hydrogen trapping sites in TiC precipitation-hardening steel through atom probe tomography," *Scripta Materialia*, vol. 63, no. 3, pp. 261–264, Aug. 2010, ISSN: 13596462. DOI: 10.1016/j.scriptamat.2010.03.012. [Online]. Available: https://www.sciencedirect.com/science/article/pii/S1359646210001508.

[113] T. L. Martin, C. Coe, P. A. Bagot, P. Morrall, G. D. Smith, T. Scott, and M. P. Moody, "Atomic-scale Studies of Uranium Oxidation and Corrosion by Water Vapour," *Scientific Reports*, vol. 6, no. 1, p. 25 618, Sep. 2016, ISSN: 20452322. DOI: 10.1038/srep25618. [Online]. Available: http://www.nature.com/articles/srep25618.

[114] G. Sundell, M. Thuvander, A. K. Yatim, H. Nordin, and H. O. Andrén, *Direct observation of hydrogen and deuterium in oxide grain boundaries in corroded Zirconium alloys*, 2015. DOI: 10.1016/j.corsci.2014.10.016.

[115] G. Sundell, M. Thuvander, and H. O. Andrén, "Barrier oxide chemistry and hydrogen pick-up mechanisms in zirconium alloys," *Corrosion Science*, vol. 102, pp. 490–502, Jan. 2016, ISSN: 0010938X. DOI: 10.1016/j.corsci.2015.11.002. [Online]. Available: http://www.sciencedirect.com/science/article/pii/S0010938X15301438.

[116] A. J. Breen, I. Mouton, W. Lu, S. Wang, A. Szczepaniak, P. Kontis, L. T. Stephenson, Y. Chang, A. K. da Silva, C. H. Liebscher, D. Raabe, T. B. Britton, M. Herbig, and B. Gault, "Atomic scale analysis of grain boundary deuteride growth front in Zircaloy-4," *Scripta Materialia*, vol. 156, pp. 42–46, 2018, ISSN: 13596462. DOI: 10.1016/j.scriptamat.2018.06.044. arXiv: 1806.10286. [Online]. Available: https://www.sciencedirect.com/science/article/pii/S1359646218304123.

[117] B. Gault, M. P. Moody, J. M. Cairney, and S. P. Ringer, *Atom Probe Microscopy*, ser. Springer Series in Materials Science. New York, NY: Springer New York, 2012, vol. 160, ISBN: 978-1-4614-3435-1. DOI: 10.1007/978-1-4614-3436-8. [Online]. Available: http://link.springer.com/10.1007/978-1-4614-3436-8.

[118] G. J. Carpenter, J. A. Jackman, J. P. McCaffrey, and R. Alani, "In Situ Hydride Formation in Zirconium and Titanium during Ion Milling," *Microscopy and Microanalysis*, vol. 1, no. 4, pp. 175–184, Aug. 1995, ISSN: 1431-9276. DOI: 10.1017/S1431927695111757. [Online]. Available: https://academic.oup.com/mam/article/1/4/175/6927499.

[119] R. Ding and I. P. Jones, "In situ hydride formation in titanium during focused ion milling," *Journal of Electron Microscopy*, vol. 60, no. 1, pp. 1–9, Feb. 2011, ISSN: 00220744. DOI: 10.1093/jmicro/dfq066. [Online]. Available: https://academic.oup.com/jmicro/article-lookup/doi/10.1093/jmicro/dfq066.

[120] Alleghany Technologies Incorporated, *Zirconium Alloys: technical data sheet*, 2015. [Online]. Available: https://www.atimetals.com/Products/Documents/datasheets/zirconium/alloy/Zr%7B%5C_%7Dnuke%7B%5C_%7Dwaste%7B%5C_%7Ddisposal%7B%5C_%7Dv2.pdf (visited on 05/11/2018).

[121] B. Gault, S. T. Loi, V. J. Araullo-Peters, L. T. Stephenson, M. P. Moody, S. L. Shrestha, R. K. Marceau, L. Yao, J. M. Cairney, and S. P. Ringer, "Dynamic reconstruction for atom probe tomography," *Ultramicroscopy*, vol. 111, no. 11, pp. 1619–1624, Nov. 2011, ISSN: 03043991. DOI: 10.1016/j.ultramic.2011.08.005.

[122] R. Gomer, *Field Emissions and Field Ionization*, 1st ed. AIP-Press, 1993, p. 195, ISBN: 978-1-56396-124-3. [Online]. Available: https://www.springer.com/gp/book/9781563961243.

[123] T. T. Tsong, "Field penetration and band bending for semiconductor of simple geometries in high electric fields," *Surface Science*, vol. 85, no. 1, pp. 1–18, Jun. 1979, ISSN: 00396028. DOI: 10.1016/0039-6028(79)90228-0.

[124] S. M. Reddy, D. W. Saxey, W. D. Rickard, D. Fougerouse, S. D. Montalvo, R. Verberne, and A. van Riessen, *Atom Probe Tomography: Development and Application to the Geosciences*, Mar. 2020. DOI: 10.1111/ggr.12313. [Online]. Available: https://onlinelibrary.wiley.com/doi/full/10.1111/ggr.12313%20https://onlinelibrary.wiley.com/doi/abs/10.1111/ggr.12313%20https://onlinelibrary.wiley.com/doi/10.1111/ggr.12313.

[125] A. J. London, D. Haley, and M. P. Moody, "Single-Ion Deconvolution of Mass Peak Overlaps for Atom Probe Microscopy," in *Microscopy and Microanalysis*, vol. 23, Cambridge University Press, Apr. 2017, pp. 300–306. DOI: 10.1017/S1431927616012782.

[126] I. Mouton, A. J. Breen, S. Wang, Y. Chang, A. Szczepaniak, P. Kontis, L. T. Stephenson, D. Raabe, M. Herbig, T. B. Britton, and B. Gault, "Quantification Challenges for Atom Probe Tomography of Hydrogen and Deuterium in Zircaloy-4," *Microscopy and Microanalysis*, vol. 25, no. 2, pp. 481–488, Apr. 2019, ISSN: 14358115. DOI: 10.1017/S143192761801615X. arXiv: 1809.03556.

[127] D. Haley, P. Choi, and D. Raabe, "Guided mass spectrum labelling in atom probe tomography," *Ultramicroscopy*, vol. 159, pp. 338–345, Dec. 2015, ISSN: 18792723. DOI: 10.1016/j.ultramic.2015.03.005. [Online]. Available: https://www.sciencedirect.com/science/article/pii/S0304399115000479?via%7B%5C%%7D3Dihub.

[128] M. E. Jones, "Enabling the 3D imaging of hydrogen in zirconium alloys via advanced atom probe," MEng, University of Oxford, 2018.

[129] G. L. Kellogg, "Pulsed laser stimulated field desorption of hydrogen from molybdenum," *The Journal of Chemical Physics*, vol. 74, no. 2, p. 1479, Jan. 1981, ISSN: 00219606. DOI: 10.1063/1.441162. [Online]. Available: http://aip.scitation.org/doi/10.1063/1.441162%20http://scitation.aip.org/content/aip/journal/jcp/74/2/10.1063/1.441162.

[130] D. J. Larson, T. J. Prosa, R. M. Ulfig, B. P. Geiser, and T. F. Kelly, *Local Electrode Atom Probe Tomography*, 1st ed. Springer New York, 2013, pp. XVIII, 318, ISBN: 978-1-4614-8720-3. DOI: 10.1007/978-1-4614-8721-0.

[131] M. S. Meier, M. E. Jones, P. J. Felfer, M. P. Moody, and D. Haley, "Extending Estimating Hydrogen Content in Atom Probe Tomography Experiments Where H2Molecule Formation Occurs," *Microscopy and Microanalysis*, pp. 1–14, 2021, ISSN: 14358115. DOI: 10.1017/S1431927621012332. [Online]. Available: https://www.cambridge.org/core/journals/microscopy-and-microanalysis/article/extending-estimating-hydrogen-content-in-atom-probe-tomography-experiments-where-h2-molecule-formation-occurs/6C9788FB28715B09BB91651D37BA5BF2.

[132] K. Thompson, D. Lawrence, D. J. Larson, J. D. Olson, T. F. Kelly, and B. Gorman, "In situ site-specific specimen preparation for atom probe tomography," *Ultramicroscopy*, vol. 107, no. 2-3, pp. 131–139, Feb. 2007, ISSN: 03043991. DOI: 10.1016/j.ultramic.2006.06.008.

[133] S. M. Hanlon, S. Y. Persaud, F. Long, A. Korinek, and M. R. Daymond, "A solution to FIB induced artefact hydrides in Zr alloys," *Journal of Nuclear Materials*, vol. 515, pp. 122–134, Mar. 2019, ISSN: 00223115. DOI: 10.1016/j.jnucmat.2018.12.020. [Online]. Available: https://www.sciencedirect.com/science/article/pii/S0022311518312340.

[134] B. M. Jenkins, J. O. Douglas, H. M. Gardner, D. Tweddle, A. Kareer, P. S. Karamched, N. Riddle, J. M. Hyde, P. A. Bagot, G. R. Odette, and M. P. Moody, "A more holistic characterisation of internal interfaces in a variety of materials via complementary use of transmission Kikuchi diffraction and Atom probe tomography," *Applied Surface Science*, vol. 528, p. 147 011, Oct. 2020, ISSN: 01694332. DOI: 10.1016/j.apsusc.2020.147011.

[135] Y. Kunimune, Y. Shimada, Y. Sakurai, M. Inoue, A. Nishida, B. Han, Y. Tu, H. Takamizawa, Y. Shimizu, K. Inoue, F. Yano, Y. Nagai, T. Katayama, and T. Ide, "Quantitative analysis of hydrogen in SiO2/SiN/SiO2 stacks using atom probe

tomography," *AIP Advances*, vol. 6, no. 4, pp. 10–17, 2016, ISSN: 21583226. DOI: 10.1063/1.4948558.

[136] H. Sepehri-Amin, T. Ohkubo, T. Nishiuchi, S. Hirosawa, and K. Hono, "Quantitative laser atom probe analyses of hydrogenation-disproportionated Nd-Fe-B powders," *Ultramicroscopy*, vol. 111, no. 6, pp. 615–618, May 2011, ISSN: 03043991. DOI: 10.1016/j.ultramic.2010.11.015. [Online]. Available: http://linkinghub.elsevier.com/retrieve/pii/S0304399110003050%20http://www.ncbi.nlm.nih.gov/pubmed/21146306.

[137] D. Haley, I. McCarroll, P. A. Bagot, J. M. Cairney, and M. P. Moody, "A Gas-Phase Reaction Cell for Modern Atom Probe Systems," *Microscopy and Microanalysis*, vol. 25, no. 2, pp. 410–417, Apr. 2019, ISSN: 14358115. DOI: 10.1017/S1431927618016240. [Online]. Available: https://www.cambridge.org/core/product/identifier/S1431927618016240/type/journal%7B%5C_%7Darticle.

[138] Y.-S. Chen, "Characterisation of hydrogen trapping in steel by atom probe tomography," Ph.D. dissertation, University of Oxford, 2017.

[139] P. E. Danielson and R. C. Sutherlin, "Metallography and Microstructures of Zirconium, Hafnium, and Their Alloys," in *Metallography and Microstructures*, ASM International, Dec. 2018, pp. 942–958. DOI: 10.31399/asm.hb.v09.a0003782.

[140] I. Mouton, Y. Chang, P. Chakraborty, S. Wang, L. T. Stephenson, T. Ben Britton, and B. Gault, "Hydride growth mechanism in zircaloy-4: Investigation of the partitioning of alloying elements," *Materialia*, vol. 15, p. 101 006, Mar. 2021, ISSN: 25891529. DOI: 10.1016/j.mtla.2021.101006. arXiv: 2009.08073.

[141] Y. S. Chen, H. Lu, J. Liang, A. Rosenthal, H. Liu, G. Sneddon, I. McCarroll, Z. Zhao, W. Li, A. Guo, and J. M. Cairney, "Observation of hydrogen trapping at dislocations, grain boundaries, and precipitates," *Science*, vol. 367, no. 6474, pp. 171–175, Jan. 2020, ISSN: 10959203. DOI: 10.1126/science.aaz0122. [Online]. Available: https://www.science.org/doi/abs/10.1126/science.aaz0122.

[142] T. Maimaitiyili, J. Blomqvist, A. Steuwer, C. Bjerkén, O. Zanellato, M. S. Blackmur, J. Andrieux, and F. Ribeiro, "In situ hydrogen loading on zirconium powder," *Journal of Synchrotron Radiation*, vol. 22, no. 4, pp. 995–1000, Jul. 2015, ISSN: 1600-5775. DOI: 10.1107/S1600577515009054. [Online]. Available: //scripts.iucr.org/cgi-bin/paper?vv5108%20http://scripts.iucr.org/cgi-bin/paper?S1600577515009054.

[143] J. Hu, B. Setiadinata, T. Aarholt, A. Garner, A. Vilalta-clemente, J. M. Partezana, P. Frankel, P. Bagot, S. Lozano-perez, A. Wilkinson, M. Preuss, M. Moody, and C. Grovenor, "Understanding Corrosion and Hydrogen Pickup of Zirconium Fuel Cladding Alloys: The Role of Oxide Microstructure, Porosity, Suboxides, and Second-Phase Particles," *Zirconium in the Industry: 18Th International Symposium*, no. August, pp. 93–126, Jan. 2018. DOI: 10.1520/STP159720160071. [Online]. Available: https://www.astm.org/doiLink.cgi?STP159720160071.

[144] H. Okamoto, "H-Zr (Hydrogen-Zirconium)," *Journal of Phase Equilibria and Diffusion*, vol. 27, no. 5, pp. 548–549, 2006, ISSN: 1547-7037. DOI: 10.1007/bf02736475. [Online]. Available: http://link.springer.com/10.1007/BF02736475.

[145] H. Khanchandani, A. A. El-Zoka, S. H. Kim, U. Tezins, D. Vogel, A. Sturm, D. Raabe, B. Gault, and L. T. Stephenson, "Laser-equipped gas reaction chamber for probing environmentally sensitive materials at near atomic scale," *PLoS ONE*, vol. 17, no. 2 February, e0262543, Feb. 2022, ISSN: 19326203. DOI: 10.1371/journal.pone.0262543. arXiv: 2107.11987. [Online]. Available: https://journals.plos.org/plosone/article?id=10.1371/journal.pone.0262543.

[146] Y. Chang, I. Mouton, L. Stephenson, M. Ashton, G. Zhang, A. Szczepaniak, W. Lu, D. Ponge, D. Raabe, and B. Gault, "Quantification of solute deuterium in titanium deuteride by atom probe tomography with both laser pulsing and high-voltage pulsing: influence of the surface electric field," *New Journal of Physics*, vol. 21, no. 5, p. 053 025, May 2019, ISSN: 1367-2630. DOI: 10.1088/1367-2630/ab1c3b. [Online]. Available: https://iopscience.iop.org/article/10.1088/1367-2630/ab1c3b.

[147] S. H. Yoo, S. H. Kim, E. Woods, B. Gault, M. Todorova, and J. Neugebauer, "Origins of the hydrogen signal in atom probe tomography: Case studies of alkali and noble metals," *New Journal of Physics*, vol. 24, no. 1, p. 013 008, Jan. 2022, ISSN: 13672630. DOI: 10.1088/1367-2630/ac40cd. [Online]. Available: https://iopscience.iop.org/article/10.1088/1367-2630/ac40cd.

[148] D. Haley, *Range Check*, 2014. [Online]. Available: https://sourceforge.net/projects/apttools/files/extras/.

[149] A. Callow, "Atom probe tomography of irradiated zirconium alloys," PhD, University of Oxford, 2021.

[150] Z. Yu, A. Couet, and M. Bachhav, "Irradiation-induced Nb redistribution of ZrNb alloy: An APT study," *Journal of Nuclear Materials*, vol. 516, pp. 100–110, Apr. 2019, ISSN: 00223115. DOI: 10.1016/j.jnucmat.2019.01.015.

[151] Z. Yu, M. Bachhav, F. Teng, L. He, M. Dubey, and A. Couet, "STEM/EDS and APT study on the microstructure and microchemistry of neutron irradiated ZIRLOTM," *Journal of Nuclear Materials*, vol. 573, Jan. 2023, ISSN: 00223115. DOI: 10.1016/j.jnucmat.2022.154139.

[152] J. Wei, P. Frankel, E. Polatidis, M. Blat, A. Ambard, R. J. Comstock, L. Hallstadius, D. Hudson, G. D. Smith, C. R. Grovenor, M. Klaus, R. A. Cottis, S. Lyon, and M. Preuss, "The effect of Sn on autoclave corrosion performance and corrosion mechanisms in Zr-Sn-Nb alloys," *Acta Materialia*, vol. 61, no. 11, pp. 4200–4214, Jun. 2013, ISSN: 13596454. DOI: 10.1016/j.actamat.2013.03.046.

[153] J. Hu, B. Setiadinata, T. Aarholt, P. Bagot, M. Moody, C. R. Grovenor, and N. Ni, "High-resolution characterization of corrosion and hydrogen pickup of Zr cladding alloys," in *TopFuel*, Sep. 2015. [Online]. Available: https://research.manchester.ac.uk/en/publications/high-resolution-characterisation-of-corrosion-and-hydrogen-pickup.

[154] L. J. Johnson, M. Thuvander, K. Stiller, M. Odén, and L. Hultman, "Blind deconvolution of time-of-flight mass spectra from atom probe tomography," *Ultramicroscopy*, vol. 132, pp. 60–64, Sep. 2013, ISSN: 03043991. DOI: 10.1016/j.ultramic.2013.03.015.

[155] F. Meisenkothen, D. V. Samarov, I. Kalish, and E. B. Steel, "Exploring the accuracy of isotopic analyses in atom probe mass spectrometry," *Ultramicroscopy*, vol. 216, p. 113 018, Sep. 2020, ISSN: 18792723. DOI: 10.1016/j.ultramic.2020.113018.

[156] M. Maus, M. Cotlet, J. Hofkens, T. Gensch, F. C. De Schryver, J. Schaffer, and C. A. Seidel, "An experimental comparison of the maximum likelihood estimation and nonlinear least-squares fluorescence lifetime analysis of single molecules," *Analytical Chemistry*, vol. 73, no. 9, pp. 2078–2086, 2001, ISSN: 00032700. DOI: 10.1021/ac000877g. [Online]. Available: https://pubs.acs.org/sharingguidelines.

[157] G. D. W. Smith, D. Hudson, P. D. Styman, and C. A. Williams, "Studies of dislocations by field ion microscopy and atom probe tomography," *Philosophical Magazine*, vol. 93, no. 28-30, pp. 3726–3740, 2013, ISSN: 1478-6435. DOI: 10.1080/14786435.2013.818257. [Online]. Available: https://www.tandfonline.com/doi/pdf/10.1080/14786435.2013.818257?needAccess=true%20http://www.tandfonline.com/doi/abs/10.1080/14786435.2013.818257.

[158] V. Kain, "Stress corrosion cracking (SCC) in stainless steels," in *Stress corrosion cracking: Theory and practice*, Woodhead Publishing Limited, 2011, pp. 199–244, ISBN: 9781845696733. DOI: 10.1533/9780857093769.3.199. [Online]. Available: http://dx.doi.org/10.1533/9780857093769.3.199.

[159] H. He, J. E. Halpin, S. R. Popuri, L. Daly, J. W. G. Bos, M. P. Moody, D. A. Maclaren, and P. A. Bagot, "Atom Probe Tomography of a Cu-Doped TiNiSn Thermoelectric Material: Nanoscale Structure and Optimization of Analysis Conditions," *Microscopy and Microanalysis*, vol. 28, no. 4, pp. 1340–1347, 2022, ISSN: 14358115. DOI: 10.1017/S1431927621012162.

[160] A. Sarkar and K. L. Murty, “Microstructure-mechanical property correlation of cryo rolled Zircaloy-4,” *Journal of Nuclear Materials*, vol. 456, pp. 287–291, Jan. 2015, ISSN: 00223115. DOI: 10.1016/j.jnucmat.2014.09.071. [Online]. Available: https://www.sciencedirect.com/science/article/pii/S0022311514006710.

[161] E. A. Gulbransen and K. F. Andrew, “Diffusion of Hydrogen and Deuterium in High Purity Zirconium,” *Journal of The Electrochemical Society*, vol. 101, no. 11, p. 560, 1954, ISSN: 00134651. DOI: 10.1149/1.2781154.

[162] I. Takagi, K. Une, S. Miyamura, and T. Kobayashi, “Deuterium diffusion in steam-corroded oxide layer of zirconium alloys,” in *Journal of Nuclear Materials*, vol. 419, Dec. 2011, pp. 339–346. DOI: 10.1016/j.jnucmat.2011.06.001.

[163] G. Sundell, M. Thuvander, P. Tejland, M. Dahlbäck, L. Hallstadius, and H. O. Andrén, “Redistribution of alloying elements in Zircaloy-2 after in-reactor exposure,” *Journal of Nuclear Materials*, vol. 454, no. 1-3, pp. 178–185, 2014, ISSN: 00223115. DOI: 10.1016/j.jnucmat.2014.07.072. [Online]. Available: https://core.ac.uk/download/pdf/70609274.pdf.

[164] J. Hu, T. Aarholt, B. Setiadinata, K. Li, A. Garner, S. Lozano-Perez, M. Moody, P. Frankel, M. Preuss, and C. Grovenor, “A multi-technique study of “barrier layer” nano-porosity in Zr oxides during corrosion and hydrogen pickup using (S)TEM, TKD, APT and NanoSIMS,” *Corrosion Science*, vol. 158, Sep. 2019, ISSN: 0010938X. DOI: 10.1016/j.corsci.2019.108109.

Appendix A

Experimental Data

The following section is for reference only and lists the experimental ID for each APT data set used in this work and analysis conditions (if known). Some of the data sets are not used in this thesis directly, but were produced as part of the project and are listed for reference. The data used to produce specific figures are recorded in Appendix B. The 'RXXX_' part of each experimental ID refers to the atom probe ID. Experiments with ID beginning 'R14_' were produced using the LEAP 3000X HR, 'R5083_' (or 'R83_') using a LEAP 5000 XR and 'R5107_' the NuMAP LEAP 5000 XR and were produced at the University of Oxford

A.1 Experimental Methods

Daniel Hudson's laser energy optimisation study is run R14_06716 [100]. The APT analysis conditions were a temperature of 60K and a 200 kHz laser pulse frequency. The laser energy was varied between 0.2 nJ and 0.6 nJ at 0.05 nJ intervals and 1 million ions were collected at each laser energy.

A.2 Deuterium Charging Protocol Development

Table A.1 contains the APT experiment ID and analysis conditions for the experiments conducted as part of the work to develop a deuterium charging protocol.

Table A.2 contains the APT experiment ID and analysis conditions for the experiments used to test the water vapour trap.

Table A.3 contains the APT experiment ID and analysis conditions for the experiments conducted to identify sources of oxidation during the APT charging protocol.

Table A.4 contains the APT experiment ID and analysis conditions for the experiments conducted during the author's MEng Project which are relevant to this work [128].

Table A.1: Details of the APT experiments of the charged Zr alloy samples conducted as part of Chapter 4, Deuterium Charging Protocol Development and analysis conditions where T is the temperature, E the laser pulse energy, PF is the laser pulse frequency and DR is the detection rate.

APT Experiment ID	Material	LEAP	APT Analysis Conditions				Notes
			T (K)	E (pJ)	PF (kHz)	DR (%)	
R14_28018	As-received Zircaloy-4	3000X HR	55	350	200	0.5	Pre-run for deuterium charge
R14_28019	As-received Zircaloy-4	3000X HR	55	350	200	0.5	Pre-run for deuterium charge
R14_28033	Deuterated Zircaloy-4	3000X HR	55	350	200	0.5	300 C, 1000 mbar for 15 mins Cooled in deuterium gas Pre-run: R14_28019
R14_28074	Deuterated Zircaloy-4	3000X HR	55	350	200	0.5	300 C, 1000 mbar for 15 mins Cooled in deuterium gas Pre-run: R14_28018
R5083_10682	As-received Zircaloy-4	5000 XR	55	50	200	0.5	Pre-run for deuterium charge
R5083_10721	Deuterated Zircaloy-4	5000 XR	55	50	200	0.5	325 C, 1000 mbar for 1.5 hours Cooled in deuterium gas Pre-run: R5083_10682
R5083_10891	As-received Zircaloy-4	5000 XR	55	50	200	0.5	Pre-run for deuterium charge

Continued on next page

APT Experiment ID	Material	LEAP	APT Analysis Conditions				Notes
			T (K)	E (pJ)	PF (kHz)	DR (%)	
R5083_11031	Deuterated Zircaloy-4	5000 XR	55	50	200	0.5	325 C, 1000 mbar for 3 hours Quenched in deuterium gas Pre-run: R5083_10891
R5083_12551	Pure Zr wire	5000 XR	55	50	200	0.5	Pre-run for deuterium charge
R5083_22891	Deuterated Zr wire	5000 XR	55	50	200	0.5	325 C, 1000 mbar for 1.5 hours Cooled in deuterium gas Pre-run: R5083_10826
R5107_10826	Pure Zr wire	5000 XR	55	50	200	0.5	Pre-run for deuterium charge
R5107_10875	Deuterated Zr wire	5000 XR	55	50	200	0.5	325 C, 1000 mbar for 1.5 hours Cooled in deuterium gas Pre-run: R5083_10826

Table A.2: Details of the APT experiments conducted to test the water vapour trap and APT analysis conditions where T is the temperature, E the laser pulse energy, PF is the laser pulse frequency and DR is the detection rate.

APT Experiment ID	Material	LEAP	APT Analysis Conditions				Notes
			T (K)	E (pJ)	PF (kHz)	DR (%)	
R14_27770	W Wire	3000X HR	55	500	200	0.5	Pre-run to test the water vapour trap
R14_27771	W Wire	3000X HR	55	500	200	0.5	Pre-run to test the water vapour trap
R14_27818	W Wire	3000X HR	55	500	200	0.5	Pump exposure under a N2 ballast Pre-run R14_27770
R14_27839	W Wire	3000X HR	55	500	200	0.5	Deuterium charge for 15 mins, 900$\sim$mbar at room temperature
R14_27840	W Wire	3000X HR	55	500	200	0.5	Deuterium charge for 15 mins, 900$\sim$mbar at 300C Pre-run R14_27771

Table A.3: Details of the APT experiments conducted to test for sources of oxidation during the deuterium charging protocol and APT analysis conditions where T is the temperature, E the laser pulse energy, PF is the laser pulse frequency and DR is the detection rate.

APT Experiment ID	Material	LEAP	APT Analysis Conditions				Notes
			T (K)	E (pJ)	PF (kHz)	DR (%)	
R5083_11046	As-received Zircaloy-4	5000 XR	55	50	200	0.5	Test for oxidation during transfer to the reaction cell
R5083_11051	As-received Zircaloy-4	5000 XR	55	50	200	0.5	Test for oxidation during sample storage in the buffer chamber
R5083_11327	As-received Zircaloy-4	5000 XR	55	50	200	0.5	Test for oxidation in VCTM transfer Compare mass spectra LEAPs Sample 1
R5083_11328	As-received Zircaloy-4	5000 XR	55	50	200	0.5	Test for oxidation in VCTM transfer Compare mass spectra LEAPs Sample 2
R5107_10414	As-received Zircaloy-4	5000 XR	55	50	200	0.5	Test for oxidation in VCTM transfer Compare mass spectra LEAPs Sample 2

Continued on next page

APT Experiment ID	Material	LEAP	APT Analysis Conditions				Notes
			T (K)	E (pJ)	PF (kHz)	DR (%)	
R5107_10415	As-received Zircaloy-4	5000 XR	55	50	200	0.5	Test for oxidation in VCTM transfer Compare mass spectra LEAPs Sample 1
R5111_12172	As-received Zircaloy-4	5000 XS	55	50	200	0.5	Test for oxidation in VCTM transfer Compare mass spectra LEAPs Sample 1
R5111_12173	As-received Zircaloy-4	5000 XS	55	50	200	0.5	Test for oxidation in VCTM transfer Compare mass spectra LEAPs Sample 2

Table A.4: Details of the APT experiments of the charged Zr alloy samples conducted by the author as part of her MEng Thesis [128] and APT analysis conditions where T is the temperature, E the laser pulse energy, PF is the laser pulse frequency and DR is the detection rate.

APT Experiment ID	Material	LEAP	APT Analysis Conditions				Notes
			T (K)	E (pJ)	PF (kHz)	DR (%)	
R14_26651	80% cold worked Zircaloy-4	3000X HR	55	350	200	0.5	Pre-run for deuterium charge
R14_26652	As-received Zircaloy-4	3000X HR	55	350	200	0.5	Pre-run for deuterium charge
R14_26666	As-received Zircaloy-4	3000X HR	55	350	200	0.5	Pre-run for deuterium charge
R14_26669	Deuterium charged Zircaloy-4	3000X HR	55	350	200	0.5	300 C, 900 mbar for 15 mins Pre-run: R14_26666
R14_26671	Deuterium charged Zircaloy-4	3000X HR	55	350	200	0.5	300 C, 900 mbar for 15 mins Pre-run: R14_26652
R14_26677	Deuterium charged 80% cold worked Zircaloy-4	3000X HR	55	350	200	0.5	300 C, 900 mbar for 15 mins Pre-run: R14_26651

A.3 Cryogenic Focused Ion Beam Sample Preparation

Table A.5: APT experiments conducted as part of work in Chapter 5, Cryogenic Focused Ion Beam Sample Preparation and the associated analysis conditions where T is the temperature, E the laser pulse energy, PF is the laser pulse frequency and DR is the detection rate.

APT Experiment ID	Material	LEAP	APT Analysis Conditions				Notes
			T (K)	E (pJ)	PF (kHz)	DR (%)	
R5083_10218	As-received Zircaloy-4	5000 XR	55	50	200	0.5	Conventional FIB
R5083_10223	As-received Zircaloy-4	5000 XR	55	50	200	0.5	Conventional FIB
R5083_10224	As-received Zircaloy-4	5000 XR	55	50	200	0.5	Conventional FIB
R5083_10225	As-received Zircaloy-4	5000 XR	55	50	200	0.5	Conventional FIB
R5083_22615	Deuterated Zircaloy-4	5000 XR	55	50	200	0.5	Cryogenic FIB
R5083_22617	Deuterated Zircaloy-4	5000 XR	55	50	200	0.5	Cryogenic FIB
R5083_22619	As-received Zircaloy-4	5000 XR	55	50	200	0.5	Cryogenic FIB
R5083_22861	Deuterated Zircaloy-4	5000 XR	55	50	200	0.5	Cryogenic FIB
R5083_22866	Deuterated Zircaloy-4	5000 XR	55	50	200	0.5	Cryogenic FIB
R5083_22872	Deuterated Zircaloy-4	5000 XR	55	50	200	0.5	Cryogenic FIB
R5083_22874	As-received Zircaloy-4	5000 XR	55	50	200	0.5	Cryogenic FIB
R5083_22876	As-received Zircaloy-4	5000 XR	55	50	200	0.5	Cryogenic FIB

Continued on next page

APT Experiment ID	Material	LEAP	APT Analysis Conditions				Notes
			T (K)	E (pJ)	PF (kHz)	DR (%)	
R5083_22895	As-received Zircaloy-4	5000 XR	55	50	200	0.5	Cryogenic FIB
R5083_22897	As-received Zircaloy-4	5000 XR	55	50	200	0.5	Cryogenic FIB

A.4 Improving the Data Analysis of Deuterated Zr Alloy APT Data

Table A.6 contains the experimental data used in Chapter 6. R96_27479 is the data set containing the deuteride. All other data sets were used to produce the H2:H ratio.

Table A.6: Details of the APT experimental data used in Chapter 6, Improving the Data analysis of Deuterated Zr alloy samples. The APT analysis conditions are given if known, where T is the temperature, E the laser pulse energy, PF is the laser pulse frequency and DR is the detection rate.

APT Experiment ID	Material	LEAP	APT Analysis Conditions			
			T(K)	E (pJ)	PF (kHz)	DR (%)
R14_06716	Zirlo	3000X HR	60	0.2-0.6 nJ	200	unknown
R5083_08154	Zircaloy-4	5000 XR	55	50	200	0.5
R5083_08156	Zircaloy-4	5000 XR	55	50	200	0.5
R5083_08478	Zircaloy-4	5000 XR	55	50	200	0.5
R5083_08482	Zircaloy-4	5000 XR	55	50	200	0.5
R96_29140	Zircaloy-4	5000 XR	60	unknown		
R96_29148	Zircaloy-4	5000 XR	60	50	250	1
R96_29328	Zircaloy-4	5000 XR	60	unknown		
R96_29334	Zircaloy-4	5000 XR	60	50	200	0.5
R96_30687	Zircaloy-4	5000 XR	50	unknown		
R83_03388	Zircaloy-4	5000 XR	55	50	200	unknown
R83_03495	Zircaloy-4	5000 XR	55	50	200	0.2
R83_03759_75pJ	Zircaloy-4	5000 XR	55	75	200	unknown
R83_03759_100pJ	Zircaloy-4	5000 XR	55	100	200	unknown
R83_03794	Zircaloy-4	5000 XR	55	50	200	0.5
R83_04056	Zr-2.5Nb	5000 XR	55	50	200	0.5
R83_04745	Zr-2.5Nb	5000 XR	55	40	200	0.4

Continued on next page

APT Experiment ID	Material	LEAP	APT Analysis Conditions			
			T(K)	E (pJ)	PF (kHz)	DR (%)
R83_05046	Zr-2.5Nb	5000 XR	55	55	200	0.4
R83_05830	Zr-0.8Nb	5000 XR	55	60	200	0.4
R83_05832	Zr-0.8Nb	5000 XR	55	65	200	0.5
R83_05834	Zr-0.8Nb	5000 XR	55	65	200	0.3
R83_05945	Zr-0.8Nb	5000 XR	60	55	200	0.2
R83_06011	Zr-0.2Nb	5000 XR	55	40	200	0.4
R83_06012	Zr-0.2Nb	5000 XR	55	50	200	0.4
R83_06013	Zr-0.2Nb	5000 XR	55	40	200	0.4
R96_27479	Zircaloy-4	5000 XR	60	60	250	1-2

A.5 Atom Probe Tomography of Cold Worked Zircaloy-4

Table A.7 and A.8 provide details of all of the APT experiments associated with this work.

Table A.9 contains the information of all of the other experimental data associated with this chapter.

Table A.7: APT experiments for Chapter 7, Atom Probe Tomography of as-received Zircaloy-4 samples and analysis conditions where T is the temperature, E the laser pulse energy, PF is the laser pulse frequency and DR is the detection rate. SPP is a second phase particle and GB, a grain boundary.

APT Experiment ID	Material	LEAP	APT Analysis Conditions				Notes
			T (K)	E (pJ)	PF (kHz)	DR (%)	
R14_26425	As-received Zircaloy-4	3000X HR	55	350	200	0.5	Electropolished
R14_26652	As-received Zircaloy-4	3000X HR	55	350	200	0.2	Electropolished
R14_26666	As-received Zircaloy-4	3000X HR	55	350	200	0.2	Electropolished
R5083_07641	As-received Zircaloy-4	5000 XR	55	50	200	0.5	Electropolished
R5083_08154	As-received Zircaloy-4	5000 XR	55	50	200	0.5	FIB, SPP in sample
R5083_08156	As-received Zircaloy-4	5000 XR	55	50	200	0.5	FIB, SPP in sample
R5083_08482	As-received Zircaloy-4	5000 XR	55	50	200	0.5	FIB, GB in sample
R5083_10218	As-received Zircaloy-4	5000 XR	55	50	200	0.5	FIB
R5083_10223	As-received Zircaloy-4	5000 XR	55	50	200	0.5	FIB
R5083_10224	As-received Zircaloy-4	5000 XR	55	50	200	0.5	FIB
R5083_10225	As-received Zircaloy-4	5000 XR	55	50	200	0.5	FIB
R5083_10682	As-received Zircaloy-4	5000 XR	55	50	200	0.5	Electropolished and FIB sharpened

Table A.8: APT experiments for Chapter 7 of cold worked Zircaloy-4 samples and analysis conditions where T is the temperature, E the laser pulse energy, PF is the laser pulse frequency and DR is the detection rate. CW stands for cold worked.

APT Experiment ID	Material	LEAP	APT Analysis Conditions				Notes
			T (K)	E (pJ)	PF (kHz)	DR (%)	
R5083_08315	30% CW Zircaloy-4	5000 XR	55	50	200	0.5	Electropolished and FIB sharpened
R5083_08317	30% CW Zircaloy-4	5000 XR	55	50	200	0.5	Electropolished and FIB sharpened
R5083_08403	30% CW Zircaloy-4	5000 XR	55	50	200	0.5	Electropolished and FIB sharpened
R5083_08882	60% CW Zircaloy-4	5000 XR	55	50	200	0.5	Electropolished and FIB sharpened
R5083_09251	60% CW Zircaloy-4	5000 XR	55	50	200	0.5	Electropolished and FIB sharpened
R14_26430	80% CW Zircaloy-4	3000X HR	55	350	200	0.5	Electropolished
R14_26433	80% CW Zircaloy-4	3000X HR	55	350	200	0.5	Electropolished
R14_26551	80% CW Zircaloy-4	3000X HR	55	350	200	0.5	Electropolished
R14_26651	80% CW Zircaloy-4	3000X HR	55	350	200	0.5	Electropolished
R14_26665	80% CW Zircaloy-4	3000X HR	55	350	200	0.5	Electropolished

Table A.9: Other experimental data associated with Chapter 7.

Data Type	Material	Associated APT Data	Notes
TEM	30% Cold Worked	30% cold worked APT data	Data produced by D. Tweddle and Z. Shen Data on nas-FIM drive
TEM	80% Cold Worked	80% cold worked APT data	Data produced by J. Haley Data on nas-FIM drive
EBSD	As-received Zircaloy-4	R5083_08154	Data on nas-FIM drive
		R5083_08156	Associated TKD data Data on nas-FIM drive
		R5083_08482	Associated TKD data Data on nas-FIM drive
TKD	As-received Zircaloy-4	R5083_08156	Data on nas-FIM drive
TKD	As-received Zircaloy-4	R5083_08482	Data on nas-FIM drive

A.6 Atom Probe Tomography of Irradiated Zircaloy-2

Table A.10 contains the details of the APT experiments conducted on a neutron irradiated Zircaloy-2 sheet. Although not featured in the thesis, a second set of experiments were conducted looking at a beta-quenched Zircaloy-2 sheet and those experiments are listed in Table A.11.

Table A.10: APT experiments for Chapter 8, Atom Probe Tomography of Irradiated Zircaloy-2 samples and analysis conditions where T is the temperature, E the laser pulse energy, PF is the laser pulse frequency and DR is the detection rate.

APT Experiment ID	Material	LEAP	APT Analysis Conditions				Notes
			T (K)	E (pJ)	PF (kHz)	DR (%)	
R5107_52000	As-received Zircaloy-2	5000 XR	55	50	200	0.5	MIDAS BOR60 material, W8-7
R5107_52001	As-received Zircaloy-2	5000 XR	55	50	200	0.5	MIDAS BOR60 material, W8-7
R5107_52002	As-received Zircaloy-2	5000 XR	55	50	200	0.5	MIDAS BOR60 material, W8-7
R5107_52067	As-received Zircaloy-2	5000 XR	55	50	200	0.5	MIDAS BOR60 material, W8-7
R5107_52068	As-received Zircaloy-2	5000 XR	55	50	200	0.5	MIDAS BOR60 material, W8-7
R5107_62100	Deuterated Zircaloy-2	5000 XR	55	50	200	0.5	MIDAS BOR60 material, W8-7
R5107_62175	Deuterated Zircaloy-2	5000 XR	55	50	200	0.5	MIDAS BOR60 material, W8-7
R5107_62176	Deuterated Zircaloy-2	5000 XR	55	50	200	0.5	MIDAS BOR60 material, W8-7
R5107_62177	Deuterated Zircaloy-2	5000 XR	55	50	200	0.5	MIDAS BOR60 material, W8-7
R5107_62179	Deuterated Zircaloy-2	5000 XR	55	50	200	0.5	MIDAS BOR60 material, W8-7
R5107_62180	Deuterated Zircaloy-2	5000 XR	55	50	200	0.5	MIDAS BOR60 material, W8-7

Table A.11: APT experiments conducted on beta-quenched Zircaloy-2 and the analysis conditions where T is the temperature, E the laser pulse energy, PF is the laser pulse frequency and DR is the detection rate.

APT Experiment ID	Material	LEAP	APT Analysis Conditions				Notes
			T (K)	E (pJ)	PF (kHz)	DR (%)	
R5107_51995	β-quenched Zircaloy-2	5000 XR	55	50	200	0.5	MIDAS BOR60 material W7-7
R5107_51996	β-quenched Zircaloy-2	5000 XR	55	50	200	0.5	MIDAS BOR60 material W7-7
R5107_51997	β-quenched Zircaloy-2	5000 XR	55	50	200	0.5	MIDAS BOR60 material W7-7
R5107_51988	Deuterated β-quenched Zircaloy-2	5000 XR	55	50	200	0.5	MIDAS BOR60 material W7-7
R5107_51989	Deuterated β-quenched Zircaloy-2	5000 XR	55	50	200	0.5	MIDAS BOR60 material W7-7
R5107_51990	Deuterated β-quenched Zircaloy-2	5000 XR	55	50	200	0.5	MIDAS BOR60 material W7-7

Appendix B

Details of Figures

This appendix is for reference only and gives the data used for each figure. ‘RXXX_’ part of each experimental ID refers to the atom probe ID. Experiments with ID beginning ‘R14_’ were produced using the LEAP 3000X HR, ‘R5083_’ using a LEAP 5000 XR and ‘R5107_’ the NuMAP LEAP 5000 XR and were produced at the University of Oxford.

B.1 Experimental Methods

Table B.1: Experimental data used to produce figures in Chapter 3, Experimental Methods

Figure	APT Experiment ID
3.3	R5083_10218
3.5	R5083_10218
3.6	R5083_10218
3.7	R14_06716
3.8	R14_06716

B.2 Deuterium Charging Protocol Development

Table B.2: APT Data used to produce figures in Chapter 4, Deuterium Charging Protocol Development

Figure	APT Experiment ID
4.1	R14_26677
4.3	R14_26677
4.10	R14_28074
4.11	R14_28074
4.12	R14_28074
4.13	R14_26677
4.13	R14_28074
4.13	R5083_10682

Table B.3: Experimental data used to produce figures in Chapter 4, Deuterium Charging Protocol Development

Figure	APT Experiment ID	RGA Scan data
4.6	R14_26677	180502-RGA-scan-post-charge
4.9	R14_26677	180502-RGA-scan-post-charge
4.9	R14_27840	20190520_RGA-scanPost2ndCharge

B.3 Cryogenic Focused Ion Beam Sample Preparation

Table B.4: Experimental Data used to produce Figures in Chapter 5, Cryogenic Focused Ion Beam Sample Preparation

Figure	APT Experiment ID	Notes
5.3	R5083_22615	Cryogenic FIB
	R5083_22617	Cryogenic FIB
	R5083_22619	Cryogenic FIB
	R5083_22861	Cryogenic FIB
	R5083_22874	Cryogenic FIB
	R5083_22876	Cryogenic FIB
	R5083_22895	Cryogenic FIB
	R5083_22897	Cryogenic FIB
	R5083_08156	Conventional FIB
	R5083_10218	Conventional FIB
	R5083_10223	Conventional FIB
	R5083_10224	Conventional FIB
	R5083_10225	Conventional FIB
	R5083_11325	Conventional FIB
	R5083_11327	Conventional FIB
	R5083_11328	Conventional FIB
	R5107_10414	Conventional FIB
	R5107_10415	Conventional FIB
5.4	R5083_22866	
5.5	R5083_22866	
5.6	R5083_22861	

B.4 Improving the Data Analysis of Deuterated Zr Alloy APT Data

Table B.5: Experimental data used to produce the figures in Chapter 4, Deuterium Charging Protocol Development

Figure	APT Experiment ID	Notes
6.2	R14_06716	Data produced by D. Hudson [100]
6.3	R14_06716	Data produced by D. Hudson [100], Section of data set analysed using 0.6 nJ laser energy
6.6	R14_06716	Data produced by D. Hudson [100], Section of data set analysed using 0.6 nJ laser energy
6.8	R96_27479	Data set produced by A. Breen [116]
6.9	R96_27479	Data set produced by A. Breen [116]
6.10	R96_27479	Data set produced by A. Breen [116]
6.11	R96_27479	Data set produced by A. Breen [116]
6.12	R96_27479	Data set produced by A. Breen [116] R96_27479-v01-roi_LineProfile2.pos
6.13	R96_27479	Data set produced by A. Breen [116] R96_27479-v01-roi_LineProfile2-LocalDecompTestroi.pos
6.15	R96_27479	Data set produced by A. Breen [116] R96_27479-v01-roi_LineProfile2-LocalDecompTestroi.pos

Continued on next page

Figure	APT Experiment ID	Notes
6.16	R96_27479	Data set produced by A. Breen [116] R96_27479-v01-roi_LineProfile2-LocalDecompTestroi-2nm.pos R96_27479-v01-roi_LineProfile2-LocalDecompTestroi-10nm.pos
6.18	R96_27479	Data set produced by A. Breen [116] Shuffled data : R96_27479-v01-roi_LineProfile2-LocalDecompTestroi-RandomIon.pos Shuffled data after local peak overlap solving: R96_27479-v01-roi_LineProfile2-LocalDecompTestroi-RandomIon-2nm.pos

B.5 Atom Probe Tomography of Cold Worked Zircaloy-4

Table B.6: Experimental data used to produce the figures in Chapter 7

Figure	APT Experiment ID
7.3	R5083_10218
7.4	R5083_10218
7.5	R5083_08317
7.6	R5083_08882
7.7	R14_26433
7.8	R14_26433
7.9	R14_26433
7.10	R5083_08156
7.11	R5083_08482

B.6 Atom Probe Tomography of Irradiated Zircaloy-2

Table B.7: Experimental data used to produce the figures in Chapter 8, Atom Probe Tomography of Irradiated Zircaloy-2

Figure	APT Experiment ID
8.2	R5107_52001
8.3	R5107_52001
8.4	R5107_52001
8.5	SIMS W8-7D_2022.06.22-10h39m22.h5
8.6	R5107_62179
8.7	R5107_62179
8.8	R5107_62179